School of Civil and Mechanical Engineering

Vibration Fault Detection for Horizontal Axis Wind Turbines (HAWT)

Mohammed Al-Hadad

This thesis is presented for the Degree of

Doctor of Philosophy

of

Curtin University

July 2019

I, Mohammed Al-Hadad, declare that this thesis titled, " Vibration Fault Detection for Horizontal Axis Wind Turbines (HAWT)" and the work presented are my own.

To the best of my knowledge and belief, this thesis contains no material previously published by any other person except where due acknowledgment has been made.

This thesis contains no material which has been accepted for the award of any other degree or diploma in any university.

Signature……..…

Date.....

Abstract

This research has investigated novel vibration condition monitoring methods for horizontal-axis wind turbines using a range of case studies simulating various failure modes of the blades and tower, including the effect of coupling of rotating and non-rotating components of the system. The research utilised a small scale experimental test rig that was developed to monitor vibration behaviour under different transient loads as a function of rotor phase, including the measurement of axial, in-plane and out-of-plane blade strain, blade tip acceleration and main shaft centre line motion in orthogonal directions, in addition to triaxial tower vibration.

The data acquisition measurement methods included utilising a slip ring assembly on the turbine hub, providing efficient low noise signals for the measurement of the rotating components of the blade strain and acceleration. A servo-motor was used to drive the rotor, providing input transient torque and power to the main shaft for testing at the desired velocity, while minimising aerodynamic effects. Rotational velocity was measured through an encoder coupled to the motor that provided phase reference data of the shaft during rotation. In addition to accelerating the turbine rotation, the motor has the ability to provide impulsive torsional loading during the operation further exciting coupling of the system components. Orthogonal laser displacement sensors have also been instrumented to measure fluctuations of the drive shaft transverse vibration, represented through shaft orbit behaviour.

Initial tests were performed using slender aluminium rods for the blades, attached at the central hub. Subsequent testing utilised fixed pitch angle aluminium blades having no twisting along the blade length for simplification. The theoretical modeling of the fixed-free rotating cantilever rods and blades in the test rig, included identifying the strains, acceleration, and deflections of the system components during low rotational speeds for the comparison with the experimental work.

Case studies conducted during the experimental testing included tower foundation failure, mass loss from a rotating blade, unbalance conditions and transient mass collision onto a rotating blade. Rotating speeds from 10 rpm to 120 rpm were tested to demonstrate the system vibration behaviour as a function of speed. The signal processing techniques utilised instantaneous time, frequency and phase synchronous

averaging methods of the rotating and non-rotating dynamic signals to confirm the coupling of the various vibration components for the case studies. The research demonstrates the coupling of the blade vibration components with the main shaft and tower response, showing particularly how rotor revolution by revolution monitoring, can be used to identify immediate changes in the system behaviour, identifying potential faults. Furthermore, the coupling characteristics between the rotating and non-rotating components can be used to confirm the nature of the failure modes.

Tower foundation fatigue failure, represented by a 4 cm crack, was detected during the implementation of the various transient and artificial faults, caused by the excessive vibration of the wind turbine test rig system. The vibration measurement analysis during the months prior to the crack observation confirmed the rapid evolution of the fatigue crack.

In short, the outcomes of this research provide novel developed techniques for vibration condition monitoring of the horizontal-axis wind turbine utilising a particular test rig. It also presents the demonstration of the wind turbine blade behaviour as a thin cantilever beam through strain and acceleration measurements based on dynamic vibrations, as well as presenting an improved understanding of the synchronous vibrations of the wind turbine components during low frequency operation.

Publications list

The papers publications arising from this research are as follows:

i. Mohammed Al-Hadad, Kristoffer K McKee, Ian Howard, (2019). Vibration characteristic responses due to transient mass loading on wind turbine blades, Engineering Failure Analysis, 102, pp. 187-202.

ii. Mohammed al-Hadad, Kristoffer McKee and Ian Howard, (2018). Vibration fault detection of fracture in a wind turbine tower foundation. Proceedings of the 11th International Conference on Structural Integrity and Failure (SIF-2018) 3-6 December 2018, UWA Perth.

iii. Mohammed Al-Hadad, Abdullah Slebe Hwais, Kristoffer K McKee, and Ian Howard, (2017). Rotating and non-rotating sensors for improving condition monitoring of wind turbines. Proceedings of Australasian Congress on Applied Mechanics, ACAM 9, Sydney, November 2017.

Acknowledgements

I would like to express my indebtedness to Professor Ian Howard who always gave inspirational guidance, support and patience during my PhD study. Professor Howard has been a great advisor who was always available to discuss and support all the technical problems and his dedication to being a research academic has truly inspired me and he has always been available to discuss many things both at the office and laboratory. He would kindly endorse me and my colleagues and gave me opportunities to attend several international conferences. His patience in revising and commenting on the thesis draft is greatly appreciated.

I am also thankful to my Co-Supervisor Dr Kristoffer McKee for his extensive suggestion and valuable advice, especially during the thesis writing and development of the Data Acquisition software. Thanks also go to Associate-Professor Ramesh Narayanaswamy for chairing my thesis committee.

My sincere thanks are also extended to: Mr. David Collier and Mr Graeme Watson from the Mechanical Engineering Department workshop at Curtin University for their technical support on manufacturing the wind turbine test rig and providing the required tools, and Mr. Frankie Sia from the Mechanical Engineering Department office for his great administration support. I would also like to thank Mr John Davidson for helping me with my test rig.

Lastly but most importantly, I would like to thank my family, especially my father, my mother, my lovely wife, and my daughters for all the sacrifices and encouragement with their great love, support and spirituality during my study.

Table of Contents

List of Tables

List of Figures

Chapter 1

1.1 Introduction

Wind turbine vibration measurement can be seen as providing a unique opportunity to assess the running condition of the complex machine and its components during routine operation. Each component in the wind turbine system has a particular vibration signature that can be used to distinguish the defect before failure occurrence. The time waveform response of the wind turbine blade and the subcomponent vibrations demonstrate the transient loading conditions during operation.

Three distinct forms of blade vibration can be characterised for the horizontal axis wind turbines which are the motion within the rotational plane (in-plane), perpendicular to the rotational plane (out-of-plane), and the longitudinal extension (axial). The most significant wind turbine blade vibrational modes are the in-plane and out-of-plane, which are substantially known as edgewise and flapwise. The excitation between the two modes affects the flexibility of the rotor blades which increases loading conditions on the blades, and hence increases the dynamic vibrations.

Notably, the out-of-plane blade motion induces undamped vibrations in wind turbines that can lead to system instability. In contrast, the in-plane mode is most likely to be aerodynamically damped, in spite of the fact that most blade fatigue damage results from the in-plane motion (Andrea Staino & Basu, 2015). The out-of-plane blade mode affects positively on the tower fluctuation due to the coupling between the rotor blade and tower fluctuation (forward and backward) (Murtagh, Basu, & Broderick, 2005). The coupling excitation between in-plane and out-of-plane modes have a further effect on the hub and driveshaft responses due to the increase in wind turbine system vibrations. The increase in blade twist angle decreases the in-plane vibrations markedly, whereas, it has only a small effect on

the out-of-plane vibrations due to the tower fluctuations. (Murtagh, Ghosh, Basu, & Broderick, 2008).

Blade-Tower vibration monitoring techniques have been investigated for small wind turbines, utilizing different types of sensors, including the use of active control systems to mitigate the dynamic vibration to the turbine system (Riziotis, Voutsinas, Politis, & Chaviaropoulos, 2004). Axial displacements of the rotor blades increased the blade flexibility due to the increase in blade surface area. This increase in axial blade dynamic displacement also resulted in increasing blade tip bending. Furthermore, the centrifugal forces that augment this axial dynamic displacement increase with increasing rotor velocity (Hall, Kielb, & Thomas, 2006).

In the last few years, researchers have shown an increased interest in modeling wind turbine blades as cantilever beams to investigate the dynamic characteristics of the turbine blades. Özdemir (Özdemir & Kaya, 2006) and Zeng (Zeng & Bert, 2001) studied flapwise bending vibration of a Bernoulli-Euler tapered cantilever beam using the linear differential transform. They addressed the effect of different tapered ratio and non-dimensional angular velocity on the increasing non-dimensional natural frequencies, while additionally, taking into consideration the hub dimension effect on the centrifugal force and angular velocity and its effect on the beam natural frequencies.

Finite element analysis has been utilized to calculate and identify the beam rotating frequency with the existence of damage over a number of cycles, where it seems that the damage effects on the beam stiffness lead to a negative impact on the beam natural frequencies. This technique has been used to assess the blade life before collapse by monitoring the blade rotating frequencies during the rotation via specifying the fatigue damage frequencies and comparing them with the measured frequencies (Beards, 1981).

Utilizing various m-files with MATLAB software for signal processing enables the provision of instantaneous monitoring of the particular rotating component during the operation, through appropriate Data Acquisition systems, hence facilitating the detection of frequencies that could be accompanied with various

faults (I. Howard, 1995). This valuable technique which uses vibration data for comparison between healthy and faulty wind turbine components has been optimised using various case studies implemented on different size wind turbines (Davide ASTOLFI, 2019).

Most of the supporting tower and driveshaft damages of wind turbines have been due to blade vibrations. To identify the fatigue fractures in these significant components required the monitoring of the turbine system vibration through particular case studies in a special set up under complex load conditions (Zhanqi Zhang, Yin, Han, & Tan, 2013). However, long-term dynamic stresses on the driveshaft and tower fluctuations are able to produce structural damage in the foundation, which begins with crack initiations.

Khatri (Khatri, 2009) demonstrated a new style of stress analysis by creating a model of the tower in ANSYS, which showed the coupling effect between yaw eccentricity and tower fluctuation and its pronounced effect on the growth of longitudinal cracks in the wind turbine foundation. Furthermore, connection flanges that contain bolts were found to be likely sites for localised crack initiation. In situ monitoring of the wind turbine foundation for the strain and lateral crack propagation utilized fiber optic strain gauges positioned along the tower structure (Hassanzadeh, 2012).

Mass collision incidents (e.g. bats and ducks) reduced the blade life due to rotation disturbance and increased blade bending of the noncolliding blade parts. Furthermore, it increased dents on the blade spanwise leading to crack initiation. Assessment of these incidents through vibrational signal analysis, enables the identification of maintenance requirements and decreases further blade damage. Furthermore, blades that experience collisions from objects carried by storms and typhoons often obtain different size defects in the blade trailing edge and spanwise and sometimes lose segments from the blade structure due to impact with solid masses. Crack initiations are subsequently likely to occur from those damage locations.

1.2 Objectives of the dissertation

The significant objective of this thesis is the detection of wind turbine faults using measured vibration at different rotor speeds and loading conditions, and confirming the blade root strain behaviour. Furthermore, the research aimed to quantify the use of contact, non-contact, rotating and non-rotating sensors for vibration fault detection through using;

- Blade strain (axial, in-plane, out-of-plane) and blade tip acceleration
- Orthogonal main shaft deflection
- Tower triaxial acceleration
- Shaft phase analysis

Additionally, this research has demonstrate improved vibration monitoring techniques using a small wind turbine test rig in the laboratory. The test rig was specifically designed with features including; servo motor drive, flexible main shaft and thin, solid cantilever rods and subsequently hollow blades. The novel techniques comprised shaft phase analysis at different loading conditions by implanting artificial faults through significant case studies.

The major limitation of the research work was the minimisation of aerodynamic effects. This deliberate approach was facilitated by using the servo motor to drive the main shaft so that the major focus of the research was the underlying rotor dynamic forced response rather than the more complex aerodynamic behaviour which was left for subsequent research.

This analysis was aimed at confirming and identifying the coupling of vibrational modes between the major rotating and non-rotating components such as the rotor blades, main shaft and tower. This can assist in diagnosing the early stage wind turbine faults using vibrational measurements, hence, avoiding failure of significant parts of the rotor system.

This research work was achieved by incorporating several procedures which can be itemised as follows;

1. Build a small wind turbine test rig in the vibration lab for implementing various vibration tests.
2. Monitoring the cantilever rotor beam behaviour at different loading conditions practically.

3. Design and build a blade model including the cantilever beam.

4. Simultaneous blade vibration monitoring in different directions (axial, in-plane, and out-of-plane).

5. Implementing different loading conditions to the blade model.

6. Monitoring the excitation due to blade vibration on the tower and driveshaft deflections.

7. Implementing various artificial faults for monitoring the blade, tower, and driveshaft vibration amplitudes.
8. Utilizing different types of sensors such as; contact, non-contact, rotating and non-rotating for vibration measurements.
9. Build a Finite Element model (ANSYS model) to simulate the practical work.

10. Detect the excessive vibrations on the test rig components which lead to fatigue failure.

11. Identify the coupling vibrational modes between the rotating and non-rotating components.

12. Assessment of the effectiveness of the various sensors in the vibration measurements and fault detection.

1.3 Scientific contribution

This work aims to contribute to the wind turbine research literature with a novel monitoring technique by utilizing a combination of contact and non-contact sensors, in a particular test rig prepared for implementing different artificial faults and monitoring the response of the rotating and non-rotating components. Further contributions can be listed as follows;

1. Demonstration of significance of rotor phase analysis on vibration response of the wind turbine components during different loading conditions.
2. Demonstration of common failure events and their typical vibration response.
3. Demonstration of novel vibration monitoring techniques using rotating and non-rotating sensors.
4. Illustration of the effectiveness of orthogonal orbit phase analysis for fault detection using main shaft deflection and tower acceleration.
5. Coupling between the blade vibrational modes and tower fluctuations.
6. Effectiveness of using simultaneous analysis of blade strain, shaft deflection, and tower acceleration

1.4 Organization of the thesis

This study is organised into nine chapters as follows and as illustrated in Figure 1.1;

Chapter one describes the motivation for the research with an emphasis on the wind turbine blade vibrational modes, and the associated coupling with other subcomponents within the wind turbine system. It further presents the significance of the artificial fault case studies that were implemented for vibration monitoring and fault diagnosis. Additionally, the thesis research focus is outlined including the research objectives, scientific contributions and limitations.

Chapter two presents a review of the wind turbine blade vibrations and the effect on the shaft and tower vibrations. The wind turbine vibration literature focusing on the blade vibrational modes and the relation with driveshaft and tower vibrational modes is presented. Furthermore, it discusses a variety of wind turbine test rigs for vibration condition monitoring, positions of measurement sensors and data acquisition techniques used.

Chapter three clarifies the method of implementing the small-scale wind turbine test rig components, including the detail of the beam and blade models and manufacturing aspects. It also explains the utilized sensors and the subsequent instrumentation, as well as the measurement signal paths from the rotating and non-rotating components to the Data Acquisition system. Additionally, the MATLAB software and subroutines for signal analysis are further outlined.

Chapter four presents the theoretical model of the test system using Finite Element Methods for the rotor cantilever beam and blade in the test rig by ANSYS software. The models included a brief analysis of predicted impact and dynamic test responses showing differences between the beam and blade behaviours and to facilitate comparison with and confirmation of the validity of the experimental results. Resonant frequencies and the fundamental modes have been calculated for both models to demonstrate the modal characteristics. Axial, in-plane and out-of-plane strain simulation has further been obtained from the models, statically and dynamically, using explicit and modal analysis. Tower acceleration and deformation have also been detected using modal analysis to differentiate the coupling effect between the rotating and non-rotating vibrational responses.

Chapter five presents the experimental analysis of the slender solid Aluminum beam model at different rotational speeds. Strain measurements have been detected using three groups of strain gauges positioned axially, in-plane, and out-of-plane near the beam root. Tower acceleration at the three dominant co-ordinates (X, Y, and Z) were measured during the experiments, simultaneously with the blade strain measurements. The driveshaft centreline orbit analysis was implemented at different rotor speeds to detect the effect of the rotor beam motion on the driveshaft dynamic behaviour. Additionally, Complex Discrete Fourier Transform analysis was used to investigate forward shaft whirling per revolution by shaft order analysis during the experiments.

Chapter six elaborates on the case studies that were implemented using the thin solid beam model. The case studies includes added and loss masses from the rotor beam to achieve imbalance effects. Furthermore, a mass collision event during 50 rpm was implemented to demonstrate the beam behaviour during the transient event, as well as, tower and driveshaft response due to the collision event. The influence of bearing bolt looseness on the beam and the test rig components vibrations was experimented with by loosening one bearing bolt to have a clearance of 2mm. The rotating and non-rotating component vibrations have been monitored during the case studies to diagnose the incipient faults by vibration signal analysis.

Chapter seven presents the hollow blade model response during the range of rotational speeds. This model was connected with the hub by a thin solid beam similar to the considered beam model that was utilized in chapter five. The effect of different rotor

speeds was experimented with on the blade, driveshaft and tower. The strain, acceleration, and displacement measurements have been captured simultaneously for monitoring the coupling effect between rotating and non-rotating components. Additionally, speed variation has been considered during one test (from 0 to 140 rpm) to demonstrate the coupling excitation between the test rig components.

Chapter eight presents the blade case studies which were implemented at different rotor speeds. Blade strain and tip acceleration were measured in this chapter simultaneously with the tower and driveshaft vibrations. The coupling between the blade and tower vibrational modes were monitored, as well as the coupling between the blade axial and in-plane modes. The blade case studies were characterised by the occurrence of a novel event which was transient mass reduction, which further led to the analysis of three different transient events in the one test.

Chapter nine summaries and discusses the significant findings that have been achieved in the thesis resulting from the various case studies, as well as an outline of important recommendations for future work.

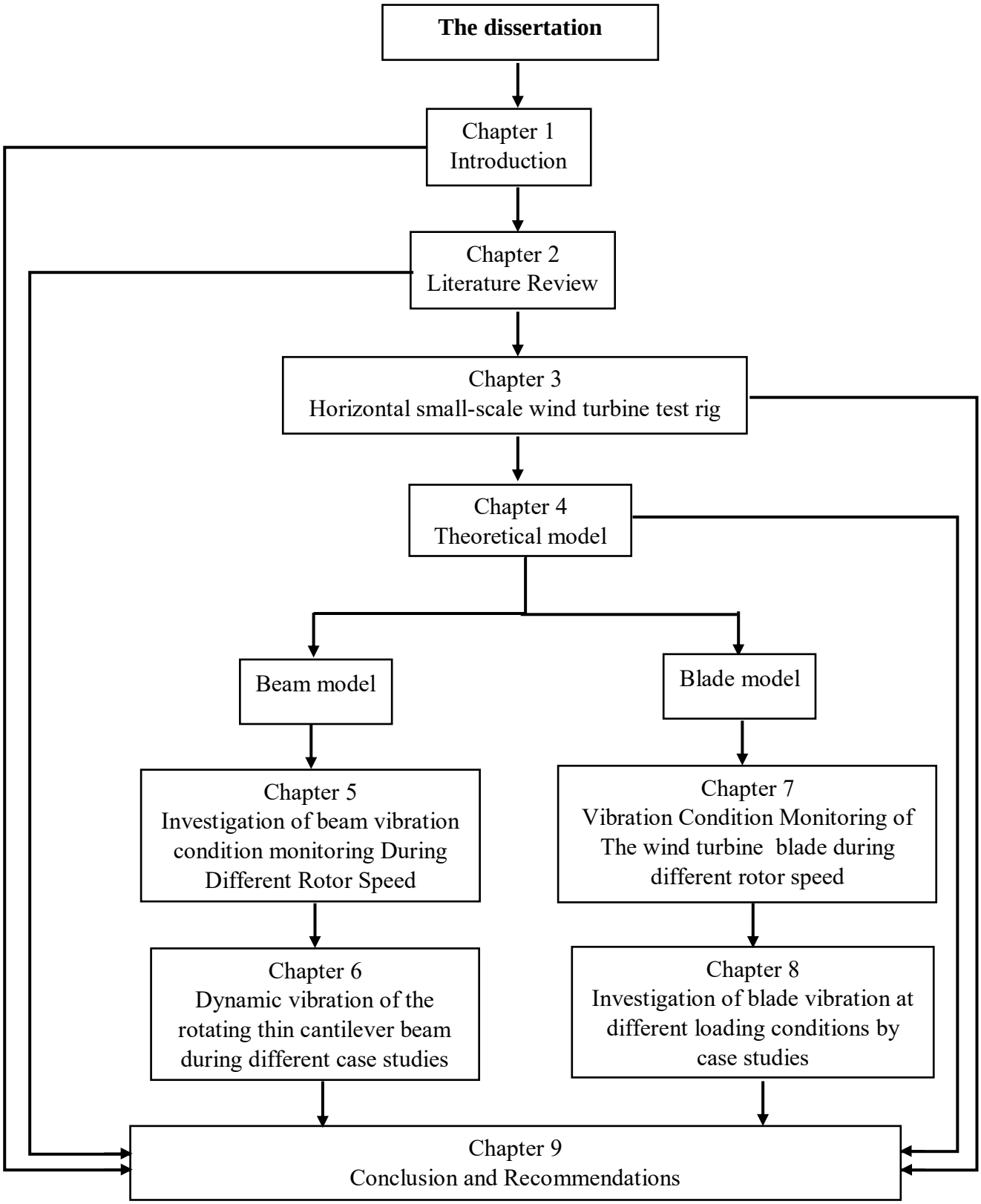

Figure 1.1 Flow chart presenting the outline of the thesis

Chapter 2 Literature review

2.1 Introduction

Vibration, which is inherent in any machine that contains rotating components, contains a wealth of information about the health of the machine. There are international standards, such as the ISO 20283-4 which specify limits for the RMS velocity values of a machine's vibration, that help to interpret what is considered "good", "healthy" or "dangerous" values.

Wind turbines consist of many parts with the blades considered to be one of the major elements of a wind turbine, and are considered one of the main sources of its vibrations. So much so, that new techniques of observing the blades and the drive train have been investigated after wind turbine life expectancies have been drastically shortened due to unexpected failings involving the blades. Blade vibrations not only causes damage in the blade itself but it can result in coupled vibrations in the nacelle and tower. Aerodynamic damping due to forward whirling modes associated with edgewise bending modes can cause damping to the wind turbine rotation. This can lead to an increase in the torque fluctuations on the generator shaft, which subsequently can affect the generated power.

This chapter will focus on reviewing the research performed in the area of horizontal axis wind turbine vibration condition monitoring and fault diagnosis, especially that affected on flapwise (out-of-plane) and edgewise (in-plane) bending vibrations. It provides a review of the wind turbine blade vibration literature as follows:

- Section 2.2: reviewing blades vibration modes; flapwise and edgewise bending.
- Section 2.3: the summary of vibration condition monitoring of Horizontal Axis Wind Turbine (HAWT) blades.
- Section 2.4: reviewing modeling of wind turbine blade as a cantilever beam.
- Section 2.5: the review of blade faults diagnosis through condition monitoring through utilizing laboratory test rig.

2.2 Reviewing blades vibration modes; flapwise (out-of-plane) and edgewise (in-plane) bending

Wind turbines are deemed as a major source of sustainable, clean energy. Due to their ability to work in different climatic conditions, these machines are prone to many issues resulting from harsh conditions such as unstable wind and waves. For example, it is common that the blade's cross-section has its centre of mass located one quarter of its chord length from the leading edge, and in conjunction with the coupling between the flapwise bending mode and the first torsional mode, can cause undesirable and often dangerously large amplitudes in vibrations in the blades and tower To help alleviate this issue, the ratio between the frequencies of the first flapwise mode to the first torsional mode should be 1 to 10 (Oette, 1974).

Avoiding the unwanted vibrations is not always obtained with the implementation of an easy solution. The amplitude of both in-plane and out-of-plane vibrations depend on several factors such as blade structure, pitch angle, wind direction angle, and aerodynamic damping, which normally has higher values in the forward vibration (out-of-plane component) than the backward vibration (in-plane direction). Moreover, the coupling between modes increases the blades aerodynamic damping, which causes rotor whirling and a drop in the rotational speed (M. Hansen, Thomsen, & Petersen, 2001). Thomson et al (2000) investigated this phenomenon by developing a method for measuring in-plane vibrations using a special mechanism installed in a wind turbine nacelle from Bonus Energy A/S. This device and setup allow the excitement of the blade edgewise vibration and identifies the positive damping of the backward vibrations in the blade edgewise position. The exciter consisted of masses screwed in to the end of a rotating cantilever beam connected to a vertical shaft installed on the drive motor. This structure was fixed on a plate at the upper part of the nacelle to create rotating forces in opposite directions, which are equivalent to the edgewise vibrations.

Furthermore, in-plane bending vibrations have a negative effect on the wind turbine rotation, which leads to a reduction in the power output through induced rotation obstruction and whirling in the drive shaft. In large wind turbines, this causes an increase in the aerodynamic damping and a drop in the rotational speed. This effect, along with the direct effect of the blade in-plane vibrations on the forward whirling

mode, had been proven both theoretically and experimentally on a small wind turbine (M. Hansen, 2003).

Blade edgewise vibrations have also been shown to be effectively reduced by using large structural damping materials. This type has a characteristic of dispersing vibration energy through damping, without affecting the rotation. Two modes are considered with this group reactionless and collective edgewise as shown in fig. 2.1. The first mode has been found to have a direct effect on increasing blade vibrations, while the second mode affected on the drive train vibrations. However, using blade pitch control would reduce the axial force due to increasing the aerodynamic forces (Lindenburg & Snel, 2003).

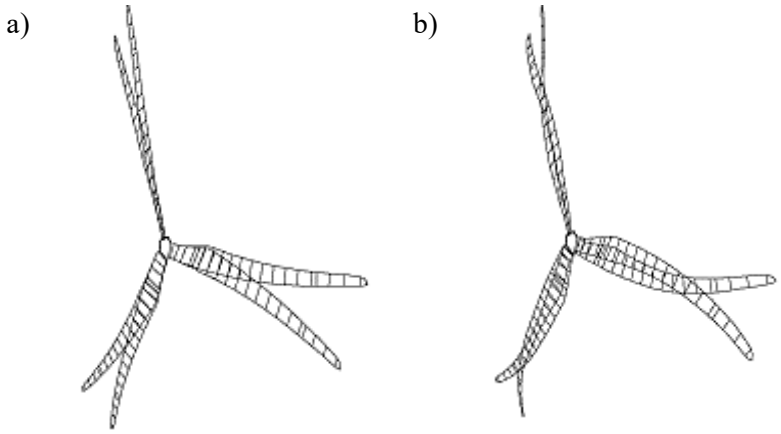

Figure 2.1 Edgewise modes a) Reactionless, b) Collective (Lindenburg, 2003)

The blade vibration direction depends on the turbine dynamics resulting from the flapwise and edgewise modes besides the twist and distribution of blade stiffness. Distribution of blade stiffness has a direct effect on the wind turbine stability at the low speeds. However, increasing drive shaft stiffness would decrease in-plane bending vibration. Additionally, decreasing blade stiffness at the edgewise part to obtain coupling between the in-plane and out-of-plane frequencies would reduce blade vibration and achieve the system stability limits, (Buhl, Markou, Hansen, Thomsen, & Rasmussen, 2006).

Hansen (2007) provided a comparison between data obtained from different analytical tools. In addition, many tests were implemented, utilizing blade pitch-regulated control

through a project to prove that edgewise modes for the specific model of the wind turbine blade are more highly damped than flapwise modes in high-speed wind. Furthermore, it listed tables which showed changes in pitch angles and its impact on both edgewise and flapwise modes. Compatibility between the blade flapwise and edgewise frequencies had been performed to achieve stability limits, by decreasing edgewise stiffness with respect to the flapwise stiffness for different wind turbine speeds. This reduction in edgewise stiffness had been carried out to different percentages (25% - 100%). Nevertheless, the blade edgewise modes showed higher damping than the flapwise modes.

Blade length has been found to have a direct impact on the stiffness and mass distribution, which in turn changed the resonance values. Changes in the blade characteristics were obtained by modeling variable blade lengths, which were created by having two portions sliding inside each other. The Short Time Fourier Transform was used to identify the damage due to the fatigue loads before failure occurred, (Fitzgerald, 2010).

Controlling of blade flapwise bending vibration using structural characteristics was validated via a tangible reduction in vibration displacement amplitude. This method was accomplished by using a mass damper in the blade structure, which changed the natural frequencies and vibration amplitudes. The dynamic model consisted of a relatively large mass, which represented the turbine nacelle, connected to three blades, one of which has the mass damper. The load was simulated by considering a simple upwind gust which changed linearly with the turbine height during the rotation, (Arrigan, Pakrashi, Basu, & Nagarajaiah, 2011).

The large amplitudes due to edgewise vibration in the horizontal axis wind turbine may lead to blade failure or reduce the life of the wind turbine. To overcome this, actuators were used to control the blade's in-plane vibrations, which would minimize the in-plane forces during the rotations by generating external forces to strengthen the blade tendons and hence terminate the edgewise force. This technique was applied to a wind turbine model utilizing the Euler-Lagrangian approach, which consisted of a blade with variable mass and stiffness, a nacelle and tower. The dynamic model considered the effects of gravity on the blade centrifugal stiffening at a specific speed as well as the vibration effects on the tower. The technique showed significant

improvement by decreasing the edgewise vibrations more than 50% when compared with the uncontrolled wind turbine system, (A Staino, 2012).

Piezoelectrical materials were used for suppression of the out-of-plane bending vibrations in wind turbine blades as well. This principle exploits coupling of the piezoelectric mechanical and electrical properties, and is used in new blade designs to decrease the vibrations. These blade structures consist of three layers, where the actuators were inserted with the glass fiber forming the outer layer, the intermediate layer which consists of a coil of thin wires, installed underneath the upper shell connected with closed loop circuit, and rigid core which was full of foam. An electrical field can also be applied to the piezoelectric material to generate a deflection or change the shape to resist the deformation in the out-of-plane direction. Additionally, the self-generated forces from the actuators caused displacements perpendicular to the rotation plane, enabling the control of the vibrations and hence reduce the resonant frequencies. The drawbacks of this technique are the signal integrity difficulties, because of the long wires installed through the rotating blades and the high cost of the control unit. Despite electrical obstacles, significant outcomes were verified through decreasing blade vibrations towards the out-of-plane direction, Qiao, Han, Zhang, Chen, and Yi (2012).

A new technique was used to mitigate blade vibrations towards an out-of-plane direction, through using new actuators to support the tendons in the blades. This actuator enables the enhancement of the blade stiffness to overcome the vibrations, as well as increase wind turbine stability. The reliability of the proposed controller came from a comparison, with the out-of-plane vibration amplitude calculated by blade element momentum theory of a 5MW wind turbine model. The blade analysis considered variable effects such as coupling between the hub and tower, and interaction with the tower and nacelle displacement. The actuators were shaped tangentially with the tendons inside the blade tip, to control the vibrations by the horizontal component of the actuator force generated during the rotations. However, increasing the blade stiffness by combining the centrifugal force with the vertical component, reduced the out-of-plane vibrations and required structural reinforcement, Andrea Staino and Basu (2013).

Prasad, et al (2014) presented an advanced software tool for horizontal axis wind turbines, to determine the effects of aerodynamic loads due to a sudden change of wind direction on the steady and unsteady state values. In addition, it can determine the blade tip and tower tip deflection with time for specific wind speeds. The software was able to accurately calculate the blade and tower bending modes, and their contribution to the out-of-plane and in-plane bending vibrations.

Imbalance phenomenon due to the addition of mass on a wind turbine blade causes operation instability, however, the addition of a small roller steel mass coupled with a special liquid damper inside a U-closed end tube enables the suppression of edgewise vibrations by working as a vibration controller. The forces generated from the new dampers with the corresponding high centrifugal forces can effectively mitigate the blade vibrations at the in-plane directions. Further, the small roller steel mass damper was found to be more effective than a liquid damper, despite the unique features that the liquid dampers offer such as simple installation and adjustment, (ZL Zhang & Nielsen, 2014).

Blade in-plane displacement has a direct impact on pitching motion, and it was noticed that blade damage increased by 4.7 percent due to in-plane rather than out-of-plane bending vibrations because of the increase in pitching motion. This method was proven through an ANSYS modelling of upwind motion with variable pitching values, where bending towards the in-plane direction was found to be higher than that in the out-of-plane direction, and its effect increased with rotor diameter resulting in imminent failure due to the occurrence of multiple cracks, (Liu, Lu, Liang, Godbole, & Chen, 2015).

Out-of-plane bending blade vibrations have a considerable negative impact on power production by decreasing the wind turbine speed and blade life. To overcome this, a new structural damper was investigated that utilized a liquid inside a circular tube to alleviate out-of-plane vibrations in a 10MW wind turbine blade. Simulation results showed active suppression of the out-of-plane vibrations in high frequencies as well as a decrease in the tower vibration amplitudes and hence increased system stability. However, the in-plane blade vibrations were relatively lowly damped due to the damper liquid being forced to the blade tip and displaced downward when the average rotor speed was below 150 rpm. To assess the outcomes, the method was successfully

tested on a 5MW wind turbine at variable rotating speeds and the comparison result was shown to be satisfactory, (Basu, Zhang, & Nielsen, 2016).

2.3: Summary of vibration condition monitoring of wind turbine blades

Vibration obtained from the drive shaft plays an important role in blade vibration condition monitoring. Proximity probes are often used for monitoring the whirling of the drive shaft centre line by plotting shaft orbits under loading conditions. The probes, which are mounted orthogonally on the shaft, provide an X-Y displacement that is used to plot shaft orbit, (Baker, et al, 1996). The two vectors that form the whirling ellipse rotate in opposite directions at the same frequency. In addition, shaft orders for certain revolutions can be obtained for the output signal as well as the frequency amplitude spectrum in terms of shaft order.

Spectrum analysis is another method of monitoring the vibration of rotating components through shaft orders and phase plots which show the shaft displacement per revolution as well as indicating the transient faults during the rotation and shaft imbalance due to bearing housing defects. Additionally, asymmetrical spectrum analysis using the complex discrete Fourier transform can be performed on data obtained by the proximity probes to show the amplitude and phase change per revolution in terms of shaft speed. This was done on a test rig drive shaft that was established in Curtin University School of Mechanical Engineering to perform fault diagnosis on a turbomachinery shaft, (Howard, et al, 1997).

To achieve effective condition monitoring and reduce the unexpected faults in the use of a machine, there must be an accurate correspondence between both the model's and the machine's aerodynamic and structural properties. However, the complexity of the wind turbine structure and operation in severe conditions have been significantly challenging when designing the aerodynamic model for vibration condition monitoring. The use of mode shapes has been shown to be a most promising technique for comparison between the model and the actual machine, (Yang, Tavner, & Wilkinson, 2009).

The out-of-plane bending vibration of the rotating blade has been found to cause more than 50% of wind turbine tower damage. To investigate this phenomenon, Kim et al. (2012) used a laser Doppler vibrometer to monitoring the blade's displacement near to the hub. This technique shines an infrared laser to the blade surface, then the reflected light is observed by the laser Doppler controller inside the tower as shown in figure 2.2. The wavelength of the reflected light is analyzed to determine the displacement of the rotating blade, and later on, assess the blade's health based on the vibration characteristics.This procedure used a non-contact method of performing monitoring and evaluating the rotating blade conditions without the need for smooth surfaces or special preparation.

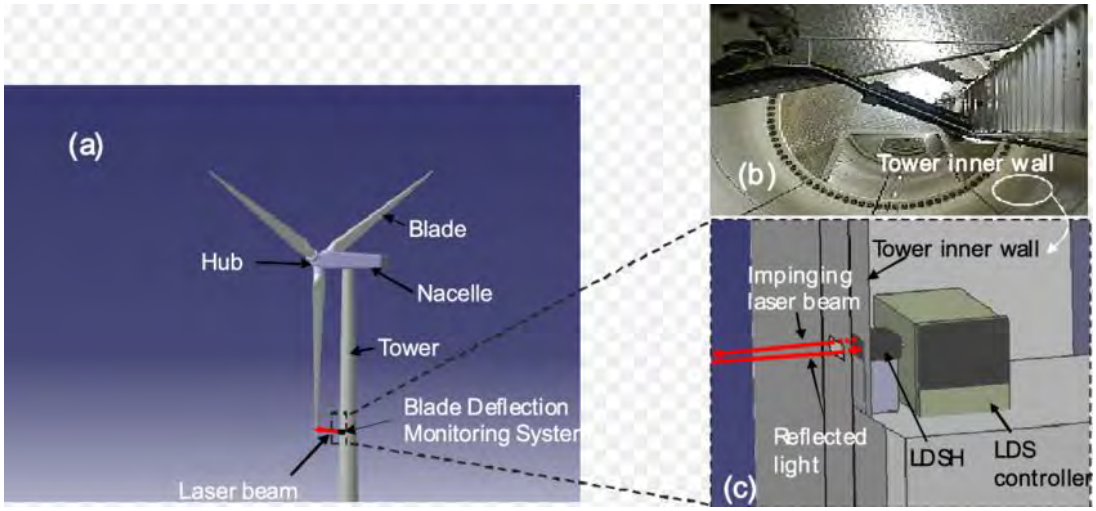

Figure 2. 2 Laser Doppler sensor inside wind turbine tower to monitor blade displacement (Kim, Giri, & Lee, 2012).

Extensible cracks in the spars, joints and between the blade's layers which often lead to failure can be found resulting from coupling between the in-plane and out-of-plane bending vibration with the blade's weight. These cracks or small defects in the blade's structure, where are sometimes invisible to the naked eye, create shear stresses between fiber layers due to in-plane and out-of-plane bending and can cause longitudinal tensile stress at different locations. These stresses can lead to cracks and ruptures in the blade's structure. To monitor this phenomenon, strain measurements were obtained using optical fibers that ran along the length of the wind turbines blades. Four optical sensors per blade were installed at the blades' surface near the hub, to

measure strain reduction due to the light reduction through the fiber. Figure 2.3 shows how the probes were connected with the main measurement unit positioned inside the hub. This technique was designed for fiber blades which depends on the capability of the fiber to transmit the light along the blade's distance, (Yang, 2013).

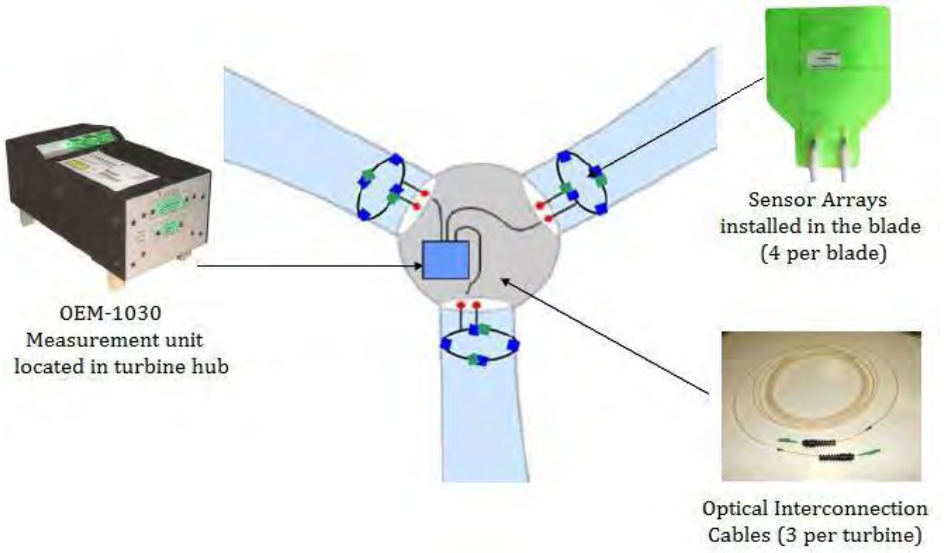

Figure 2.3 Optical sensors and the measurement unit locations in the wind turbine (Yang, 2013).

Research has also been done in creating low-cost measurement sensors to help diagnose faults in wind turbines. Miniature Low-Cost Accelerometers (MLCA) were coupled to a piezoelectric transducer in a simple wind turbine blade model, in an attempt to obtain accurate vibration data measurements. This technique was validated through a comparison of vibration displacement amplitude between on-site and laboratory blades. Natural frequencies were observed to have decreased when the surface crack was generated in the laboratory whereas no effect was found on the on-site blades. MLCA has the capability of detecting structural faults when the cracks are found close to the blade's root. The sensitivity of the piezoelectric transducer tends to decrease as the frequency increases, therefore it was thought to be unfavorable for use in high-frequency applications, (Esu, 2016).

2.4: Reviewing modeling of wind turbine blades as a cantilever beam

Blades are the important part in power generation of a wind turbine and thus are expected to remain straight, without defects and with vibration amplitudes staying within limits, during their rotation. Many researchers have been modelling blades as a tapered, twisted and isotropic cantilever beam.

Modelling a wind turbine blade as a rectangular beam simplifies the blade profile so as to obtain dynamic vibrations that are predictable using MATLAB or ANSYS software. A finite element analysis (FEA) model with 20-30 elements in the blade mesh can be used to effectively calculate the stiffness matrices to monitor the in-plane vibrations in dynamic applications. In addition, ADAMS software can be used to perform an aeroelastic analysis and validate the stiffness and inertia matrices for the FEA model, (Malcolm & Laird, 2003).

Representing wind turbine blades as rotating cantilever Bernoulli-Euler beams, enables the study of significant effects of complex structural parameters on its vibration characteristics. Natural frequencies resulting from this model have been found to increase as the angular speed increases due to an increase in the centrifugal forces. This principle has been proven by considering a constant hub radius and different taper ratio effects (0 – 0.9) in the out-of-plane and in-plane bending vibration governing equations. It has also been observed that the beam's natural frequencies have decreased with the increase of the taper ratio because the beam's stiffness becomes higher. Additionally, the coupling between the in-plane and out-of-plane blade vibration increased at the critical taper ratio, (Özdemir & Kaya, 2006).

In addition, modeling of the blades as cantilever beams due to their very large aspect ratio enables the identification of the impact of both transient wind load and aerodynamic damping on the blade's dynamic response. Blade dynamic equations have been calculated for a three-bladed wind turbine model using an FEA model that describes each blade as a beam element with two nodes. Additionally, the model considers the gravity and centrifugal loads to calculate the blade load matrix as well as the time-variable angle of attack due to the variation of the wind speed during blade rotation. Aerodynamic damping ratio for specific modes was determined in both in-plane and out-of-plane directions. It was concluded that the large size and flexibility of the rotating blades, allowed it to endure high fatigue loads and vibrations, which

have a negative impact on the dynamic response and the turbine stability (Xiong, Xianmin, Gangqiang, Yan, & Zhiquan, 2010).

High wind speeds can cause severe buckling when wind gusts strike the blade surface before the control system is able to change the pitch angle. These large repetitive flapwise bending vibrations in wind turbine blades can lead to considerable damage in the structure due to its ability to aid the propagation of a crack. Studies have shown that more than 60% of the blade mass can be lost from bending vibration towards an out-of-plane direction, (Chantharasenawong & Tipkaew, 2010).

A developed dynamic model that represents the wind turbine blades as rotating Bernoulli-Euler cantilever beams considers coupling between the blade and the tower, to minimize the flapwise bending vibrations. The new model consists of a mass damper on each blade and at the nacelle, to reduce the vibrational amplitudes at certain rotating speeds in the flapwise direction. The model uncouples the in-plane and out-of-plane vibrations caused by the nacelle's motion during rotation. The Frobenius method was utilized to determine the blade natural frequencies. While the Lagrangian formulation was used with: (1) a constant mass for the blade and (2) nacelle displacement, to determine the displacement of the blade tip (Arrigan et al., 2011).

Maganti and Nalluri (2015) investigated the effects of model beam parameters on the blade's out-of-plane bending vibrations considering a double-side tapered cross-section, untwisted, graded, and non-homogenous cantilever aluminum beam. The beam's equations of motion were derived using Rayleigh-Ritz theory and considered the variation of hub radius and angular speeds. It was found that an increase in the rotary beam natural frequencies due to an increase in the angular speeds caused large amplitudes in the blade bending vibrations in the out-of-plane direction. Out-of-plane bending vibrations were verified to be altered based on different material models, where alumina and steel experienced increased out-of-plane bending vibrations at high angular speeds with the same modal properties.

Mazanoglu and Guler (2017) used ANSYS to model a wind turbine blade as a cantilever, graded axially, tapered solid beam. An analysis on the static structure determined the axial displacements and stresses due to gravity and centrifugal forces. A dynamic analysis was performed for variable rotating speeds which considered the effects of hub dimensions, thickness reduction, and the graded material properties to

determine natural frequencies and different element's displacements. It was found that hub dimensions and speed have a direct effect on the blade out-of-plane vibrations, especially at high rotational speeds.

Table 1 shows a group of researchers who examined a cantilever beam for modelling horizontal axis wind turbine blades.

Table 2. 1 Illustrates the details of modeling wind turbine blade as a cantilever beam

Authors	Blade model	Model characteristics	Effect on out-of-plane vibrations	Effect of in-plane vibrations
(Banerjee & Sobey, 2002)	Twisted and double-tapered rotating Timoshenko Beam	Using Exact Dynamic Stiffness(EDS) theory coupled with Wittrick-Williams algorithms to calculate rotating Timoshenko beam natural frequencies.		Taper ratio has a significant effect on increasing the vibrations at In-plane direction.
(Malcolm & Laird, 2003)	Uniform, rectangular cantilever beam model	-The beam model with specifications of Length= 20 m, width=1 m, and thickness=0.250 m. - A finite element model generated using ANSYS software of 20 elements and 8 quadrilateral nodes.		The resulted model has reduced out-of-plane bending vibrations due to using spar caps inside the blade model.

		- ADAMS software utilized coupled with ANSYS to generate the final dynamic model.		
(Özdemir and Kaya, 2006)	Double tapered, rectangular cross-section rotating cantilever Bernoulli-Euler beam		Increasing the vibration in the out-of-plane direction with increasing the angular speeds.	Increase with certain angular speeds and with average less than out-of-plane vibrations.
(Das, Sahoo, & Saha, 2009)	Double side tapered and constant thickness rotating beam at constant angular speed.	ANSYS software was used to create A finite element model with 188 elements connected with a hub.	- Out-of-plane vibration has a direct effect on the axial strain of the rotating beam. - A crack initiation due to out-of-plane vibration likely to occurrence near to the root.	
(Huang, Lin, & Hsiao, 2010)	A Slender Euler beam model with a uniform cross-section, rotating at high angular speeds.	A rotating cantilever beam divided into three		The out-of-plane bending vibrations have a direct effect on the

		small parts connected with the hub.		axial bending vibrations at high rotational speeds.
(Hu, Sun, Wu, & Xu, 2012)	Euler-Bernoulli rotating cantilever beam.	Finite element beam of 49 elements and 50 nodes.	Decreased with decreasing beam elements.	
(Ju & Sun, 2014)	A uniform shape, rectangular rotating cantilever Euler-Bernoulli beam	-Variable pitch angle. - Using Input shaping method to reduce the induced vibration resulted from changing the pitch angle	This technique has the ability to reduce the out-of-plane vibrations induced by change blade pitch angle.	
(Yin, Zhang, Li, & Lu, 2015)	Rotating rectangular cross-section Aluminum Timoshenko Beam.	Length= 24 cm, height= 0.8 cm, and width= 2 cm	Increasing with increase beam natural frequencies owing to raising the rotating speed.	Increase at high rotating speeds.

2.5: Review of blade fault diagnosis through condition monitoring through utilizing laboratory test rig

In 1987, a small-scale test rig was manufactured by NASA for rotor vibration condition monitoring, utilizing blades made from fiberglass and carbon fiber mixed with foam and boron to increase the stiffness. The rig was instrumented with accelerometers on the shaft housing and two types of actuators; low-speed, and high-speed. The measurement analog signal received from the strain gauges in the rotating blades and accelerometers operating simultaneously, were converted to digital signals by the specific converter, and transferred to the computerized control system as an analog signal, to show frequency response per revolution. The shaft resonant conditions were found to change when the blade pitch changed, however, it remained below the blade resonant frequencies. This test rig achieved monitoring of the bladed-shaft vibration system (Jacklin & Leyland, 1987).

Howard (1997) identified a method for diagnosing turbomachinery malfunctions through vibration condition monitoring of the rotating shaft during high speeds in a developed test rig. It consisted of a 2150mm long and 97mm diameter rotating shaft connected with a variable speed drive motor, supported by two bearings mounted on a frame bolted to the ground. To achieve additional mass case, five different size impellers were centred in the middle of the shaft. For shaft vibration condition monitoring techniques, proximity probes were instrumented orthogonally on the bearing housing near to the shaft end to plot the shaft centre line, as well as an accelerometer that was added to obtain time-frequency data at high speeds. The results showed a reduction in the first resonant frequency and a change in the shaft centreline displacement which verified development in reducing the shaft vibration during load conditions at a specific speed.

Forward and backward whirling modes can be observed with blade vibrations towards in-plane direction at stall conditions. The coupling between the two whirling modes induced high-frequency vibrations in the rotor shaft and tower, and forward mode frequencies increased with decreasing of the backward mode frequencies owing to centrifugal inertia forces. Additionally, both vibrational modes were experimentally found that showed quasi-symmetrical behaviour of the mode shapes and natural

frequencies. Monitoring of such in-plane blade vibration modes during the rotation was accomplished by an exciter equipped in the turbine nacelle. Synchronization of out-of-plane vibration with the forward mode during aerodynamic damping can potentially lead to high torsional vibration in the blade structure, (M. Hansen, 2003).

Epaarachchi (2004) design a mechanical test rig to experiment with a 2.5m long wind turbine blade. The experiments included the effect of maximum bending displacement due to out-of-plane vibration, on the blade fatigue loading in this direction. A repetitive bending condition in this direction leads to the occurrences of microscopic cracks in the bend lines, that increases with the severe weather and vibration conditions. Surface fatigue spots on the wind turbine blades lead to reduced stiffness, and out-of-plane vibration condition monitoring through the use of strain gauges spread out over the blade span, was an effective method for blade health assessment. This technique was used by the researcher to predict the time required to identify crack visibility. The test rig was instrumented by a drive motor to provide the required torque to a particular crankshaft, which generated sinusoidal motion equivalent to the flapwise bending in the wind turbine. This research concluded that the growth of a 6cm surface crack was rapid after high flapwise bending, represented by high fatigue load.

A laser transducer was used in a small-scale test rig constructed to experiment with blade vibrations remotely. This technique was effectively used for testing with large-scale blades and high- rotation speeds, to provide non-contact vibration measurements depending on the Doppler effect, for scanning the vibratory surface to measure in-plane and out-of-plane deflections during rotations. This method can be used to track dynamic vibrations of rotating blades in the turbomachinery for any case of blade numbers, due to the capability of the device to experiment with bladed-discs. Additionally, for drive shaft vibration and phase measurements, a special mirror was located on the shaft flanges in front of the laser sensor and enabled to rotate and generate a signal per 1 revolution. The laser sensor was fixed securely in a base at a specific distance from the blades. This test rig was designed for blade vibration condition monitoring for maximum speed up to 4000 rpm, with the potential of speed change during the test. A particular servo motor was instrumented to provide more than 11 Nm torque with the drive belt. Moreover, the rotor shaft speed and position was identified by an encoder which can provide 1024 pulses per revolution to a computerized Data Acquisition system assembled for this purpose. The researcher

added that this small-scale test rig enables measuring dynamic vibrations for any blade's type or shape, or so-called " mistuning" (Sever, 2004).

A small wind turbine test rig was constructed by Wilkinson et al. (2007), to achieve new techniques for fault detection in the wind turbine blades. It was driven by a DC motor providing 50 KW power to two drive shafts, having low and high speeds. Additionally, the specific gearbox was designed for two stages considering the drive shafts and a large mass generator identical to that designed by (Spooner, et al, 2005), having a large inertia connected to the rotor. This test rig simulated wind gusts input through the distributed blades around the generator's diameter, which can control the wind speed as well. Further, the drive motor gave the potential of having wind speed control by the variation of rotating speeds. Vibration condition monitoring and fault diagnosis were conducted through different instruments such as; high accuracy accelerometers and different task transducers distributed on the generator's shaft and gearbox, to provide data measurement controlled by data acquisition system assembled particularly for this test rig. Load condition monitoring was one of the vibration monitoring techniques, which used the torque transducer signal to plot torque-speed variation during specific rotational speeds. The second technique utilized the spectral analysis to determine the rotating component's natural frequencies, which were changed with the drive train stiffness.

Yang et al.(2009) utilized the same test rig with enhancements in the generator to improve the vibration condition monitoring and fault diagnosis, in wind turbines using a torque-speed variation technique. Wind power and drive motors were both available to provide variable torque. The experiments included monitoring the gearbox, low and high-speed shafts during various rotational speeds, as well as using rotating and non-rotating transducers for monitoring shaft torsional vibration and torque. Further, the data acquisition system was controlled by LABVIEW, while Wilkinson et al. (2009) proved that the data acquisition system, can effectively work on the SCADA program despite being instrumented by LABVIEW as well. Fault diagnosis techniques and analysis were conducted using the continuous wavelet transforms, which enabled it to distinguish the characteristics frequencies during the experiments.

During wind turbine operation, changing wind speed and direction during upwind can increase the out-of-plane vibration on the rotating blades. This vibration load was the

reason for designing a test rig from (Lai et al., 2011), to test the fatigue load on a small wind turbine blade made from fiberglass, weighing 1.781 kg and having different blade length including 1m, 2m, and 3m. The experiments included identifying fatigue loads during out-of-plane blade vibrations. The blade was instrumented by one group of strain gauges and one accelerometer for vibration condition monitoring during the test operation. The tested blade was positioned as in figure 2.4, where the servo motor provided a torque to a linear slide beam, to generate vibration motion equivalent to the out-of-plane vibration. Three different masses were installed at a specific distance for modelling wind loads. The blade velocity was modelled by the linear motion which was converted from the servo motor rotational speeds. The increase in out-of-plane vibrations caused loss of part of the blade after (1 revolution) due to adding mass 1, where the experimental frequency was 3 Hz. Additionally, increasing mass 1 leads to a reduced blade life and increase the fatigue in this position. Increasing mass 2 leads to a destruction of the blade's root that connects the beam to the test rig, when the test frequency was 4 Hz.

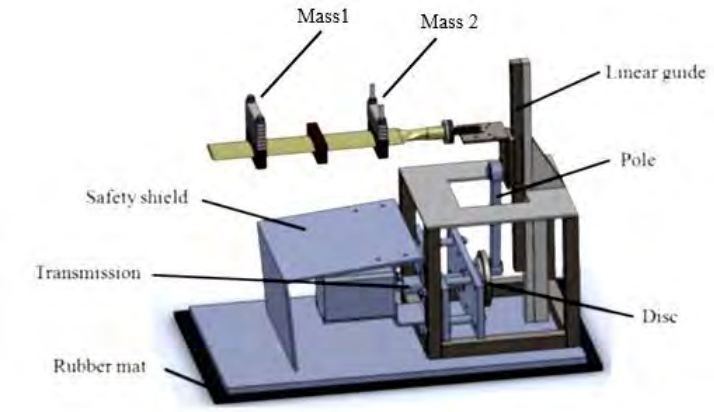

Figure 2.4 The view of a developed experimental test rig for testing wind turbine blades (Lai et al., 2011).

In order to investigate blade and shaft vibration condition monitoring in wind turbine and other turbomachinery, Gubran et al. (2014) constructed a small-scale test rig to study shaft torsional vibrations due to blade vibrations towards in-plane. All the

rectangular blade models were made from steel (ρ= 7800 Kg/m^3, and E= 210 GPa), of length=0.11m, width= 0.02m, and 0.002m thickness. The test rig was instrumented by four accelerometers located vertically and horizontally on the two bearings at the shaft ends, having a rotary encoder placed in the shaft end that allowed the pickup of 360 pulses per shaft revolution, and a tacho optical sensor located on the motor shaft before the flexible joint with the rotating shaft. The blades were also instrumented by a small accelerometer for measuring blade dynamic vibration response. The experiments included three different case studies; transverse crack near to the blade root, looseness in the blade root with the hub, and blade without sabotage. The tests included rotating the shaft at different rotating speeds by an AC drive motor, between 600rpm – 1800rpm on three stages and collecting the data from the instruments to the computer. The experimental data showed increases in the shaft fluctuation up to 600rpm, where blade resonance frequencies were different after several tests due to the following points:

I. Growth and opening of the small crack that was inserted in one blade near the root (crack simulation).
II. High looseness in the blade root during the operation.
III. Changing in the healthy blade first natural frequency during the four tests that were implemented in the speed range of 600rpm – 1800rpm.

The writer had validated the experimental results by modeling the shaft and blades of a simple mathematical model, to identify the model natural frequencies and displacements.

Krull (2014) utilized a small wind turbine test rig to show the direct impact of gearbox faults on blade in-plane bending vibration, which may lead to deep cracks in the blade tip. It was found that torsional vibrations due to stall application were the main reason for the initiation of 40% of the cracks in the blade spanwise. A cold room was used to provide the difficult working conditions for the gearbox for vibration condition monitoring. Based on the study, it was determined that freezing temperatures lead to a decrease in the lubrication oil flow between the gears which causes system instability and an increase in the vibration amplitudes.

Piezoelectric accelerometer sensors have been used to monitor high-frequency vibrations resulting from damage propagation in the rotating blades. These sensors

help provide an effective assessment of blade structure integrity when used on a 1m section of the rotating blade with high-frequency analysis. Two types of experiments have been fulfilled to detect blade damage, firstly by applying high-frequency vibrations on the blade section with piezoelectric sensors, and the second with the use of the lamb wave propagation technique. The first method showed more ability to track the damage with few number of sensors whereas the second needed more sensors to evaluate the fault. However, the Lamb wave method has effectively detected the faults in the inner surfaces of the blade composite structures which detected variable-depth cracks due to the different frequency of Lamb waves, (Choi, Farinholt, Taylor, Light-Marquez, & Park, 2014).

Faults that are normally unexpected in a wind turbine can be studied using a model to help create methods on how to predict the incipient faults in the actual wind turbine. Test rig models provide significant advantages over actual machines by allowing the monitoring of high-frequency signals utilizing accelerometers and strain gauges attached to the blades, drive shaft, gearbox, and tower in an easily-accessible, down-scaled model. In the test rig assembly, a data acquisition system should consist of rotating and non-rotating sensors to be able to monitor dynamic vibration. To achieve correct monitoring of the rotating components, acoustic sensors have to be mounted in the vicinity of the parts. Data acquired from this set up were analyzed through intelligent techniques to indicate the primary faults and the change in frequencies due to fatigue in the wind turbine blades, (Biswal & Sabareesh, 2015).

Laser technique was used for monitoring blade deflection based on blade tip and mid-span displacement measurements. A laser Device (LD) mounted on the tower, underneath the plate that supports the bearing and DC drive motor, enabled the detection of blade displacements from just two locations. The lasers were calibrated on the test rig itself utilizing the change in the voltage with the frequency of random points on the blade. This small wind turbine test rig had three blades of 1m length and 0.05m width and operated at a maximum speed of 120 rpm. Further, a variation of applied torque with the rotational speed was also considered when monitoring the laser voltage during the experiments, which was the indicator of blade vibrations. The case study was performed by using 200g mass at the blade tip and mid-span, for monitoring bending displacements at the maximum speed (120 rpm). All blade deflections were considered for the comparison between the deflections with and without additional

mass. The main feature of the laser location was the capability to detect blade bending displacements when located on the support tower. Moreover, it demonstrated the potential of identifying the angular misalignment between the rotating blade and nacelle, which was considered another benefit of the laser in this test rig (Mankowski & Wang, 2016).

Esu (2016) showed the utilization of low-cost piezoelectric sounders in a set up constructed for an experiment with different types of wind turbine blades. This equipment proved the ability to analyze the vibrations due to the existence of cracks in the blade's spanwise. Additionally, the typical efficiency of this sensor in measuring blade natural frequencies was shown, considered the resulting signal was quite reliable in preempting the failure due to in-plane and out-of-plane vibrations, through specifying the amplitude of high-frequency modes. It also demonstrated vibration condition monitoring through the potential of detecting the variation in blade natural frequency when the failure occurred. This technique was proved theoretically in this research by using the same model in ANSYS software. The sensitivity was found to be decreasing slightly when the frequencies reached high orders, while the stiffness was higher than the usual case, however, the received signal was still considered allowable. This sensor was described by the researchers was "effective" in monitoring blade vibration modes namely out-of-plane, in-plane and torsional vibrations due to the comparison between the experimental and theoretical outcomes. Further, this research considered that this type of piezoelectric sensor can provide vibration condition monitoring in-situ, through successful experiments conducted on the wind turbine blades.

A new technique was used by the Fraunhofer Institute for blade vibration monitoring, utilizing a laser for detecting blade vibrations during operation remotely. The developed test rig consisted of a laser camera mounted on an automatically controlled structure, that has an ability to track a point in the moving object (a point on the blade tip). The vibrometer camera has an emitter and receiver lenses, where the comparison between the tracking point in the two positions, actual and desired, produces camera 3D motion. The frequency analysis of the emitted and refracted laser can measure the vibration amplitude. This equipment was used with a small wind turbine model (2 m rotor diameter), for the distance 10 m from the rotating blades, as well as, isolating the moving components (the rotating blades) from the medium by a black curtain to avoid

laser signal modulation changes. This blade vibration monitoring technique had the following advantages;

- Non-rotating sensor measurement enables detection of dynamic vibrations remotely.
- Doesn't need any changes in the structure or preparations for vibration measurements.
- Can track the rotating object at any working condition.
- High resolution and frequency range of approximately 0.1 Hz – 10 Hz.

However, the wind turbine rotor has to rotate separately from the background because any moving object behind the turbine, might disperse the tracking operation. For this reason, a black curtain was positioned behind the rotor to provide isolation from the atmosphere.

Table 2 shows a summary of researchers that have investigated vibration monitoring techniques to detect dynamic vibration in horizontal axis wind turbine blades.

Table 2. 2 Blade vibration monitoring techniques used for vibration monitoring in a horizontal axis wind turbine system.

Author	Monitoring technique	Equipment and sensors used	Important results
(Blanch & Dutton, 2003)	Acoustic emission technique with a developed damage ranking software for monitoring fatigue positions during in-service rotating blades	Acoustic sensors	The developed software with the sensors successfully classified different cracks and monitored crack propagation to failure in wind turbine blades after its application in the laboratory.
(Park et al., 2005)	Using functions of high-frequency response through high-frequency vibrations on specific spots of blade section.	Piezoelectric sensors	Frequency response technique presents precise data about blade damage with a small time interval and low sets of sensors than the Lamb wave propagations approach.
(Park, Farrar, di Scalea, & Coccia, 2006)	Measuring the change in piezoelectric sensor capacitance current due to bending vibrations by high-frequency vibration monitoring technique.	Piezoelectric sensors	High possibility of using this method in-situ on the rotating blades for monitoring incipient faults and fatigue failure regions.
(Adams, White, Rumsey, & Farrar, 2011)	Monitoring of blade's natural frequencies during three different types of damages.	Triaxial Piezoelectric capacitive	- A small change in blade's natural frequencies causes a significant reduction in the stiffness of blade root.

		acceleration sensors.	- Due to the instability in wind loads which leads to change in vertical wind shear, the blade vibration changes stochastically. - Transient change in wind speed accompanied a linear change in blade's acceleration.

2.6: Conclusion

This chapter has documented a review of wind turbine blade vibration modes utilizing vibration condition monitoring techniques. The first part, reviewed blade vibrations towards the in-plane and out-of-plane direction. It was found that in-plane vibrations have less damping than out-of-plane blade vibrations, and the blade length adversely impacts on the stiffness which in return change resonant frequencies. Additionally, blade structural characteristics have a positive impact on mitigating the vibrations towards the out-of-plane direction. Rotor shafts that experience high fluctuations due to the coupling between the two vibrational modes show an increase in the fatigue loads.

The next section has reviewed vibration monitoring techniques of the wind turbine's rotating and non-rotating components which is an effective method for diagnostic blade defects. The imbalance in the wind turbine components leads to an increase of the edgewise vibration (in-plane vibration) amplitude to be relatively higher than the flapwise vibration (out-of-plane vibration). Further, it was found that the rotating cantilever beam is still the optimal representation of the wind turbine blades which provides a useful model to achieve accurate displacements and dynamic load calculations. Finally, using small-scale wind turbine test rigs for vibration condition monitoring was a significant method of vibration measurements in rotating and non-rotating components with the potential of utilizing various types of sensors, signal processing, and monitoring techniques. It enables the assessment of the integrity of the rotating components through vibration condition monitoring. The techniques and knowledge reviewed in this chapter have been considered to improve blade vibration monitoring through the use of novel methods for detecting the blade vibration modes and transient fault diagnosis. The next chapter will clarify the modeling method used to build the mathematical model, which was an extension of previous researches, depending on modeling wind turbine system theoretically and experimentally to give a comprehensive understanding for vibration condition monitoring.

Chapter 3: Wind turbine test rig components

3.1 Introduction

Increasing demand for the clean energy leads to the increasing importance of the renewable energy sources. The use of traditional coal and oil-fired electricity power plants has started to recede in comparison to the increasing demand for building new wind turbines due to the latter's ability to harness renewable energy to produce electrical power. Wind turbines have developed to the extent that they are now recognised as providing safe and reliable sources of power and have been seen to provide an ideal alternative to fossil fuel plants for electricity generation. Biswal and Sabareesh (2015) designed and developed a test rig for studying vibration condition monitoring of wind turbines. Many fault conditions were created to simulate the actual wind turbine operating conditions. The faults included those drive train of the turbine and focused on the bearings and gearbox which might have unexpected damages resulting in high frequency vibration response of the system. In addition, many parts such as the gears were replaced with cracked, worn and pitting to demonstrate the faulty system vibration signals that could be manifest during turbine operation. Accelerometers were used for analyzing the vibrations due to the applied faults. A special motor was used to provide the torque in the test rig and data acquisition systems were used to collect and analyze the accelerometer signals from different faults for further investigation. It demonstrated healthy and faulty signals to assist in distinguishing between different faulty parts through monitoring of the operational states. A comparison between the states using signal processing techniques was used to detect the faults in the turbine gearbox especially in the intermediate gears between high and low speeds.

Lutschinger and Howard (Lutschinger & Howard, 2013)have also studied the gearbox failure mechanisms through design of a test rig manufactured for this purpose. It used the transient wind gusts from a large fan in front of the three-bladed turbine to drive the rotor. Vibration signals have been observed in the rotor shaft due to the

displacement between the shaft and bearing. Proximity probes were used to detect the small displacement of the shaft with a special camera to show the shaft movement. This research has been focused on the gearbox shaft failures due to aerodynamic loads which result in a bending vibration in the rotor shaft and fluctuations in the turbine hub. This paper shows the current test rig components, which have been used to study the vibration frequencies resulting from blade vibration modes that were modeled as cantilever beams.

Abdelrahman and Johnson (Abdelrahman & Johnson, 2014) designed a wind turbine test rig to investigate the impact of blade trailing edge flaps on flapwise bending vibration and its effect on power generation. The turbine had three blades with a length of 1.7 m and 6^{o} of pitch, each one having five sections connected by a beam to achieve flaps in the trailing edge. The test rig was assembled and operated in a wind tunnel to provide speed. The linearity of the relationship between decreasing load and blade angle deflection has been proved, however, it was found to be non-linear between trailing edge flaps and flapwise bending vibration. In general, blade bending moment was found to be linearly varying with deflection angle.

3.2 Design of wind turbine test rig

A small wind turbine test rig has been manufactured to investigate the high vibration response obtained from the blades and to analyse the transient response coming from different implanted faults for monitoring the subsequent behavior on the rotating shaft and the tower. Measurement of the components has been determined according to the laboratory area as well as ease of installation. Different instruments have been used to provide the required outcomes and to be able to be calibrated accurately to decrease the error in the findings.

3.2.1 Upper and lower test rig bases

The different vibration frequencies which are expected to be obtained from the test rig resulted in the shaft support base being thick enough to prevent distortion during operation. Both lower and upper bases were made from Aluminium, with the foundation base dimensions being 850x650x18mm bolted with four brackets to the

ground. The tower rises from the centre with a hollow Aluminium tube 1750 mm long with an inner and outer diameter of 32 mm, and 52mm respectively, connected with the 500x300x12 mm upper base as indicated in figure 3.1. It has been welded carefully together to support the bases of the test rig. Laser displacement instrument brackets have been bolted vertically after calibration at the top in the middle of the shaft free end to monitor the bending displacement at this point.

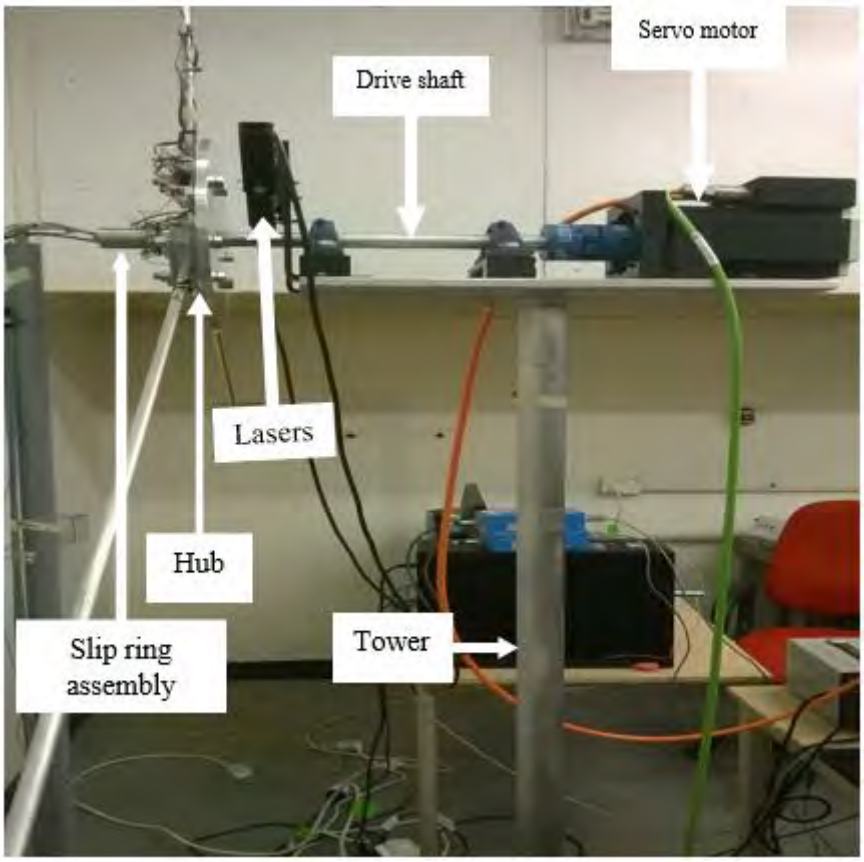

Figure 3.1: Side view of the test rig.

A hollow drive shaft has been chosen for the test rig to provide strength, flexibility and high amplitude response for the vibration during blade rotation. Those parts have been designed to endure the high amplitude forced vibration which might be faced by the test rig during the faulty operation.

3.2.2 Servo motor and control system

An A.C servo motor with 1-10 N.m Torque and 0.003 kg.m^2 rotor inertia has been used in the test rig to drive the drive shaft which is supported in two ball bearing housings, and to provide excitation of torsional vibrations during blade rotation. This motor has been chosen initially to drive the 0.7 kg.m^2 total load of the thin beams, hub and drive shaft to achieve various rotor speeds to 150 rpm. This operational speed is less than the blade bending resonance frequencies, though higher than the tower bending resonances. In addition, the servo motor can provide successful angular velocity profile and continuous acceleration during tests with various applied faults on the system as well as successfully control the larger blade inertia angular velocity as required. The servo motor has small inertia comparative to the blades and hub, so that the torsional system can be represented by a large inertia at the hub end and small inertia for the servo motor at the other end. Furthermore, the thin hollow shaft was designed to facilitate shaft bending about the two support bearings.

The servo motor works on advanced motion programming to drive the test rig. It consists of a controller assembled from a set of components placed in an electrical enclosure having clear PVC with square faces, where the front face is screwed on from the corners to allow access to the inside of the enclosure for any maintenance. Furthermore, it has a safety button with safety key to stop the rotation in an emergency case and it must be on before the test is started.

This alternative test rig design simulates the impact of a wind gust on the rotor hub by producing a significant twist onto the drive shaft with the possibility of adding mass loading at the blade tip. Furthermore, it has the ability to accelerate the rotor shaft of 15mm and 25mm inner and outer diameter respectively and 33.5mm long during periods of torsional vibration excitation to assist in identifying the vibration characteristics of the system. However, carefully controlling the angular velocity at higher rotational frequencies is required to avoid any damage in the system. An encoder has been included with the motor to provide feedback of the shaft angular position as well as precise speed control at the critical speeds and variable frequency due to its position at the shaft end. Additionally, it has the ability to stop the rotation and give a signal (FAULT) in the Data acquisition system indicator when the vibration reaches high levels, to protect the system. Furthermore, it has functionality for

controlling the speed with chosen velocity profile, as shown in the Mint workbench software, by adjusting the controller PID gains. This includes the ability to control the current output power and required time to reach the desired velocity, as well as stop the rotation when the limit current is reached.

A special software tool designed by ABB provides rotational velocity through the control of specific parameters of distance, speed, and acceleration. It has a capability of linear motion and indexing as well as control of the motor by closed loop velocity control using software designed for this purpose. The particular adjustment between the factors would give the desired velocity profile. Additionally, adjusting the system acceleration and deceleration can give smooth rotational speed without error code in the Mint Workbench. Velocity preview profiles can be visualized before starting the rotation which normally takes a trapezoidal form. The Mint Workbench fine-tuning window includes multiple parameters instance profile parameters (acceleration, decceleration, and sample time) which enable to set the velocity parameters, which gives the related Data-Time graph showing system acceleration and deceleration during the test. Additionally, the velocity profile can give the reader's the velocity overshoot proportion to velocity demand at the real time. The closed-loop control system can correct the servo motor torque to obtain the desired torque to achieve the required velocity.

In order to make the experiments safer to conduct, an emergency button has been added and must be on after the AC power is provided. Once the input data is complete, the desired velocity will be previewed to check the required runtime.

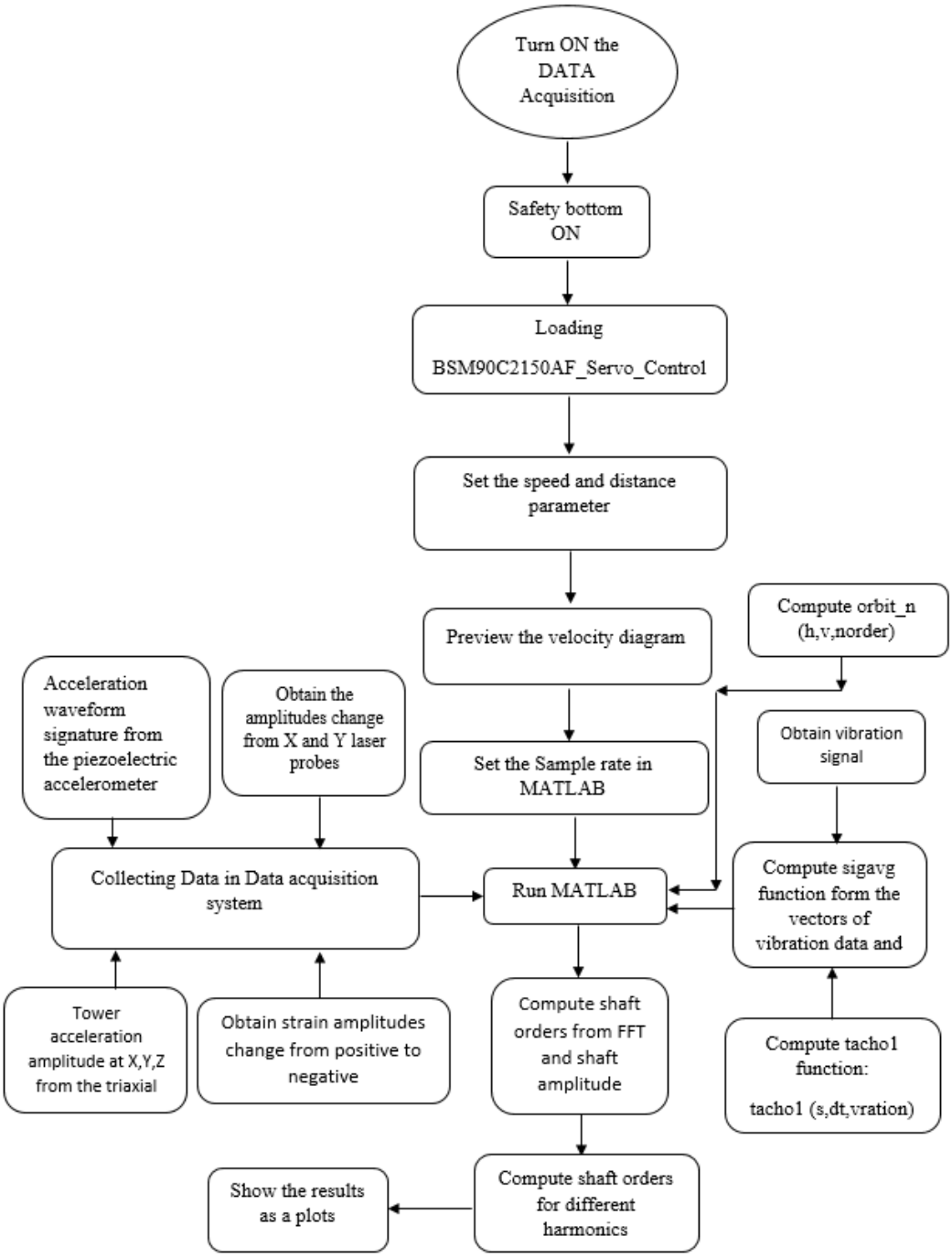

Figure 3.2 Mint Workbench processing to produce the required torque.

3.2.3 Data acquisition system

The data acquisition system is a powerful part of the instrumentation set up which enables the transfer of all signal and commands that come from/to the instruments connected with the computer through the use of MATLAB software. The analog signals coming from the measuring instruments (strain gauges and accelerometers) have been converted to digital I/O signals by the compaqDAQ National Instruments equipment type NI cDAQ-9178 with 8-slot in the chassis. The signal was successfully transferred to the data acquisition system as a digital signal using MATLAB software which enables ease of data-logging and generates automatic code. After each experiment, the results are saved with a date/time stamp followed by analysis and display using MATLAB software on the computer.

MATLAB software is required to be working for each test which contains mfile commands written for each instrument to be ready for the required measurements. After the test rig has stopped (the test time duration is completed), the transient vibration from the blades and tower with time will show graphically in time-domain response and plots.

Developed software has been designed for Mint workbench to achieve correct velocity and drive servo motor precisely. It has important parameters to control the rotation to the required velocity profile and prevent any inappropriate jerk from the servo motor that can induce undesirable vibration. Different gains in the Mint workbench windows, for instance, KPROP, KINT and KDERIV (PID), which have properties for achieving the desired velocity after setting the required speed and prevent any deviation of the servo motor, as well as reduce the error between the actual and desired velocities. The values of these commands have a direct effect on fine tune rotation and reduce motor speed oscillation, where random values can lead to unfavorable vibration.

Sensors which form the main part of vibration measurements have been attached at rotating and non-rotating components on the test rig, are listed in Table 3.1 and categorized by position and function as well as the connection in the CompaqDAQ system. Additionally, measurement signal and wiring system including branches from all sensors are illustrated in figure 3.3.

Table 3.1 shows all the measurement sensors that are used in the test rig with the position in the rotating and non-rotating components as well as the channels that transfer the signal to the Data acquisition system.

Name	Type	Function	Position	Channel in the CompaqDAQ		
				Module		Channel
Strain gauges	FLA-3-350-23	Axial strain measurements	Blade 1	1		0
Strain gauges	FLA-3-350-23	In-plane strain measurements	Blade 1	1		1
Strain gauges	FLA-3-350-23	Out-of-plane strain measurements	Blade 1	1		2
Strain gauges	FLA-3-350-23	In-plane strain measurements	Blade 2	1		3
Digital I/O encoder	Incremental encoder	Provides precise motor shaft speed and position data at each rotation by closed-loop feedback signal	End-shaft of the servo motor	2		
Laser Probe 1	Distance sensor M5	Measuring deflection of the drive shaft at X-direction	45° with shaft centre line (left side)	3		0
Laser Probe 2	Distance sensor M5	Measuring deflection of the drive shaft at Y-direction	45° with shaft centre line (Right side)	3		1
Piezoelectric accelerometer	ISOTRON accelerometer	Acceleration at the blade tip in the direction of rotation	Blade 1	3		2
Triaxial accelerometer	Triaxial DeltaTrone accelerometer	Triaxial acceleration at the tower	Tower	4	X	0
					Y	1
					Z	2

Table 3.1Measurement sensors for rotating and non-rotating components in the wind turbine test rig.

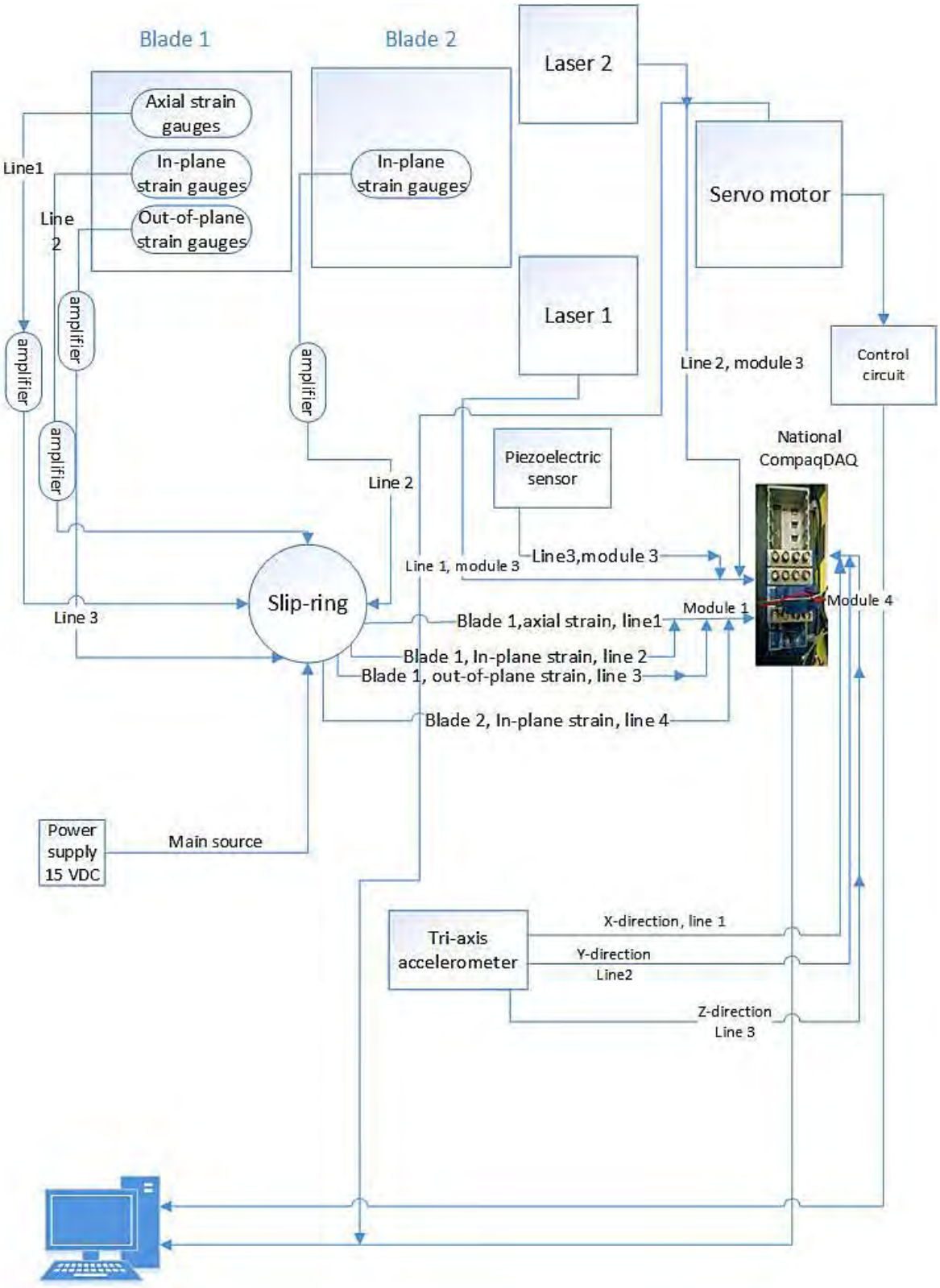

Figure 3.3 Paths of measurement signals from rotating and non-rotating sensors.

Figure 3.4 Diagram of MicroFlex e150 servo drives with the connections(ABB, 2012).

3.2.4 Strain measurements equipment

Stresses generated in the blades due to the vibration leads to bending deformation during the rotation which leads to excessive strain on these components. The coil of the bounded gauges (strain gauges) has high sensitivity to the voltage variation due to the variation of the blade strain in spite of being very thin. This change, either tension or compression, leads to changes in conductor resistance as shown in figure 3.5. This resistance changes with the applied forces on the blade and have to be within the elastic limits of the strain gauge material and the rotor blade. Voltage variation due to conductivity changes appears as strain amplitude values when the rotor blades deform under the action of the applied forces. Typically, strain gauges are attached near the blade root to measure the variation of the strains resulting from the fluctuating loadings as well as due to bending vibration. The strain gauge frequency response depends on the required strain size that will be measured (Davidson, 2015). The low-level output

signal from the gauges has been amplified on the rotor hub prior to being sent through the slip rings and transferred to the compaqDAQ for data acquisition.

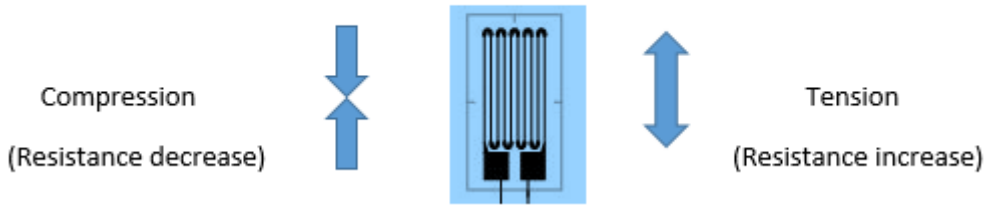

Figure 3.5 Strain gauges resistance in tension and compression

Three groups of strain gauges have been attached near to the blade root to measure the strain in different positions and modes as illustrated in figure 3.6. Gauge type FLA-3-350-23 has been used with a gauge factor 2.13 which can detect small changes in resistance. The first pair has been used to measure axial strain along the blade which is sensitive to any elongation in the blade due to the rotation, the second pair was attached in the direction of rotation to be sensitive to the in-plane strain and lastly another pair was positioned to pick up the out-of-plane strain perpendicular to the direction of rotation.

Figure 3.6 Rotating beam instrumented with three groups of strain gauges

They have all been connected according to the Wheatstone bridge arrangement as a half-bridge configuration as shown in figure 3.7.

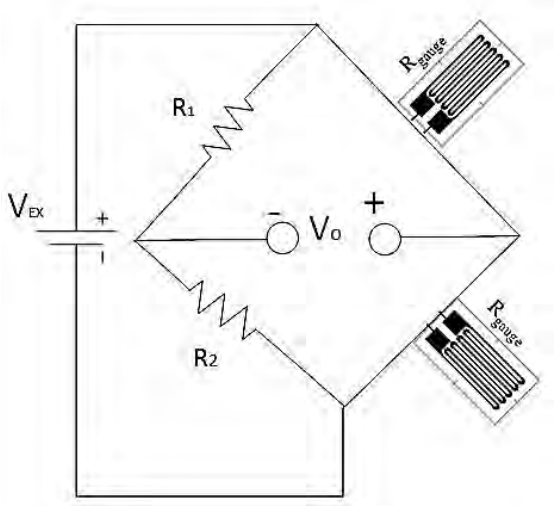

Figure 3.7 Half-bridge configuration for the test rig.

Resistors have been connected with the strain gauges to control the applied voltage between the two nodes of the circuit. This configuration was applied for all strain measurements (Axial, In-plane, and Out-of-plane bending) in the test rig including the three amplifiers for the blade 1 strain gauges and an additional one for blade 2 which has strain gauges for in-plane strain measurement for bending vibrations.

The strain sensitive transducers have size 3mmX1mm and 350 Ω with 3m length wires with a temperature coefficient of the gauge factor is +0.1±0.05 mm, and are effective for use in the current tests. The cables were shortened and were soldered to the amplifiers positioned on the rotor hub and were then connected with the slip ring from the other side prior to connection to the CompaqDAQ and with DC voltage source.

Miniature amplifiers have been used, type AMP-SG-MH-10, with each strain gauge pair, due to the small level signal of the output voltage across the gauge circuit. The amplifier output provides large adjustable gain and facilitates low noise connection through the slip ring assembly into the data acquisition system.

The strain parameters have to be known in MATLAB software to get correct strain measurement. Gauge factor (G_f) describes the variation of wire resistance (R) with the strain (ε), which should be constant during the variation of wire length when the beam bends. The strain factor value determines the sensitivity of the calculated strain obtained through gauge factor (Hoffmann, 1974), and is given by,

$$G_f = \frac{\Delta R/R}{\Delta L/L},$$

$$= 1 + 2\nu + \frac{\Delta\rho/\rho}{\varepsilon} \quad , \qquad \text{…….. (3.1)}$$

where $\frac{\Delta\rho/\rho}{\varepsilon}$ is the change in resistance and ν is Poisson's ratio (relative compression to relative expansion ratio).

The strain has been calculated theoretically for calibration purposes after the gauge voltage was measured and a known weight was attached to the beam tip. This technique was also applied to both groups of strain gauges for in-plane and out-of-plane as well as axial strain calibrations. The linear variation of the output voltage across the gauge circuit with strain value during load change indicates the integrity of the calibration and hence correct strain measurements, as illustrated in figure 3.8.

(a)

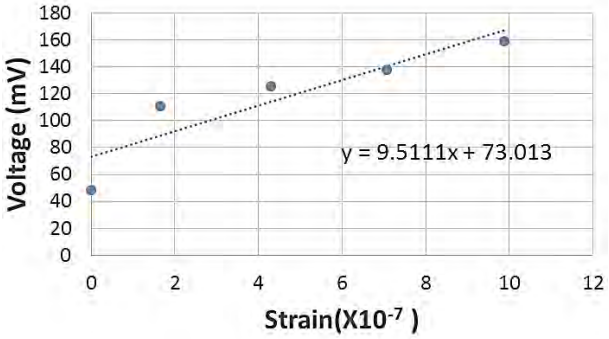

(b)

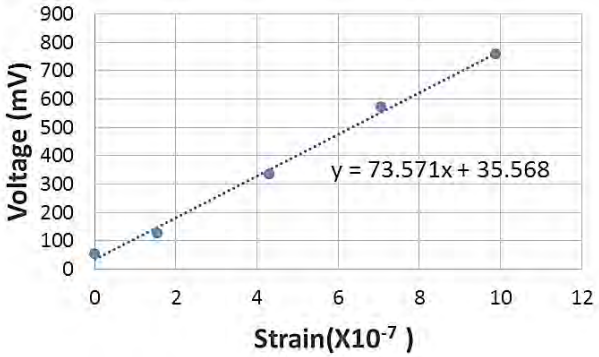

(c)

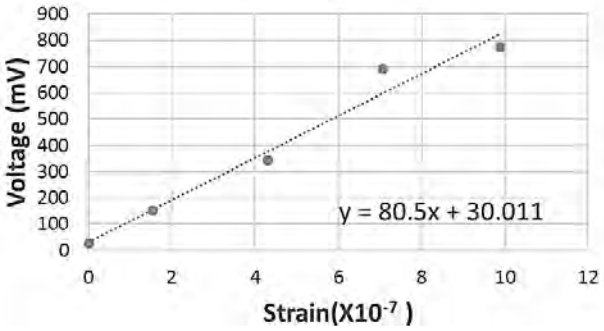

Figure 3.8 Strain gauge calibration data, a) axial strain, b) In-plane strain and c) out-of-plane strain.

3.2.5 Hub and the slip ring

The hub and slip rings have been designed according to the specification and size of the small parts that would be placed around it. The hub dimensions of 400 mm diameter and 10 mm thickness have been taken into consideration, considering all the instruments which would be attached. The circular rotating hub was connected to the drive shaft by a keyway and carried the sensitive components. The strain gauge connections have been soldered to the amplifiers and placed inside brackets, designed according to its dimensions, and bolted onto the hub (each bracket has two amplifiers).

All wires have been soldered carefully according to a special circuit map for all the components and the wires fixed by strips, to avoid looseness during the rotation.
The Michigan Scientific SR-Series Slip Ring Assembly (SR-SSRA) has been installed on the side of the hub in the centre. It has been chosen for ease of mounting on the shaft end and contains 20 terminals for signal transmission from the strain gauges and accelerometers, with high efficiency, low-level instrumentation signals and low noise. All strain gauge devices have been connected with the AC Remote Amplifier Control Unit (RACU) to give ±15V. It provides power and control excitation of more than 18 spinning strain gauge amplifiers. Additionally, the excited on/off gauge bridge has the capability of calibrating the electronic shunt remotely as well and was an adequate size for the setup.

Wiring of the rotating sensors through the slip ring assembly has been performed after creating a wiring map for each group of strain gauge amplifiers and accelerometer according to colored pins at the slip ring stator and rotating parts as indicated in figure 3.9 Additionally, effective wiring connections has been conducted by multimeter to check the system integrity.

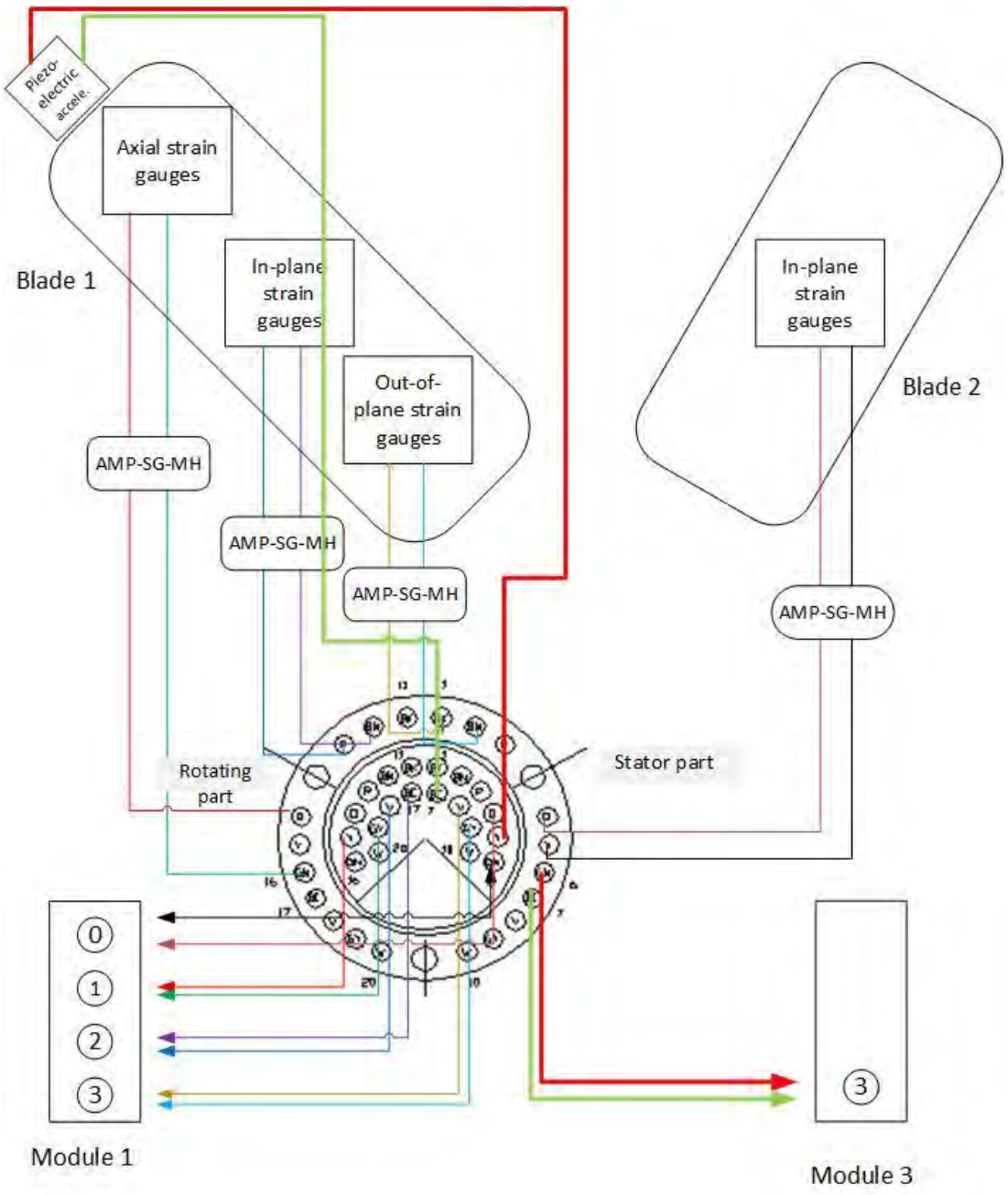

Figure 3.9 Wiring diagram of the rotating sensors to/from the slip ring assembly (wire colors according to the test rig wires).

Soldering has carefully been performed due to the small and precise components as well as avoiding circuit damage inside the rotating part.

The high sensitivity nature of the slip ring assembly circuit makes for stable transmitted signals, without noise through a relatively small sized device.

3.2.6 Laser measurement instruments (LED Sensors)

Laser equipment has been utilized instead of proximity probes for monitoring the bending fluctuation of the rotor shaft due to blade vibrations. The laser beam scans the shaft surface using two probes mounted on the upper base with orthogonal (90^0) configurations between them, measuring the displacement of the rotor shaft center during the shaft and blade rotation. Two horizontal holders have been designed and manufactured to carry the lasers at 45^0 with respect to the horizontal axis and the rotor shaft center, so it can adjust the distance between the LED sensors and the shaft to obtain calibrated linear voltages, as indicated in figure 3.10. Voltage dividers have been connected with the voltage source to reduce it to 1.3-1.7V. Displacement has a linear range such as 23.5-23.8mm, where the measuring distance of the instruments is about ±1 mm. In addition, the suitable laser signal traveling and reflection which leads to the appropriate position of the instruments from the rotor shaft surface was specified by the green light indicator on the laser generator. The LED sensors have two conditioning units with special cables and three indicators at the sides to adjust the distance between the lens and the object and hence give the appropriate voltage response.

The laser equipment was calibrated with the holders before the installation in the test rig. The lathe table was used in the calibration, where it used a shaft with the same dimensions as the rotor shaft as illustrated in figure 3.10.

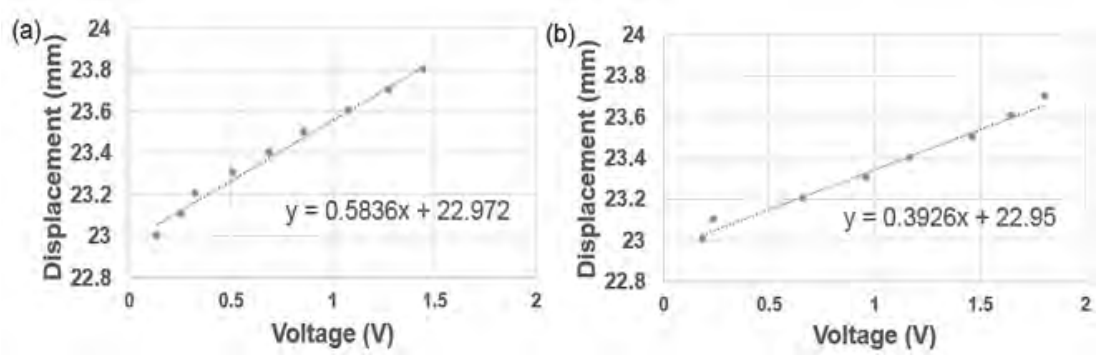

Figure 3.10 Displacement-Voltage calibration curves, a) axis 1 and b) axis 2.

The calibration has been performed on the basis of reading the voltage drop resulting from moving the laser instrument away from the rotor shaft. The distance should be between 23.0 - 24.0mm to receive suitable laser wavelength for measurement. The lasers have been fixed on the lathe tool holder with a dial gauge, with starting distance of 23.0mm with an increment of 0.1mm of each step until they reach 25.0mm as shown in figure 3.11 when the yellow light indicator turns on indicating an out of range measurement. The increase in distance leads to an increase in laser voltage and the operation was performed within a period of the green light indicator meaning good strength of the laser signal. The calibration steps have to apply for both instruments separately as well as adjust the distance between the shaft and lasers and the clamp slide on the holders by the adjustment bolts on the test rig to ensure that no movement occurs leading to incorrect results. The output voltage has been measured by an oscilloscope during this operation to make sure it was in the linear part of the curves.

Figure 3.11 Lathe table with the laser instrument during the calibration.

This method has been repeated with the voltage dividers to check the distance with the reduced voltage. Running the test rig is the last step to get the results of the distance and voltage, which must be within the allowable limits (linear parts) according to the calibration curves in figure 3.10. The LED sensor calibration steps must be performed in an accurate manner because these equipment are sensitive to any vibrations as well as all the bolt adjustment should be tightened correctly to avoid any movement, which

may lead to incorrect results. In addition, the power amplifier should provide +24 VDC / 200mA to avoid any damage to the instrument and circuits.

Safety requirements should be taken into account during the calibration and installation because the human eyes might be harmed due to the laser beam, hence, special glasses will be useful when working near to the laser sensor. Furthermore, working out of the laser field is favorable and the laser safety glasses should be kept on when the laser is working.

3.2.7 Accelerometers and piezoelectric sensors

A piezoelectric accelerometer sensor has been utilized at the beam and blade tip as shown in figures 3.13, to monitor vibratory acceleration in the components during rotating and non-rotating tests. Piezo accelerometers have wide frequency range and provide reliable results in different working conditions as well as being robust and readily mounted on the sensitive and rotating components. In addition, the ISOTRON accelerometer requires an independent current source which, typically designed with a built-in source of constant current, provides a compliance voltage of the sensor. Synchronizing this voltage with the bias voltage that appears in static condition, defines characteristics of the output signal as in figure 3.12.

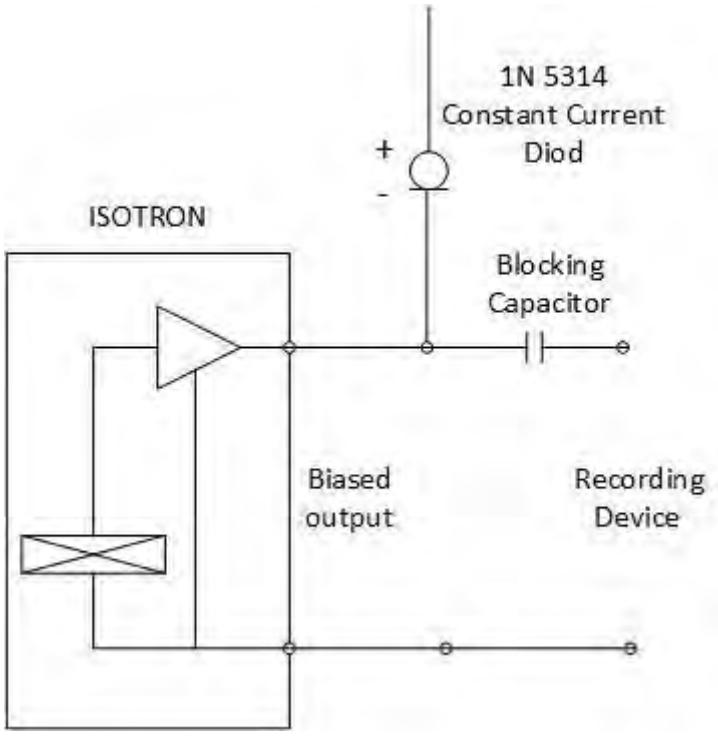

Figure 3.12 Simple ISOTRON accelerometer circuit diagram.

Figure 3.13 Piezoelectric accelerometer on the beam and blade tip.

A triaxial accelerometer has also been used at the top of the tower to detect the fluctuation in three perpendicular planes (XYZ directions) due to transient loads with special characteristics, for instance, very low vibration signals, and hard shocks. The seismic mass inside of this type of accelerometer has the ability to transfer the force to the piezoelectric element by compression. In addition, it has a slide base which sticks to the structure by wax to be sensitive to low-frequency vibration, as shown in figure 3.14.

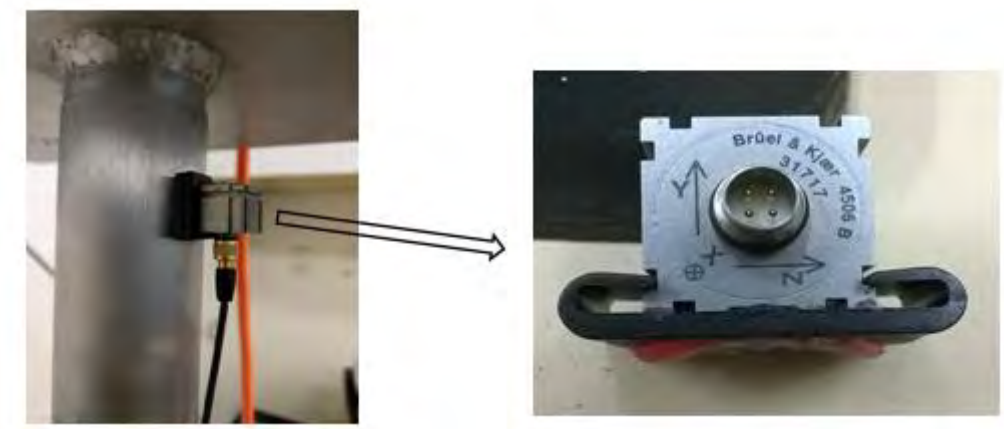

Figure 3.14 Tri-axial accelerometer with the holder on the tower.

3.2.8 Rotating beam

Creating a simple cantilever beam in the setup for modeling wind turbine blades provides an understanding of the vibrational behaviour of the simple rod structure through strain and acceleration measurements. In addition, the blade and hub connection will be a basic part of carrying the blade that will be used in upcoming tests. The uniform and homogenous aluminum beam utilized is 1 m long and 10 mm in diameter respectively. The flexibility of the aluminum beam with this length makes the structural deflections of the simulated blade considerably large due to transient loads.

Furthermore, it is known that the long slender rod has similar characteristics in many ways to a normal turbine blade undergoing axial, in-plane and out-of-plane bending and can be used to confirm many of the expected theoretical models. Additionally, instability due to the coupling of bending and torsional vibrations can obviously be detected through transient loads, which lead to flutter even in low rotating speeds. A beam inertia of 0.067 $kg.m^2$ about the shaft centre provides significant sensitivity for rotating or non-rotating strain and acceleration fluctuations and hence vibration measurement can be monitored. It has been instrumented with three sets of strain gauges near to the blade root to detect structural vibration by strain measurements. Strain measurements in all directions were calibrated through the use of different weights hanging off the tip, as illustrated in figure 3.15. A hanger has been used to carry the required weights, screwed axially in the beam and the hub was supported by a column to support the beam at 0^o angle. Various weights have been used in the calibration as well as the hanger weight to get the correct voltage across the gauges. The oscilloscope was used for measuring and displaying the voltage during tests which must be near to 0 volts without load.

Figure 3.15 Strain gauge calibration test with weight holder

Moving on to the other strain gauge groups, the beam has been rotated clockwise 90° around the end to be in the vertical position as in figure 3.16, with the previous calibration technique used to calibrate the strain gauges positioned in the axial direction.

Figure 3.16 The rotating beam in the vertical position with experiment mass screwed in the end.

An extension of 35mm long and 14.95g has been created for each blade to allow the addition or removal of weight at the beam tip.

Figure 3.17 The Aluminium optional extension part of 35mm long and 14.95g

3.2.9 Rotating blade

A simple blade profile model has been designed and manufactured from aluminum of a given length to investigate wind turbine vibration condition monitoring features using the test rig. Vibration and dynamic strain measurements allow the accurate monitoring of deformation and defects due to dynamic stresses. An aluminum sheet of 1000mm long, 200mm width and 4mm thickness has been folded to create a hollow blade of 1m long and 100 mm width with 6mm and 15mm diameter at the trailing and leading edges respectively, as shown in figure 3.18, 19 and 20.

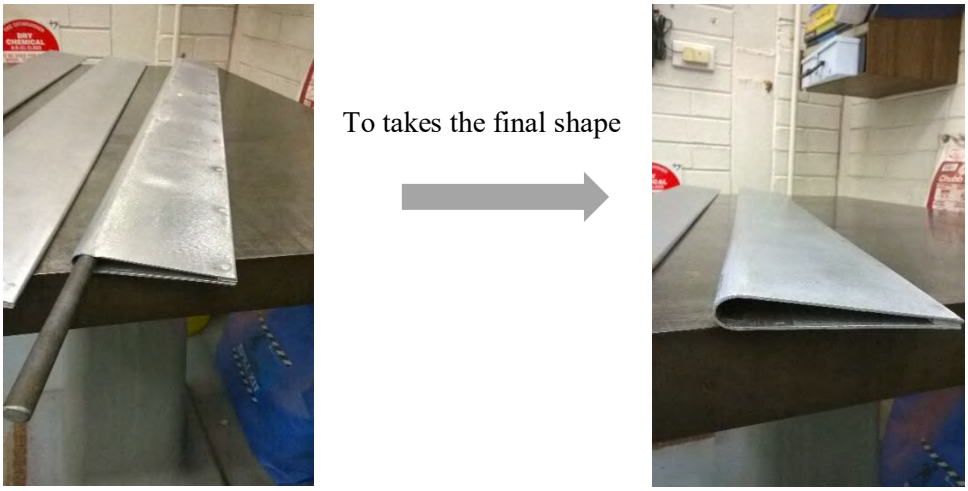

Figure 3.18 Aluminium blade manufacturing stages in the workshop.

Figure 3.19 Final Blade profile after complete manufacturing at 90° pitch

The edges of the sheet have carefully been riveted and blade ends covered by two pieces of the same material, welded and chamfered to create the blade box and the slender support beam. This untwisted blade weight was 1.203 Kg each, which makes it relatively heavy and easier to induce the dynamic stresses into the circular rod supporting member. Additionally, this model with a moment of inertia of 0.129 kg.m^2 has high fatigue strength compared with epoxy and fiber composite and high stiffness and damage resistance.

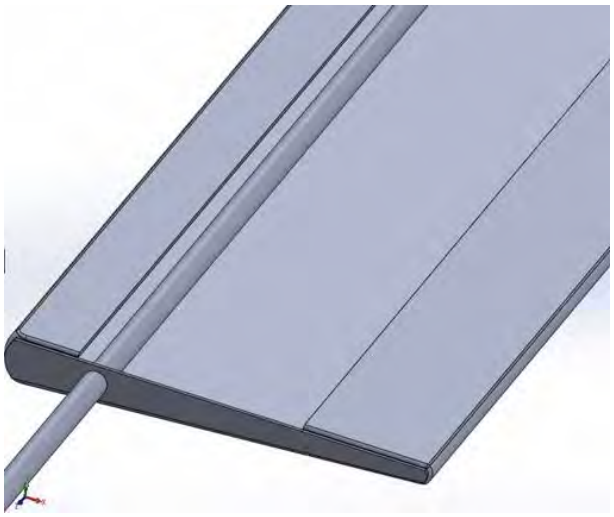

Figure 3.20 Hollow blade section

A slender aluminum beam of 1250 mm long has also been utilized inside the blade for support along the whole blade length and to assist in supporting it on the hub. It can

be used to provide the yaw motion in the wind turbine setup to effectively change the blade pitch in the test rig. A set of the strain gauges has been attached to the beam, in and out of the plane of the rotor blade, for bending measurements. The piezo accelerometer has been attached to the blade tip to detect bending vibrations on the tip as well as assist in understanding the blade dynamic behaviour during transient loading cases.

This model designed to withstand bending and torsional stresses due to aerodynamic loads and transient loads that would be applied during the experiments.

Additionally, strain gauge calibrations have been performed on the blade model in the same method as that implemented with the beam model, as illustrated in figure 3.21.

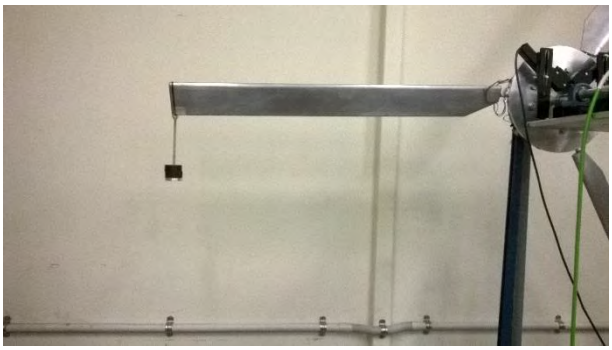

Figure 3.21 Blade model at the horizontal position during bending calibration

.

Adding masses to the blade model has been implemented by attached certain weight near to the blade tip according to the test method. The added mass during the artificial imbalance test as shown in figure 3.22, has been chosen to be adequate relative to the blade model mass.

Figure 3.22 The blade model during imbalance test (adding 200g mass).

However, to achieve an imbalance test with loss of mass, two 200g masses have been attached to two blades at the same position, while keeping the third free. This technique has been utilized with different rotor speeds.

Particular equipment has been used for the high-speed gust experiment. The system was assembled besides the wind turbine test rig to provide a variable air pressure burst towards the rotating blade; upwind and downwind. This test was significant for monitoring the rotating and non-rotating components behaviour during the transient gust, as shown in figure 3.23.

Figure 3.23 Compressed air system for providing a variable air burst towards upwind and downwind.

3.3 Conclusion

A small wind turbine test rig has been created for vibration condition monitoring-based strain and acceleration measurements. Blade premature failures due to vibration are the main cause of a significant number of turbine failures. This set up has been designed to facilitate improvements in condition monitoring methods for the early detection of significant failure modes. The test rig instrumentation includes the provision of novel techniques for signal transmission and measurements for vibration condition monitoring as well as the possibility of developing advanced methods for understanding coupled transverse, torsional and axial vibration behaviour during various implanted defects.

Chapter 4 Theoretical model of the horizontal-axis wind turbine test rig with the cantilever beam and blade models.

4.1. Introduction

A finite element model of the test rig was created in ANSYS 17.2, which modelled the blades of the HAWT as cantilever beams. The blade finite element model was created using SOLIDWORKS software and imported into ANSYS to assemble with the test rig's rotating components. This chapter discusses the analysis performed on the strain, deformation and acceleration of the cantilever beams. The cantilever beam was 1 meter long with a 10 mm diameter. The applied torque was considered fixed along the drive shaft. The component material was considered to be aluminum type 1060-H12, as detailed in Table 1. The full model included 152 contact regions starting from the lower base foundation up to the cantilever beams.

Table 4. 1Specifications of the test rig materials components

Property	Value
Density	2720 Kg/m^3
Young's Modulus	69 GPa
Ultimate Tensile strength	110 MPa
Tensile Yield Strength	280 MPa
Compressive Yield Strength	280 MPa
Tensile Ultimate Strength	310 MPa

4.2. The Finite element horizontal-axis wind turbine test rig model with a rotating thin cantilever beam

Three cantilever beams, representing the 3 blades of the HAWT, were inserted into the FEA model of the test rig. The torque was applied to the end of the shaft, which simulated the servo-motor, to generate the angular velocity as shown in figure 4.1. The servo-motor inertia was determined during the design of the upper base to substitute for the motor inertia in the model. The beam strain measured near the beam root was found to be similar to the simulated strain gauge results in the test rig model. The local coordinate system was considered at each rotor beam, as well as the global coordinate system at the lower base. Boundary conditions have been considered in the ANSYS model to simulate the bending load and unbalance conditions.

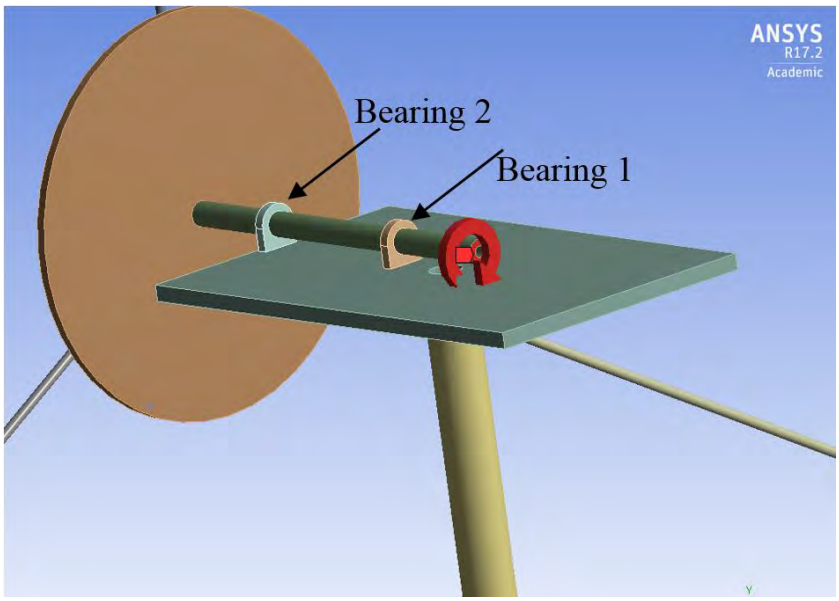

Figure 4.1The torque applied at the end of the rotor shaft

The FE beam model has been created to study the vibrations of the rotating and non-rotating component as different loads are applied. The upper and lower base had a coarse type mesh, while the other parts had a finer type mesh as illustrated in figure 4.2. The maximum number of elements used were 9258 elements, corresponding to 14932 nodes.

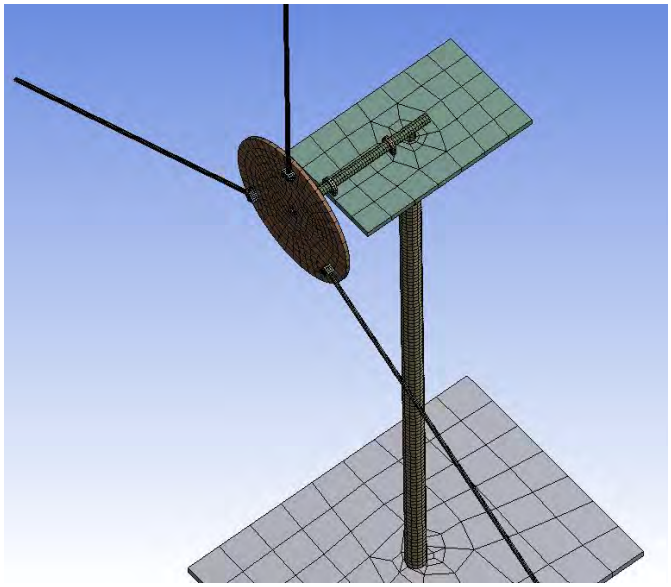

Figure 4. 2 Finite Element test rig model during the meshing method

Figure 4.3 illustrates the first five beam mode shapes of the cantilever beam from modal analysis. The maximum deformation was detected at the free end, while the minimum was on the clamped down end, as expected.

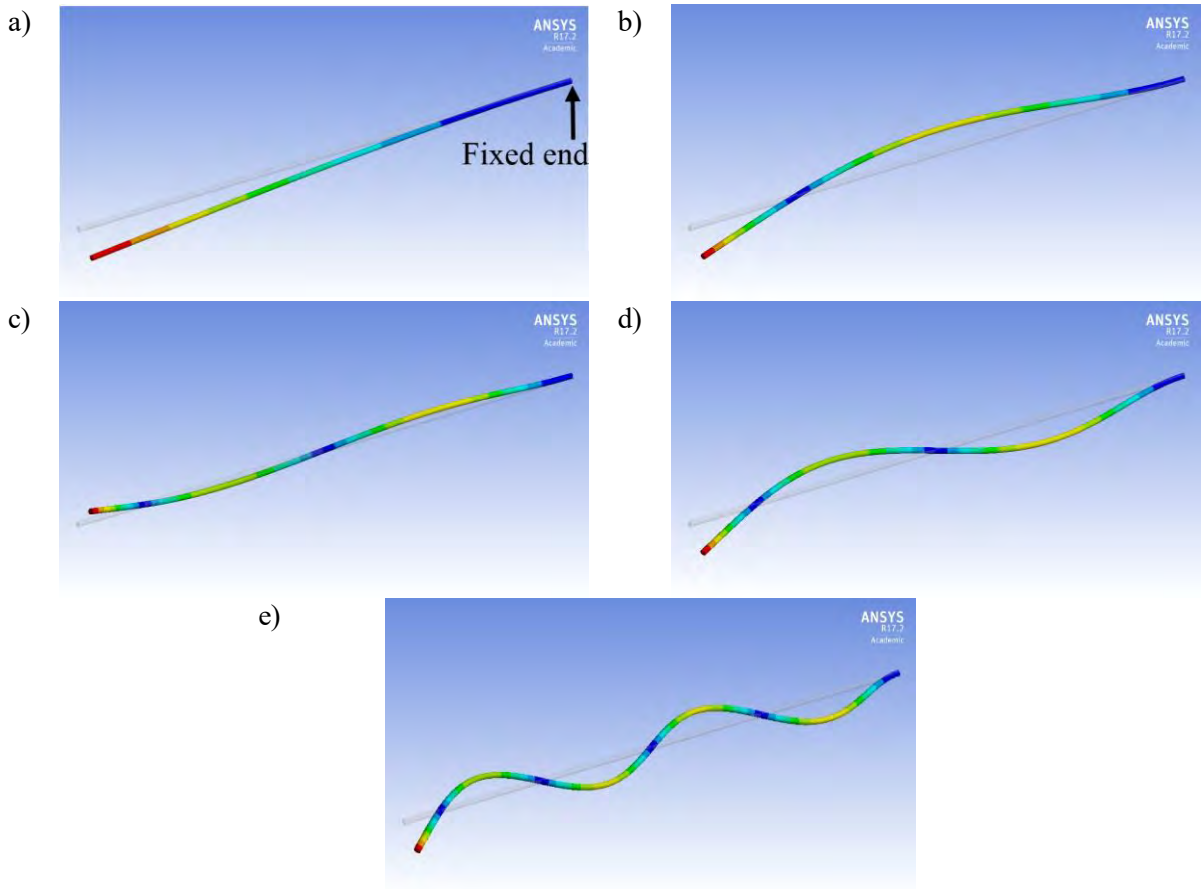

Figure 4. 3 First five fundamental mode shapes of the cantilever beam model.

Additionally, table 4.2 shows the the first 7th natural frequencies of the rotor cantilever beam which were calculated through modal analysis.

Table 4. 2 Calculated first 7th beam natural frequencies

Modes	Natural frequencies
1	7.851
2	49.231
3	136.1
4	267.3
5	448.2
6	659.5
7	922.4

4.2.1. Directional strain distribution at the impact test

The impact test was simulated by applying a 1N force as an implusive load in the in-plane direction. Figure 4.4 shows the beam strain simulation results during in-plane bending. Maximum in-plane strain has been measured near the beam root of 26.29µstrain.

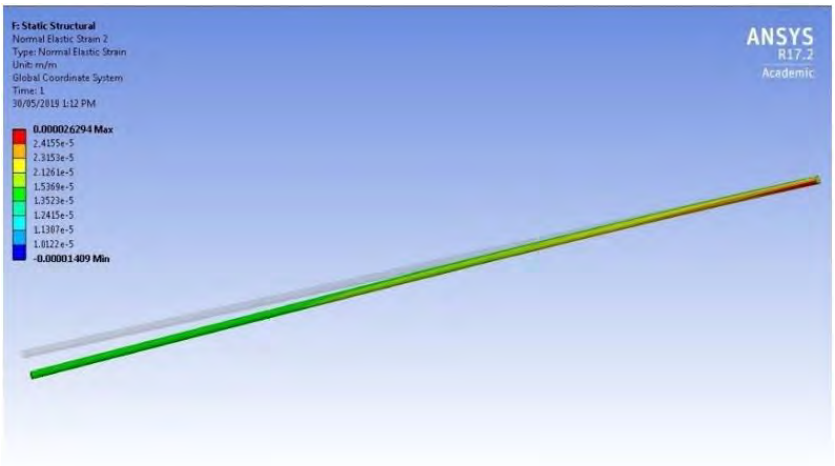

Figure 4. 4 In-plane beam strain during impact test with deformed and undeformed parts in the cantilever beam.

Figure 4.5 shows the in-plane strain distribution during the impact test. The impact time was set to 250 msec to identify the transient strain along the cantilever beam. The strain signal reduced with time due to the absence of the effective source and internal damping.

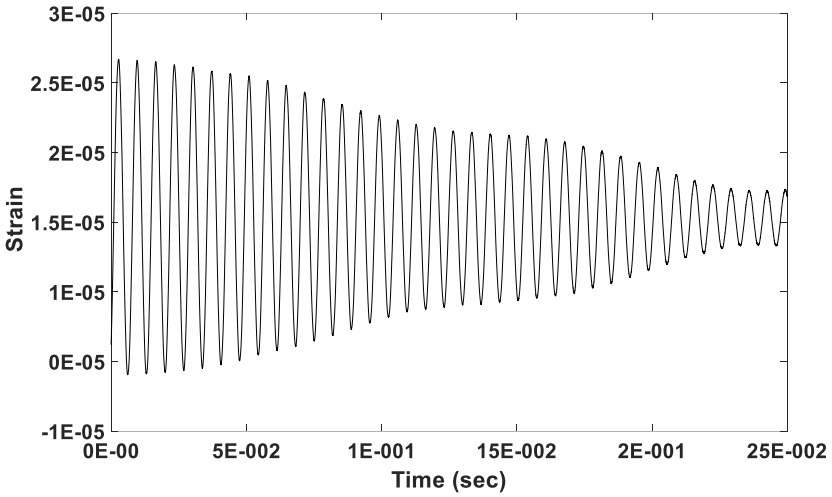

Figure 4. 5 In-plane strain of thin cantilever beam during impact test

Figure 4.6 illustrates the out-of-plane strain measurements excited due to the impact test of 1N force at the beam tip towards the rotation plane. The strain results have been measured near the beam fixed end as for the in-plane strain, where the maximum out-of-plane was 0.536 μstrain as can be seen in the figure.

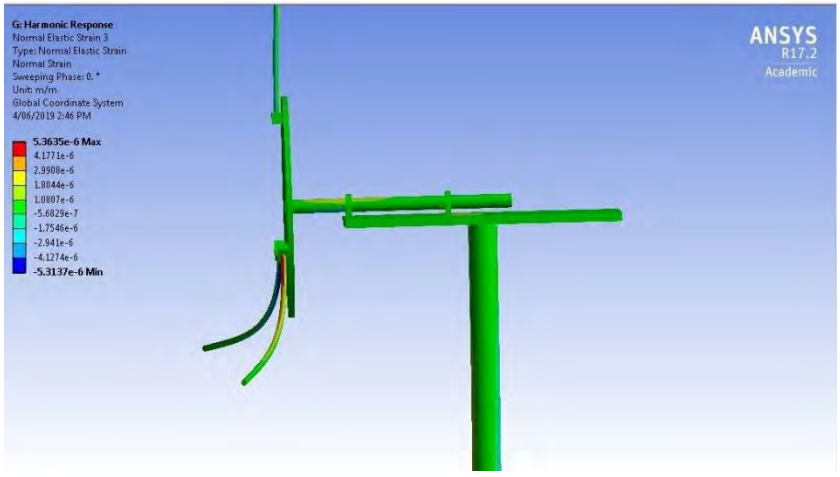

Figure 4. 6 Out-of-plane beam strain amplitudes during 1N impact test.

Additionally, figure 4.7 shows the out-of-plane strain signal during the impact test. It can be seen that the in-plane strain amplitudes were greater than the out-of-plane strain.

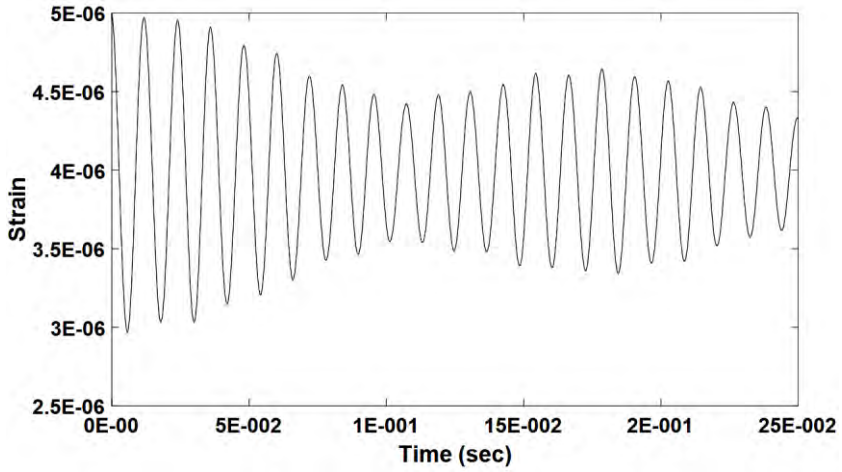

Figure 4. 7 Beam out-of-plane strain during impact test; Maximum (Green), and minimum (Red).

4.2.2. Dynamic beam strain during rotational motion

Modal analysis has been utilized to determine the response of the system while the shaft rotates. The rotational speed was set at 100 rpm for which the dynamic strain and deformation in the rotor beam and the test rig components were obtained. Beam rotation positively affected the dynamic bending of the rotating components due to the increase in centrifugal forces on the rotor beam. This can excite dynamic vibrations in the non-rotating components which increase as the rotating component's vibration increases.

Figure 4.8 shows the in-plane beam strain distribution along the beam length. The strain probe has been located near the fixed end for strain measurement.

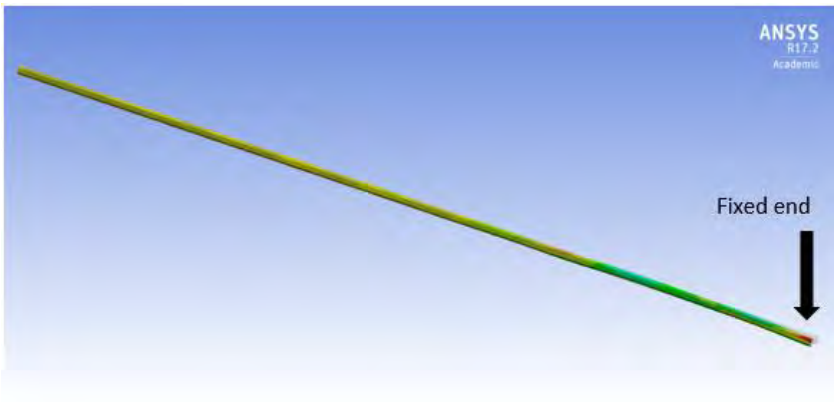

Figure 4. 8 Dynamic in-plane strain predictions during 100 rpm rotational velocity.

Additionally, figure 4.9 shows the maximum and minimum in-plane beam strain calculated for a rotational velocity of 100 rpm. The maximum in-plane beam strain was found to be 388.6 µstrain while minimum beam strain was found to be 47.8µstrain.

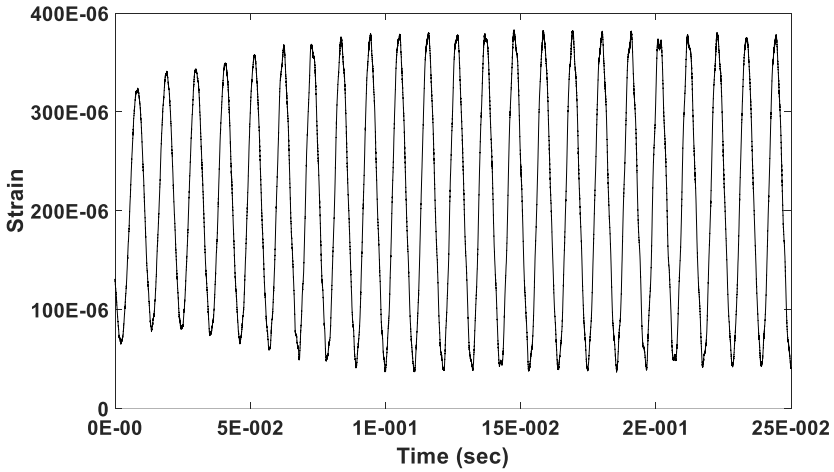

Figure 4. 9 Beam in-plane strain at 100 rpm rotational velocity

The axial beam strain is shown in figure 4.10. The maximum strain was 30µstrain, while the minimum axial strain was 20.9 µstrain. Both in-plane and axial strain increased with time due to the increase in beam bending due to the rotation at 100 rpm (the rotation increased from 0 to the required speed 100 rpm during 100 sec) .

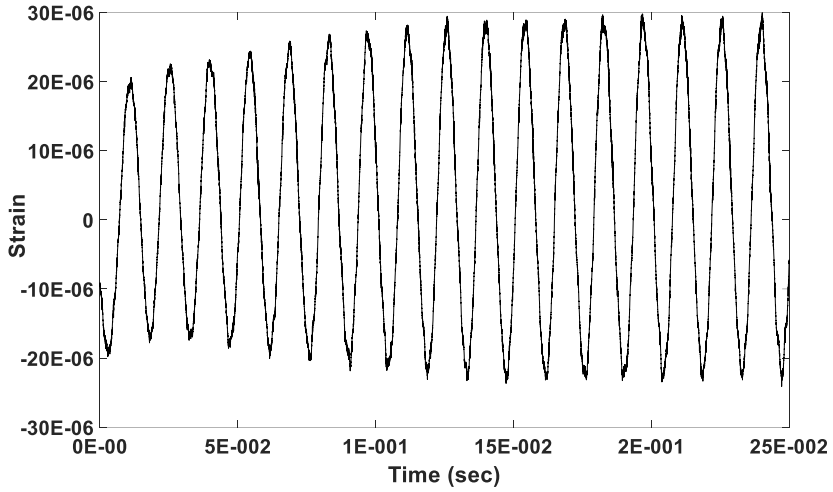

Figure 4. 10 Beam Axial normal strain during 100 rpm rotational velocity

The beam vibration excited perpendicular to the rotational plane can be measured by out-of-plane strain. Figure 4.11 shows the predicted out-of-plane strain at the 100 rpm rotor speed. The maximum strain is 47.52 μstrain and the minimum is 3.82 μstrain.

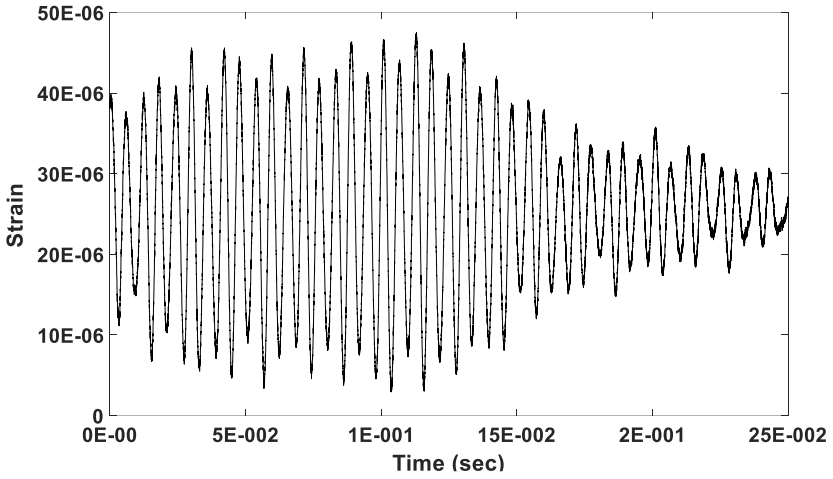

Figure 4. 11 Beam out-of-plane strain during 100 rpm rotational velocity

4.2.3. Dynamic tower acceleration during rotational motion

Tower directional acceleration was calculated via modal analysis corresponding to the beam and driveshaft. Figure 4.12 shows the tower acceleration towards the Z-direction

(lateral vibration). This figure shows the tower acceleration having a maximum value of 0.75 m/s^2 and a minimum value of -0.39 m/s^2.

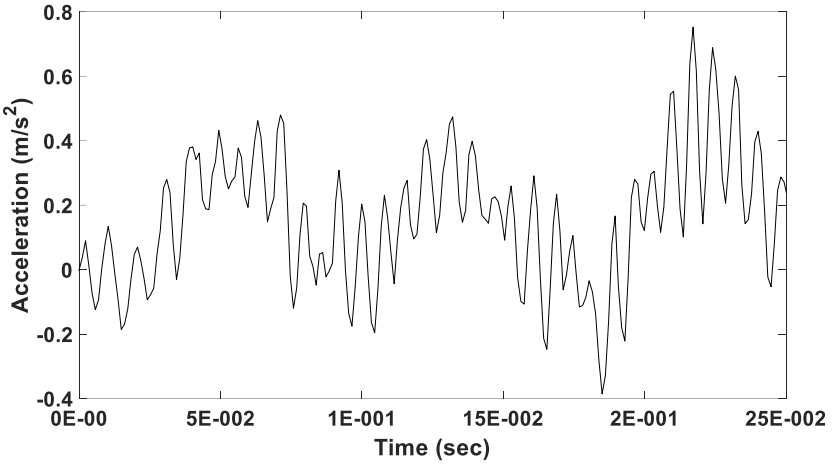

Figure 4. 12 Directional tower acceleration at Z-direction during 100 rpm rotational speed.

Coupling can be seen between the tower maximum acceleration in the X and Z directions due to the excitation between the two modes. Additionally, the maximum tower acceleration at X-direction is 0.5 m/s^2 while the minimum is 0.12 m/s^2 as shown in figure 4.13.

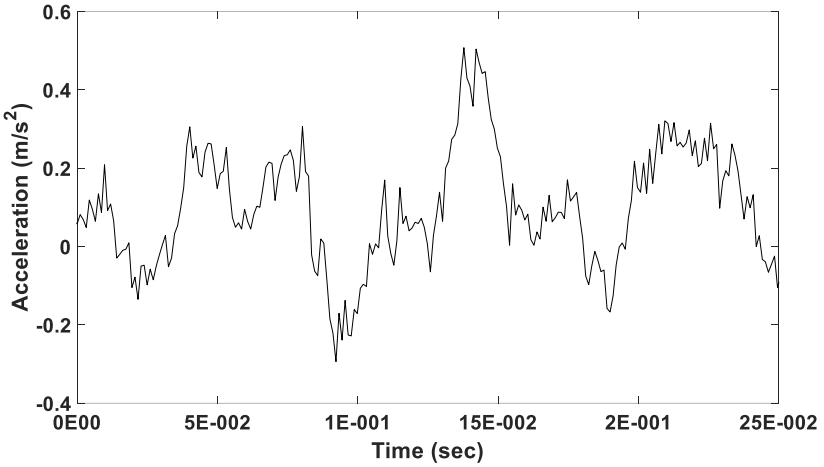

Figure 4. 13 Directional tower acceleration at X-direction during 100 rpm rotor speed.

Due to the increase in the centrifugal forces as the speed increases, tower vibration in the Z-direction excites vibration towards the Y-direction, where the maximum tower acceleration in this direction is -0.6 m/s^2, and the minimum is 0.015 m/s^2 as shown in figure 4.14. Decreasing acceleration can be observed in the tower response at this mode when the rotor reaches the required speed, while this doesn't occur at Z and X

tower modes. This can be attributed to the increase in centrifugal forces which leads to increasing in-plane and axial beam vibrations, which decreases the fluctuation towards the Y-direction.

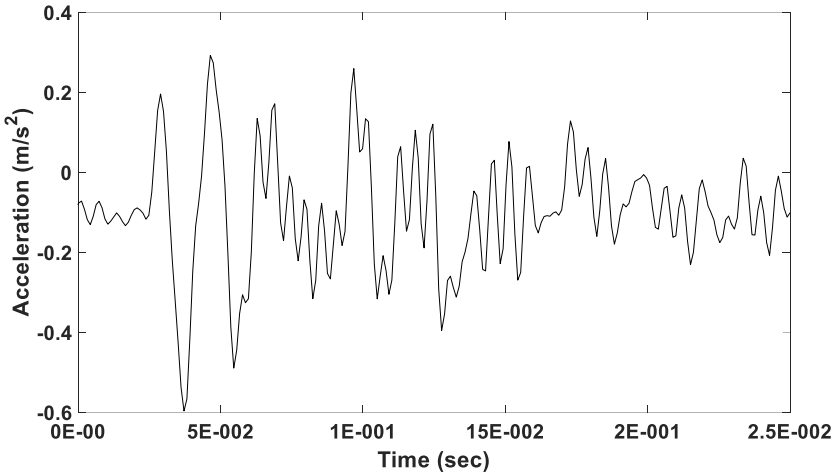

Figure 4. 14 Directional tower acceleration at Y-direction during 100 rpm rotor speed.

Figure 4.15 shows the tower acceleration along its length in the Y-direction. Maximum acceleration was found to be near the upper base, which is the preferred location to attach an accelerometer.

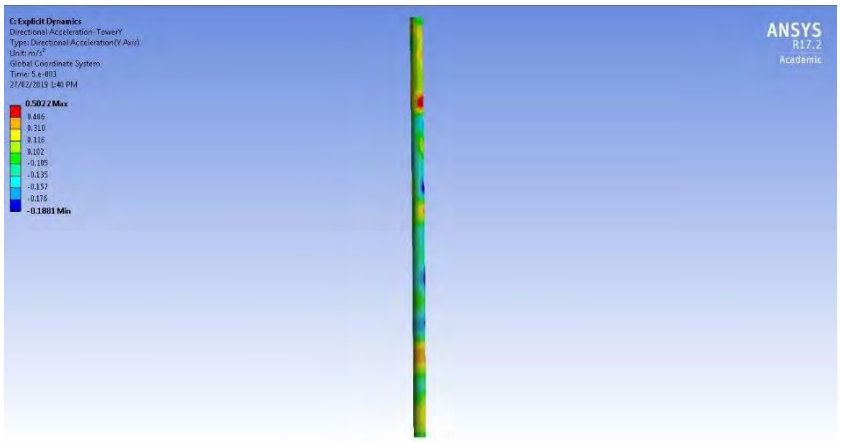

Figure 4. 15 Distribution of acceleration amplitude along with the supporting tower at 100 rpm rotational speed towards the Y-direction.

Figure 4.16 illustrates the tower deflection response after implementing the 100 rpm rotational speed on the drive shaft, to identify the deformation towards the Y-direction. Maximum tower deflection of 0.012 m occurred at the upper part due to the drag from the beam vibrations towards the out-of-plane directions.

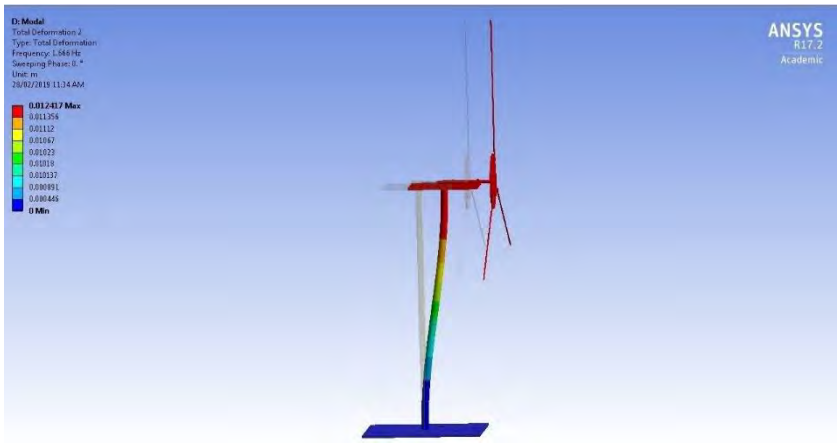

Figure 4. 16 Deformation of the tower and the rotating components towards the Y-direction.

Figure 4.17 illustrates the tower lateral deformation (Z-direction) corresponding to the beam's maximum deformation of 0.014 m at 100 rpm. The tower deformation occurs as a result of the coupling with the beam in-plane vibration. Additionally, the hub is excited as a rotating component during this speed and is deformed by 0.001 m in the Z-direction.

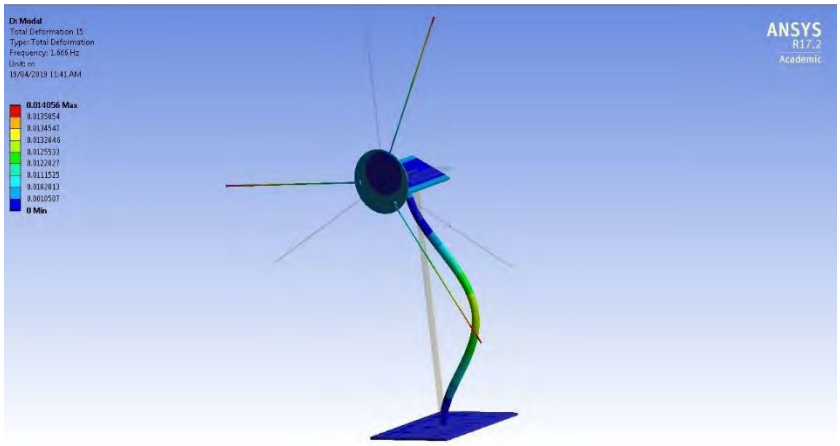

Figure 4. 17 Deformation of the tower corresponding to the rotating components towards Z-direction at 1.66 Hz

The tower vibration towards the X-direction has been identified through the axial deformation as shown in figure 4.18. The tower has different deformation levels along the length, with a maximum at the top of 0.006 m simultaneously with the rotor shaft, hub, and the deformation of the rotating beam.

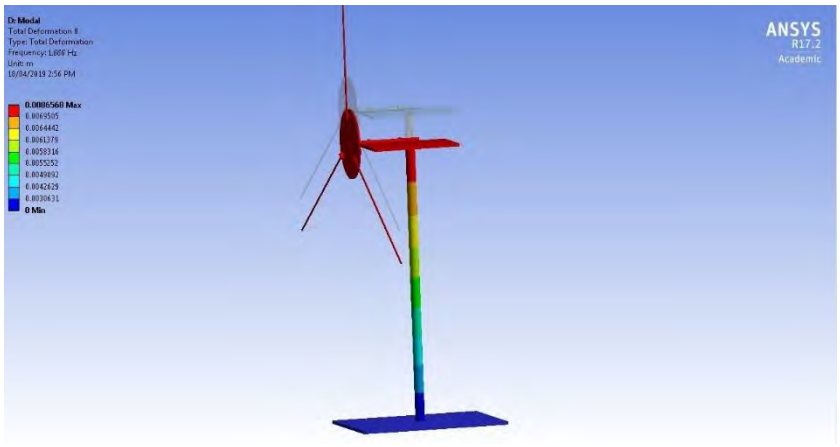

Figure 4. 18 Axial tower deformation corresponding to the drive train at 100 rpm.

4.2.4. Rotor shaft deformation during rotational motion

The bending vibration of the rotor shaft is shown in figure 4.19. Maximum bending (611 microns) occurred at the free end that was connected with the hub. The dynamic bending decreased towards the fixed end which was connected with servo-motor and was found to have minimum shaft bending (42.3 microns).

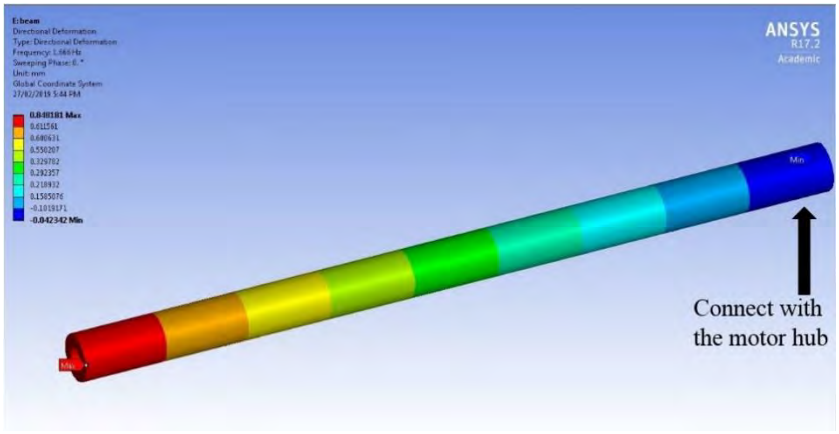

Figure 4. 19 The hollow rotor shaft deformation during 100 rpm rotating speed.

The deformation of the drive shaft can be seen in figure 4.20. The upper base has been affected by the rotation due to the shaft deformation. Additionally, the maximum hub deformation of 837.8 microns increased the cantilever beam vibration during the rotation. The other two beams bend by about 292.1 microns at the tip, and the third had a bend of 550.2 microns which was close to the maximum hub bending.

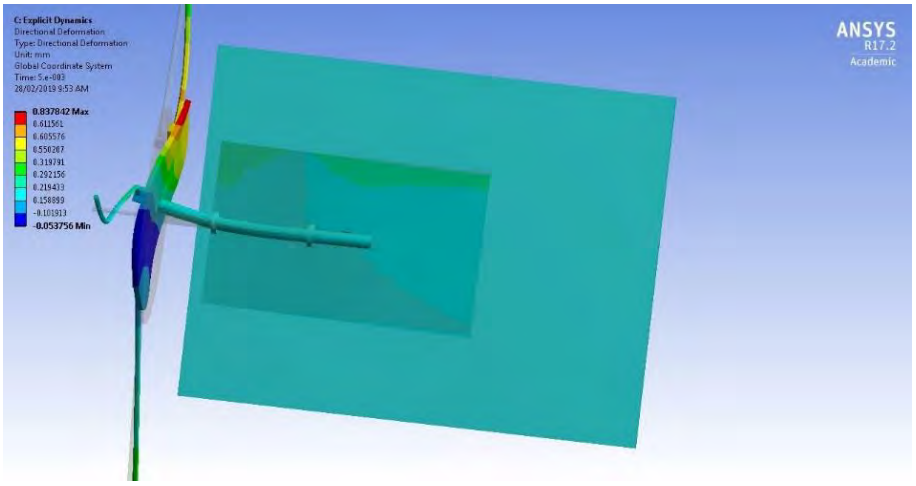

Figure 4. 20 Deformation of the rotor shaft corresponding to the drive train in the test rig model system at 100 rpm.

4.3. Horizontal-axis wind turbine test rig with a rotating blade model

A model of the blade was created to replace the cantilever beam in the wind turbine test rig. This was created using the finite element beam model which was utilized in the previous section. The new model has been bonded to the hub through a circular solid beam extended along the blade length to the blocks in the hub as shown in figure 4.21. This figure also illustrated the meshed system which was applied with the new blade mathematical model. The mesh contained 24006 nodes and 4787 elements(solid elements for the plates and hub, and hollow elements for the blades, drive shaft and tower).

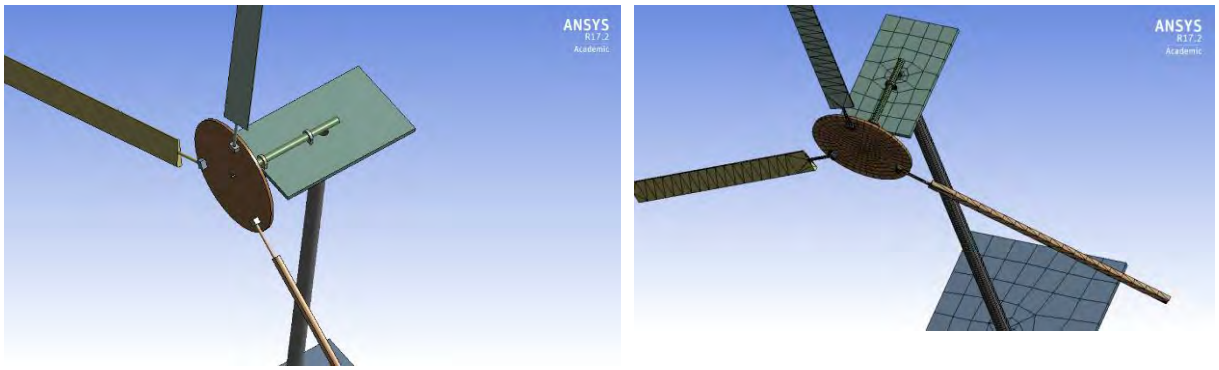

Figure 4. 21 Blade mathematical meshed and unmeshed model in the test rig simulator.

Figure 4.22 shows the first five natural frequencies of the blade finite element model. The maximum deflections for the first, second and third modes occurred at the blade tip, whereas, in the fourth and fifth modes it occurred near the blade root. Additionally, table 4.3 shows the first seven blade natural frequencies detected from the modal analysis.

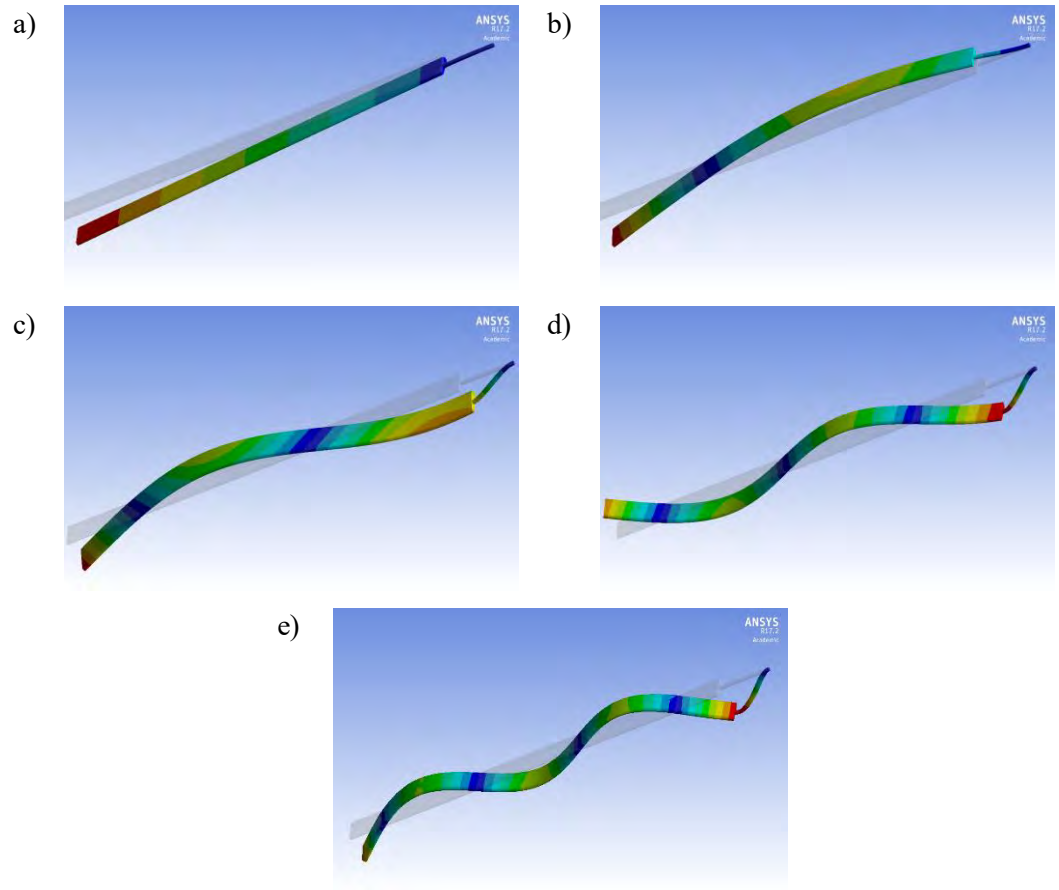

Figure 4. 22 The first dominant five modes of the blade mathematical model.

Table 4. 3 First 7 natural frequencies of the blade

Modes	Natural frequency (Hz)
1	3.25
2	14.04
3	54.79
4	103.34
5	144.97
6	171.03
7	204.7

4.3.1. Blade Directional strain distribution during the impact test

An impact test was implemented on one blade by subjecting it to a 1N force on the blade, spanwise in the in-plane direction. A static structural and modal analysis was applied to identify the directional and total strain and deformations on the test rig components.

Figure 4.23 illustrates the distribution of the axial strain on the blade model during the impact test. The maximum and minimum axial strain were 137.4 µstrain and -141.5 µstrain respectively.

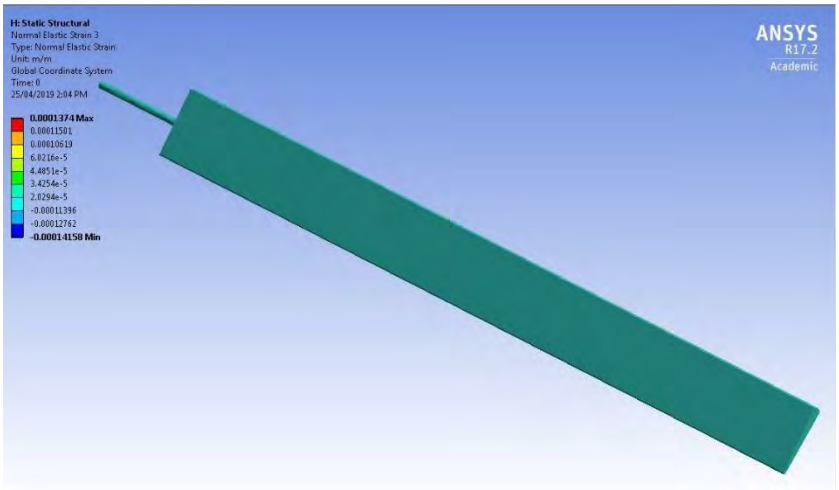

Figure 4. 23 Normal elastic axial strain on the rotor blade during the impact test.

Figure 4.24 shows the blade in-plane strain measurement during the impact test, which shows that the maximum in-plane strain occurs at the connection beam. The maximum in-plane strain was 478.4 µstrain, while the minimum strain was -466.9 µstrain.

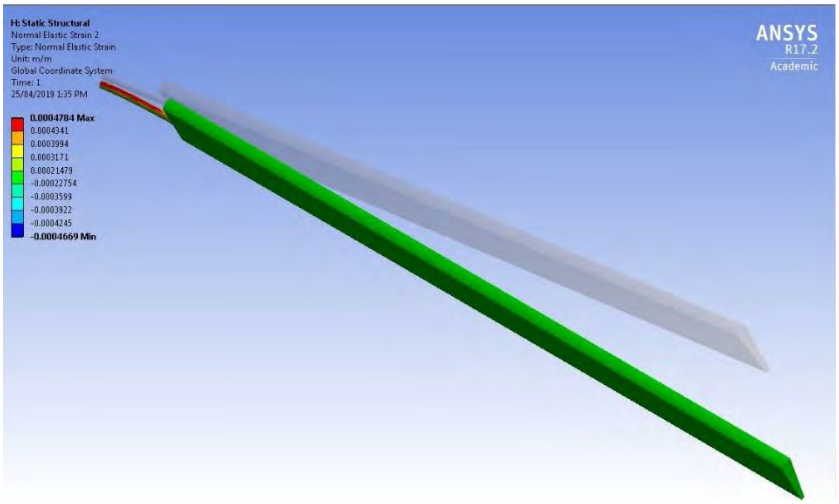

Figure 4. 24 Deformed and undeformed parts of the rotor blade during in-plane strain measurement at the impact test.

Figure 4.25 shows the maximum (418.5 µstrain) and minimum (414.3 µstrain) out-of-plane strain obtained during the impact test. The supporting beam experienced a high strain during the blade deformation perpendicularly on the rotor plane.

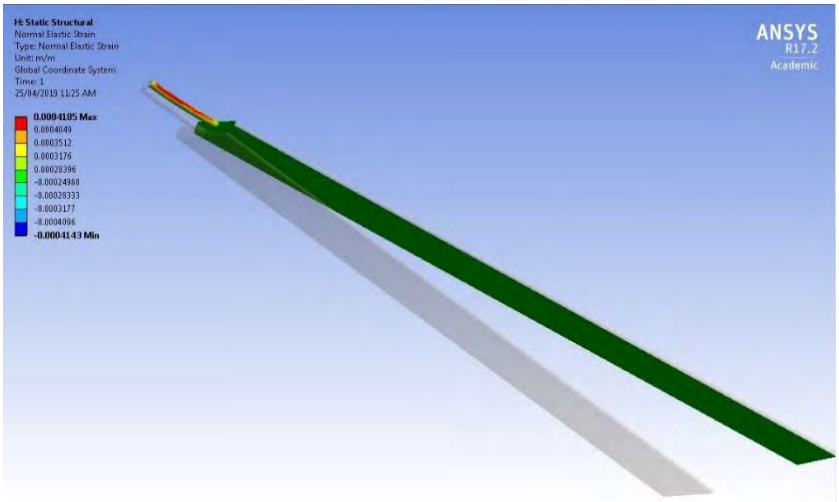

Figure 4. 25 Deformed and undeformed parts of the rotor blade during out-of-plane strain measurement at the impact test

4.3.2. Dynamic blade strain during rotational motion

A dynamic modal analysis was performed on the test rig theoretical model with the rotor blade utilizing boundary conditions similar to the practical model, with a rotational speed of 100 rpm during the analysis. The maximum axial strain was 338.8 µstrain as illustrated in figure 4.26, due to the centrifugal forces that were developed during the rotation.

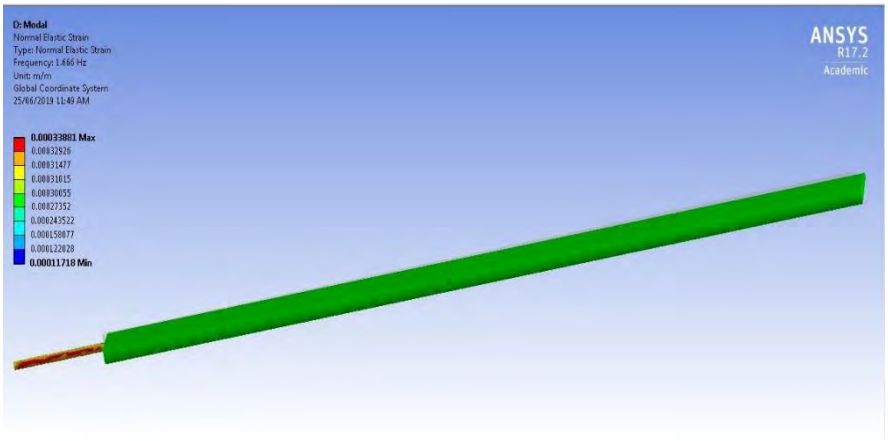

Figure 4. 26 Normal elastic blade axial strain calculated from modal analysis at 100 rpm.

Figure 4.27 illustrates the blade in-plane strain calculated from the modal analysis at 100 rpm. The maximum strain occurred at the supporting beam, reaching a maximum of 833.8 µstrain, whereas, the minimum in-plane strain was -827.1 µstrain. The figure has also shown the deformed and undeformed blade parts.

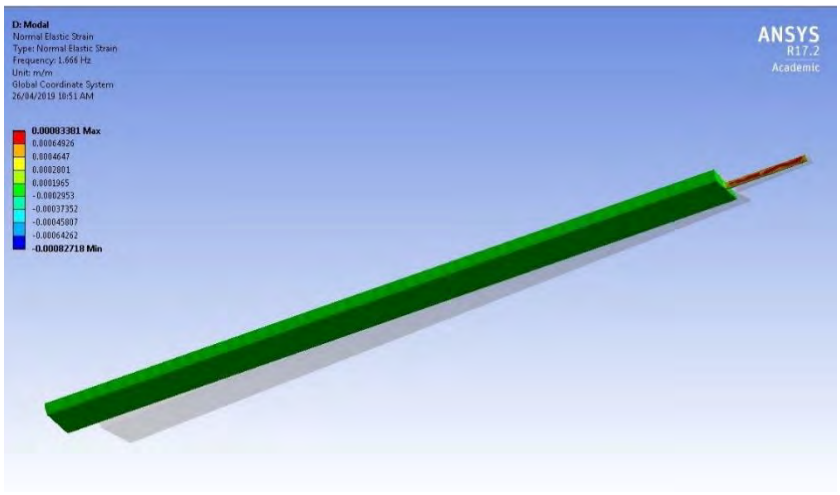

Figure 4. 27 Normal elastic blade in-plane strain specified by modal analysis at 100 rpm.

Furthermore, blade out-of-plane strain can be determined through modal analysis by calculating the normal elastic strain measurement along the blade vibration direction, as shown in figure 4.28. The maximum strain was 482.08 µstrain near the blade root, whereas at the blade spanwise it was 108.8 µstrain.

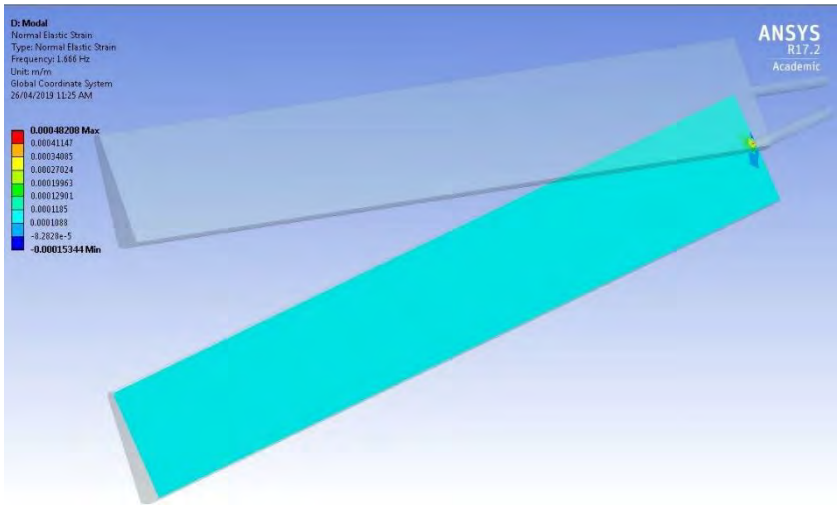

Figure 4. 28 Normal elastic blade out-of-plane strain identified by modal analysis at 100 rpm.

4.3.3. Dynamic blade deformation during rotational motion

The blade in-plane deformation was simulated by positioning a rotational velocity (100 rpm) on the rotor shaft end instead of the servo-motor end. Figure 4.29 illustrates the deformation of the rotor blades with the rotational plane (in-plane direction) at 100 rpm. The maximum blade deformation of 0.097 m occurred at the blade tip. Additionally, the hub deformed by 0.05 m due to the excitation from the rotor blades.

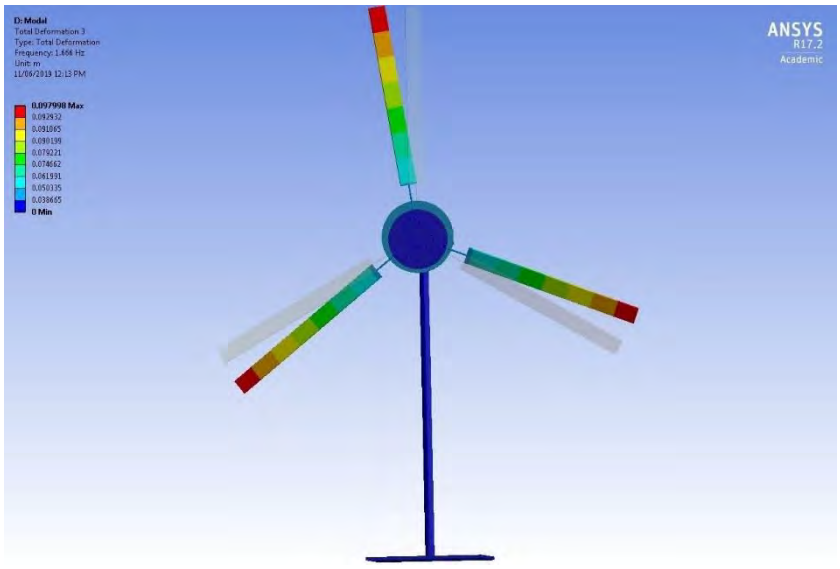

Figure 4. 29 Deformed and undeformed parts during in-plane blade vibrations at 100 rpm.

Additionally, modal analysis was used to simulate the blade out-of-plane deformation at 100 rpm with the loading conditions perpendicular to the rotation plane by making the blade out-of-plane direction free, without considering the deformation of the other components. Figure 4.30 shows the deformed and undeformed parts from the rotor blade during 100 rpm, where the maximum out-of-plane deformation was 0.034 m. It can be observed that the blade out-of-plane amplitude is less than the in-plane amplitude. This was attributed to the blade out-of-plane vibration.

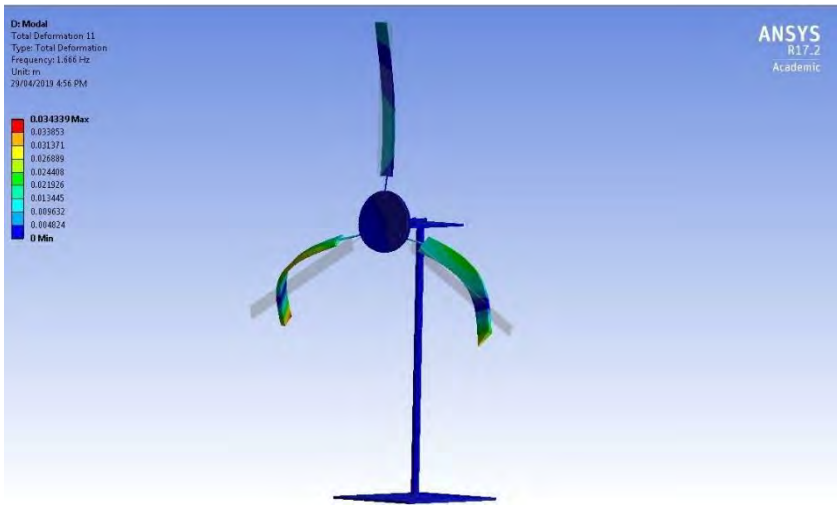

Figure 4. 30 Deformed and undeformed parts during out-of-plane blade vibrations at 100 rpm.

4.3.4. Dynamic shaft deformation during rotational motion

The modal and explicit dynamic analysis was conducted with particular conditions for the drive shaft deformations. The displacement directions were identified according to local coordinates which were positioned on the front shaft end at the connection with the hub, to detect the local displacement (the distance between the hub and the bearing) corresponding to the other drive shaft parts. The maximum driveshaft deformation was measured to be 443.7 microns at the free end that connected with the hub, as shown in figure 4.31. The deformation direction was identified perpendicular to the shaft rotation. The shaft bending displacements were measured during a condition of free blade out-of-plane vibration and tower front deflection.

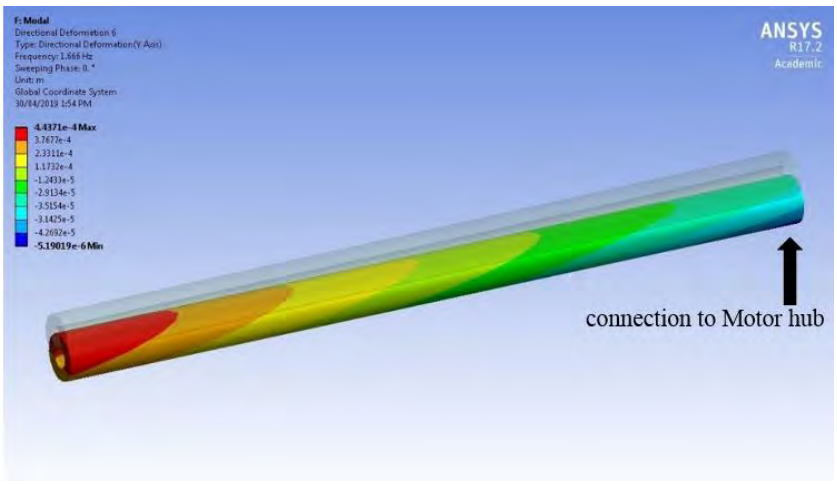

Figure 4. 31 Driveshaft deformation during modal analysis at 100 rpm.

4.3.5. Dynamic tower deformation during rotational motion

Harmonic response analysis was performed on the test rig model to show the tower lateral deformation during 100 rpm motion. The maximum tower deformation was 0.03 m which occurred in the middle part from the supported tower which was coupled with the blade in-plane deformation, as shown in figure 4.32.

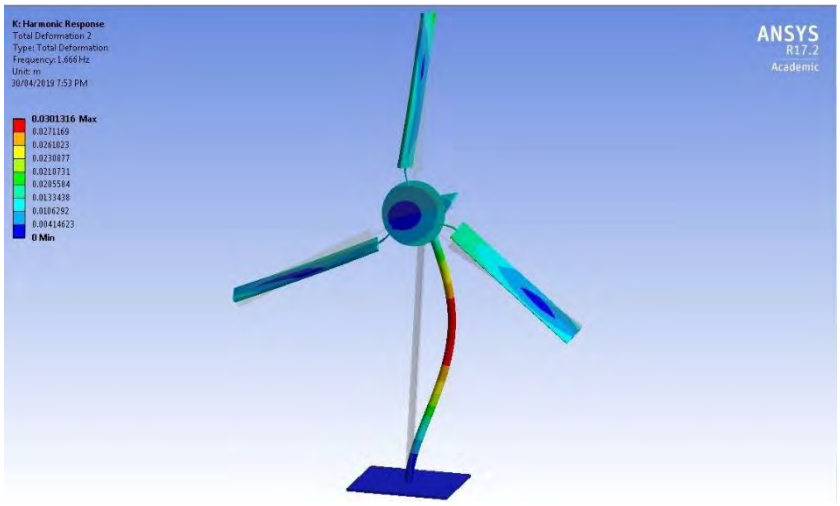

Figure 4. 32 Harmonic response analysis shows tower lateral deformation during 100 rpm.

4.3.6. Dynamic tower acceleration during rotational motion

During the blade rotation, the tower experienced various types of excitation due to the coupling between the blade and tower vibration. Figure 4.33 illustrates the acceleration distribution along the tower utilizing dynamic analysis. The maximum acceleration amplitude at 100 rpm was 0.774 m/s^2 axially. The analysis considered the inertia of the rotating components on the upper base and constrained displacement of the lower base as the loading conditions.

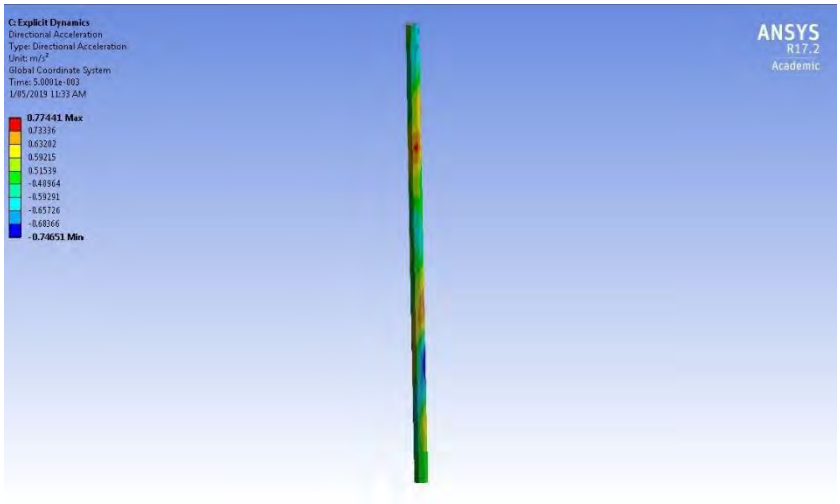

Figure 4. 33 The acceleration distribution on the tower mathematical model towards the axial direction at 100 rpm (from the top).

The frontal (Y-direction) acceleration distribution of the tower which resulted from its dynamics is shown in figure 4.34. This figure shows the maximum acceleration of 0.694 m/s^2 occurred near to the fixed base of the test rig mathematical model during the rotation at 100 rpm. The analysis considered the loading conditions of the rotating parts. The blade out-of-plane vibration has a direct effect on the increase in the tower frontal acceleration due to the coupling between those modes.

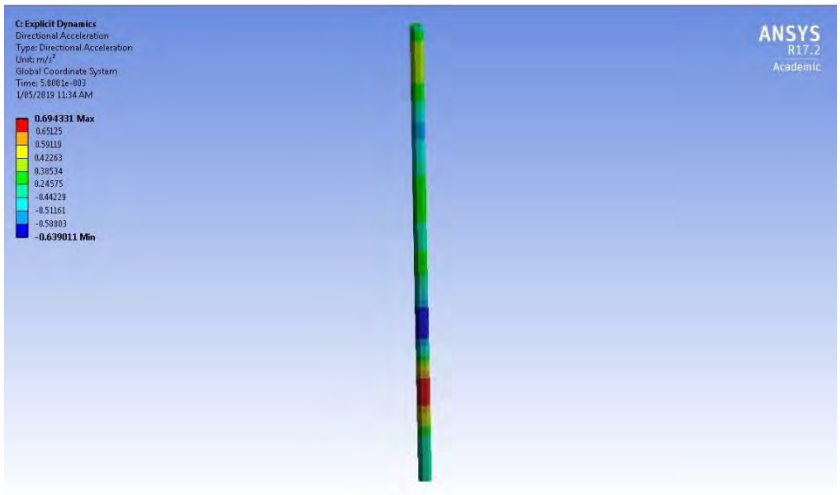

Figure 4. 34 The acceleration distribution on the tower mathematical model towards the front direction at 100 rpm.

Figure 4.35 illustrates the acceleration distribution of the tower model in the lateral Z direction. Two positions of maximum acceleration of 0.813 m/s^2 were detected, as well as the increase in tower acceleration compared with the other directions. Additionally, the coupling between this tower mode and the blade in-plane vibration increased the acceleration amplitude in this direction.

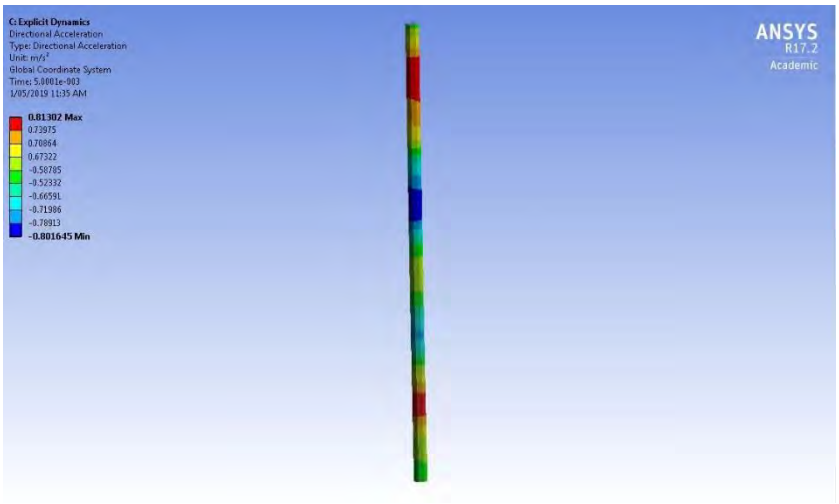

Figure 4. 35 The acceleration distribution on the tower mathematical model towards lateral (Z) direction at 100 rpm.

4.4. Conclusion

This chapter presents the theoretical analysis of the test rig system utilizing finite element analysis (ANSYS 17.2). The test rig finite elemnent model was created and assembled with two models; a rotating cantilever beam and hollow blade similar to the practical models for the comparison between the outcomes. The loading conditions that were used with the beam model and blade model is similar to the corresponding practical models to achieve a comprehensive vibration monitoring of the rotating and non-rotating components. A developed meshing procedure was used with the two models to increase the calculation accuracy and decrease the calculation time. The test rig structure was analysed statically to detect force distribution on the cantilever beam and blade models. A rotational velocity was utilised with the analysis to achieve the dynamic simulation of the mathematical models, to identify the strain, acceleration and deformation amplitude of the test rig components. The dynamic deformations in the test rig system considered a 100 rpm rotational speed for the comparison between the outcomes. A coupling between the blade in-plane vibrations and the lateral tower vibrations from the side and blade out-of-plane vibration with frontal tower vibrations from the other side was detected during the analysis due to the mutual excitation between the test rig rotating and non-rotating components. The experimental variation with rotor speed is considered in the next chapter to achieve vibration condition monitoring for various loading conditions.

Chapter 5 Investigation of beam vibration condition monitoring during different rotor speed in the horizontal small-scale wind turbine test rig.

5.1 Introduction

Wind turbine blades are vulnerable to high fatigue loads due to working in severe conditions. Identifying vibration characteristics during different conditions based on dynamic displacement has been found to be a key factor in reducing operating faults to ensure safe working and longevity. Modelling wind turbine blades as a tuned rotating cantilever beam is a further technique to simplify the vibration calculations. This chapter investigates the dynamic response of the rotating beam model, whereby effective condition monitoring was achieved using rotating and non-rotating sensors. The analysis performed includes time-variant strain and acceleration measurements of the blades and tower in the horizontal axis wind turbine test rig.

5.2 Dynamic modelling of wind turbine blade as a thin solid cantilever beam

Three lightweight and slender Aluminum solid beams were manufactured and positioned radially in the hub, to model the wind turbine blades in the developed test rig. The beams' specifications are provided in table 5.1. The beams were clamped at the end of the hub as shown in figure 5.1. The cantilever beam has been instrumented with calibrated rotating sensors such as strain gauges and piezo-accelerometers.

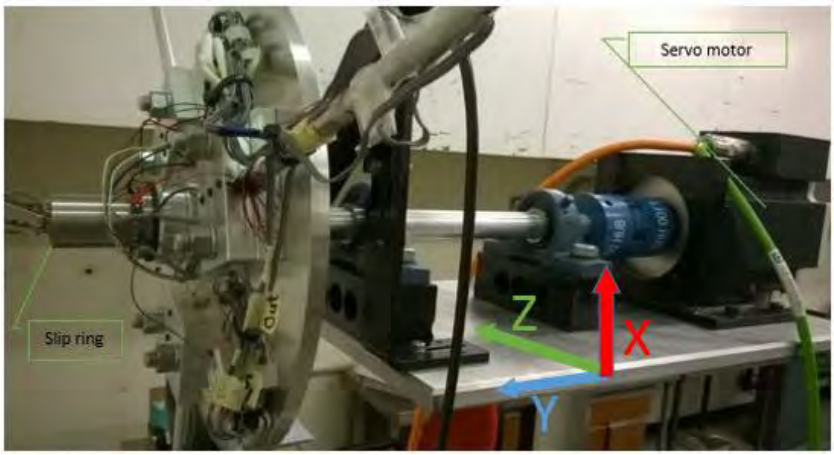

Figure 5. 1 Three rotating beams on the small wind turbine test rig

Table 5. 1specifications of the rotating beams

Material	Aluminum
Radius (m)	0.005
Length (m)	1
Volume (m^3)	$7.8539x10^{-5}$
Mass (kg)	0.212
Young's modulus, *E* (GPa)	69
Poisson's Ratio	0.3

5.3 Beam acceleration and strain measurements at a standstill

Initially, the beam and tower of the small-scale wind turbine test rig were forced to vibrate to analyse the measurements signals from the strain gauges and accelerometers. Sensors were calibrated and their transmitted signal integrity was inspected. The beam's natural frequencies were experimentally obtained during this initial analysis.

5.3.1 Influence of static tip load on the cantilever beam response

The impact test is an essential technique to assess the beam structure by applying different static loads and monitoring the conditions through the measurement sensors. This method has been adopted for the beam and tower to simulate the external force and analyse the strain statically, as well as providing variable deformed data of the test rig components. The signal integrity experiment analysis from components before the rotation is capable of providing the pre-rotation conditions of both the component and measurement sensor. The test was performed by an impact force to the beam and tower and after a few seconds, recording the corresponding measurement using the data acquisition system and MATLAB.

Figure 5.2 shows the fluctuation of the tower due to applying a force along the y-direction.

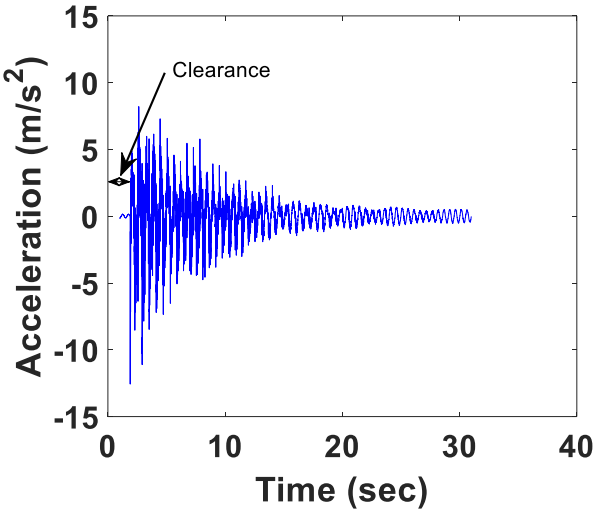

Figure 5.2 Tower vibration amplitude at a standstill

The resulting acceleration amplitude is noticed to be at high values when applying the external force which indicates the high vibration amplitude of the components. The signal integrity, gauge, and component installation is inferred by the regularity of the vibration decay with time. Additionally, figure 5.3 represents the beam response obtained from the piezoelectric accelerometer attached to the beam tip due to an impact test with applied external force near the beam tip.

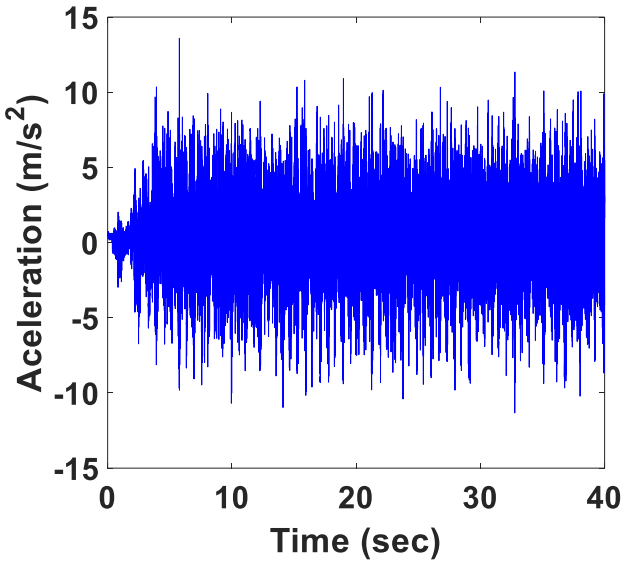

Figure 5.3 Beam vibration amplitude due to impact test.

Beam natural frequencies have been obtained experimentally via spectral analysis of the impact test. Figure 5.4 indicates the first ten natural frequencies of the rotating beam, which are also listed in Table 5.2. The beams have been designed to have a large difference between each of the modes to avoid unpredictable stops that normally result from exceedingly large vibration amplitudes. Beam strain in the axial, in-plane, and out-of-plane directions for the rotating beam has been considered to assess the response during load conditions. In this test, monitoring for large deformations in the beam structure was essential due to the applied loads.

The resulting acceleration amplitudes, strain amplitudes, and dynamic responses were analysed for each experiment.

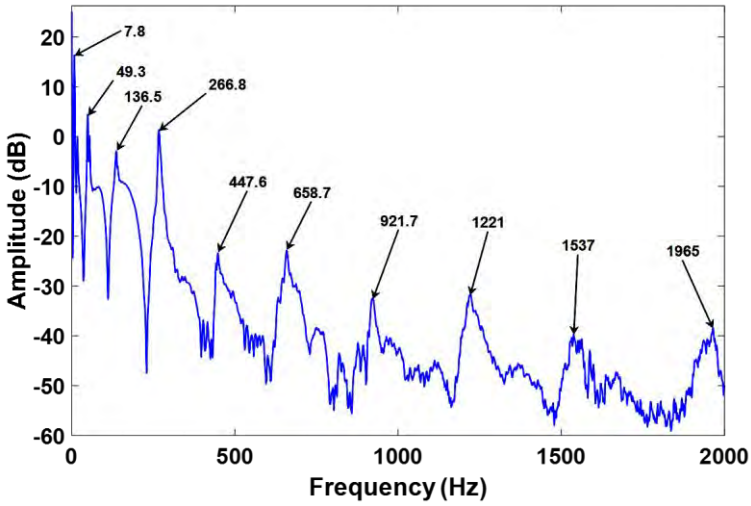

Figure 5.4 Power spectrum of the rotating cantilever beam at a standstill from impact test.

Similarly, the first 7th natural frequencies of the tower have been presented in figure 5.5, which were identified from an impact test before the experiments during the calibration and test procedures of the rotating and non-rotating sensors.

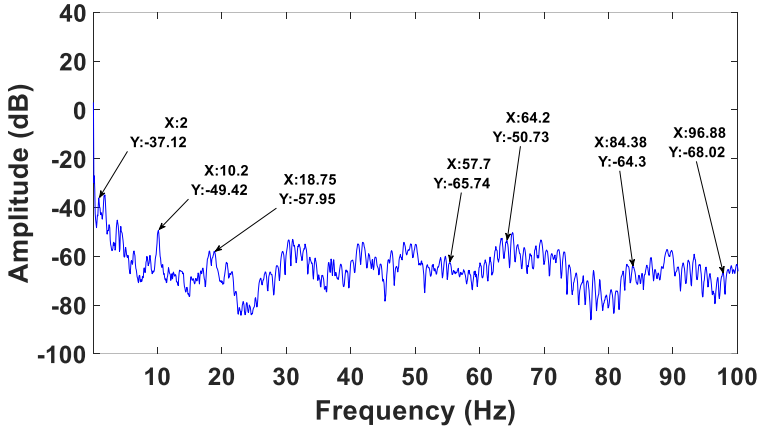

Figure 5.5 Tower spectral analysis at standstill showing the first 7th resonances.

Table 5.2 First modes and natural frequencies of the applied cantilever beam and tower

Mode	Beam Practical natural frequency	Tower Practical natural frequency
1	7.813	2
2	49.31	10.2
3	136.5	18.75
4	266.8	57.7
5	447.6	64.2
6	658.7	84.38
7	921.7	96.88
8	1221	
9	1537	
10	1965	

Evaluation of the beam and test rig components vibrations are based on strain and acceleration assessment. Additionally, the practical evaluation of the test rig period was selected as 40 seconds. All the raw measured signals were considered according to ISO 10816-21 group 2 (ISO10816, 2015).

5.4 Influence of rotating conditions of the cantilever beam on the vibrational modes through strain and acceleration measurements

The dynamic response of the system across a wide-range of rotating speeds was used to validate the small-scale horizontal axis wind turbine test rig. Once validated, acceleration and strain measurements were obtained for different faults conditions that were implemented into the system. Tower and drive shaft vibrations were analysed in an effort to detect the impact of beam fluctuations on the test rig system.

5.4.1 Dynamic axial strain analysis of the cantilever beam at different angular speeds

MATLAB, in conjunction with Mint Workbench (MWb), was used to control a series of tests that captured the vibrations of the flexible beam at several rotational speeds. Figure 5.6 illustrates beam vibration-induced axial strain at different rotating speeds. All axial strain signal amplitudes were found to fall between -50 μstrain to 50 μstrain, which indicates small displacement at the beam tip. In figure 5.6(d), it is noted that large vibration amplitude values start in the first 5 seconds until it reaches the desired speed. Moreover, figures 5.6(e), (f), and (g) show the decrease in the strain before reaching the target rotation distance in MWb software (40 sec). High strain values can be seen in figures 5.6(e), (f), and (g) before rotation stops, which reaches maximum values of 50 μstrain in figure 5.6(f) owing to stall-induced vibrations. The coupling of Coriolis (although it's small) and Centrifugal forces have been found to have a direct effect on increasing the axial strain through increasing the displacement, particularly at high rotational speeds. In the dynamic systems and especially with slender rotating beams, Coriolis effect has a direct impact in coupling longitudinal and transverse displacements. This effect causes axial and in-plane strain in the rotor beams, it varies simultaneously with the excitations forces and moments from another component in

the test rig namely rotor shaft and tower (Shum & Lin, 2010). The governing equations according to Lagrangian coordinates are ;

For axial displacement (Inman, 2017),

$$\frac{\partial^2 u}{\partial x^2} = \frac{\rho_0}{E}\left[\frac{\partial^2 u}{\partial t^2} - 2\Omega * \frac{\partial v}{\partial t} - (x+u) * \Omega^2\right] \quad \ldots (1)$$

For in-plane displacement (Bhuta & Jones, 1963),

$$\frac{\partial^2 v}{\partial x^2} = \frac{\rho_o}{EI_o}\left[\frac{\partial^2 v}{\partial t^2} + 2\Omega * \frac{\partial u}{\partial t} v\Omega^2\right] \quad \ldots (2)$$

The above equations for the cantilever rotating slender beams at a conditions ;

x = 0, u = 0, v = 0, and $\left[\frac{\partial v}{\partial x}\right]_{x=0}$

Where u and v are axial and in-plane displacements, x is the Lagrangian distance meausured from the clamp on the hub, t is the time, ρ_0 is the beam material density, and E is the Young's modulus.

Additionally, the centrifugal force arises with the rotating speeds, increases the beam stretching due to the increase in axial loading, which increase the wind resistance and decreases the required power of rotation (Ke, Ge, Wang, Cao, & Tamura, 2015).

At figure 5.6(g) can be seen reducing axial strain amplitude compared with the strain at 80 rpm and 90 rpm, it attributed to increasing root forces and moments at the clamps with speed increases despite increasing centrifugal and Coriolis forces, which caused axial stretching of the beams.

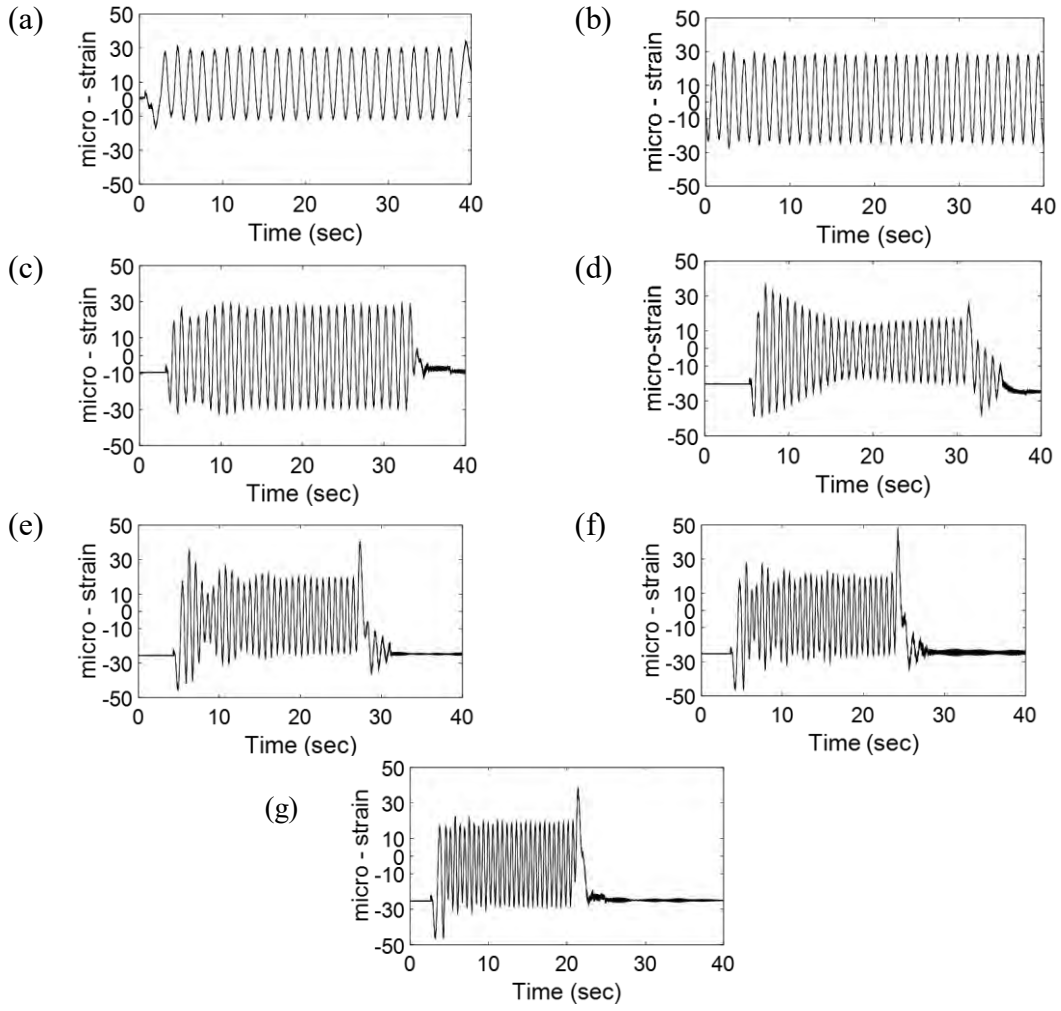

Figure 5.6 Axial strain amplitude of beam1 at a) 40 rpm, b) 50 rpm, c) 60 rpm, d) 70 rpm, e)80 rpm, f) 90 rpm, and g) 100 rpm.

Using associated MATLAB software, the subsequent analysis included the capability of analyzing the digital encoder signal to calculate the number of rotations, compute shaft speed and the vector of signal arrival times by zero crossing detector. The resulting signal averaging analysis indicated the average shaft behaviour during one rotation at the test rotor speed.

Average axial strain amplitude per one revolution is presented in figure 5.7, showing axial strain amplitude variation at the speed range from 40 rpm to 100 rpm. It shows increasing axial strain from 20.27 µstrain at 40 rpm to 20.59 µstrain at 60 rpm which is the maximum axial strain at this range due to increasing axial vibrations. After that, a decrease in the axial vibrations as the speed increases, at 70 rpm, 80 rpm, and 90 rpm

due to reduction in the beam axial displacement. At 100 rpm, the beam axial vibrations further increase due to increasing strain amplitude from 16.38 µstrain at 90 rpm to 18.12 µstrain at 100 rpm, which is nearest to the strain at 70 rpm, with phase shifting to the right.

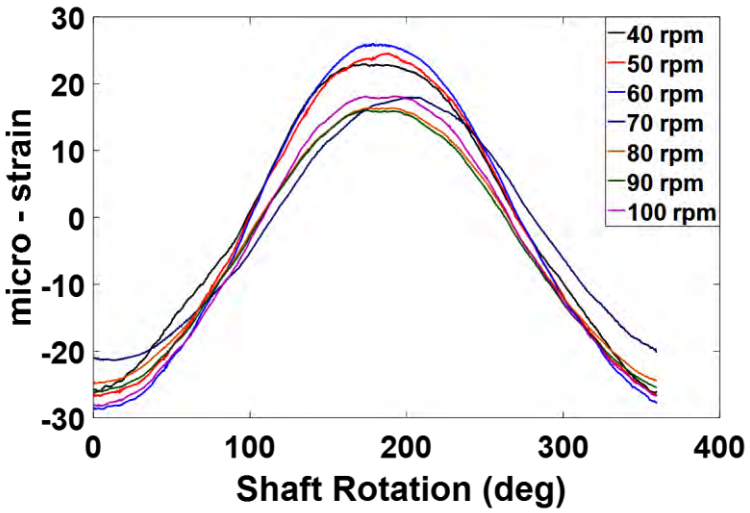

Figure 5.7 Average axial beam strain over exactly one revolution at the speed range from 40 rpm to 100 rpm.

Figure 5.8 illustrates three dynamic raw axial strain measurements of the rotating cantilever beam induced by dynamic displacement at three different rotating speeds. Small changes in the strain in this mode due to the small displacement in the axial direction are easily observed.

This behavior, namely the decreasing in the dynamic axial displacement with an increase in speed is further attributed to the increase in beam dynamic stiffness in the direction of rotation (Murtagh et al., 2005). Additionally, the coupling between in-plane and axial vibrations can be observed due to Coriolis forces and centrifugal effect which can further stiffen the beam centrifugally, through increasing axial and in-plane vibrations with speed increases (Banerjee & Kennedy, 2014). The stall-induced vibrations can further be noticed in this speed range as in figures 5.6e, 5.6f, and 5.6g, through the spikes near the end of the rotation. Maximum axial strain amplitude occurs at 150 rpm due to vibration increases with speed increases.

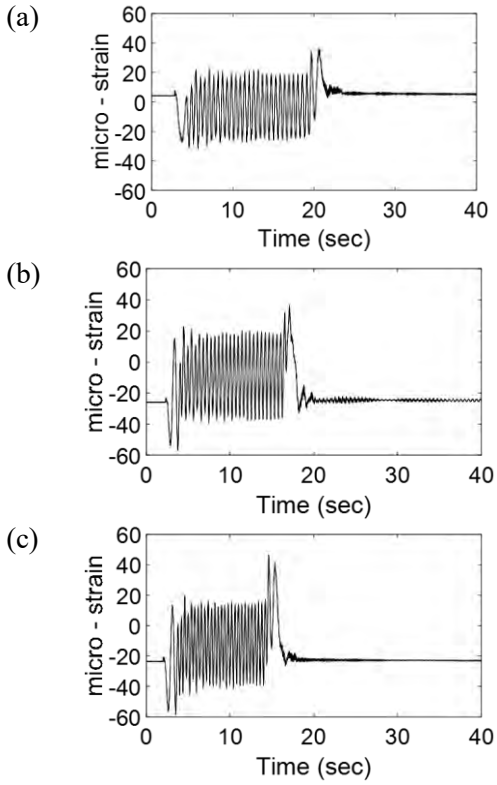

Figure 5.8 Axial strain measurements induced by dynamic vibration at a) 110 rpm, b) 130 rpm, c) 150 rpm.

Furthermore, figure 5.9 illustrates the behaviour of beam axial strain per one revolution at speeds 110 rpm,130 rpm and 150 rpm respectively. Shifting can be observed in the axial strain at 130 rpm, while decreasing axial strain appears when the speed reaches 150 rpm, despite the increase in the centrifugal forces.

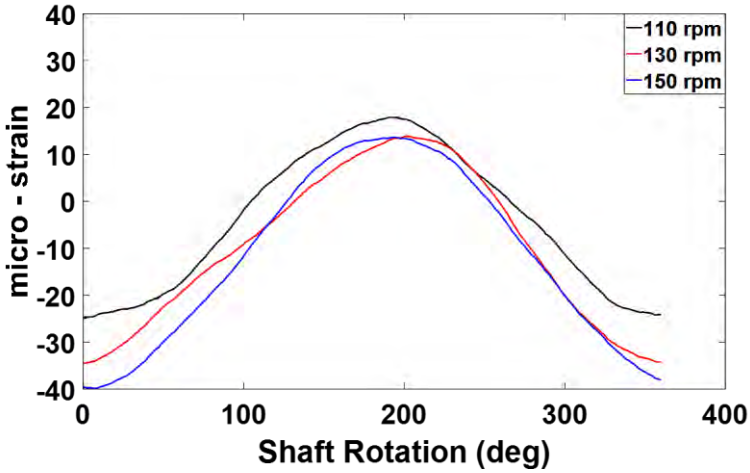

Figure 5.9 Average axial beam strain over one revolution at 110 rpm, 130 rpm, and 150 rpm.

Figure 5.10a shows peaks of the average beam axial strain over one revolution for the full speed range from 40 rpm to 150 rpm. It can be seen that maximum average axial strain is 25.97µstrain that occurs at 60 rpm, after that it decreases with the speed increases until it reaches 13.64 µstrain at 150 rpm. Additionally, figure 5.10b illustrates maximum and minimum average axial strain, the two amplitudes make maximum divergence at 60 rpm with the difference of 54.56 µstrain, while maximum convergence occurs at 70 rpm with the difference 38.07 µstrain.

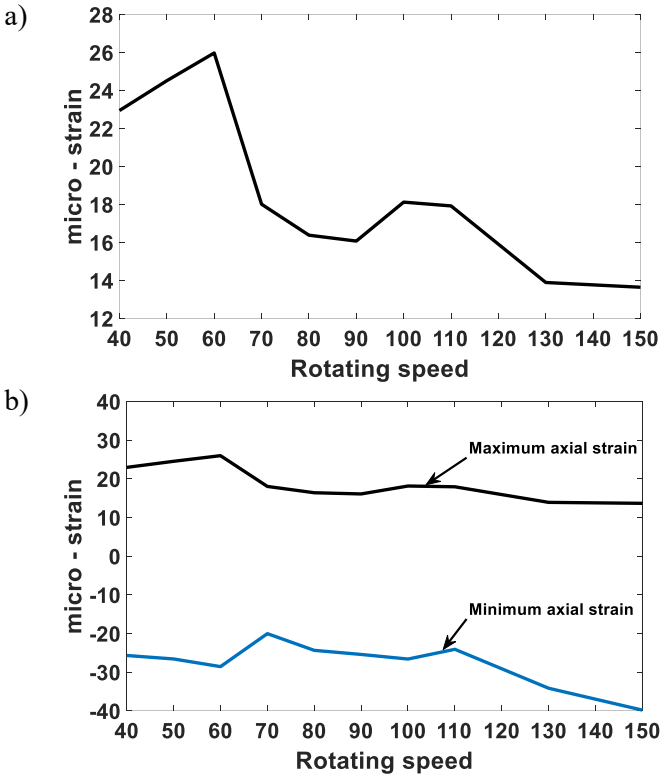

Figure 5. 10 a) peaks of average axial beam strain over exactly one revolution at the speed range from 40 rpm to 150 rpm, b) maximum and minimum average axial beam strain over exactly one revolution at the speed range from 40 rpm to 150 rpm.

5.4.2 Dynamic In-plane strain analysis of the cantilever beam at different angular speeds

Figure 5.11 shows that in-plane strain amplitudes increased due to high dynamic displacement, which resulted from maximum bending vibration. Angular speeds have a positive correlation on vibration amplitudes in the in-plane direction, (maximum of

250.3 μstrain occurs at 90 rpm). At 90 rpm, a high tower fluctuation towards Z-direction occurred, which has a positive effect on increasing beam in-plane vibrations. Additionally, the in-plane strain amplitude at 70 rpm seems to be similar to the axial strain at the same speed, starting with high strain then reducing with slight increase before the end of the rotation.

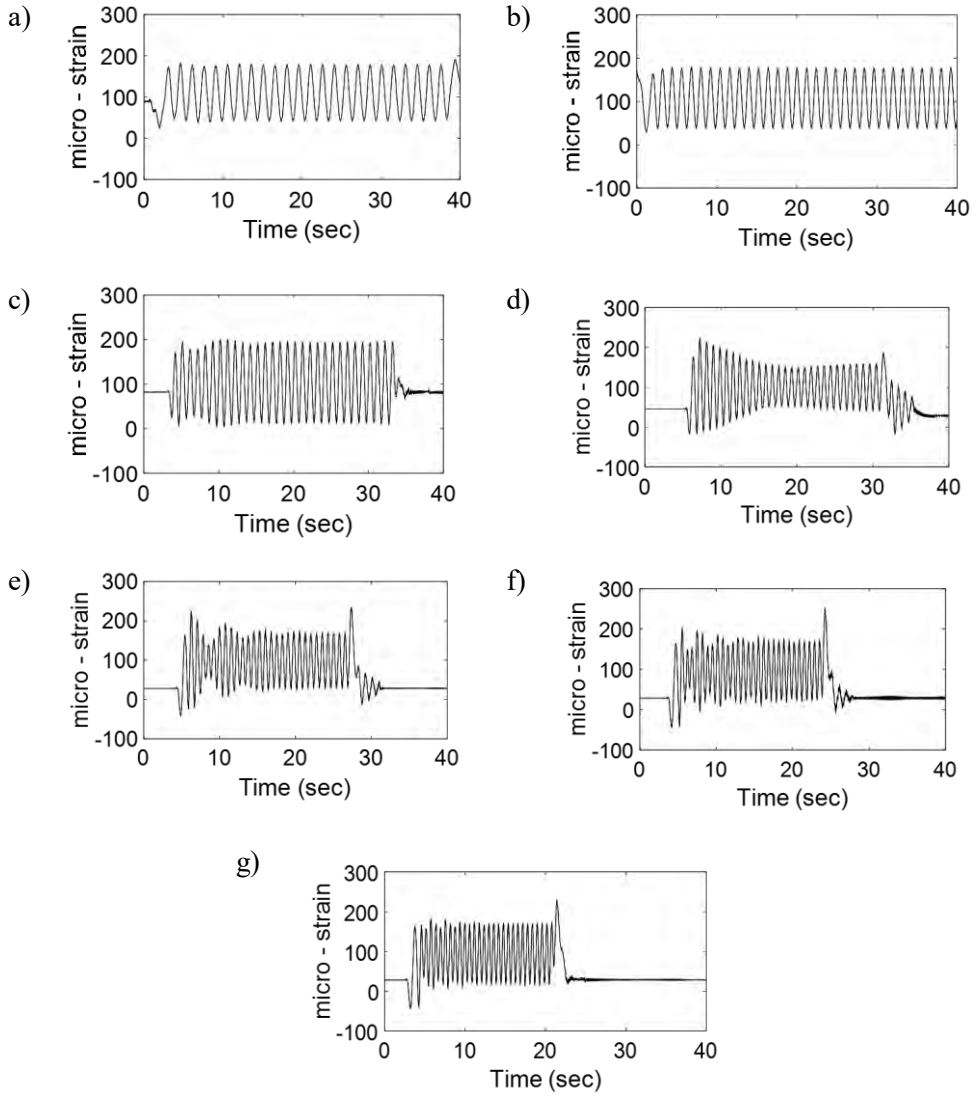

Figure 5.11 In-plane strain measurements of beam 1 at a) 40 rpm, b) 50 rpm, c) 60 rpm, d) 70 rpm, e)80 rpm, f) 90 rpm, and g) 100 rpm.

Additionally, figure 5.12 illustrates the average dynamic strain towards the in-plane direction per revolution for the range of 40 rpm to 100 rpm. The increase in the test rig rotational speed from 40 rpm to 60 rpm leads to an increase in in-plane bending displacements. Additionally, the further increase in the angular speed leads to strain decrease at 70 rpm down to 90 rpm, due to the decrease in the dynamic in-plane bending resulted from the increase in beam stiffness. Increasing speed to 100 rpm leads to increase in the beam strain to 169.3 µstrain but still below the maximum strain in this speed range, which occurs at 60 rpm, 191.8 µstrain. Further, tower torsional vibrations increase when the speed increases, which excited high beam strain towards in-plane directions.

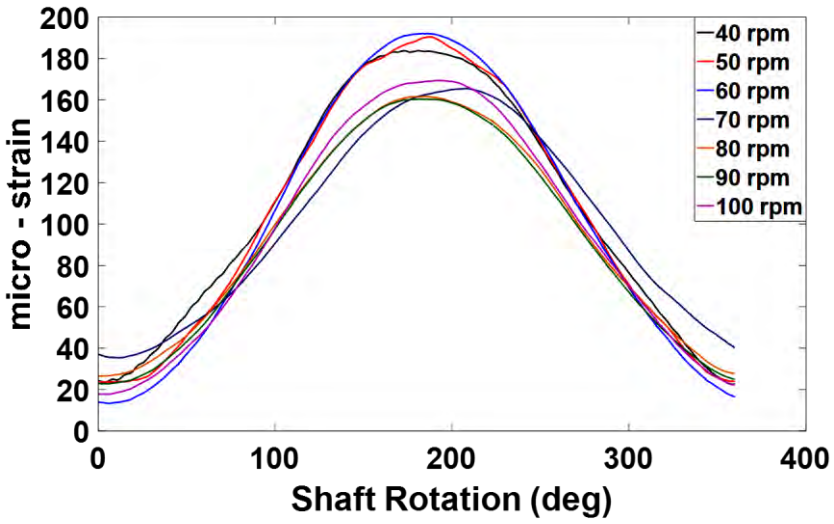

Figure 5.12 Average in-plane strain amplitude of beam 1 per one revolution at different rotational speeds.

As the speed increases, in-plane beam vibration further increases as can be seen in strain amplitude in figure 5.13, which illustrates in-plane strain amplitude at speeds of 100 rpm, 130 rpm, and 150 rpm respectively. It can be seen that there was a small difference between the maximum and minimum in-plane strain amplitude at 110 rpm, with high differences at both 130 rpm and 150 rpm. This was attributed to high dynamic bending when the speed increases and the bending value increases with the increase of beam length, despite the increase of beam stiffness when the speed increases. Additionally, tower fluctuation in the Z-direction and torsional vibrations affected the strain mode, where the spikes in figures 5.13a, 5.13b, and 5.13c were

observed to be due to the continuing vibration after the rotation stopped due to the rotor stall affecting the tower torsional vibrations.

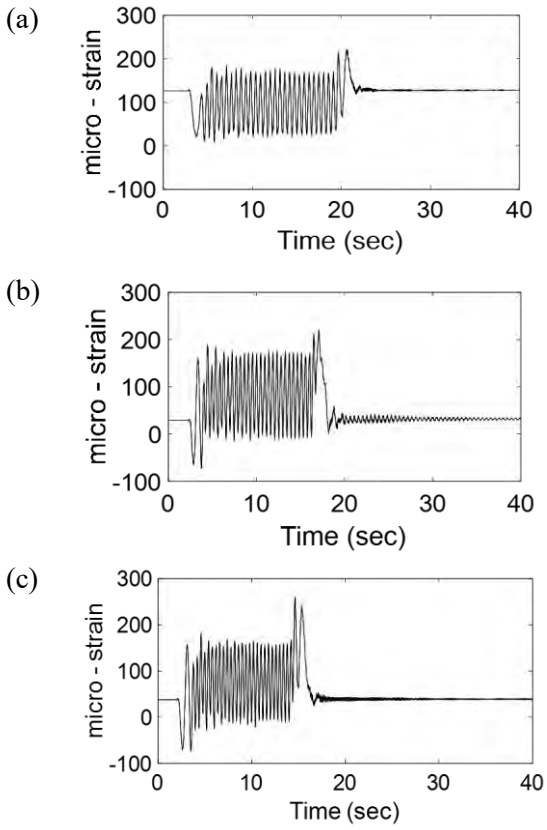

Figure 5.13 In-plane strain measurements of beam1 induced by dynamic vibration at a) 110 rpm, b) 130, and c) 150 rpm.

Additionally, figure 5.14 shows the behaviour of beam in-plane strain per one revolution at 110 rpm, 130 rpm, and 150 rpm respectively. Maximum in-plane strain amplitude occurs at 110 rpm due to the increase in bending vibration corresponding to increase in the rotor speed. After that, in-plane strain amplitude decreases gradually when the speed increases due to the increase in beam stiffness. Further, shifting of in-plane strain at 130 rpm can be noted with increasing rotor speed giving a slight increase of in-plane strain amplitude from 165.2 μstrain at 130 rpm to 166.4 μstrain at 150 rpm.

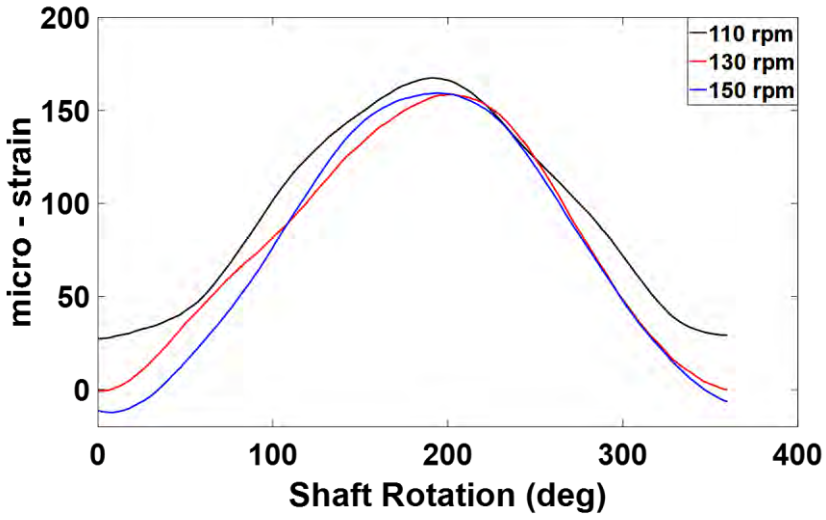

Figure 5. 14 In-plane strain measurements of the rotating beam per revolution at 110 rpm, 130 rpm, and 150 rpm..

Figure 5.15 represents a synopsis of figures 5.12 and 5.14 by showing the average maximum and minimum in-plane strain amplitudes over one revolution. The maximum divergence between the maximum and minimum in-plane strain (21.43 µstrain), occurs at speed 150 rpm. However, the minimum convergence (11.70 µstrain) occurs at 110 rpm.

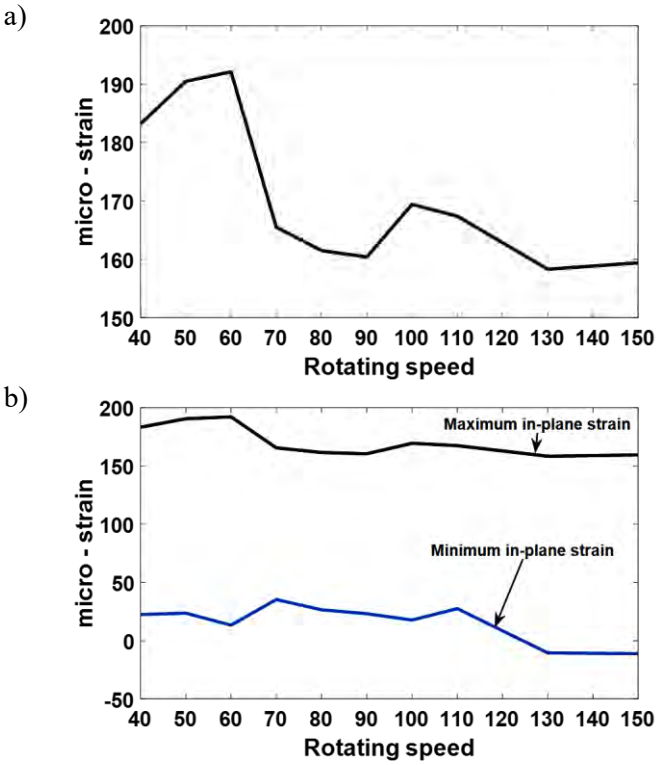

Figure 5.15 a) peaks of average in-plane beam strain over exactly one revolution at the speed range from 40 rpm to 150 rpm, b) maximum and minimum average axial beam strain over exactly one revolution at the speed range from 40 rpm to 150 rpm

5.4.3 Dynamic out-of-plane strain analysis of the cantilever beam at different angular speeds

Continuing the monitoring of the beam dynamic behaviour at different rotating speeds, figure 5.16 provides the dynamic out-of-plane strain for the speed range from 40 rpm to 100 rpm rotating speeds. It can be seen that bending vibration was relatively high at 60 rpm and 70 rpm due to beam flexibility and strain values tend to take the stochastic path. While at higher speeds the strain amplitude started to become uniform after the test rig reached the required speed (after 5 seconds). Furthermore, rotor inertia forces increasing during the rotation lead to increased dynamic vibration in different directions. For this reason, the beam motion generated out-of-plane bending displacement, which was shown by the strain amplitude in this direction. Additionally, the increase in the dynamic bending displacement leads to an increase in the vibration amplitude in the test rig system, which is due to the collective vibration effect of the test rig components, namely the tower, hub, and rotor shaft.

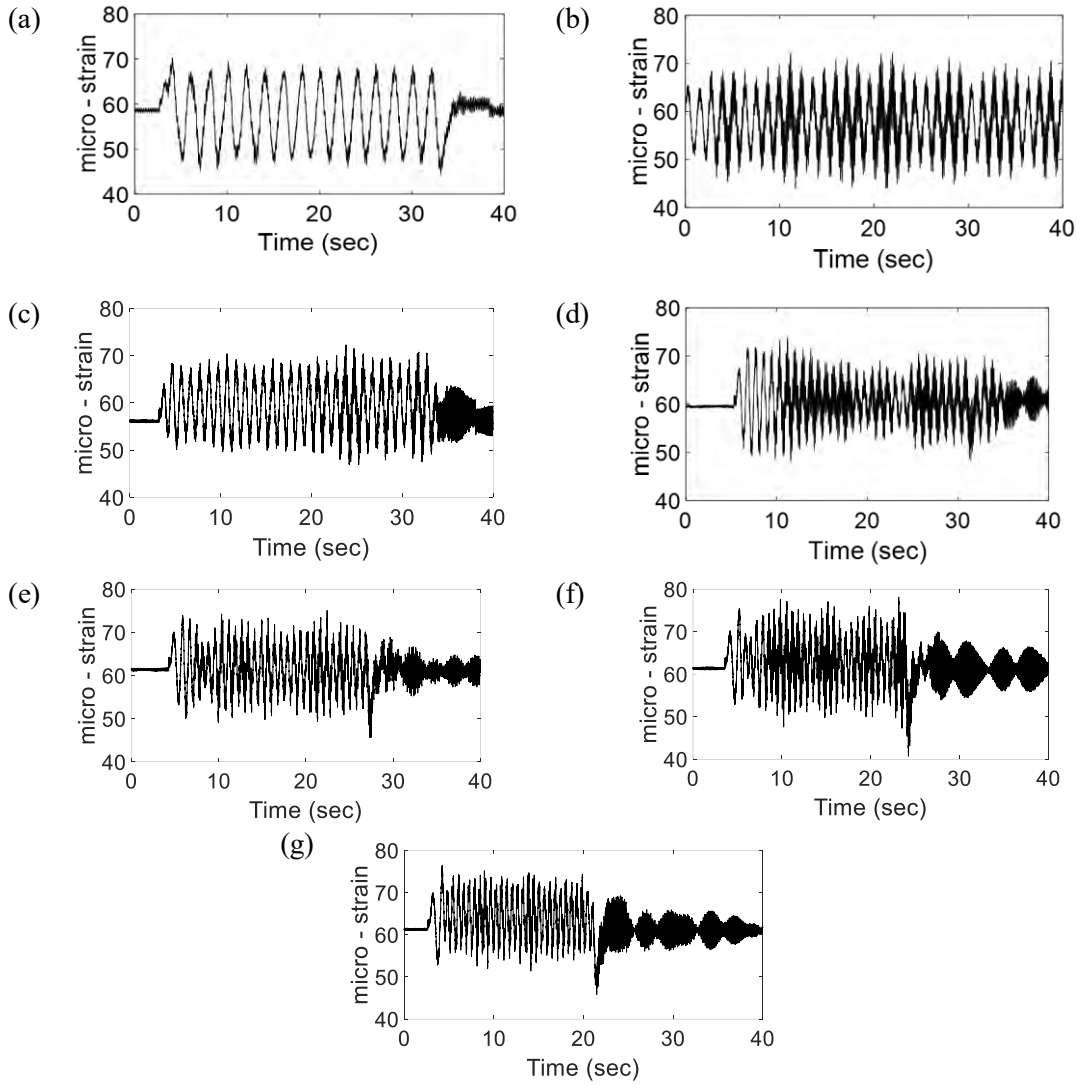

Figure 5.16 Out-of-plane strain amplitude of blade 1 at a) 40 rpm, b) 50 rpm, c) 60 rpm, d) 70 rpm, e) 80 rpm, f) 90 rpm, g) 100 rpm.

Furthermore, the out-of-plane strain amplitudes increased slightly due to the increase in the rotational speed. The interaction of the rotating beam with the hub and tower has an effect on increasing in-plane and out-of-plane beam vibrations. The tower fluctuation has a direct effect on increasing beam vibrations, particularly the out-of-plane vibrations. This vibrational mode can cause additional load on the servo motor, as well as fluctuation in the rotor shaft.

Figure 5.17 shows beam out-of-plane strain per one revolution for the speed range from 40 rpm to 100 rpm due to out-of-plane bending vibrations during the rotation. Minimum strain values can be identified at 40 rpm, the strain values increased gradually when the speed increases to 100 rpm which has the maximum out-of-plane

strain. In this mode can be identified the effect of tower vibration on the beam out-of-plane vibrations, where tower vibration in the y-direction during the rotation has a direct impact on increasing beam out-of-plane vibrations.

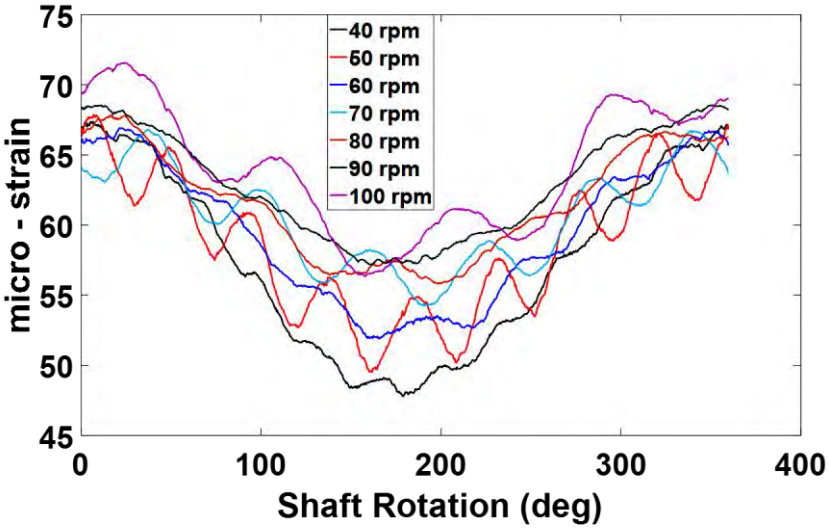

Figure 5. 17 Out-of-plane strain amplitude measurements of the rotating blade per one revolution for the range from 40 rpm to 100 rpm.

The collective effects of the vibration that is mentioned above can be noted in figure 5.18a.5.18b and 5.18c, where all the three beams and tower remain vibrating after the servo motor stops. This behaviour can be seen solely in out-of-plane direction due to restricted motion (servo motor stopped).

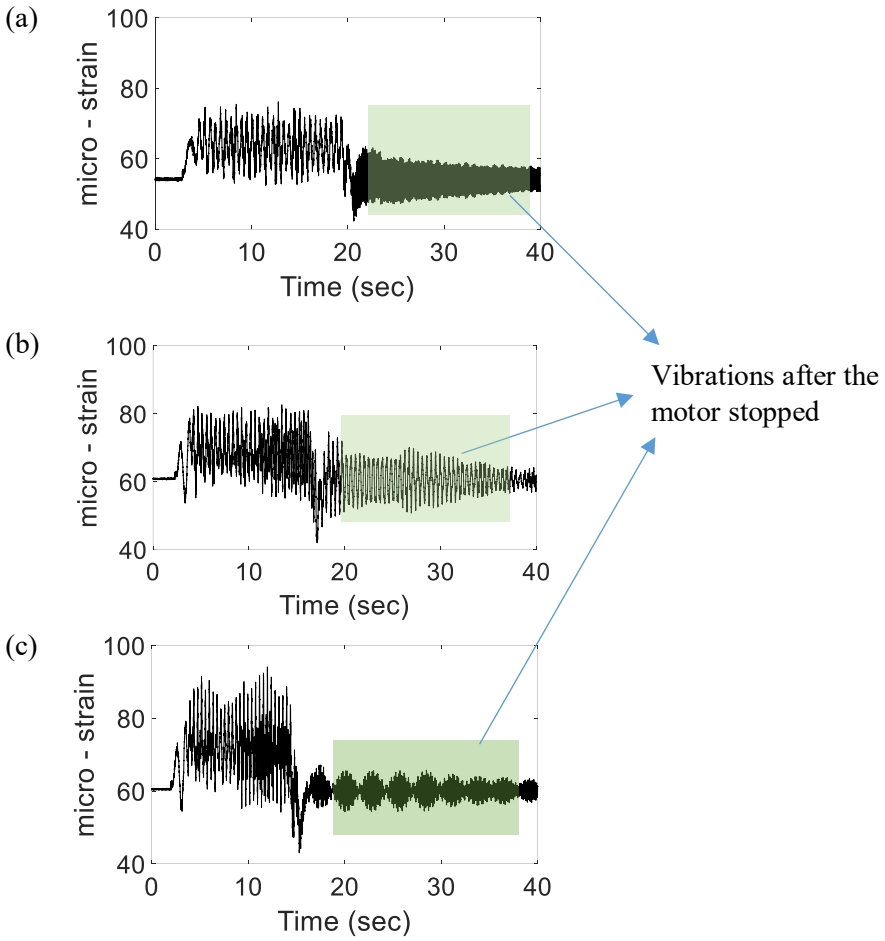

Figure 5.18 Out-of-plane strain amplitude of the rotating blade at a)100 rpm, b) 130 rpm, and c) 150rpm.

Tower effect can be markedly noticed in out-of-plane mode, where the raw and per one revolution strain measurements showed tower vibrations affected the increasing beam vibrations, as well, even after the rotor has stop spinning. The green zones in figure 5.18 show tower effects on beam strain, which indicates that the beam still vibrates after the servo motor stopped. Figure 5.19 shows the final part (from 22.5 sec to 40 sec) of the raw strain signal at 130 rpm, to explain the tower effect through utilizing FFT in MATLAB, specifically by using the Spectra 3 subroutine to analyse the acquired data from the raw strain measurements. Shifting has been adopted to simplify the analysis as shown in figure 5.19b.

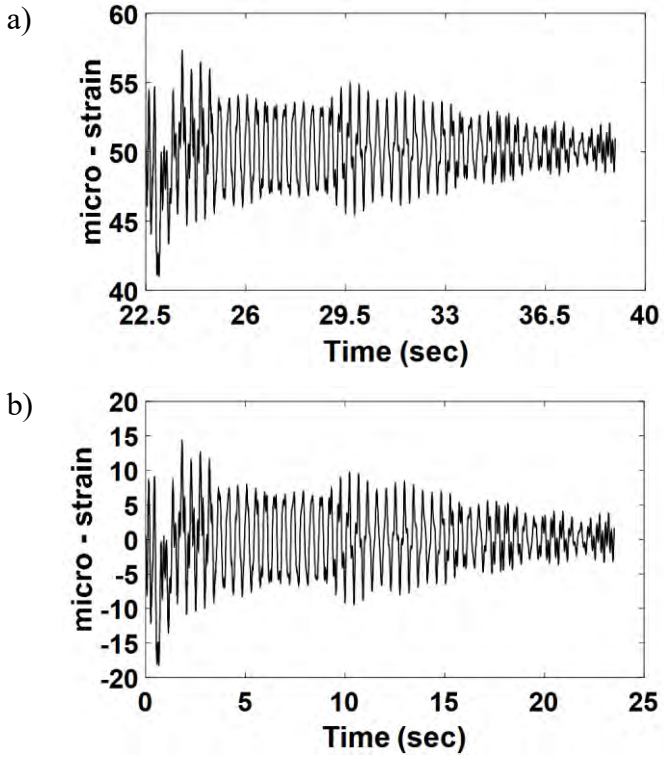

Figure 5. 19 a) real strain-time domain, b) shifting strain-time domain, at 130 rpm and 40 sec.

Spectrum analysis has been conducted for this range to show coupling of beam and tower frequencies at this domain. Figure 5.20 shows beam and tower frequencies at a specific time from the rotation, to explain coupling effect of tower and rotor beam in the out-of-plane mode. Additionally, this mutual effect has a direct impact on the tower frequency, particularly in the Y and Z directions. The observer can recognize the coupling effect by the significant fluctuation of the tower during the experiments.

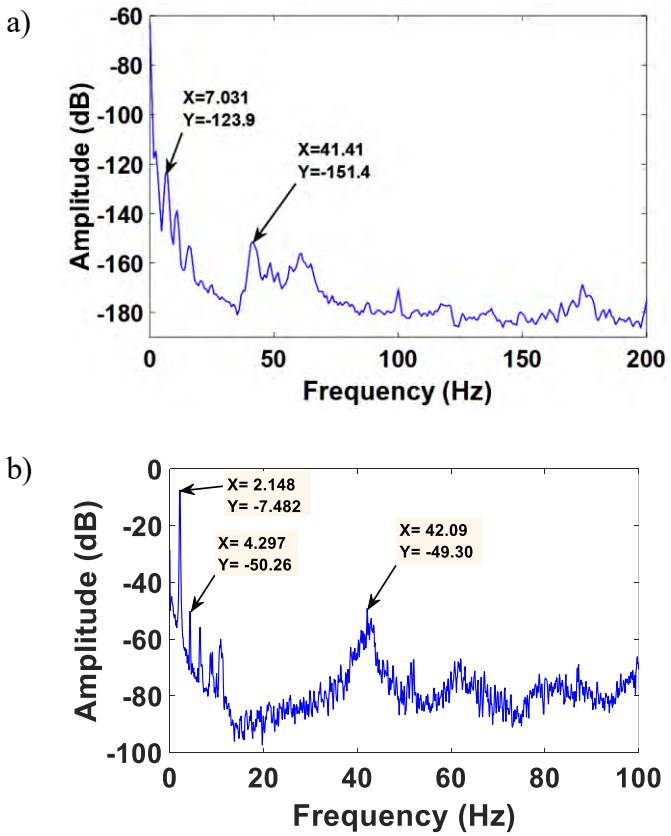

Figure 5.20 Spectrum analysis of specific time of raw out-of-plane strain signal using a) blade strain signal and b) tower acceleration signal.

To demonstrate beam out-of-plane vibration at each rotation step, strain amplitude per one revolution plot of the three high speeds can identify the dynamic bending towards out-of-plane direction during the rotor shaft positions.

In figure 5.21 shows the change in the out-of-plane beam strain per one revolution at 110 rpm, 130 rpm, and 150 rpm respectively. It is clear that the highest strain occurs at 150 rpm, which is the highest speed in the experiment. The strain amplitude reduces on the shaft rotational position 180.2° at 150 rpm and for 196.3° at 110 rpm, while it is higher at 130 rpm at this point. Additionally, beam bending behaviour towards out-of-plane at 130 rpm and 150 rpm were nearly the same despite high bending at 150 rpm. Shifting in the amplitude can be noticed at 130 rpm due to increase in the out-of-plane bending, however, different behaviour can be observed with 110 rpm.

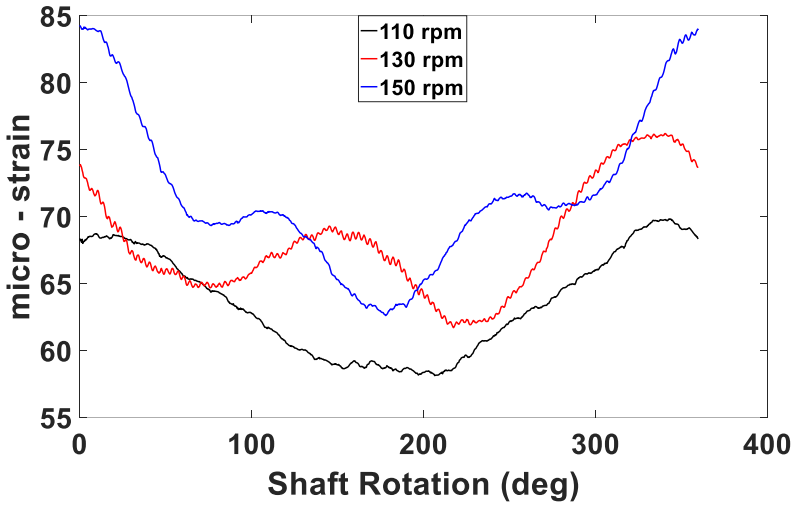

Figure 5. 21 Out-of-plane strain amplitude of the rotating beam per revolution at 110 rpm, 130 rpm, and 150 rpm.

Figure 5.22 represents a synopsis of figures 5.17 and 5.21 by introducing average maximum and minimum in-plane strain amplitudes over one revolution. The maximum divergence between the maximum and minimum in-plane strain (21.43 μstrain), occurs at the speed of 150 rpm. However, the minimum convergence (11.70 μstrain) occurs at 110 rpm.

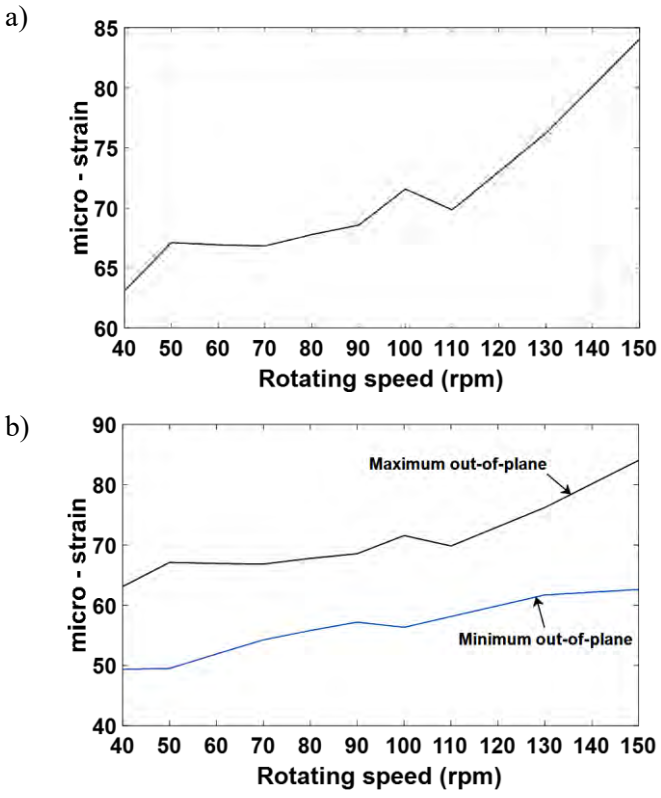

Figure 5. 22 a) peaks of average out-of-plane beam strain over exactly one revolution at the speed range from 40 rpm to 150 rpm, b) maximum and minimum average axial beam strain over exactly one revolution at the speed range from 40 rpm to 150 rpm

Strain analysis demonstrates beam behaviour towards the three vibrational modes namely; axial, in-plane, and out-of-plane directions at different rotational speeds. The next part addresses different technique for monitoring beam vibrations utilizing the piezoelectric accelerometer on the beam tip. This instrument enables the measurement of the beam acceleration based on in-plane vibration at different rotor speeds.

5.4.4 Dynamic acceleration analysis of the cantilever beam at different angular speeds

Two types of acceleration sensors (rotating and non-rotating depending on the component's function) have been used on the test rig and will be presented as part of another vibration monitoring method. Piezoelectric accelerometers, which are small and lightweight, are able to detect a component's acceleration across a wide frequency range. The acceleration amplitude reported by the piezoelectric accelerometer results from applied forces across the piezoelectric material due to bending displacement during the operation, which results in a voltage that is then correlated to an acceleration value. Figure 5.23 shows acceleration amplitude of the rotating beam at different rotating speeds from 40 rpm to 150 rpm. The figure shows the non-uniform bending displacement, particularly within the first 10 sec. Subsequently, the amplitude tends to spike due to tower fluctuation, as in figure 5.23b, which is due to high tower vibration effect in the Z-direction. Additionally, in figure 5.23d at 70 rpm, different behaviour was observed where the beam bending displacement reduces in middle of the time interval of the experiment, which occurs namely at the required speed.

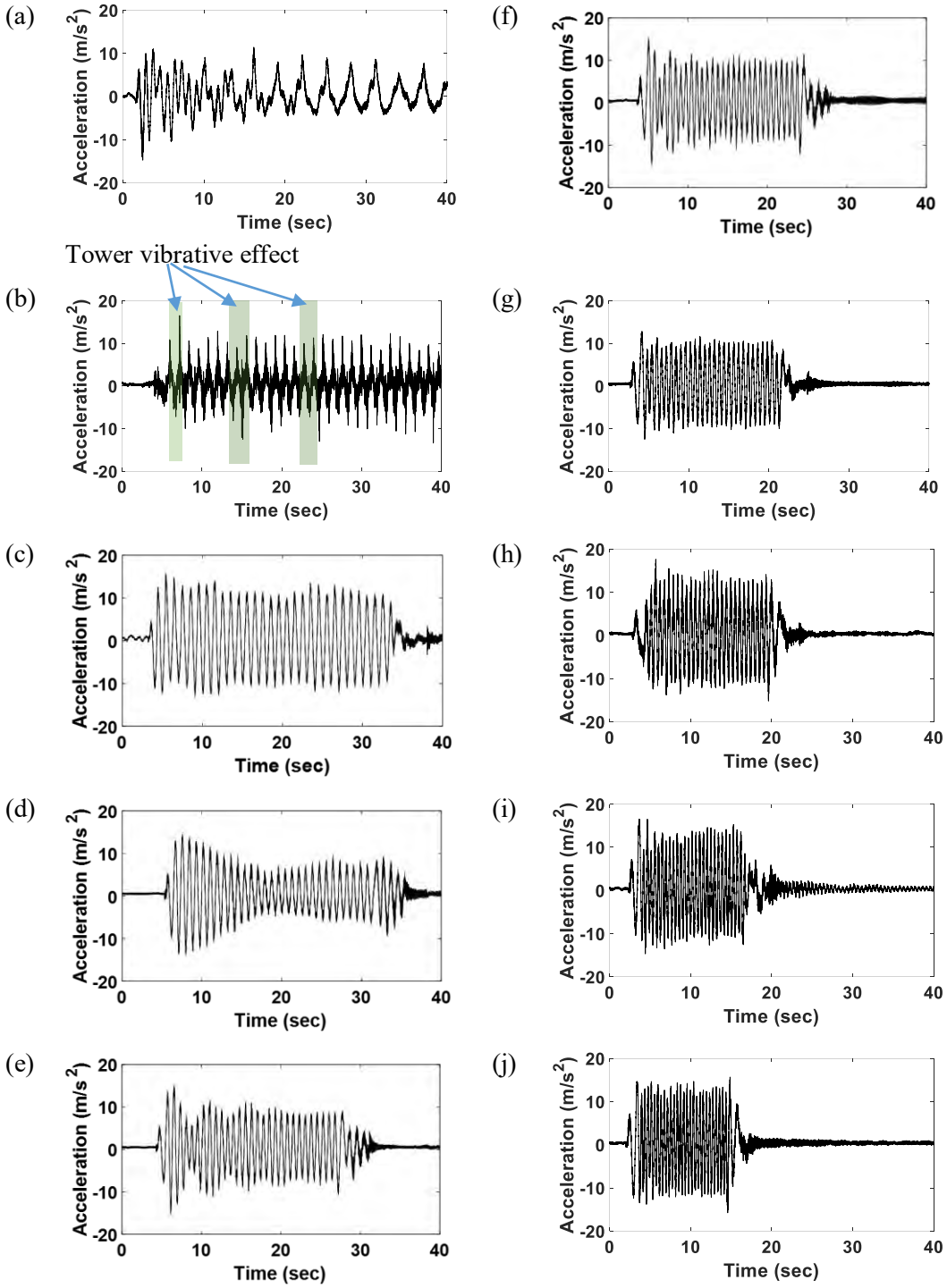

Figure 5. 23 Piezoelectric acceleration amplitude during beam1 rotation at a) 40 rpm, b) 50 rpm, c) 60 rpm, d) 70 rpm, e) 80 rpm, f) 90 rpm, g) 100 rpm, h) 110, i) 130 rpm, and j) 150 rpm.

Utilizing shaft phase signal averaging analysis with MATLAB to identify beam acceleration during one revolution as shown in figure 5.24, shows acceleration changing with the rotational speeds. The effect of the tower vibration can be observed in figures 5.24a, 5.24b, and small effects at speeds 110 rpm, 130rpm, and 150 rpm at figures 5.24h, 5.24i, and 5.24j.

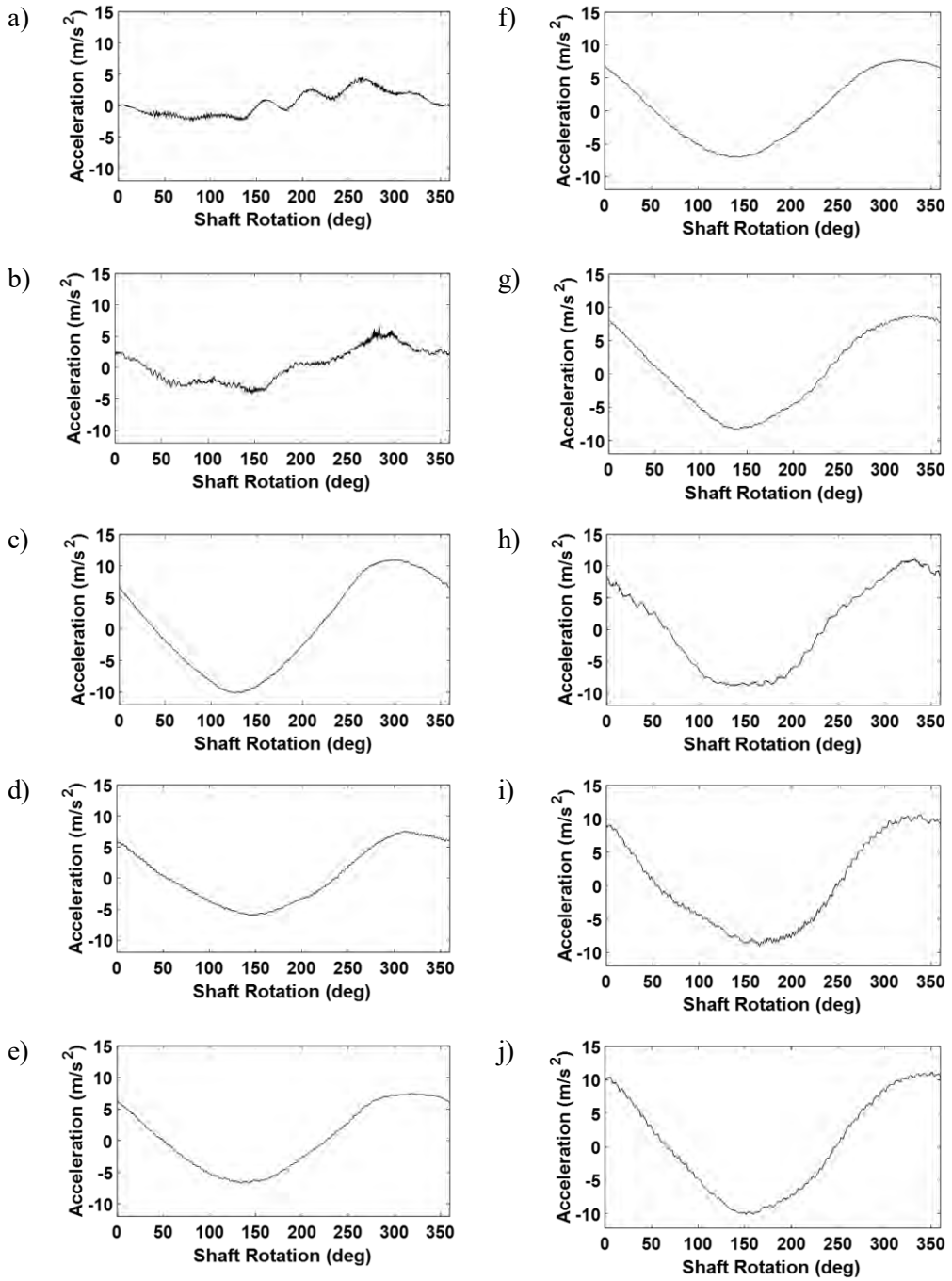

Figure 5. 24 Beam acceleration per one revolution measured by piezoelectric accelerometer for the speed range from 40 rpm to 150 rpm.

Maximum acceleration amplitude 11.28 m/s^2 occurs at 110 rpm, while minimum acceleration -2.572 m/s^2 occurs at 40 rpm, as can be seen in figure 5.25. Additionally, maximum divergence 21.22 m/s^2 happened at 150 rpm, following 21.13 m/s^2 at 60 rpm.

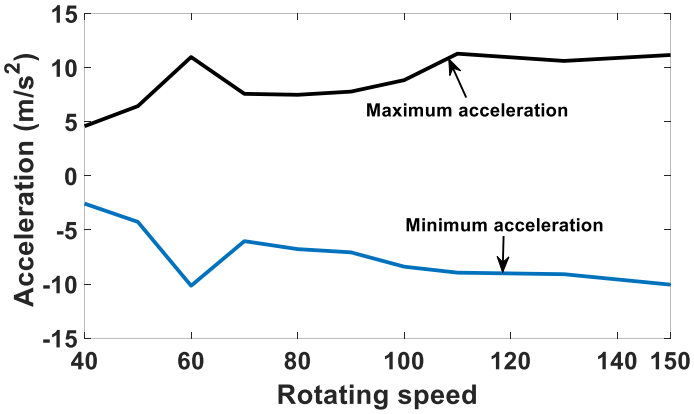

Figure 5. 25 Maximum and minimum beam acceleration amplitude per one revolution measured at beam tip by the piezoelectric accelerometer

After this period, a small increase in the acceleration amplitude, which is due to a small bending displacement, occurs until the rotation stops. This corresponding behaviour can further be seen with an in-plane strain at the same speed, where it is shown that the reduction in beam acceleration amplitude and in-plane strain are due to the beam vibrating in the out-of-plane direction simultaneously with the tower vibrating in the Y-direction. Therefore, monitoring beam vibration during each speed can help identify time-variable beam behaviour during each rotational speed.

5.5 Monitoring of tower vibrations during different rotating speeds.

Rotary inertia forces which produce vibration in the tower in different directions are detected by the triaxial accelerometers positioned in the upper part of the tower. Figure 5.26 shows tower vibrations based on the acceleration sensor in the X, Y, and Z direction for speeds ranging from 40 rpm - 60 rpm. At 40 rpm and despite the low speed, it can be seen that there is an increase in the acceleration in the X-direction and Z-direction coupling with the increase of in-plane vibration. This case also correlates with the speed of 50 rpm, where increasing tower vibrations towards the X and Z

directions is synchronized with increasing speed. However, a decrease in tower vibration in the X-direction and increasing the average acceleration towards the Z-direction occurred due to vibration increases when the speed reached 60 rpm. The spike in acceleration amplitude in figure 5.27b which occurred at 33.5 sec, was due to the coupling of beam in-plane and out-of-plane vibrations when the servo motor decelerated. This effect can also be noted in figures 5.27a, and 5.27c at the same time at the speed of 70 rpm. As the speed increases, there is a salient increase in tower lateral vibration in the Z-direction increases as shown in figure 5.27i. The coupling effect can further be observed in figures 5.28a and 5.28c, at 20.31 sec and 29.86 sec towards X and Z directions respectively. When the rotating speed reaches 110 rpm, the average acceleration amplitude increases prominently in the X and Z directions as shown in figures 5.28d and 5.28f. Additionally, the coupling effect with beam vibration can be observed in all directions at 25.53 sec in figures 5.28d, 5.28e, and 5.28f. At 130 rpm, tower vibration towards Z-direction increases, counter to X and Y directions which experience decreasing vibration, due to rotary inertia speed increases, as shown in figures 5.28a, 5.28b, and 5.28c. The maximum average tower acceleration occurs at 13.89 sec which shows high fluctuations of the tower in the Z-direction coupling with the rotation plane. The reduction in tower average vibrations at those two directions increases at 150 rpm, where the maximum average acceleration amplitude at this speed occurs at around 5.18 sec in Z-direction, however, the coupling effect of in-plane and out-of-plane beam vibrations can further be identified at 5.52 sec, 8.34 sec, and 14.31 sec; see figure 5.29d. The increase of tower lateral vibrations increased the occurrence and growth of several cracks in the tower foundation where it joins with the base, which subsequently resulted in system failure.

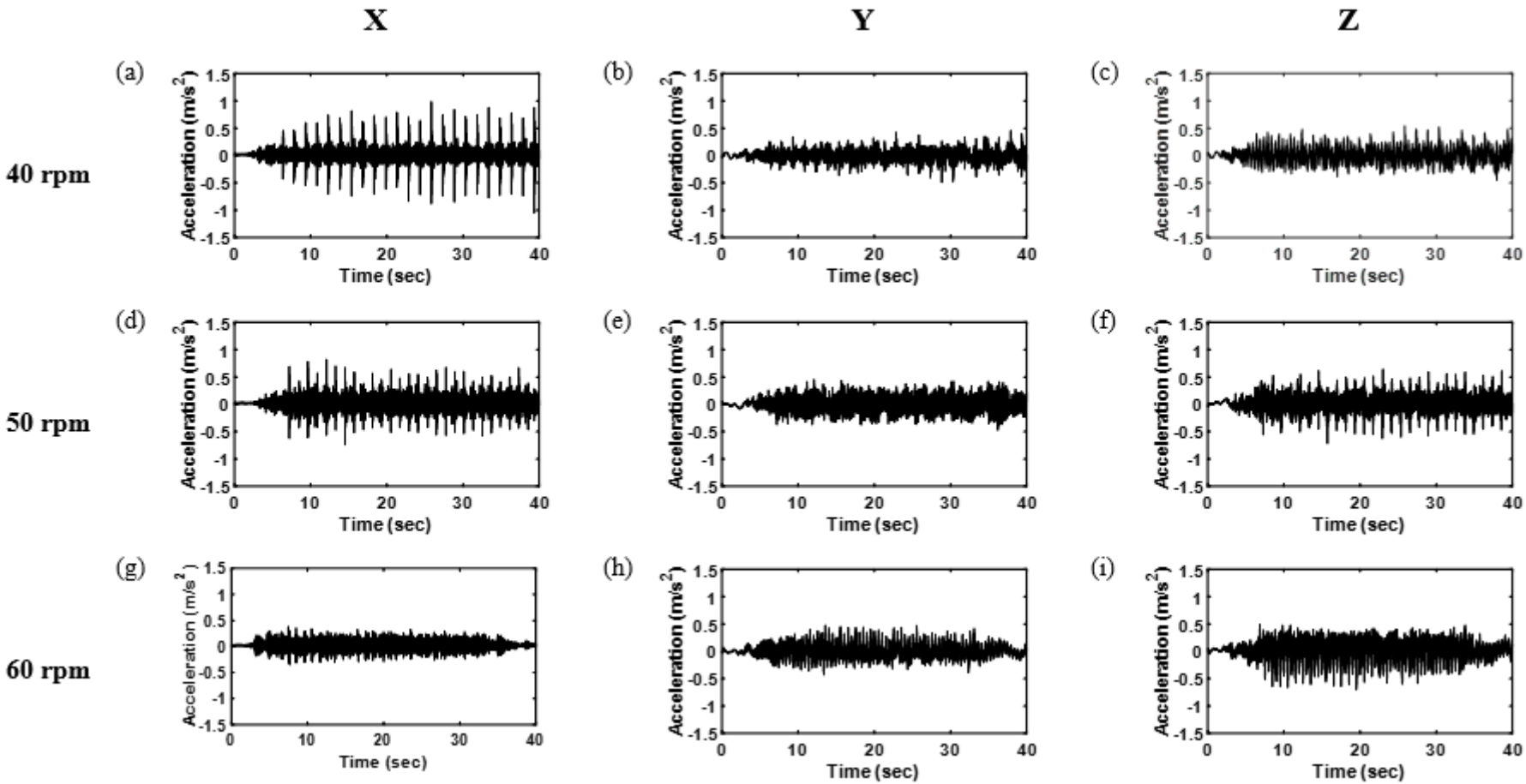

Figure 5. 26 Tower acceleration amplitude at X, Y, and Z direction measured by triaxial acceleration sensor at 40 rpm, 50 rpm, and 60 rpm.

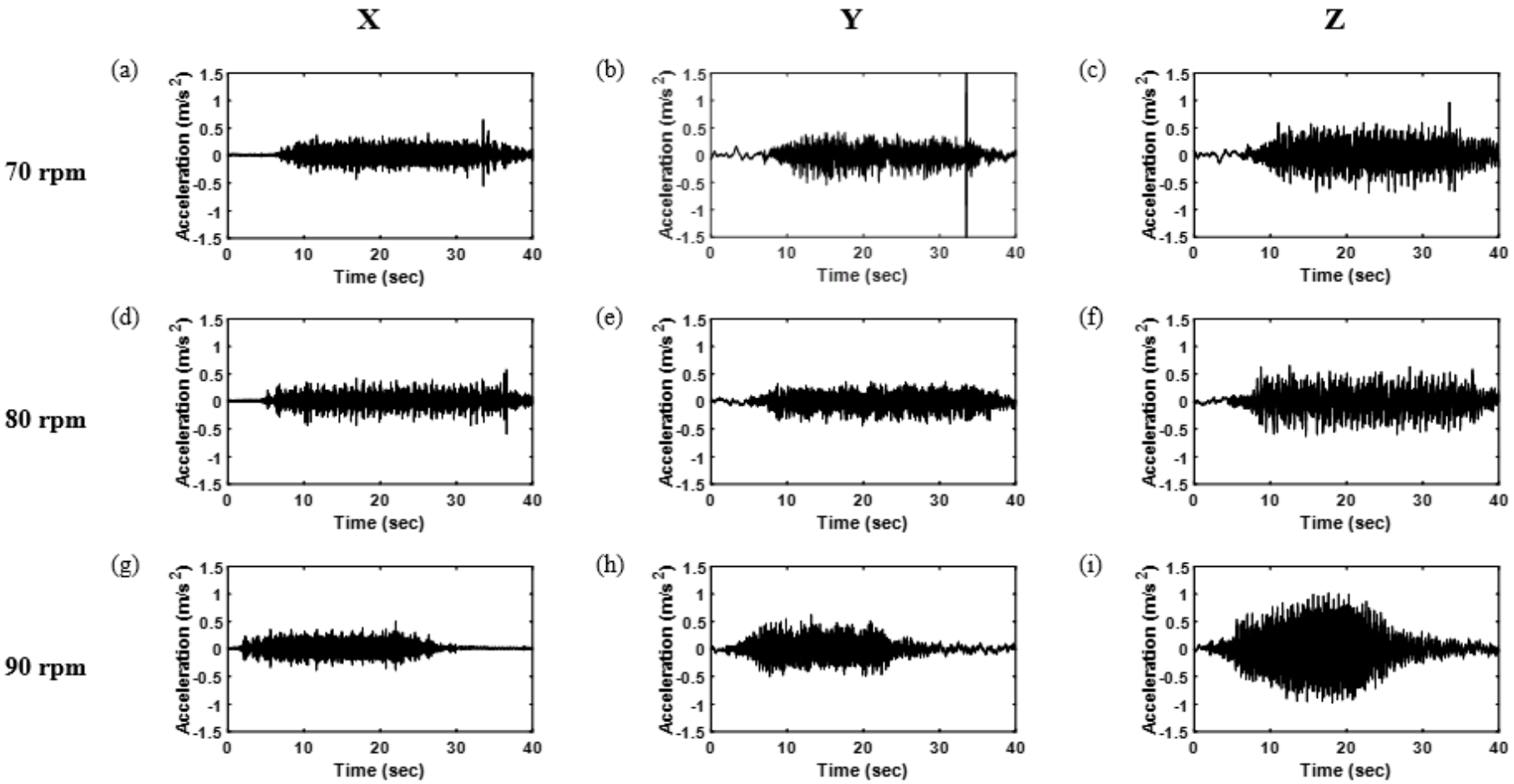

Figure 5. 27 Tower acceleration amplitude at X, Y, and Z direction measured by triaxial acceleration sensor at 70 rpm, 80 rpm, and 90 rpm.

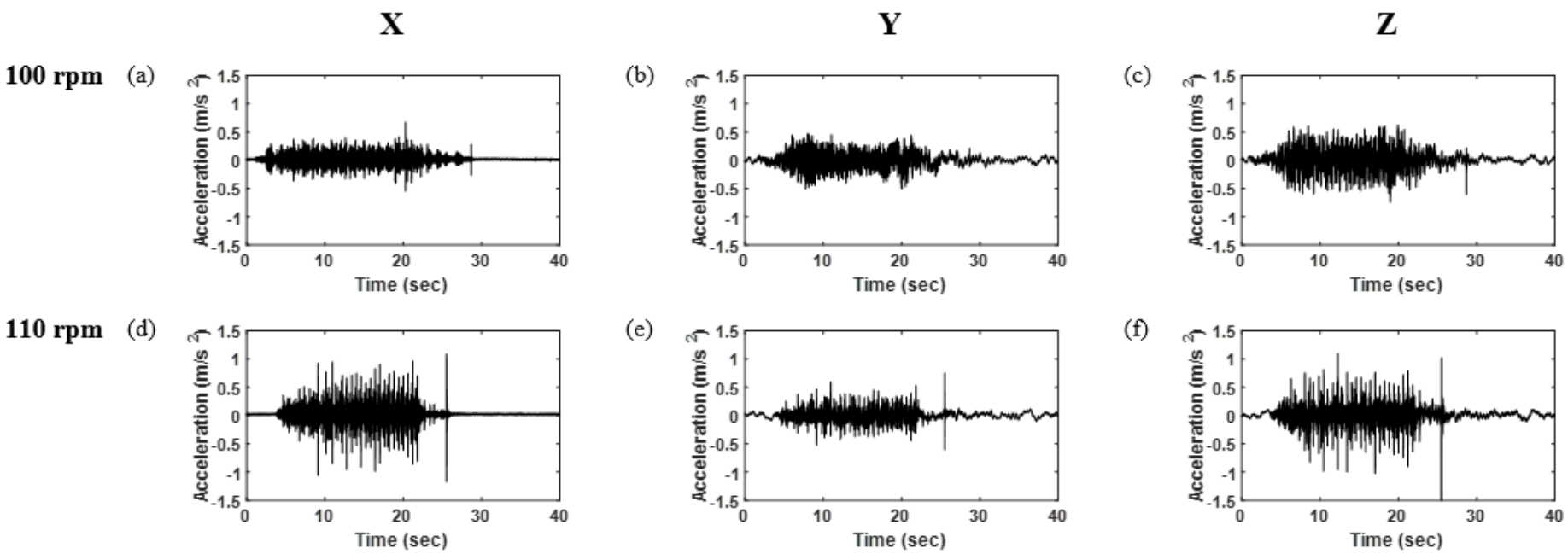

Figure 5. 28 Tower acceleration amplitude at X, Y, and Z direction measured by triaxial acceleration sensor at 100 rpm, and 110 rpm.

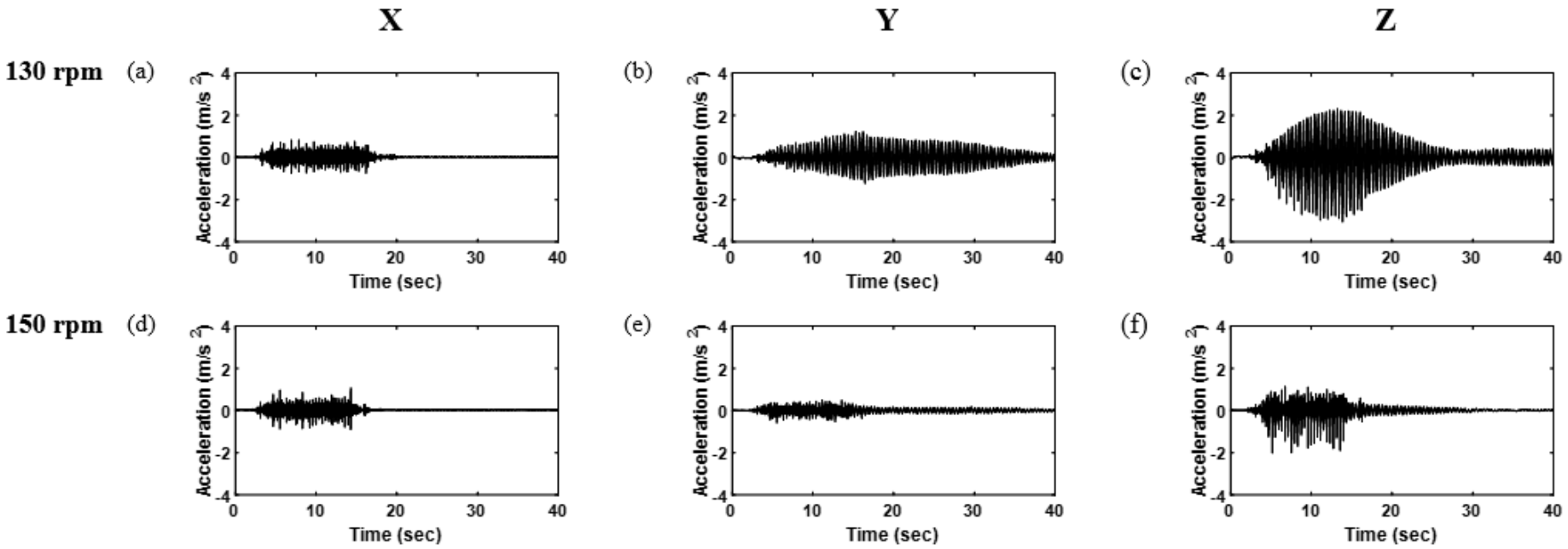

Figure 5. 29 Tower acceleration amplitude at X, Y, and Z direction measured by triaxial acceleration sensor at 130 rpm and 150 rpm.

5.6 Monitoring of the rotor shaft vibrations during different rotating Speeds

The torque is transmitted from the servo motor to the hub through an Aluminum shaft supported by two bearings, to provide the rotational motion of the test rig. To achieve comprehensive monitoring during the experiments, lasers were used for detecting shaft dynamic displacements orthogonally at axes1 and 2 directions as in figure 5.30, which shows the laser probes positioned perpendicularly and aligned on the rotor shaft. Various rotational speeds have been presented to observe the shaft fluctuation particularly after bearing 2, (free end), which has high flexibility. The effective distance between the laser sensors and the shaft surface was found to be between 23.0 mm to 23.8 mm, hence the starting point will be away from the shaft centre by 35.5 mm.

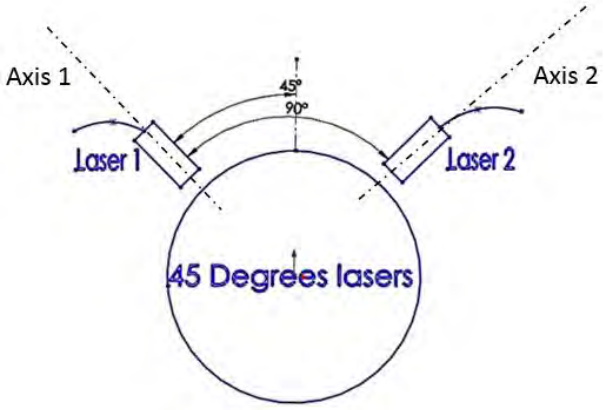

Figure 5.30 Configuration of laser probes perpendicularly on the rotor shaft with the proposed axes.

Figure 5.31 illustrates rotor shaft dynamic displacement at the range from 40 rpm to 60 rpm, which shows different behaviour of the rotor shaft through the laser measurement monitoring technique. It can be seen that the maximum rotor dynamic displacement of 630 microns occurs at 50 rpm towards axis1, whereas maximum displacement at axis2 was 280 microns which is small relative to axis1. Additionally, maximum dynamic displacement at 60 rpm was 581 microns and 231 microns at axes1 and 2 directions respectively, which was higher than the displacements at 40 rpm, that

was 531 microns and 201 microns at the same axes. This indicates that the rotor shaft fluctuated more towards the axis1 direction than the axis2, due to increasing tip load represented by in-plane and axial beam vibrations. Additionally, increasing tower vibration in the Z-direction can further affected an increase in rotor shaft vibrations at axis1 direction. However, shaft vibration has already been affected by beam axial vibrations during the rotation, hence the centrifugal force has a key role in increasing rotor dynamic displacement towards axis 2 direction.

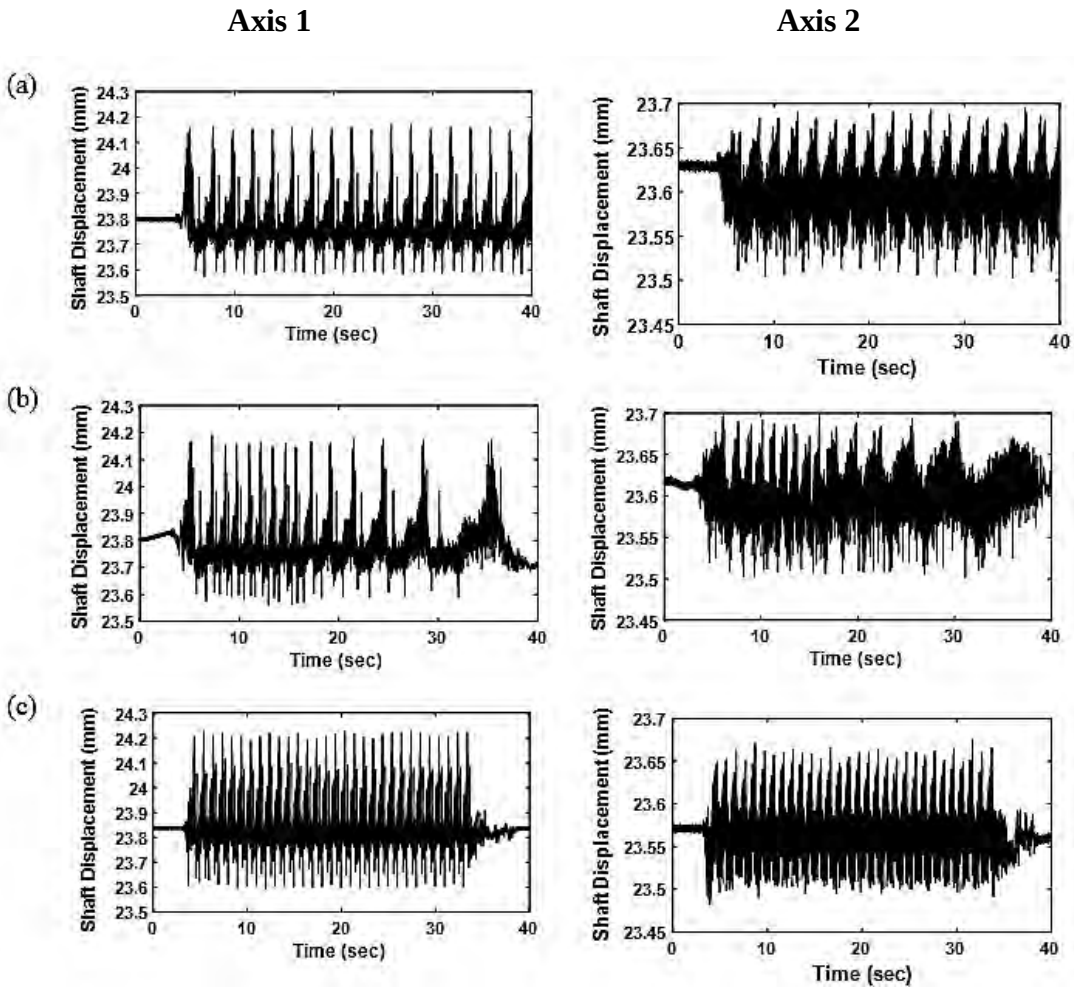

Figure 5.31 Rotor shaft displacements towards axes 1 and 2 through laser measurement at a) 40 rpm, b) 50 rpm, and c) 60 rpm rotating speeds.

Increasing rotor speed to the range from 70 rpm to 90 rpm has slightly decreased shaft displacement in the axis2 directions as illustrated in figure 5.32, which means that the shaft oval shape path is decreased towards axis2. Maximum bending displacement in axis1 direction was found to have small changes with increasing speeds in this range.

Maximum displacement in the axis 1 direction was 431 microns at 90 rpm, as shown in figure 5.32c, while maximum displacement in the axis2 direction was 202 microns at the same speed. However, maximum shaft displacement towards axis1 at 70 rpm and 80 rpm was 421 microns and 393 microns respectively, while maximum shaft displacements at axis2 were 193 microns and 168 microns at the same speeds. Rotation duration was decreased when the speed increased, due to the servomotor control software, which decreases rotation distance when the speed increases within the same experiment time.

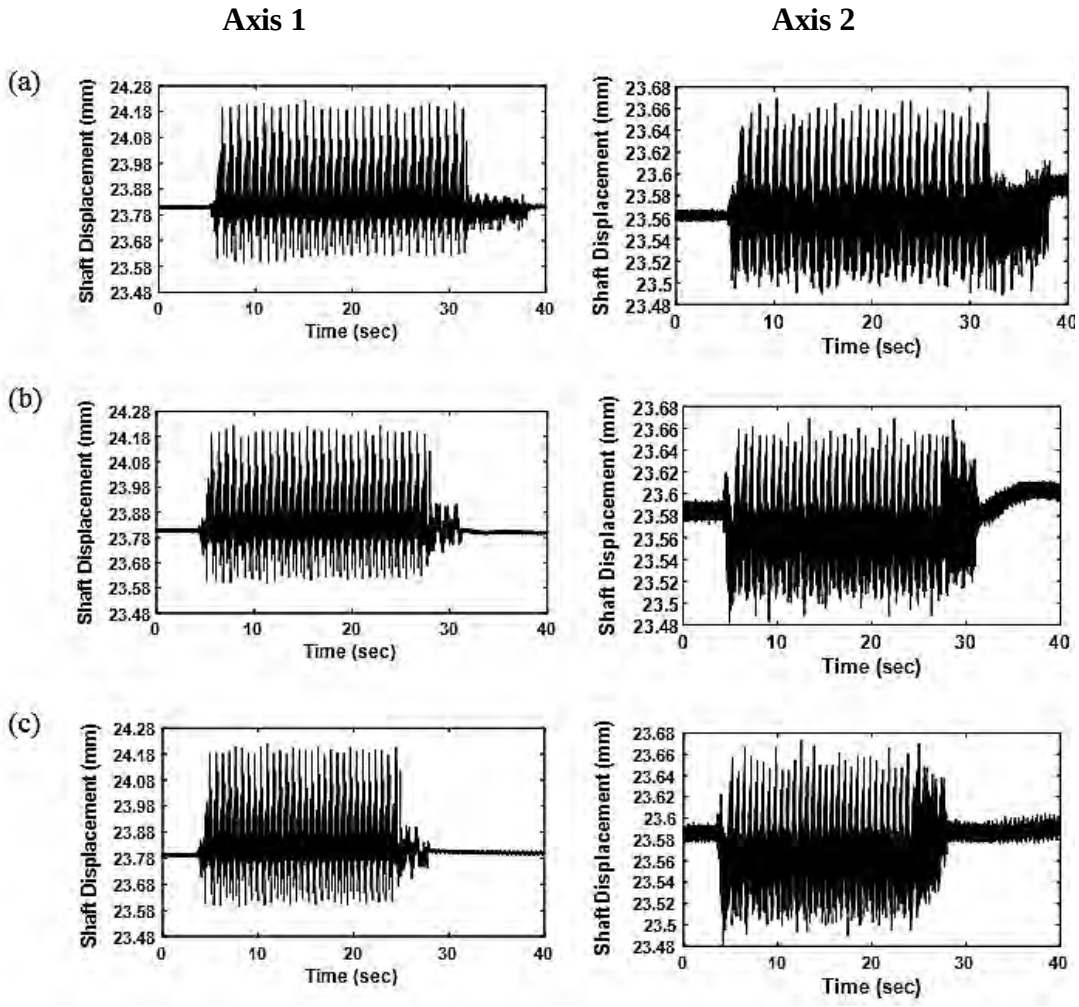

Figure 5. 32 Rotor shaft displacements through Laser measurement at a) 70 rpm, b) 80 rpm, and c) 90 rpm rotating speeds (axis1 on the left and axis2 on the right).

Moving on to higher speeds as shown in figure 5.33, there was a slight increase in the bending displacement towards axis 1 to 567 microns and to 223 microns at axis2 at 150 rpm. The maximum displacements towards axes1 and 2 at 110 rpm were found to be 530 microns and 202 microns respectively. While at 130 rpm a decrease was noticed

for the shaft displacements towards both axis1 and axis2 directions to 490 microns and 197 microns respectively. However, shaft displacements at 100 rpm were 542 microns and 218 microns at the directions of axis1 and axis2 respectively, as shown in figure 5.33a.

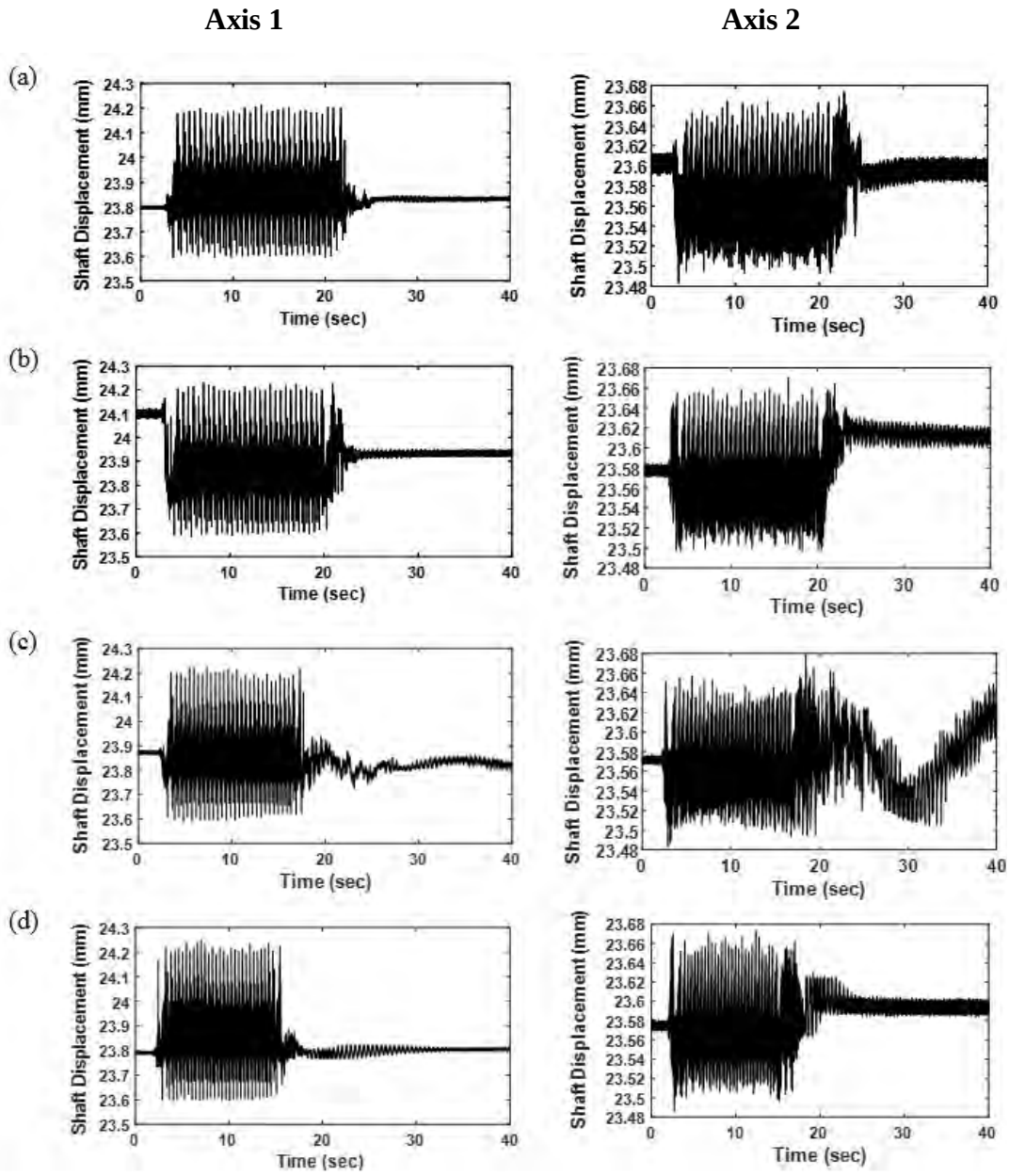

Figure 5.33 Rotor shaft displacement through Laser measurement sensors at 100 rpm, 110 rpm, 130 rpm, and 150 rpm (axis1 on the left and axis2 on the right).

Monitoring rotor displacement amplitude for each revolution is another technique to measure and identify the shaft vibrational movement during the experiment, to detect bearing-shaft system faults.

Figure 5.34 illustrates the result of different rotational speeds to identify rotor shaft amplitude without beam or shaft faults. Laser measurements enable the position of maximum and minimum shaft motion amplitudes by analysing the produced and reflected beam voltage, from the rotor shaft surface during the operation. Monitoring shaft motion within the bearing housing by two lasers sensors can identify the small displacements corresponding to the shaft position. As can be seen in figure 5.34a, the maximum amplitude at axis1 was 635 microns at 40 rpm, whereas the maximum amplitude at axis2 was 201 microns. In figure 5.34b, the maximum amplitude at axis1 occurs at 50 rpm, which is 690 microns, corresponding to 280 microns being the maximum amplitude at axis2. Tower vibrations in the Z-direction and beam in-plane vibrations, have a pronounced effect on increasing the rotor shaft displacements. Minimum amplitude towards axis1 was 393 microns corresponding to the minimum amplitude at axis2 of 168 microns.

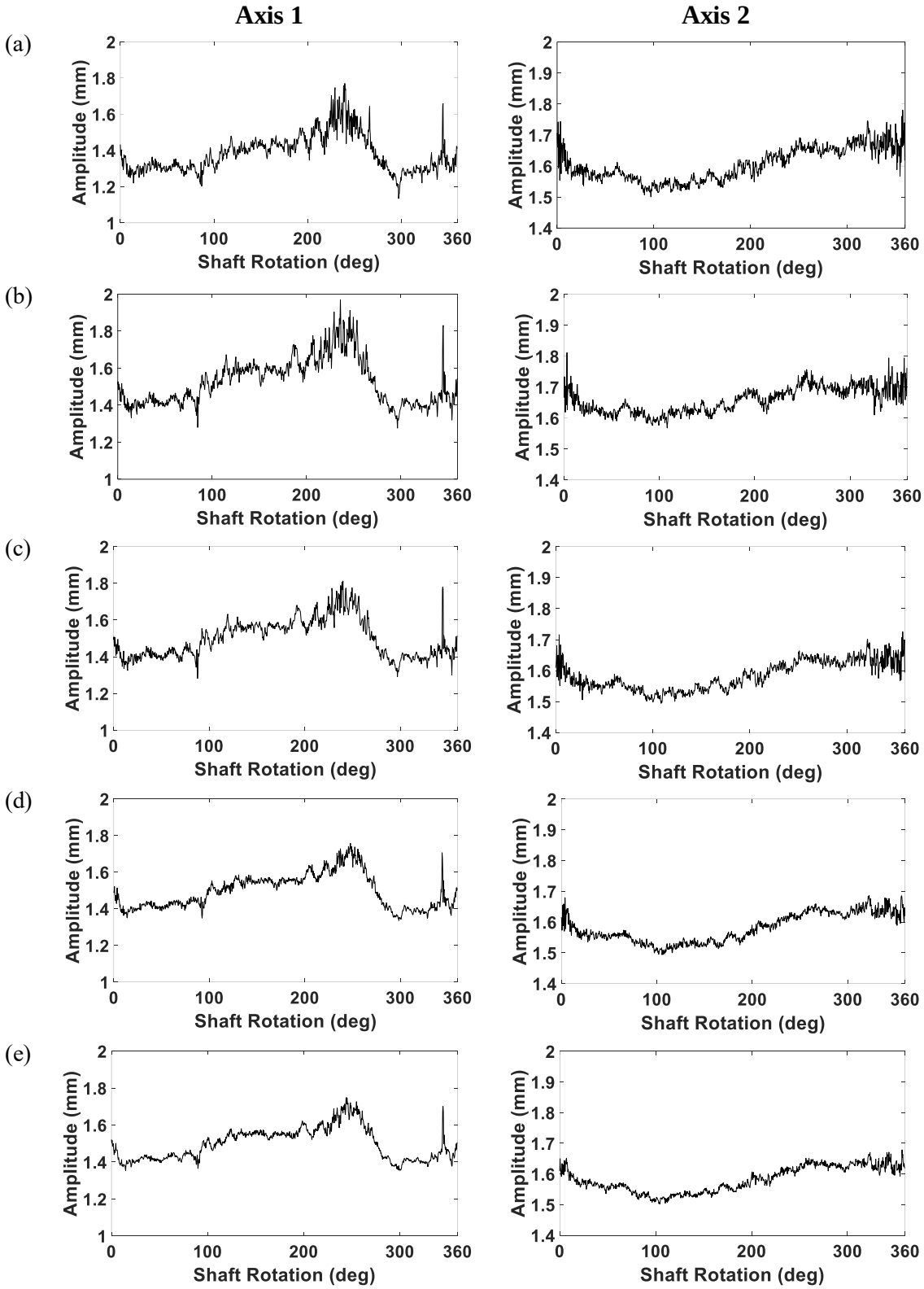

Figure 5. 34 Rotor shaft deflection amplitudes measured by laser sensors per rotation towards axes 1 and 2 at a) 40 rpm, b) 50 rpm, c) 60 rpm, d) 70 rpm, and f) 80 rpm.

Similarly, figure 5.35 shows rotor shaft deflections at higher speeds, which can further be seen to decrease the rotor shaft bending while rotor speed increases. Maximum bending at axis1 was 567 microns corresponding to the maximum bending of 223 microns at axis2 which occurs at 150 rpm. At 100 rpm in figure 5.35a, it was noticed that the second maximum bending towards axis1 was 542 microns and the bending at axis2 was 218 microns. After that, the amplitude decreased at axis1 to 530 microns, however, bending at axis2 increased to 202 microns at 110 rpm. Moving on to 130 rpm, in figure 5.35d the values of 490 microns and 197 microns were obtained which were the rotor shaft dynamic bending at axes1 and 2 respectively. As speed increases from 140 to 150 rpm, the rotor shaft bending displacement increases, after that bending displacement tends to decrease. Additionally, the spike at 347^{o} was attributed to coupling with tower vibration in the Y-direction, which is explicit in the shaft displacement at the axis1. However, at this angular position, it was noticed that the maximum shaft displacement at axis2 occurred, which demonstrates the effect of tower vibration in the Y-direction on the drive shaft fluctuations.

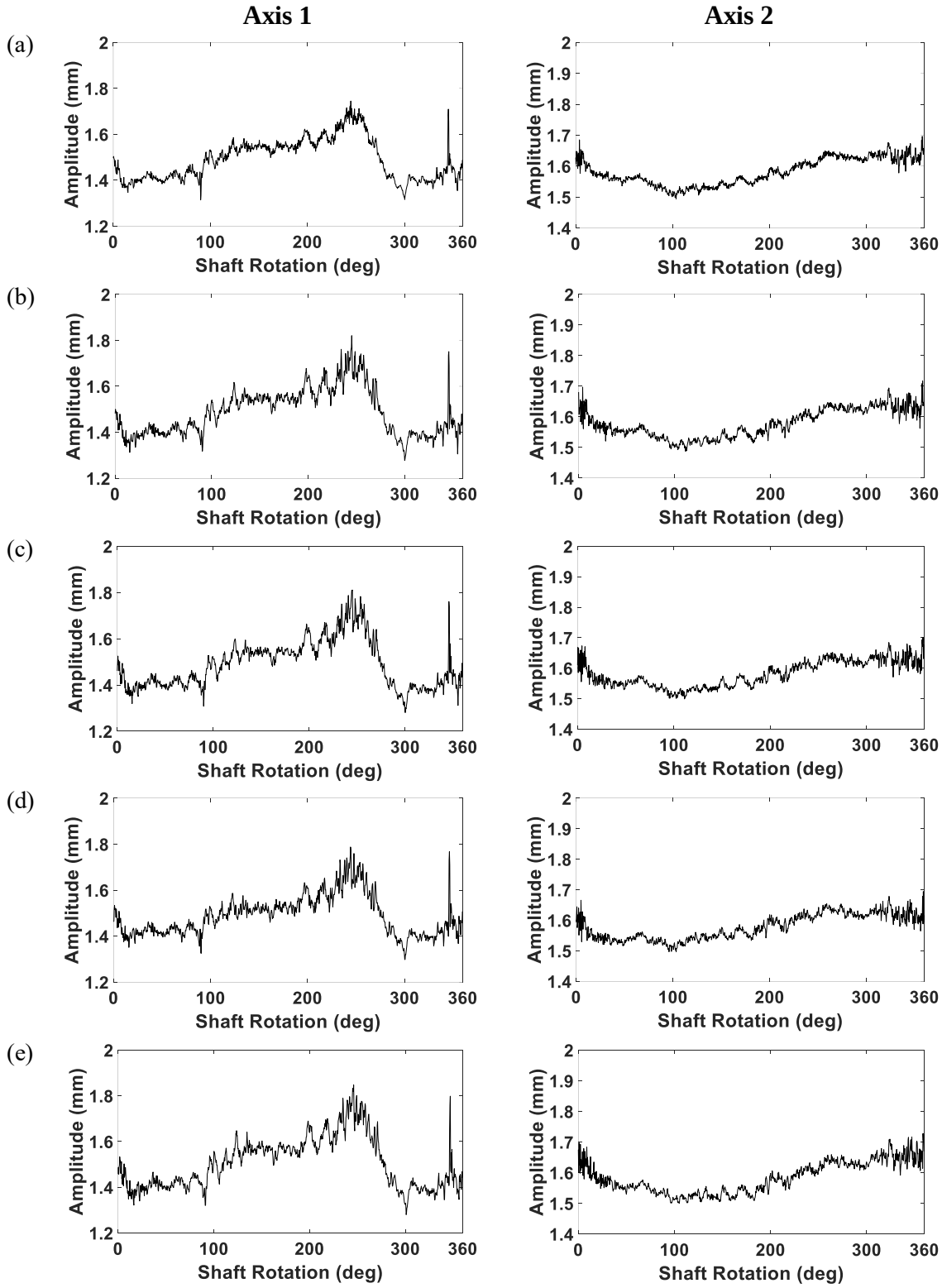

Figure 5.35 X and Y rotor shaft deflections amplitude measured by laser sensors at a) 90 rpm, b) 100 rpm, c)110 rpm, d) 130 rpm, and e) 150 rpm.

Orbit analysis is a further monitoring technique of shaft behaviour. Figure 5.36 illustrates orbit plots of 1X for the speed range of 40 rpm to 100 rpm which can be

observed by the oval shifting to the right due to forward whirling resulting from an increase in speed. The shaft centre line extended at axis1 more than axis2 at 40 rpm, however, this extension was reduced with 12.4 microns at 50 rpm. Shifting to the right can be observed for the orbit motion when rotor speed rises to 60 rpm, then decreasing to 100 rpm. Additionally, shaft centre line motion decreases at 80 rpm, return to increasing at 90 rpm and continue to increase up to 100 rpm, where the difference between displacements at axes 1 and 2 was 324 microns. The minimum difference was at 70 rpm, which means that the shaft centre line fluctuations along axis 2 increases to be close to axis 1. However, maximum difference was 434 microns at 40 rpm.

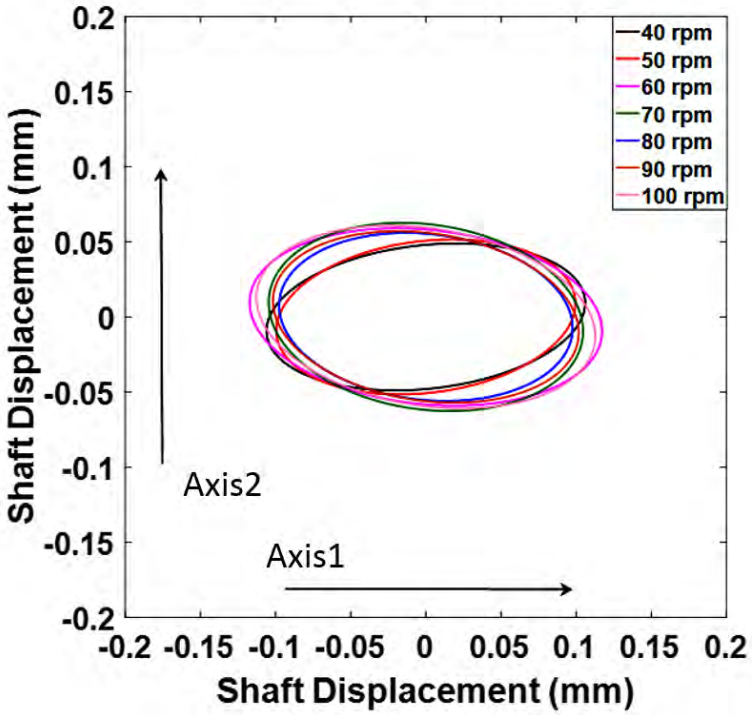

Figure 5. 36 Orbit plots (1X) for the drive shaft per on revolution motion at the speed range from 40 rpm to 100 rpm.

Figure 5.37 shows shaft centreline orbit plots for the speed range from 110 rpm to 130 rpm, shifting the oval path in the right(increasing +ve displacement in the axis 1 direction) at 110 rpm, while shifting in the axis 2 direction and reducing its oval extension at 130 rpm. Increasing speed leads to increase rotor shaft centre line eccentricity of the shaft centre line due to shaft whirling, and hence shifting the elliptical shaft motion in the Axis 1 direction. High speed leads to increases in centre line displacement in both directions due to increasing shaft bending displacement,

resulting from coupling effects of rotary inertia vibrational modes and tower fluctuations. This type of analysis can be used to monitor shaft behaviour inside the bearing housing and detect bearing-shaft faults during operation.

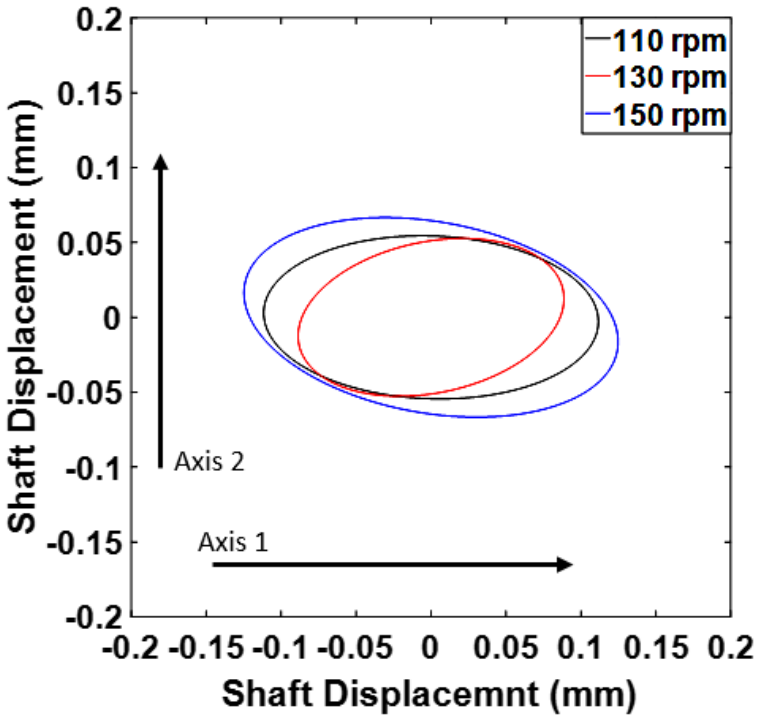

Figure 5. 37 Orbit plots (1X) of the drive shaft per one revolution motion at the range from 110 rpm to 150 rpm.

To increase the understanding of shaft whirling motion during the test rig experiments, second harmonic orbits (2X) have been presented as in figure 5.38, for the speed range from 40 rpm to 90 rpm, which shows shifting of the orbit to the right with extending of the shapes compared to the (1X) on axis1. Additionally, shifting can be observed in the shaft centre line motion paths for the speed range from 60 rpm to 100 rpm, where the paths tend to take the same diamond shape with shifting in the axis 1 direction, while at 40 rpm and 50 rpm the diamond shape was almost the same with further shifting to the axis 1 direction. This tendency has further been identified in (1X).

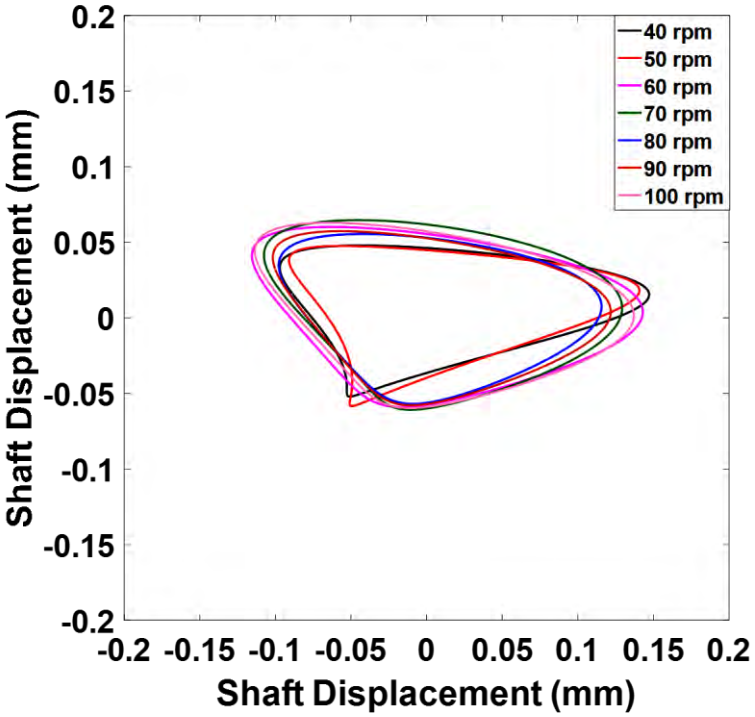

Figure 5. 38 Shaft orbit plots (1X+2X) per one revolution of the speed range from 40 rpm to 100 rpm.

Additionally, figure 5.39 shows shaft orbit plots of second harmonics (2X) at higher speeds namely 110 rpm, 130 rpm, and 150 rpm. Shifting to the axis 1 direction in the diamond shape orbits can be seen with the speed increases, which is further demonstrated for changing the orbit plots with the speed changes. This significant tool for monitoring rotor shaft centre line motion utilizing laser measurements during operation can show the drive shaft elliptical path, which indicates the lateral and vertical vibrations due to dynamic load excitations. Further, it varies according to speed, load conditions, and material stiffness, which determines the dimensions of the elliptical shape.

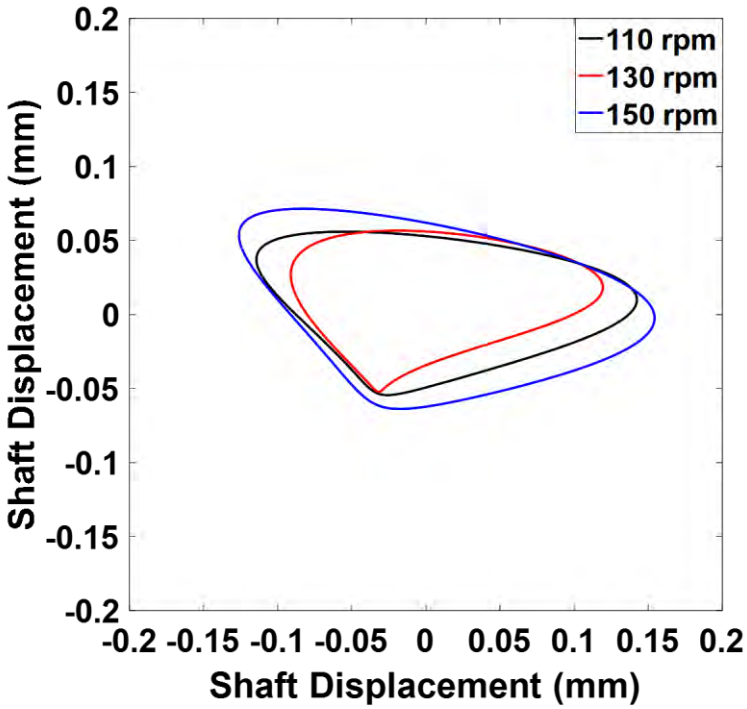

Figure 5. 39 Shaft orbit plots (1X+2X) per one revolution at g) 110 rpm, h) 130 rpm, and i) 150 rpm.

Moreover, the extension at both axes1 and 2 identified the bending displacements values at the applied speed range. Shaft speed (the absolute measurement of shaft encoder rotation) at different rotating speeds can be seen in figure 5.40, which illustrates the drive shaft speed behaviour during the experiments. The free part of the drive shaft (after bearing 2) experienced high frequencies during beam rotation within the test range of 40 rpm to 150 rpm. Maximum shaft frequency of 2.5 Hz at 11.6 sec, occurs at 150 rpm after the first 10 seconds of the experiment, during which the observer can see the test rig vibrate completely when the rotation approaches the required speed. Additionally, the shaft exhibited nearly the same behaviour at 110 rpm and 150 rpm when the shaft reached the desired speed. It further shows the ramp up, constant phase and ramp down of the motor speed during the experiment.

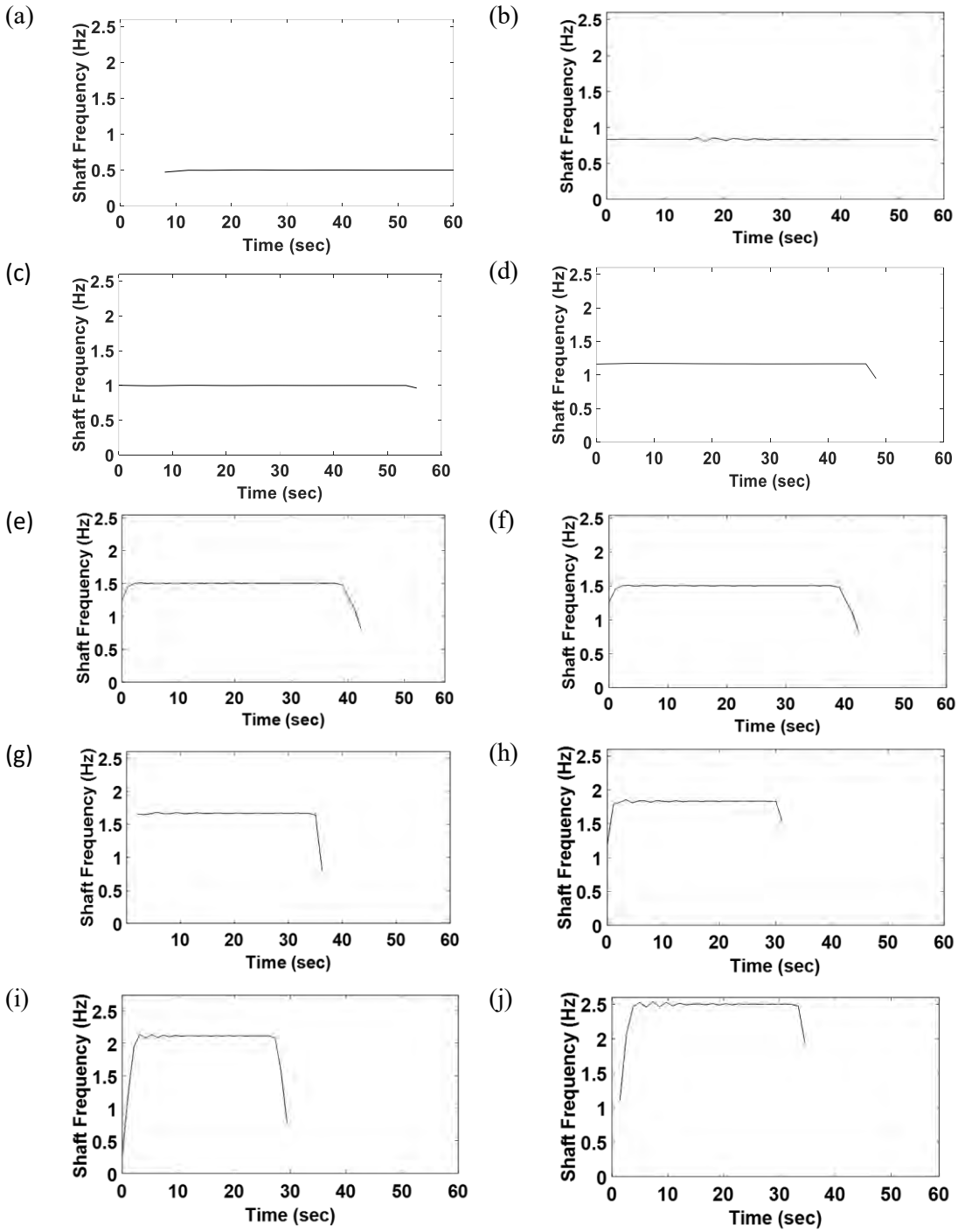

Figure 5. 40 Spectrum analysis of shaft frequencies amplitude measured at a) 40 rpm,b)50 rpm, c) 60 rpm,d) 70 rpm, e) 80 rpm, f) 90 rpm, g) 100 rpm, h) 110 rpm, i) 130 rpm, and j) 150 rpm.

The forward shaft whirling per revolution can further be investigated by shaft order analysis in figure 5.41, that shows forward and backward whirling components during the speed change. The variation of shaft orders is similar to imbalance effect due to shaft misalignment which increases the shaft frequencies and whirling vibrations.

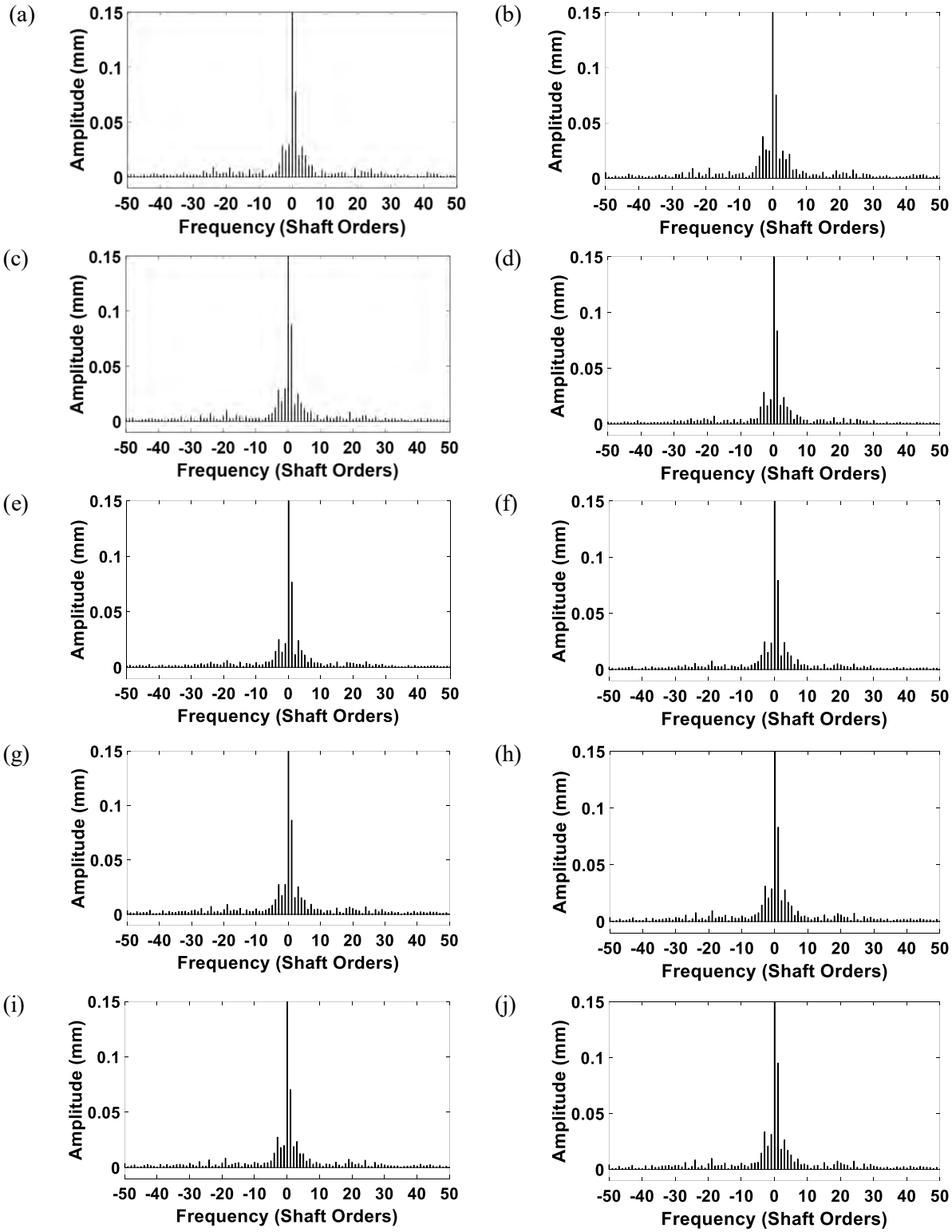

Figure 5. 41 Complex Discrete Fourier Transform of the shaft orders at a) 40 rpm, b) 50 rpm, c) 60 rpm, d) 70 rpm, e) 80 rpm, f) 90 rpm, g) 100 rpm, h) 110 rpm, i) 130 rpm, and j) 150 rpm.

Clarifying the positive and negative shaft frequencies in figure 5.41, figure 5.42 illustrates the first positive and negative rotor shaft frequencies over the speed range from 40 rpm to 150 rpm. Maximum amplitude difference of 0.0638 mm can be recognized at 150 rpm. The major shaft orbit motion is seen to be caused by forward shaft whirl, where the forward whirl component is almost 4 times larger than the backward whirl component. These components can be used for assessment of the main rotor shaft, where the trends over time can be used to indicate changes to the condition.

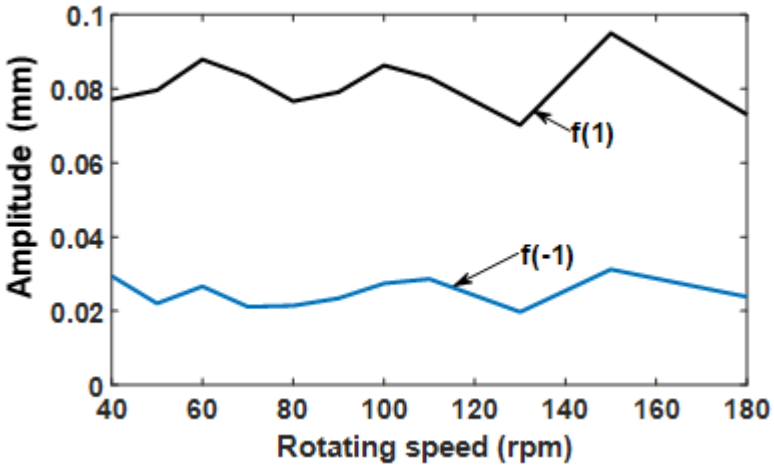

Figure 5. 42 First positive and negative shaft frequencies for speed range from 40 rpm to 150 rpm.

5.7 Conclusion

The influence of increasing beam speed on the small horizontal axis wind turbine test rig components has been presented in this chapter. Three solid thin cantilever beams have been utilized for modelling wind turbine blades, two beams have been instrumented with different contact measurement sensors for vibration condition monitoring during different rotating speeds. Axial vibrations were noted to have a coupling correlation with in-plane vibration due to Coriolis and centrifugal forces in the rotational plane. However, increasing the rotational speeds leads to decrease in the beam axial vibrations due to the increase in beam stiffness. At 130 rpm, the test rig was vibrating profusely due to increasing vibrational modes of the rotating components. Additionally, increasing rotor speed to 150 rpm leads to increasing out-of-plane vibrations due to increasing bending forces. However, the in-plane vibration was decreased due to decreasing the dynamic bending towards the direction of

rotation, this is evidence of the decoupling between in-plane and out-of-plane modes. The tower vibrations are further affected by the gyroscopic effect, through increasing the vibrations in the Y and Z directions. Laser measurements have been utilized for drive shaft vibration condition monitoring instead of proximity probes, as non-contact sensors enable to detect the small shaft displacement due to beam dynamic vibrations. High rotational speeds can trigger large vibrational amplitudes while the rotor beam passes through critical speeds (resonance speeds), which is due to rising centrifugal forces that excited beam vibrations as an external unbalanced force, and the rotor beam responding to lateral forces trying to overcome this restraint force to sustain rotation. Additionally, drive train (the drive shaft, hub, and tower) frequencies have further excitation forces on beam vibration frequency. The described excited forces above, as well as gravitational forces, produce synchronizing unbalance forces which can excite beam vibrations towards in-plane and out-of-plane. The change in wind gust also excites another type of vibration due to the change in the applied torque on wind turbine blades. This was modelled by allowing a sudden maximum torque of 10Nm produced by the servo motor, which caused an instantaneous variation in angular velocity and acceleration due to time-variant torque, thereby causing a short-time effect of triggering transient vibrations in the test rig system. Consequently, the dynamic vibrations were transmitted to the non-rotating parts as an external excitation that generates synchronous vibrations which increase with the rotational speeds. This category of vibrations will be addressed in the next chapter of this thesis. Tower vibration has a pronounced effect on the rotating beam vibrations, this was obvious on beam out-of-plane vibrations. Additionally, the coupled effect of beam axial and tower Z-direction vibrations, have a direct effect on increasing the drive shaft axis1 vibrations at around 245^{o} of the shaft rotation.

Spectrum analysis and orbit plots were proved effective monitoring techniques for detecting shaft whirling vibrations and long-term eccentricity, which caused subsequent foundation fatigue cracks to the tower in normal conditions. The first and second harmonic orbit plots have been determined to give further understanding of the shaft behaviour within the bearing housing. Moreover, this technique has advantages of detecting incipient rotor and fault diagnosis within the bearing housing that will be further investigated in the following chapter.

Chapter 6 Dynamic vibration of the rotating thin cantilever beam during different case studies

6.1 Introduction

This chapter presents several case studies that investigate the behaviour of the rotating and non-rotating components of the small wind turbine test rig while instilling artificial faults, which model in-situ wind turbine faults. Prevalent blade faults can produce high-vibrations during working conditions, often causing unavoidable failure. These blade faults also affect the vibrations found in the tower and shaft of the wind turbine.

6.2 Influence of add and loss mass from the rotating cantilever beam

The flexibility of the aluminium beam varies with rotational speed was discussed in chapter 5. As the beam's velocity passes through the critical speeds, induced bending displacements change the balanced state due to the presence of synchronous vibrations. In addition, any loss or addition of mass onto the rotating beam would lead to an additional imbalance in the rotation.

The addition or removal of mass from one of the rotating beams has been utilized to simulate various behaviours in the test rig system for a range of rotating speeds. Acceleration and strain measurements were collected from these various conditions to establish a data bank for the condition monitoring and fault diagnosis of rotor shaft vibrations.

6.2.1 Influence of Add Mass (AM) and Loss Mass (LM) on the beam axial vibrational modes.

Losing mass from the balanced rotating blade leads to unbalance in the system, which results in a high vibration component, potentially leading to further failure. As discussed in Chapter 3, all beams have extensions of 35 mm and the ability to attach an additional 14.95 g mass. Losing mass experiments have been performed by

connecting two beams with an extension while keeping the third (beam 1) without the extension piece. Figure 6.1 shows a comparison of beam axial vibration-based strain measurements due to the loss of the 14.95 g weight and an added 130 g mass in the beam tip. From this figure, the maximum strain at 30 rpm is 30.13 µstrain which occurs at 0.651sec during the Losing Mass Case (LMC), while maximum strain is 50.25 µstrain that occurs at 1.437 sec during the Added Mass Case (AMC). This is attributed to Coriolis forces which increases beam vibrations axially due to beam stretching (30 µstrain corresponding to a minute amount of beam stretching) (Banerjee & Kennedy, 2014). Strain values are shown to increase continuously in the AMC as speed increases to a maximum strain value of 80.01 µstrain at 2.83 sec at 50 rpm. The maximum strain increased slightly to 80.39 µstrain at 100 rpm, even though when the rotation commenced, the average axial strain decreased as it reached the desired speed due to the increase in beam stiffness (Murtagh et al., 2005) However, the maximum strain at the same speed (100 rpm) during LMC is noticed to be different, which is consistently 20.92 µstrain. At 150 rpm with LMC in figure 6.1d, there is an increase in the axial strain starting at 9.22 sec with an initial value of 39.81 µstrain which indicates that the centrifugal forces increase more than the beam stiffness. In AMC, at 150 rpm, beam axial strain increases to 80.81 µstrain when the rotation begins and then decreases gradually. Likewise, there is an increase of beam stiffness when the speed increases. Since both cases in figure 6.1 show an imbalance, the high vibrations can be seen to be due to the added mass. Adding mass to the rotating beam leads to increases in the rotary inertia, which in return increases the centrifugal force.

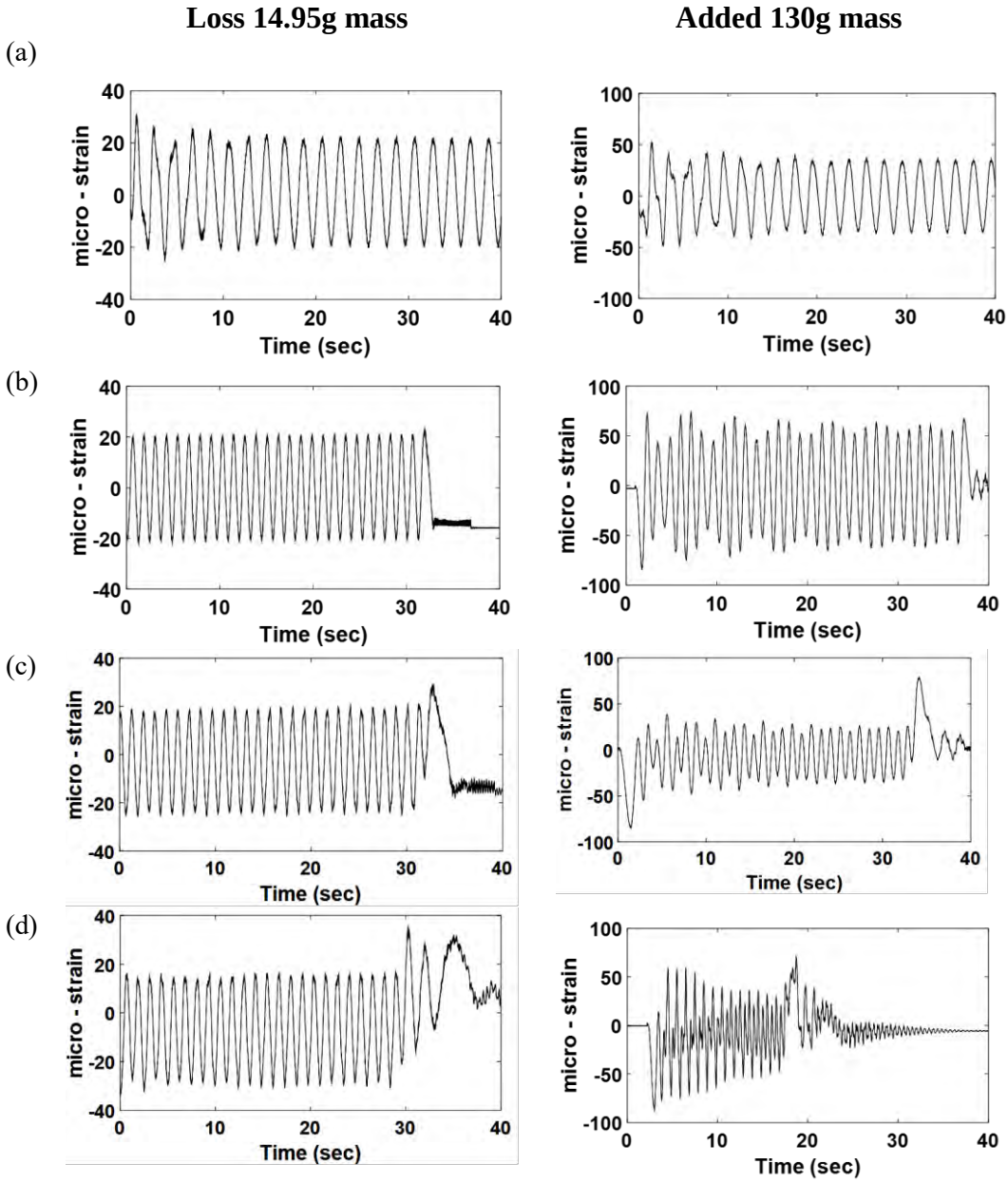

Figure 6. 1 Beam axial vibrations based on strain measurements with loss and add mass at a) 30 rpm, b) 50 rpm, c) 100 rpm, and d) 150 rpm.

Additionally, figure 6.2 illustrates beam axial strain measurements per revolution, showing a significant increase in AMC amplitudes from 34.19 µstrain at 30 rpm to 56.84 µstrain at 50 rpm as can be seen in figures 6.2a and 6.2b. A decrease in the axial strain can be identified in LMC from 21.42 µstrain at 30 rpm to 20.43 µstrain at 50 rpm. Further, beam maximum axial strain decreases to 19.17 µstrain on LMC and to 22.79 µstrain on AMC, when the rotor speed reaches 100 rpm. After that, increasing speed to 150 rpm leads to an increase in the strain amplitudes in AMC to 24.57 µstrain,

as shown in figure 6.2d. The existence of additional weight in the beam tip led to prolonging the beam length, which causes an increase in the dynamic vibrations. LMC causes a different imbalance at the test rig system by reducing the rotary inertia, this effect led to decreasing the strain values in some rotating speeds, as shown in figure 6.3. However, centrifugal and Coriolis forces on the LMC beam were decreased compared with the other two beams, hence increasing beam speed has little effect on axial vibration in this case.

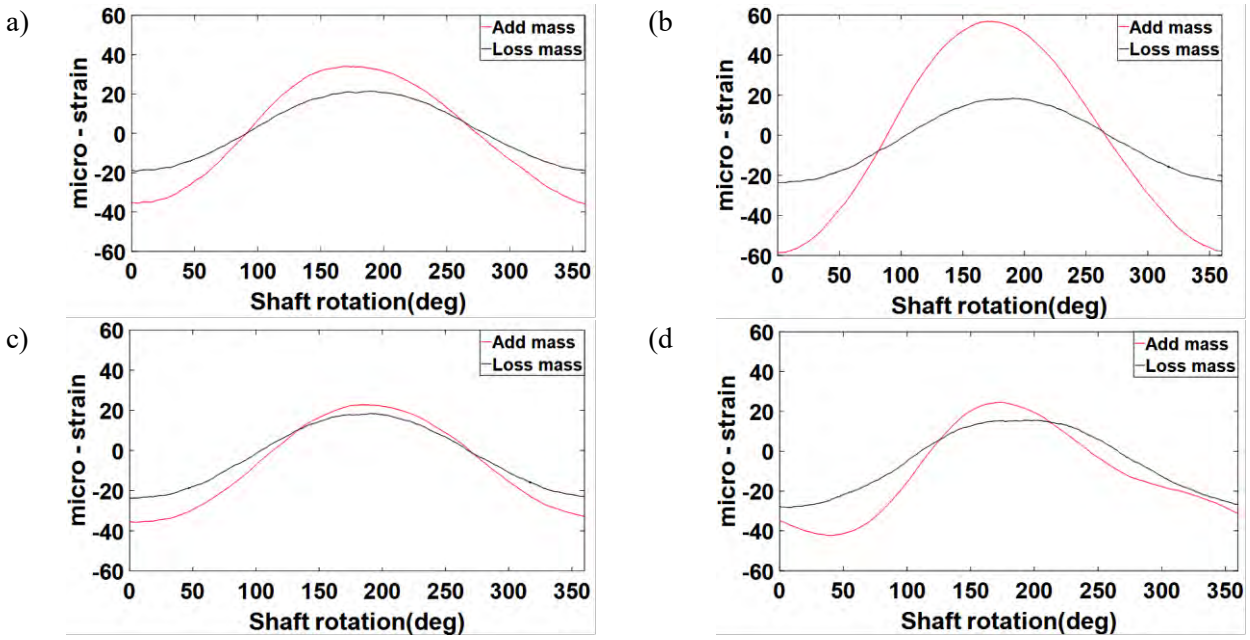

Figure 6. 2 Beam axial strain per one revolution during loss 14.95 g and added 130 g masses at a) 30 rpm, b) 50 rpm, c) 100 rpm, and d) 150 rpm.

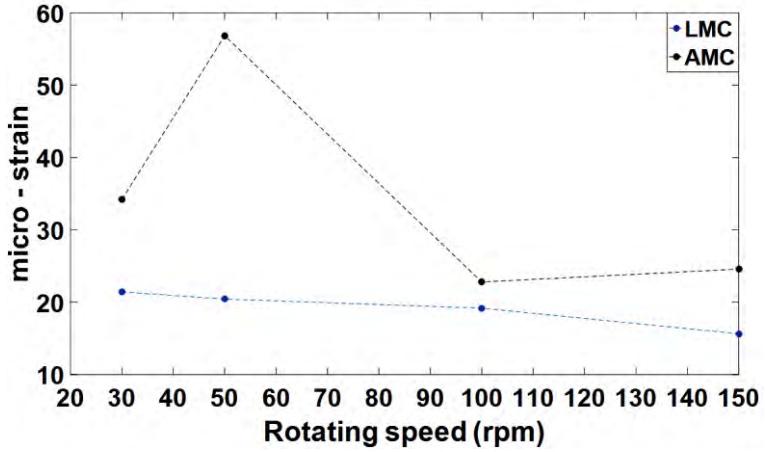

Figure 6. 3 Maximum beam axial strain amplitudes during both losing 14.95g and adding 130g masses in the beam at speeds 30 rpm, 50 rpm, 100 rpm, and 150 rpm.

6.2.2 Influence of Add Mass (AM) and Loss Mass (LM) on the beam in-plane vibrational modes by strain measurements.

In-plane vibrations show a different response to axial vibrations, which can be seen from figure 6.4 showing in-plane vibration in terms of strain measurements. AMC excited high vibration due to the imbalance effect, as seen through the increase of in-plane strain to the maximum value at 100 rpm of 357.9 μstrain in figure 6.4c. While maximum in-plane strain during LMC occurs at 150 rpm which was 214.2 μstrain in figure 6.4d. With existing imbalance effect due to additional mass, increasing the rotor speed to 150 rpm led to a slight decrease in the strain as can be noted in figure 6.4d, due to decreasing blade dynamic bending. This was attributed to the increase in beam angular velocity being close to the bending resonance frequency towards in-plane as well as the increase in beam stiffness. However, in-plane strain decreases for the LMC when rotor speed increases to 50 rpm as indicated in figure 6.4b. At 100 rpm, the in-plane strain increases and continues to increase to 150 rpm, as shown in figure 6.4d. This behaviour between the two different unbalance cases can further be seen in the axial strain at the same speeds, which is due to the difference between the added or losing mass causing the imbalance effect.

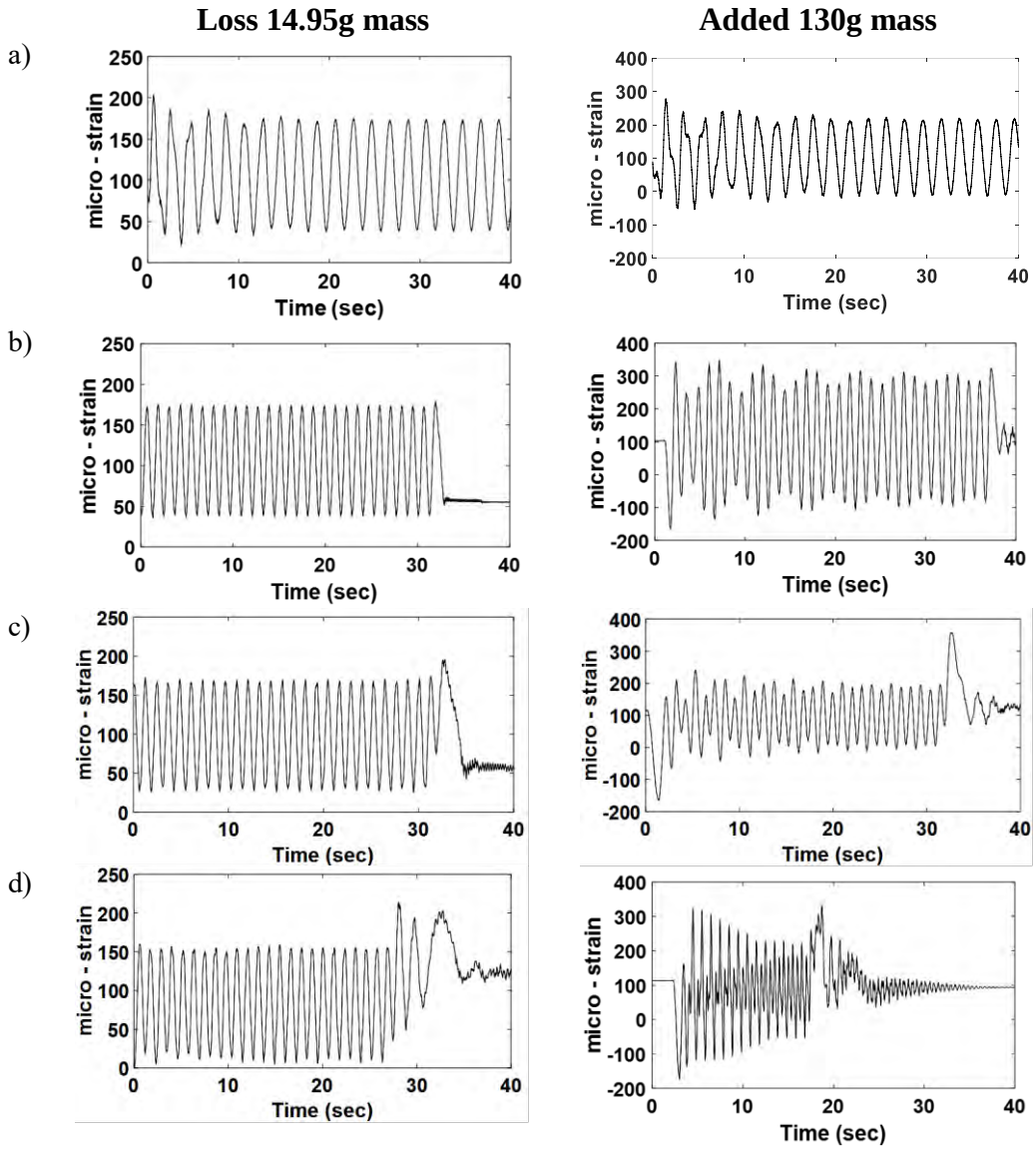

Figure 6.4 Beam In-plane vibrations based on strain measurements during loss 14.95g and added 130g masses a) 30 rpm, b) 50 rpm, c)100 rpm, and d) 150 rpm.

In figure 6.5, in-plane strain per one revolution is presented for the two fault cases. Increasing the rotor speed from 30 rpm to 50 rpm caused an increase in the in-plane strain from 239.1 µstrain to 292.4 µstrain during AMC, while decreasing strain occurs from 172.5 µstrain to 167.7 µstrain during LMC. A slight drop in the in-plane strain can be identified when rotor speed increases to 100 rpm to be 166.5 µstrain in LMC, and a pronounced decrease to 188.7 µstrain on AMC. This drop then makes only a small difference between the maximum amplitudes as in figure 6.5c. Increasing speed to 150 rpm results in an increase to the maximum in-plane stain values with a slight shift to the left to 197.9 µstrain in AMC, while the maximum in-plane strain value further decreases to 156.9 µstrain in LMC as in figure 6.5d. The maximum difference

between AMC and LMC is 124.7 µstrain at 50 rpm and the minimum difference is 21.2 µstrain at 100 rpm, as shown in figure 6.6.

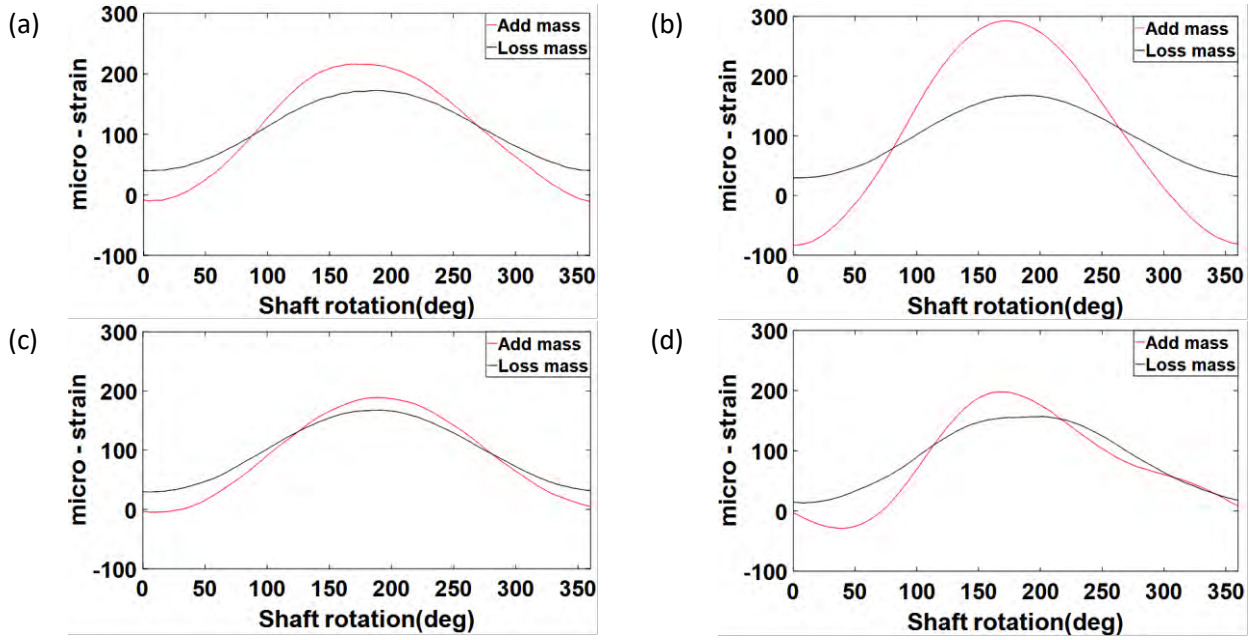

Figure 6. 5 In-plane beam strain measurements per one revolution with two case studies of 130g additional mass and 14.95g losing mass from beam 1 at a) 30 rpm, b) 50 rpm, c) 100 rpm, and d) 150 rpm.

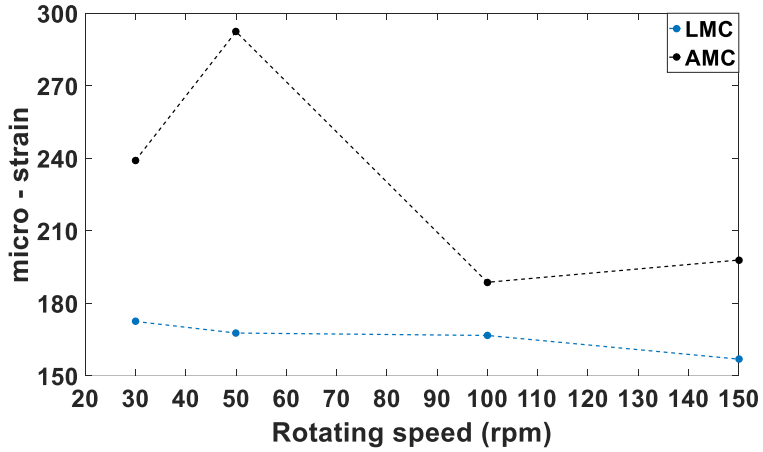

Figure 6. 6 Beam In-plane vibrations based on strain measurements during loss 14.95g and added 130g masses at a) 30 rpm, b) 50 rpm, c)100 rpm, and d) 150 rpm.

6.2.3 Influence of Add Mass (AM) and Loss Mass (LM) on the beam acceleration.

Beam in-plane vibrations can further be monitored by the piezoelectric accelerometer that was located at the beam tip. Figure 6.7 shows the maximum in-plane acceleration amplitude on LMC of 20.31 m/s^2 at 150 rpm in figure 6.7d, compared with 28.37 m/s^2 on AMC. Additionally, both imbalance cases have increased the acceleration amplitude due to the increase in the beam vibration at multiple planes. In figure 6.7a, the maximum average beam acceleration is 11.62 m/s^2 at 30 rpm. This amplitude increases to 13.45 m/s^2 at 50 rpm as shown in figure 6.7b, after that, beam acceleration increases to 16.92 m/s^2 at 100 rpm as indicating in figure 6.7c. In AMC, increase in acceleration amplitude can also be seen as the rotating speed increases with different amplitude, from 14.89 m/s^2 at 30 rpm to 15.91 m/s^2 at 50 rpm and to 18.11 m/s^2 at 100 rpm. At 150 rpm, high beam vibration can be observed with the imbalance effect, with 20.31 m/s^2 in LMC and 28.78 m/s^2 in AMC in figure 6.7d.

This difference between the two imbalance cases affirms that imbalance forces due to adding mass to the rotor beam is higher compared to the losing mass. Additionally, there is an increase in the beam acceleration measured by the piezoelectric accelerometer at LMC with speed, converse to the in-plane strain measured from strain gauges, which indicates that the beam tip experiences large vibration compared to the root.

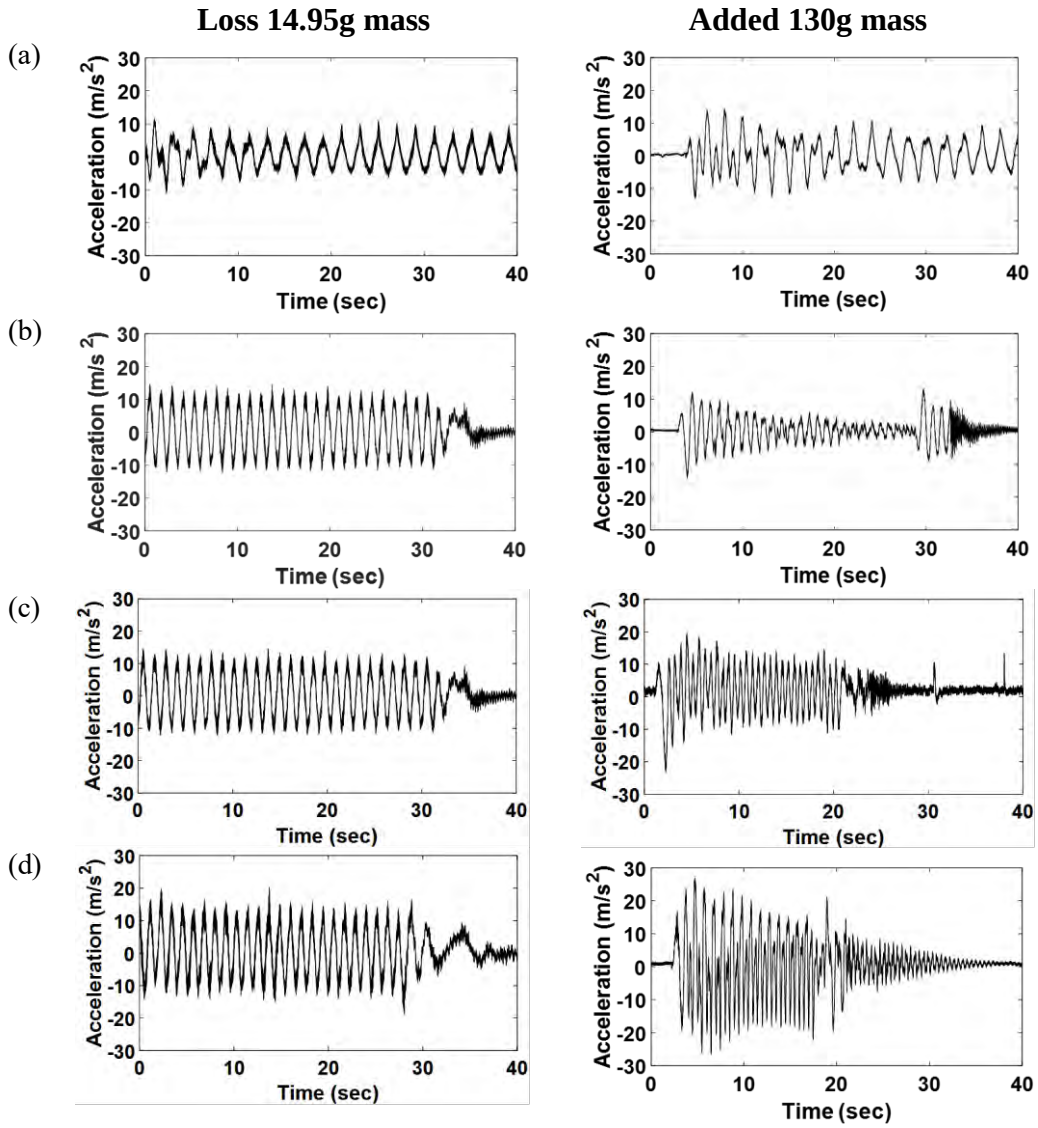

Figure 6.7 Beam in-plane vibrations based on acceleration measurements by piezoelectric sensors on the beam tip at 30 rpm, 50 rpm, 100 rpm, and 150 rpm during LMC and AMC.

In order to identify beam acceleration details, figure 6.8 illustrates the beam acceleration per one revolution measured by the piezoelectric sensors in both LMC and AMC. Blade and Tower vibration resonances have some effect on beam vibrations at speeds 50 rpm, 100 rpm, and 150 rpm in LMC, however, it is pronounced at 50 rpm and disappeared at 100 rpm and 150 rpm in AMC. This could be attributed to increasing dynamic bending on one side (in-plane). Additionally, the rotating beam has the same behaviour with imbalance effect in both cases with amplitude differences when the speed increases.

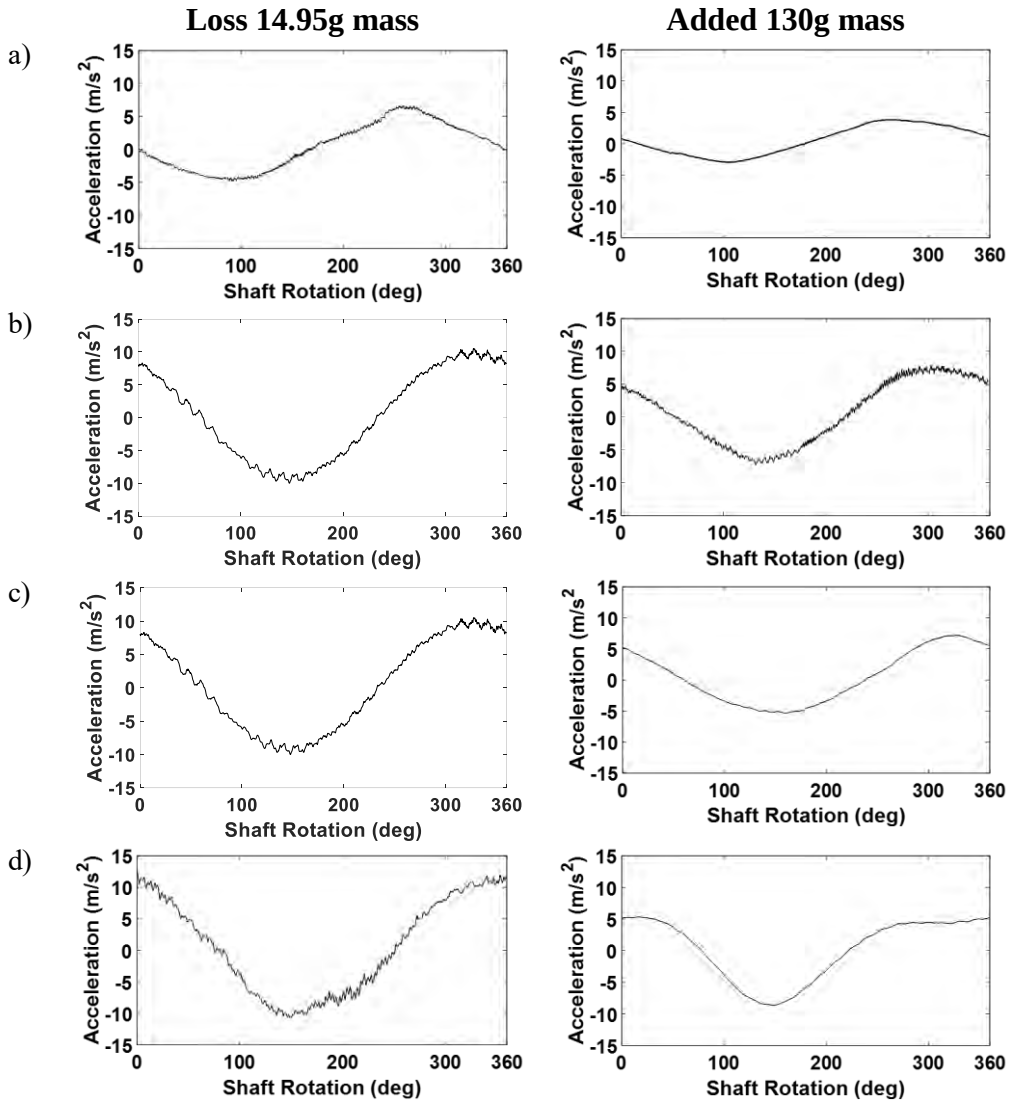

Figure 6.8 Beam in-plane acceleration per one revolution by the piezoelectric sensor on beam tip at 30 rpm, 50 rpm, 100 rpm, and 150 rpm during LMC and AMC

6.2.4 Influence of Add Mass (AM) and Loss Mass (LM) on the beam out-of-plane vibrational modes.

Uncoupled behaviour can be observed between the increase in out-of-plane and in-plane vibrations according to figure 6.9 which shows the two imbalance cases. Maximum strain at 30 rpm is 64.93µstrain at LMC, while it is 73.49 µstrain at AMC, as indicated in figure 6.9a. These amplitudes increase with speed to 76.79 µstrain and 82.71 µstrain at 50 rpm in LMC and AMC respectively - see figure 6.9b. A small decrease in strain amplitude can be seen at 100 rpm in both LMC and AMC to 73.18 µstrain and 81.51 µstrain respectively, However, further increase in out-of-plane strain

can be seen at 150 rpm to 84.19 µstrain in LMC and 114.4 µstrain in AMC. The difference in the strain values can be attributed to the differences between the imbalance masses in both case studies. The fluctuation of the support tower and its effect on beam strain, can be observed in this mode through LMC in figures 5.9b, 5.9c and 5.9d at the end of the rotation, while a small effect on AMC can be seen at 150 rpm in figure 5.9d due to the additional mass which increases the beam inertia.

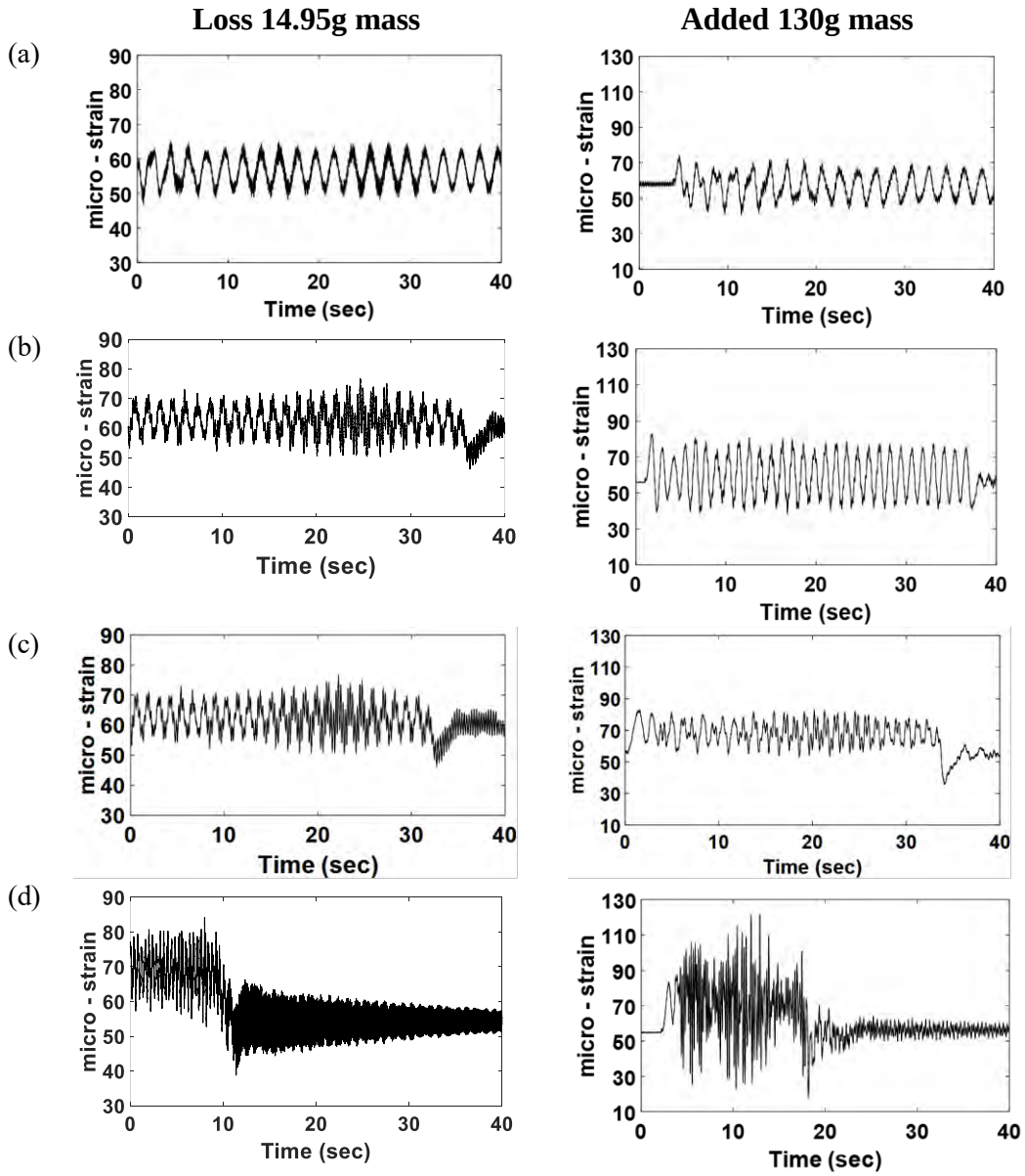

Figure 6. 9 Beam out-of-plane strain measurements during losing 14.95g and added 130g masses at a)30 rpm, b) 50 rpm, c)100 rpm, and d) 150 rpm.

Further, figure 6.10 illustrates beam out-of-plane strain per one revolution during implementing the additional 130g mass and losing 14.95g mass from the rotating beam at the same speeds. At 30 rpm in figure 6.10a, maximum strain amplitude in LMC is

62.22 µstrain, while it rises to 67.29 µstrain in AMC, where the tower effect can further be observed on both amplitudes. Maximum strain amplitudes increase to 68.42 µstrain and 75.23 µstrain at 50 rpm in LMC and AMC respectively, as illustrated in figure 6.10b. That increase in maximum strain at LM decreases to 67.62 µstrain, while it increases to 77.67 µstrain at AMC when speed rises to 100 rpm as in figure 6.10c. Tower vibration have a pronounced effect on AMC through the oscillation in the results. In figure, 6.10d can be recognized the apparent increase in beam out-of-plane strain to 95.38 µstrain in AMC, as well as, high tower vibrations when speed set to 150 rpm, while at LMC it increases to 74.25 µstrain.

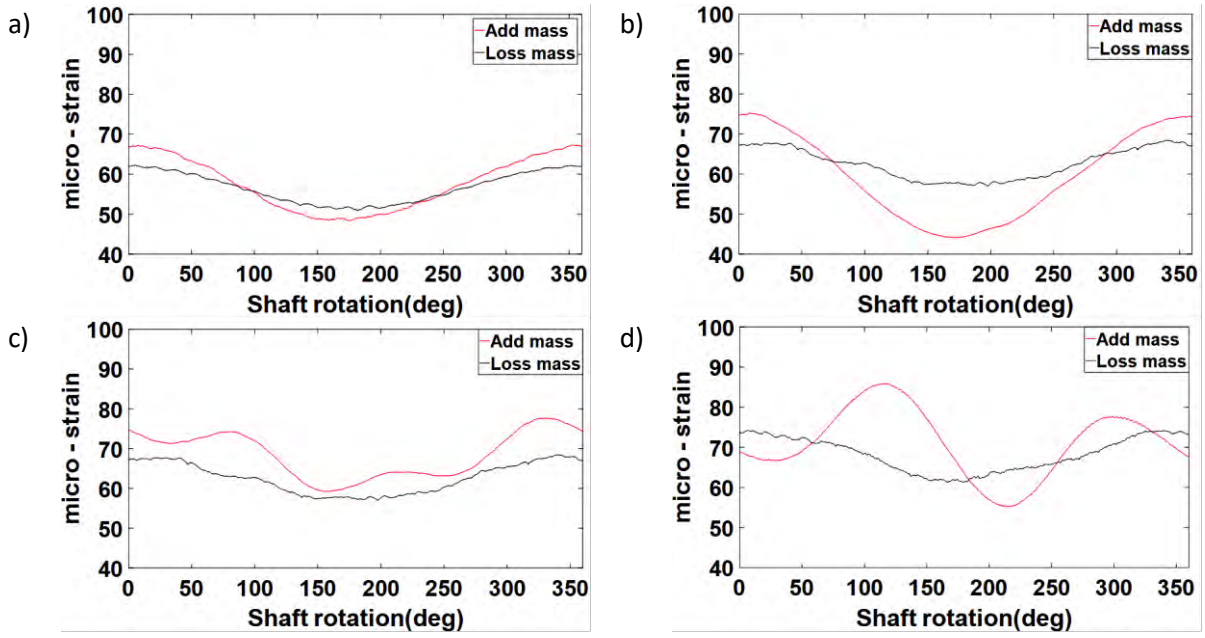

Figure 6. 10 Out-of-plane beam strain measurements per one revolution with two case studies of 130g additional mass and 14.95g losing mass from beam 1 at a) 30 rpm, b) 50 rpm, c) 100 rpm, and e) 150 rpm.

Additionally, figure 6.11 shows maximum amplitudes of beam out-of-plane strain per one revolution shown in figure 6.10 for both LMC and AMC. The AMC strain amplitudes are higher than LMC for all the rotating speeds, with the maximum difference between the values being 21.13 µstrain which occurs at 150 rpm where high strain amplitude has been identified with AMC. However the minimum difference of 5.03 µstrain can be noted at 30 rpm.

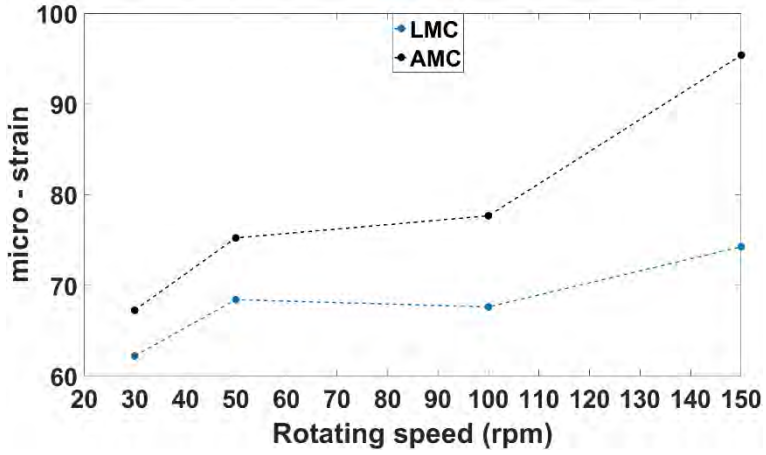

Figure 6. 11 Maximum beam out-of-plane strain amplitudes per one revolution during both losing 14.95g and adding 130g masses in the beam at speeds 30 rpm, 50 rpm, 100 rpm, and 150 rpm.

6.2.5 Influence of Add Mass (AMC) and Loss Mass (LMC) on the tower vibrations

The supporting tower was affected by the imbalance of forces due to AMC and LMC. Furthermore, unstable rotation due to lack of or increase in the rotary inertia, can increase tower vibrations in multiple directions due to the coupling with the rotor beam. Figure 6.12 shows tower vibration amplitudes in the X, Y, and Z directions at speeds of 30 rpm, and 50 rpm during the AMC and LMC faults. At 30 rpm, the tower experienced an increase in vibration during the imbalance condition towards the X-direction showing coupling with axial and in-plane beam vibrations. Maximum acceleration amplitude was seen for the AMC of 1.04 m/s^2 in the X-direction, while 0.469 m/s^2 and 0.506 m/s^2 were measured in the Y and Z-directions. The LMC showed lower acceleration amplitudes, 0.711 m/s^2 in the vertical (X) direction, 0.305 m/s^2 in the front (Y) direction and 0.467 m/s^2 in the lateral (Z) direction. These results showed that losing mass from the rotor blade leads to decreases in dynamic bending due to the blade length decrease, despite the imbalance effect, on the tower fluctuation.

The second speed in figure 6.12 is 50 rpm, where the tower acceleration amplitude in the X-direction for the AMC (0.983 m/s^2) was close to the LMC (0.982 m/s^2) result. The same affect was seen for the Y-direction (AMC=0.412 m/s^2 and LMC=0.453 m/s^2). For the lateral (Z) direction, AMC (0.776 m/s^2) was higher than LMC (0.54

m/s^2) due to both imbalance cases having a direct effect on the tower when the speed increases.

In order to achieve a comprehensive understanding, the rotor speed was further raised to 100 rpm with resulting tower accelerations shown in figure 6.12. It should be noted that spikes in accelerations were in all directions with AMC (at 4.58 sec), resulting in high fluctuation in the Y and Z directions at the start of the test. The cause of the spikes in acceleration was unknown, but its response in all directions is significant as it showed the close vibration coupling that often occurs in the turbine systems. Whereas lower tower vibration can be identified with the LMC, acceleration spikes were also noted in the three directions, though particularly in the X-direction.

Further, tower vibration based on acceleration amplitude rises when the rotor speed increases to 150 rpm in AMC, where the acceleration amplitude increased to 7.29 m/s^2 in the Y-direction at 3.75 sec, with X-direction results of 2.0 m/s^2 and 2.17 m/s^2 for the Z-direction at the same time, as shown in figure 6.13. Additionally, vibration increases can further be seen in the Z-direction (maximum amplitude of 4.89 m/s^2), where the relatively high speed with imbalance condition leads to increase in tower fluctuations, as the Z-direction tower vibration couples with the axial and in-plane beam vibrations.

Speed	Condition	X	Y	Z
30 rpm	Add mass	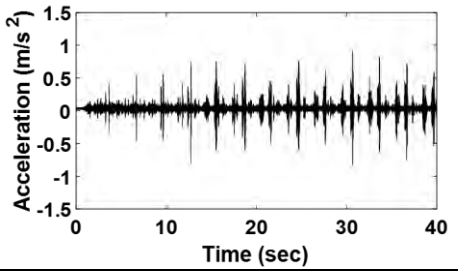	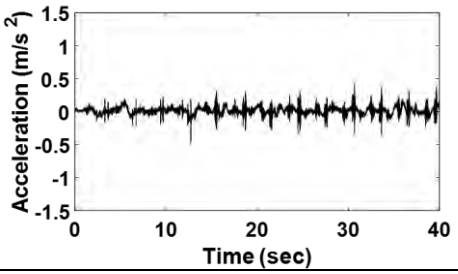	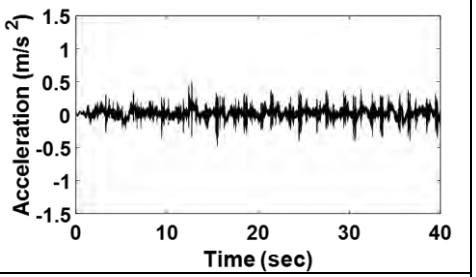
	Loss mass	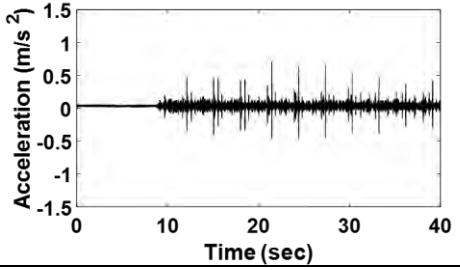	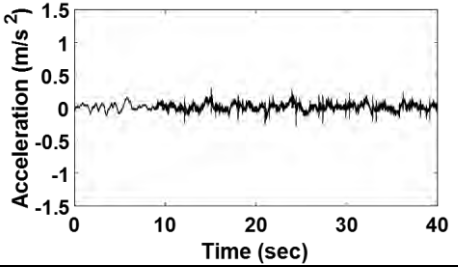	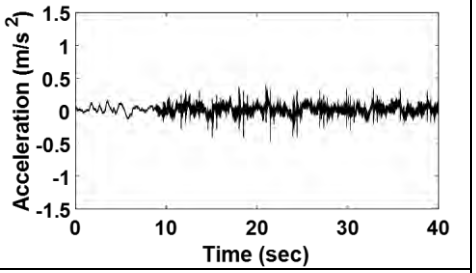
50 rpm	Add mass	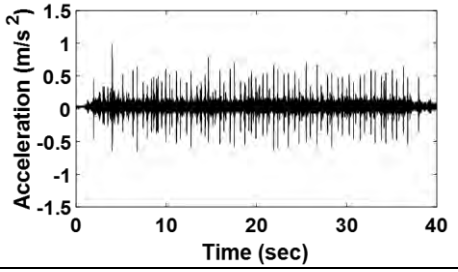	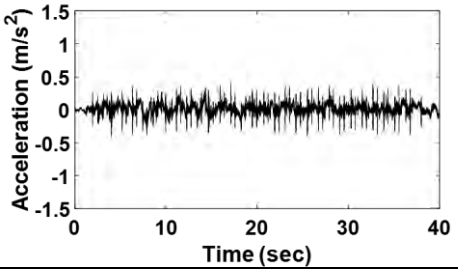	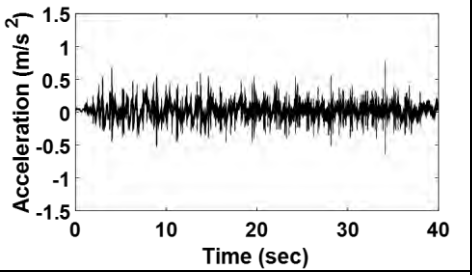
	Loss mass	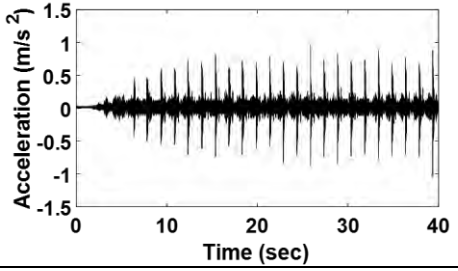	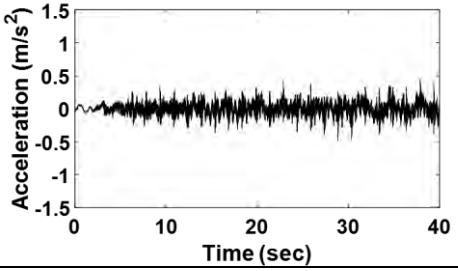	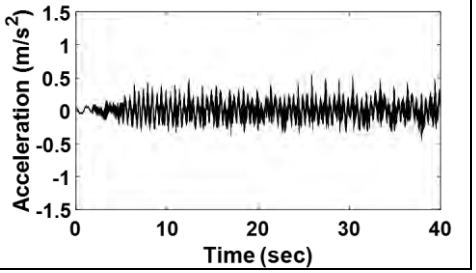

Figure 6. 12 Tower acceleration at X, Y, and Y directions, at 30 rpm during LMC and AMC.

Speed	Condition	X	Y	Z
100 rpm	Add mass	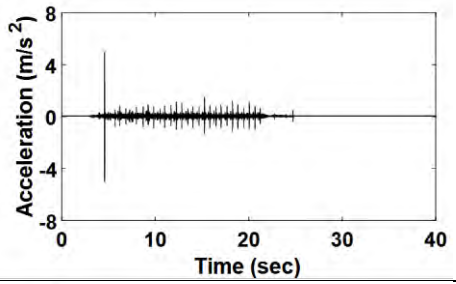	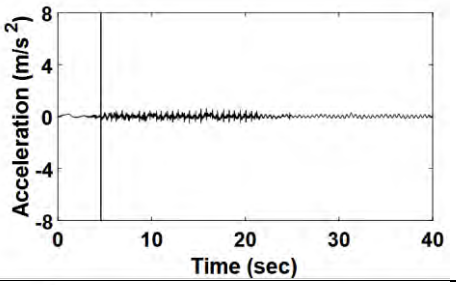	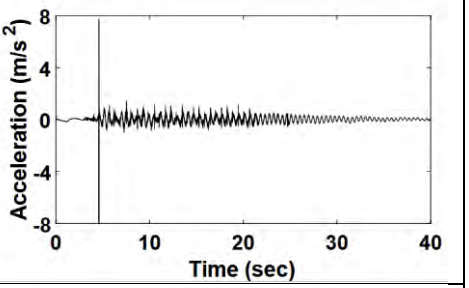
	Loss mass	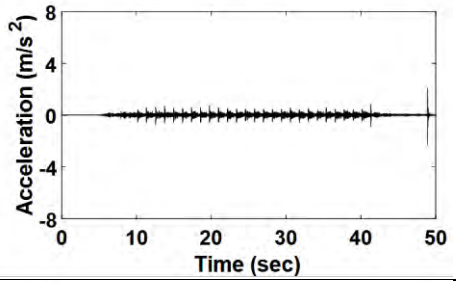	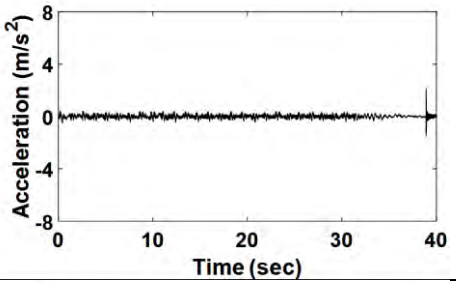	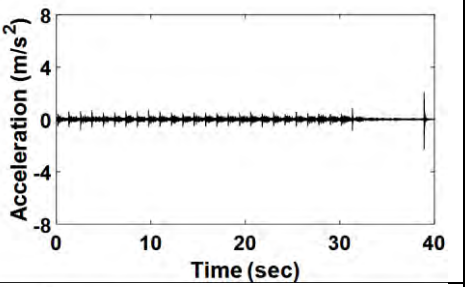
150 rpm	Add mass	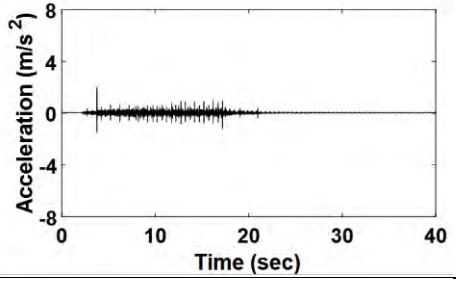	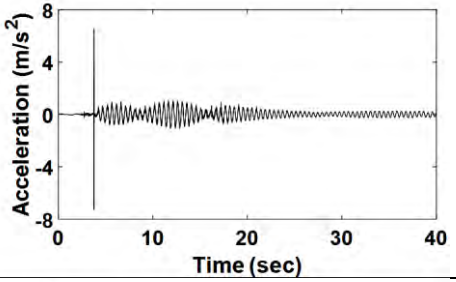	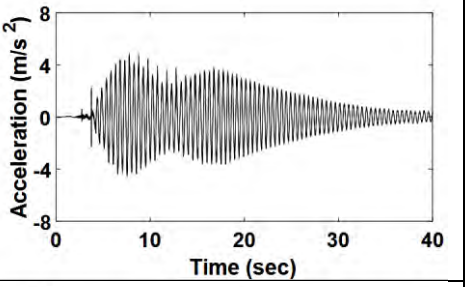
	Loss mass	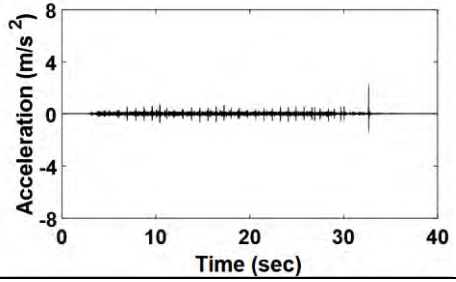	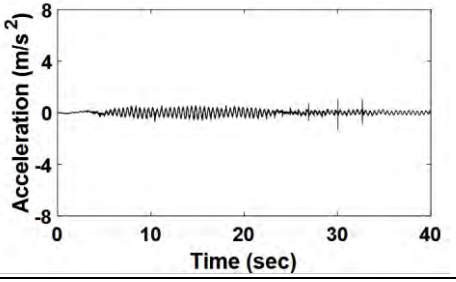	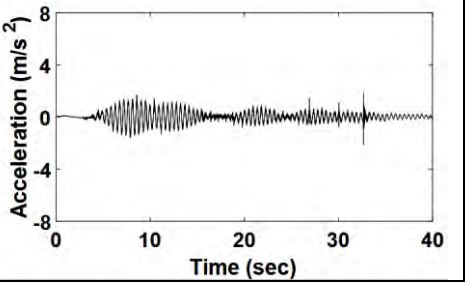

Figure 6. 13 Tower acceleration at X, Y, and Y directions, at 100 rpm and 150 rpm during LMC and AMC.

6.2.6 Influence of Add Mass (AMC) and Loss Mass (LMC) on the drive shaft vibration response

The main rotating shaft was predominantly affected by imbalance effect due to coupling with the rotor beam. Figure 6.14 shows the shaft displacement measured by laser sensors positioned at axis1during rotation with AMC and LMC across the range of rotating speeds. Maximum dynamic displacement of the rotor shaft during AMC was 720 microns at 150 rpm in figure 6.14d, while minimum shaft displacement was 610 microns at 30 rpm in figure 6.13a. However, maximum dynamic displacement on LMC was 690 microns at 150 rpm (figure 6.14d) and minimum shaft displacement was 600 microns at 30 rpm (figure 6.13a).

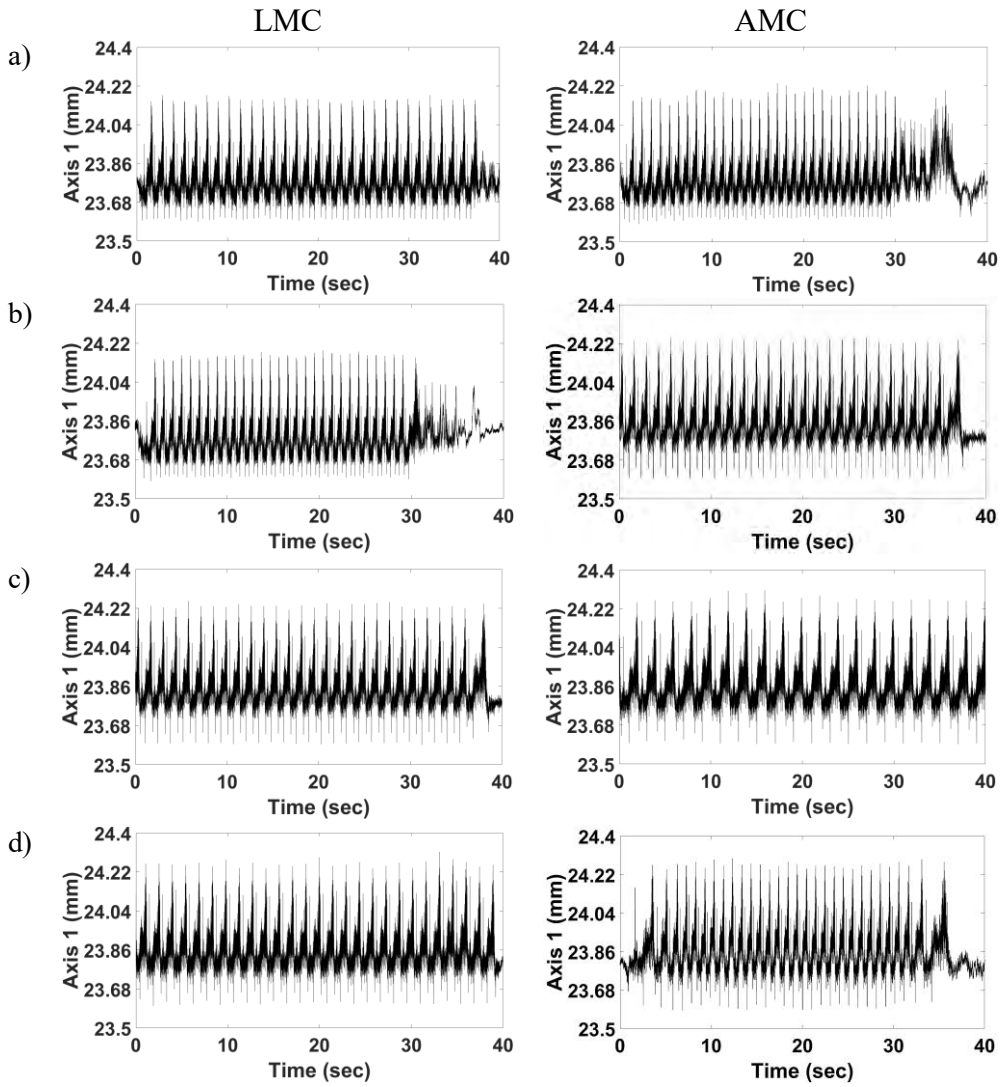

Figure 6. 14 Shaft displacement measured by laser sensor located at axis1 during both LMC and AMC at a) 30 rpm, b)50 rpm, c)100 rpm, and d) 150 rpm

To identify the differences between the maximum shaft bending displacements at both AMC and LMC, figure 6.15 illustrates the maximum shaft displacements in both imbalance cases. Increase in shaft bending occurred with the added imbalance mass at the rotor shaft tip with speed increase, whereas different behaviour can be observed when losing mass from the rotor beam at different rotor speeds. The maximum difference was 120 microns at 30 rpm.

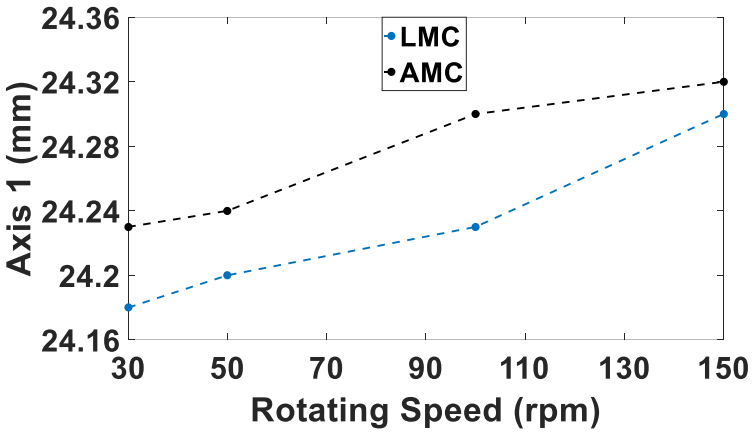

Figure 6. 15 Maximum dynamic displacements of the rotor shaft at AMC and LMC for the certain speed range measured by laser1.

Moving on to bending displacement of the rotor shaft at axis2, figure 6.16 shows the rotor shaft dynamic bending according to axis2 during both imbalance case studies, namely AMC and LMC at 30rpm,50 rpm,100 rpm, and 150 rpm. The data collected from the laser sensor located in, axis2 indicates that the bending in this direction is less than towards axis 1. The maximum bending at AMC was 240 microns at 30 rpm shown in figure 6.15a, while the minimum shaft displacement of 200 microns occurred at 50 rpm, shown in figure 6.16b. At LMC, maximum rotor bending of 210 microns occurs at 30 rpm as shown in figure 6.16a, whereas 180 microns is the minimum shaft bending which occurs at 50 rpm. It can be observed that minimum rotor dynamic bending at axis 2 occurs at 50 rpm for both unbalance events with different amplitudes. Additionally, maximum rotor dynamic bending occurred at axis 1 at the maximum applied speed (150 rpm), while, minimum shaft displacement occurs at the minimum speed. The significant point to note is that the beam vibration increased coupling in the in-plane direction as the speed increases, hence leading to increased rotor shaft displacement fluctuations.

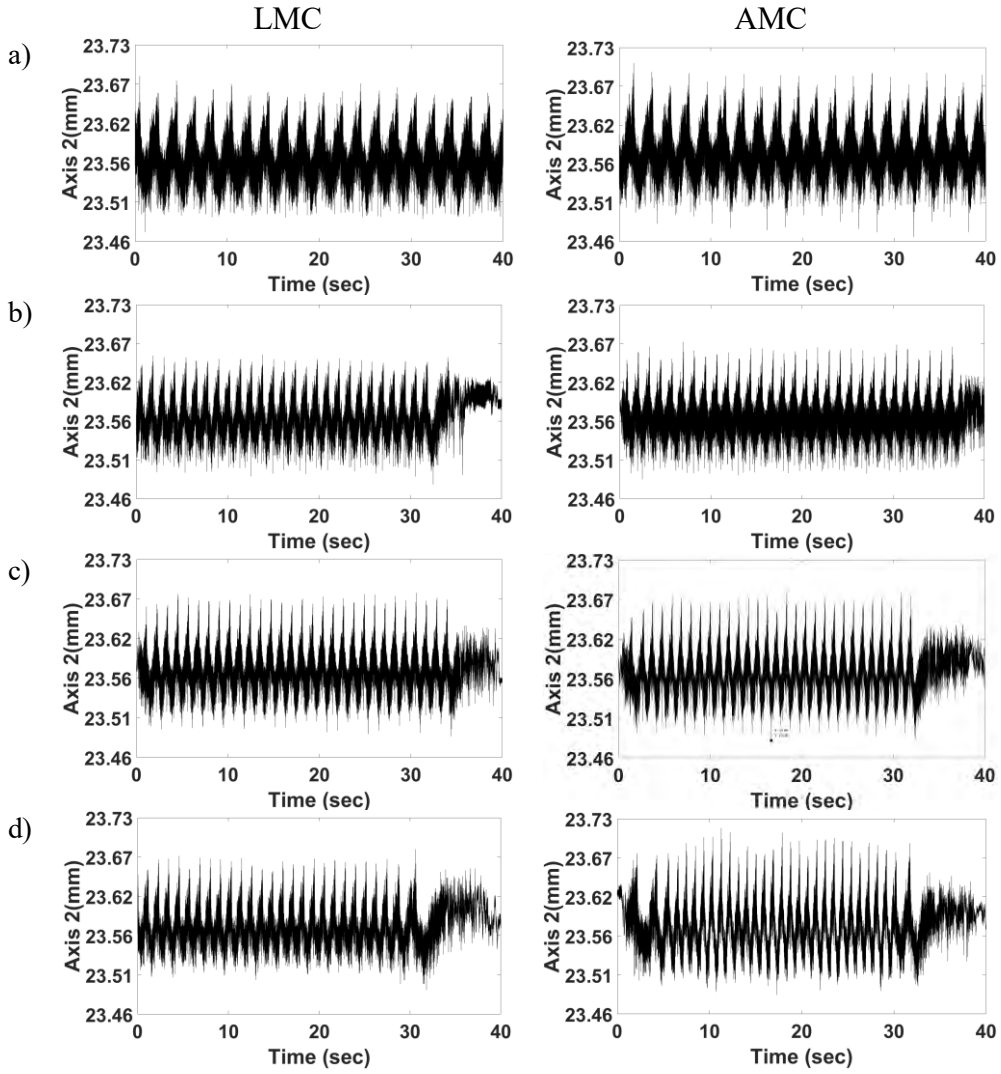

Figure 6. 16 Raw signals of shaft displacement measured by laser sensor located at axis2 during both LMC and AMC at a) 30 rpm, b)50 rpm, c)100 rpm, and d) 150 rpm.

To further analyse maximum shaft dynamic bending displacement corresponding to rotor speed at both AMC and LMC, figure 6.17 provides the variation of maximum shaft displacement for both imbalance cases as rotor speed increases. The maximum difference of a pronounced 30 microns occurred at 150rpm.

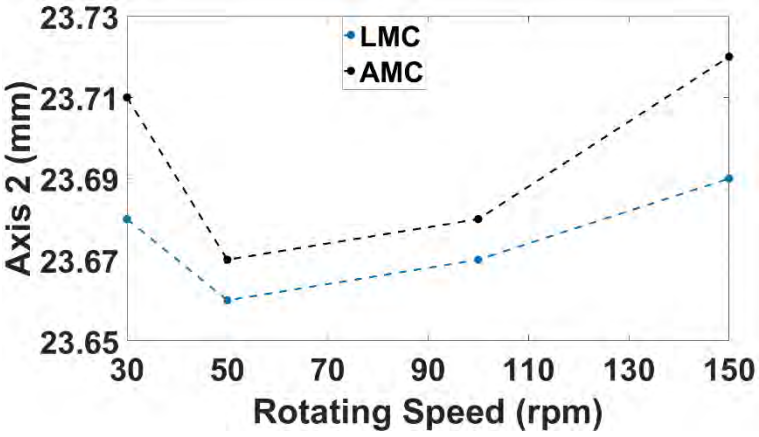

Figure 6. 17 Maximum rotor shaft displacements at both AMC and LMC corresponding to the rotor speeds measured by laser2.

Figure 6.18 identifies the average bending of the rotor shaft per one revolution during AMC and LMC towards axis1 at different speeds. Figure 6.18a shows that the average maximum bending at 30 rpm is 210 microns on AMC, while the average maximum bending on LMC is 209 microns at the same speed. However, at 50 rpm the bending of the shaft is decreased to 180 microns on AMC even with the increased centrifugal forces. Conversely, at LMC maximum bending increases to 215 microns at 50 rpm as can be observed in figure 6.18b.

Moving on to 100 rpm case shows that AMC results in increased rotor shaft bending to 193 microns whereas shaft bending at LMC was 215 microns, as shown in figure 6.17c. Increased bending in the rotor shaft can be seen at 150 rpm on AMC to 250 microns, whereas the increase in shaft bending reaches 222 microns on LMC, as seen in figure 6.18d. The difference between both imbalance cases is attributed to the increase of the rotary inertia and rotor beam length which affected the rotor shaft bending displacements.

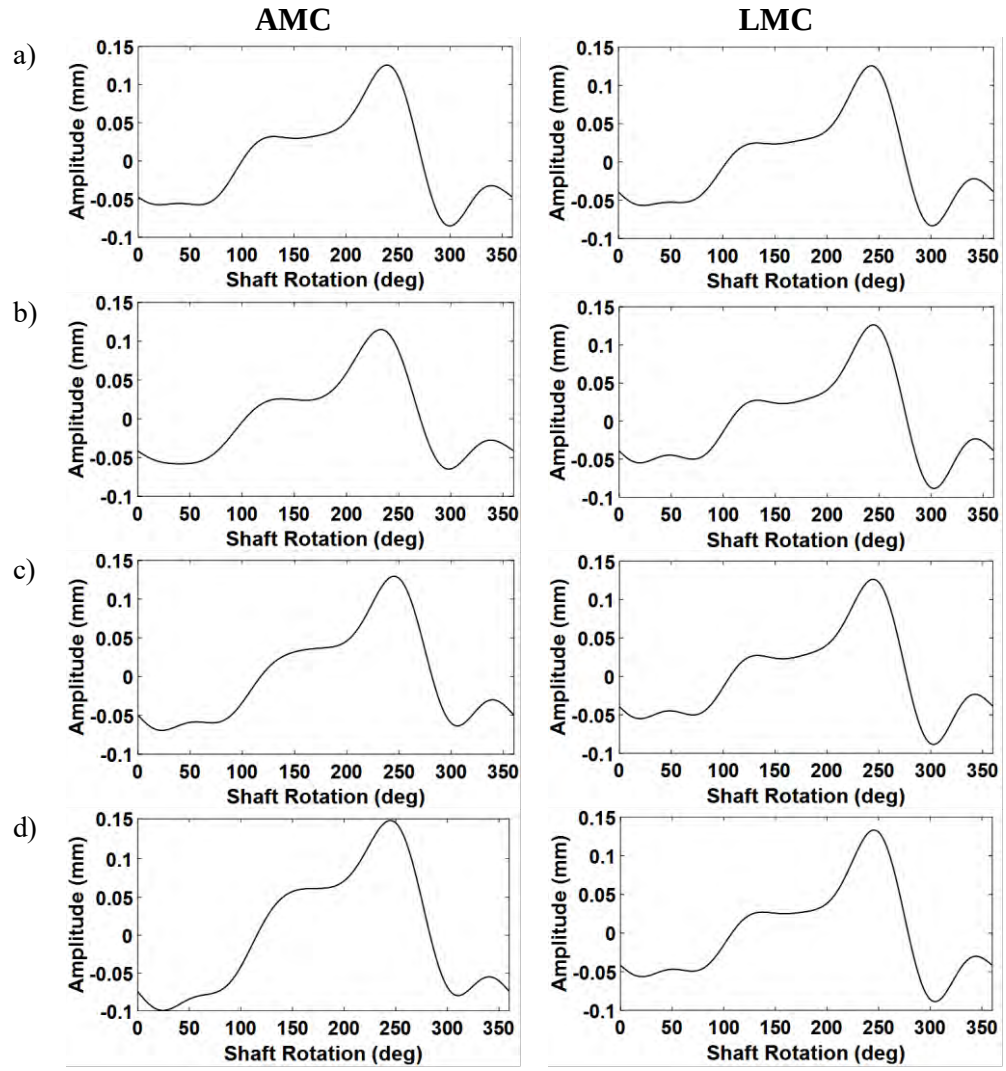

Figure 6. 18 Shaft displacement per one revolution towards axis1 during both AMC and LMC at speeds; 30 rpm, 50 rpm, 100 rpm, and 150 rpm.

The rotor shaft has further bending on axis2 as shown in figure 6.19 which depicts the shaft displacement per one revolution on both AMC and LMC at speeds of 30 rpm, 50 rpm, 100 rpm, and 150 rpm. According to the laser signal located at axis2, shaft displacements on both imbalances cases were less than the displacements at axis1. The maximum shaft bending of 153 microns occurs at 150 rpm during LMC as shown in figure 6.19d, whereas minimum bending amplitude of 55 microns occurs at 50 rpm on AMC as seen in figure 6.18b. At AMC, shaft bending decreases from 80 microns at 30 rpm to 55 microns at 50 rpm, while at LMC the bending further decreases from 78 microns at 30 rpm to 70 microns at 50 rpm, as shown in figure 6.18b. Moving on to 100 rpm case, shaft bending increases to 80 microns on LMC, whereas the bending reaches 90 microns on AMC. Increasing rotor speed to 150 rpm leads to further

increase in shaft bending due to the increased imbalance forces, which can be observed on both AMC and LMC amplitudes.

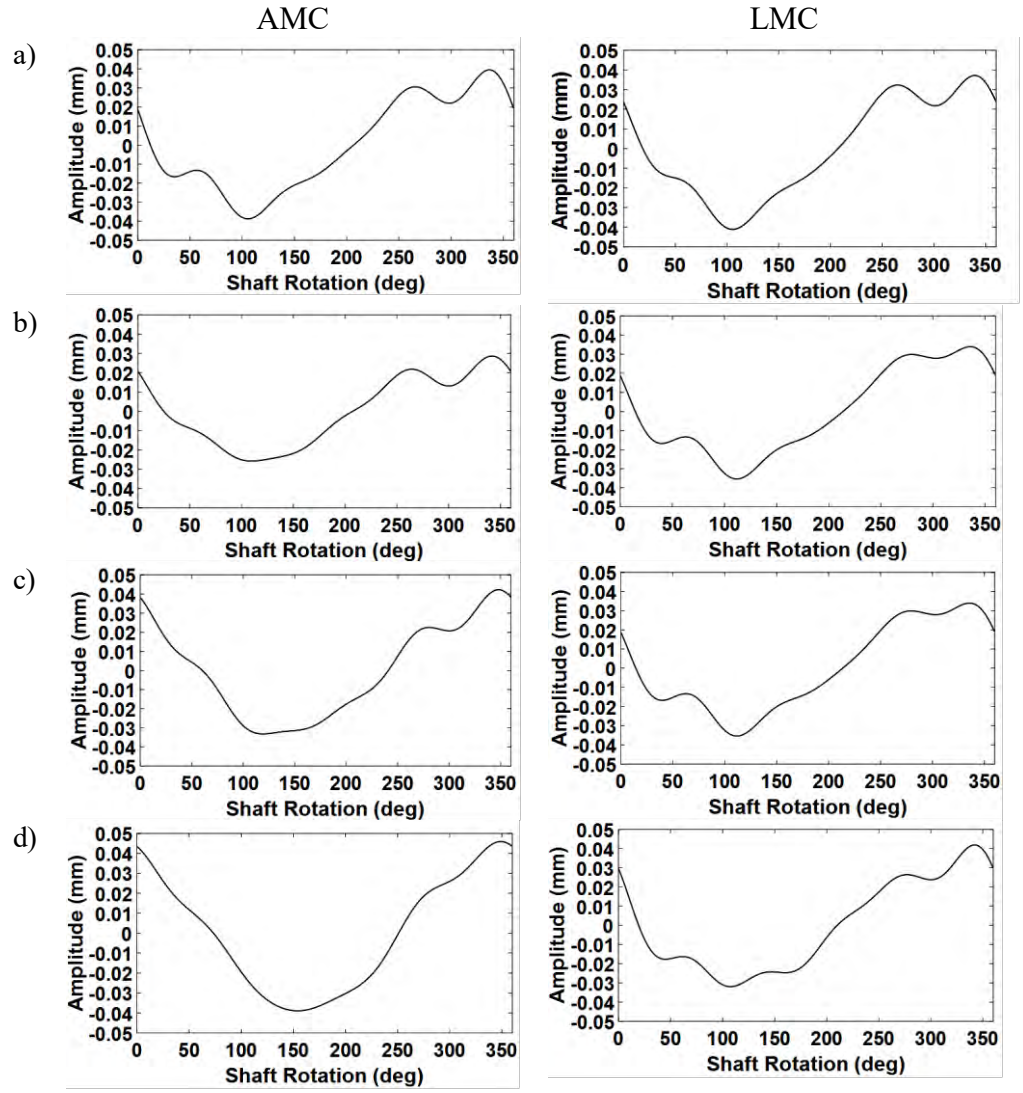

Figure 6.19 Shaft displacement per one revolution towards axis2 during AMC and LMC at speeds; 30 rpm, 50 rpm, 100 rpm, and 150 rpm.

Additionally, orbit plots are used to indicate shaft centreline motion during the test rig operation. Both AMC and LMC imbalance conditions can be investigated for the various rotating speeds. Figure 6.20 illustrates a comparison between the two imbalance cases at 30 rpm. Here the consecutive inclusion of shaft harmonics 1X, 2X, 3X, 4X and 5X are shown.

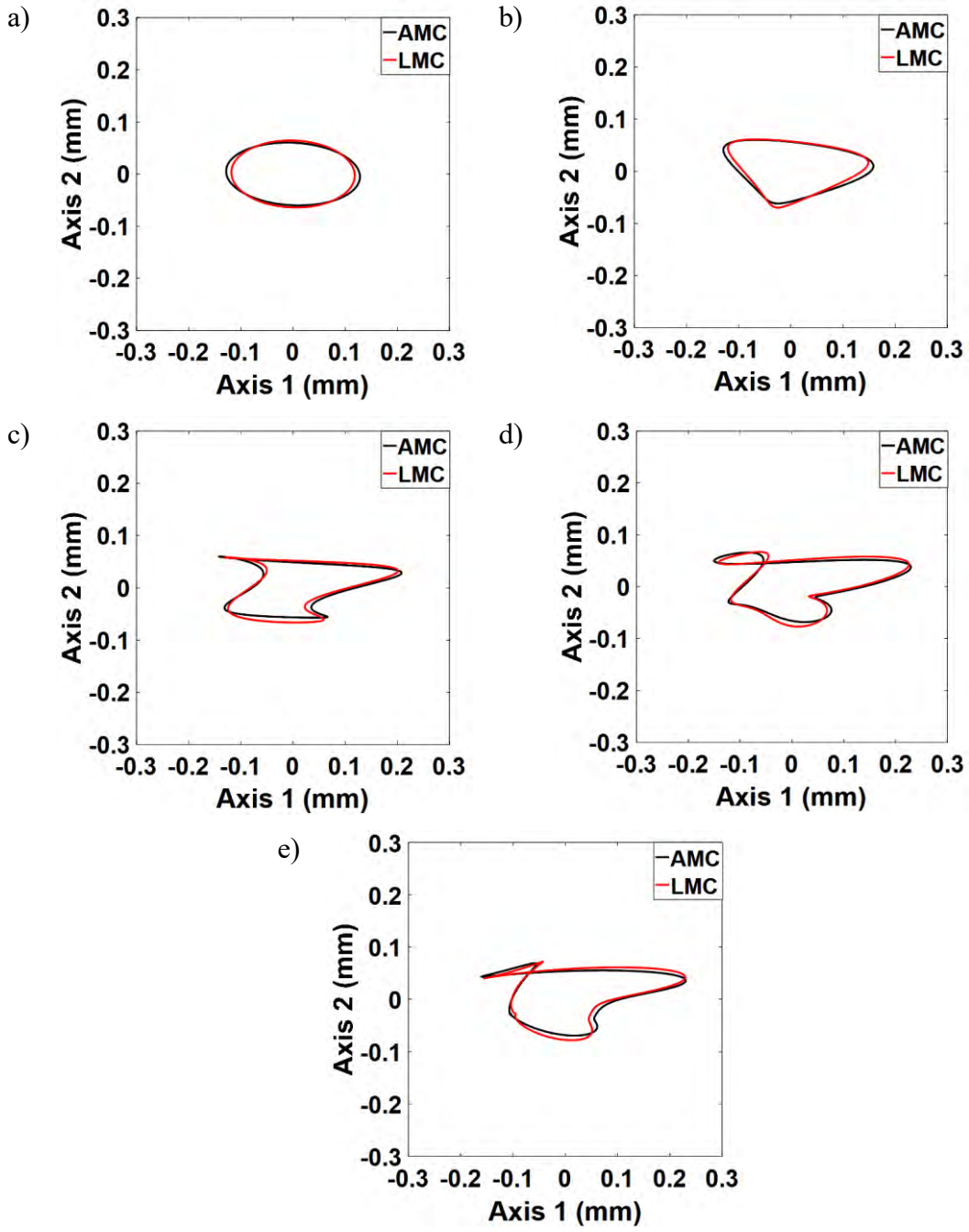

Figure 6. 20 The drive shaft orbit plots of the two imbalance cases AMC and LMC at 30 rpm including harmonics of 1X, 2X, 3X, 4X, and 5X.

Figure 6.21 shows the consecutive orbit plots when the rotor speed rises to 50 rpm. At the increased speed, an increase in orbit extension towards axis 2 can be seen, especially for the LMC. In figures 6.21c and 6.21d (3X and 4X), AMC orbits start to create a different path due to the increase in dynamic vibration which in turn increases the shaft bending.

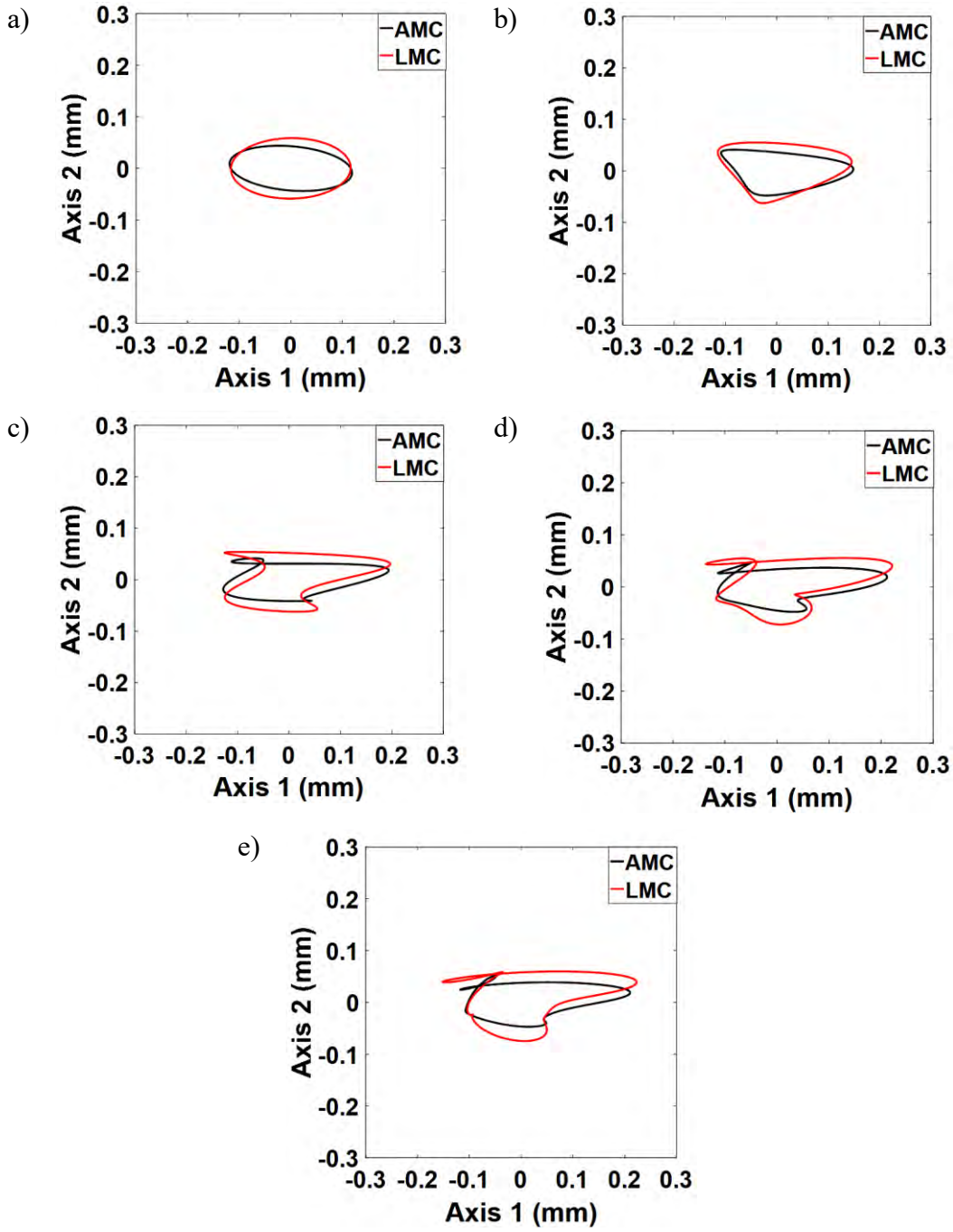

Figure 6. 21 The drive shaft orbit plots of the two imbalance cases AMC and LMC at 50 rpm of 1X, 2X, 3X, 4X, and 5X.

Figure 6.22 shows a further increase in AMC oval extension as the speed increases at 100 rpm. Additionally, a pronounced shifting along a 45 degree axis occurs in figures 6.22a and 6.22b namely in 1X and 2X. The differences between AMC and LMC orbits can clearly be seen in the 5X orbits, as shown in figure 6.22e.

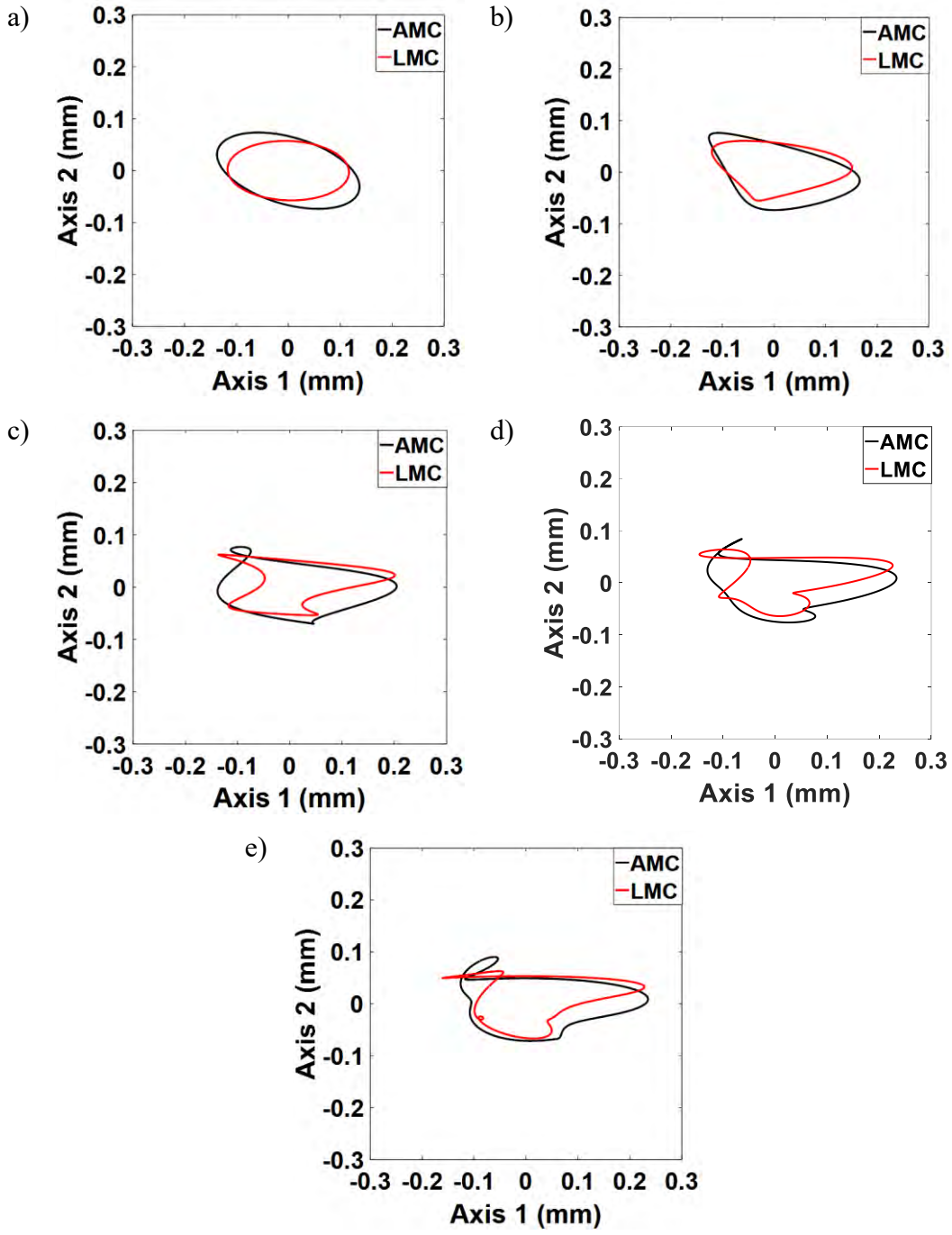

Figure 6. 22 The drive shaft orbit plots of the two imbalance cases AMC and LMC at 100 rpm of 1X, 2X, 3X, 4X, and 5X.

Furthermore, figure 6.23 illustrates the shaft orbits with up to five harmonics during both imbalance cases AMC and LMC at 150 rpm. A pronounced shifting to the 45 degree axis can be observed in all harmonics, with a different path in AMC, especially in figures 6.23d and 6.23e. This 45 degree shift as speed increases indicates that the dominant shaft orbit motion is actually in the vertical direction, after the 45 degree

orientation of the laser sensors is taken into account, as seen in Chapter 3. The increase in rotor speed leads to an increase in beam dynamic bending with the additional mass which in turn causes an increase in the rotor shaft bending. Tower vibration has the additional effect on the increase in shaft bending, which further increases with increases in rotor speed.

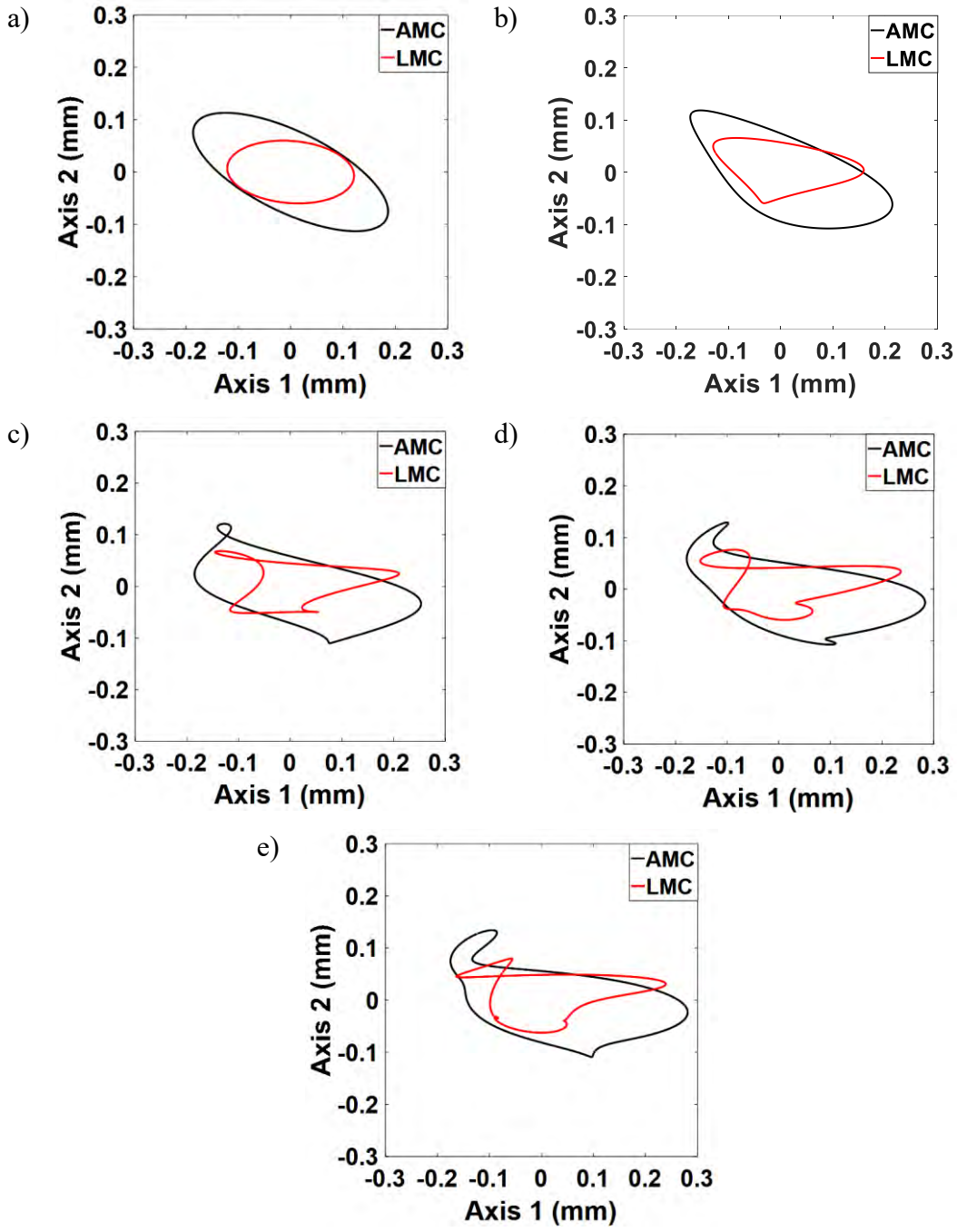

Figure 6.23 The drive shaft orbit plots of the two imbalance cases AMC and LMC at 150 rpm of 1X, 2X, 3X, 4X, and 5X.

Figure 6.24 illustrates the complex frequency spectrum per one revolution obtained from the orbit motion. The DC component of the spectrum is the largest component, which is often zeroed out as shown in figures 6.20 to 6.23. Here the forward shaft whirling can be identified for the two imbalance cases as a function of shaft speed. The results show that the AMC forward whirl component is greater than the LMC component as speed increases.

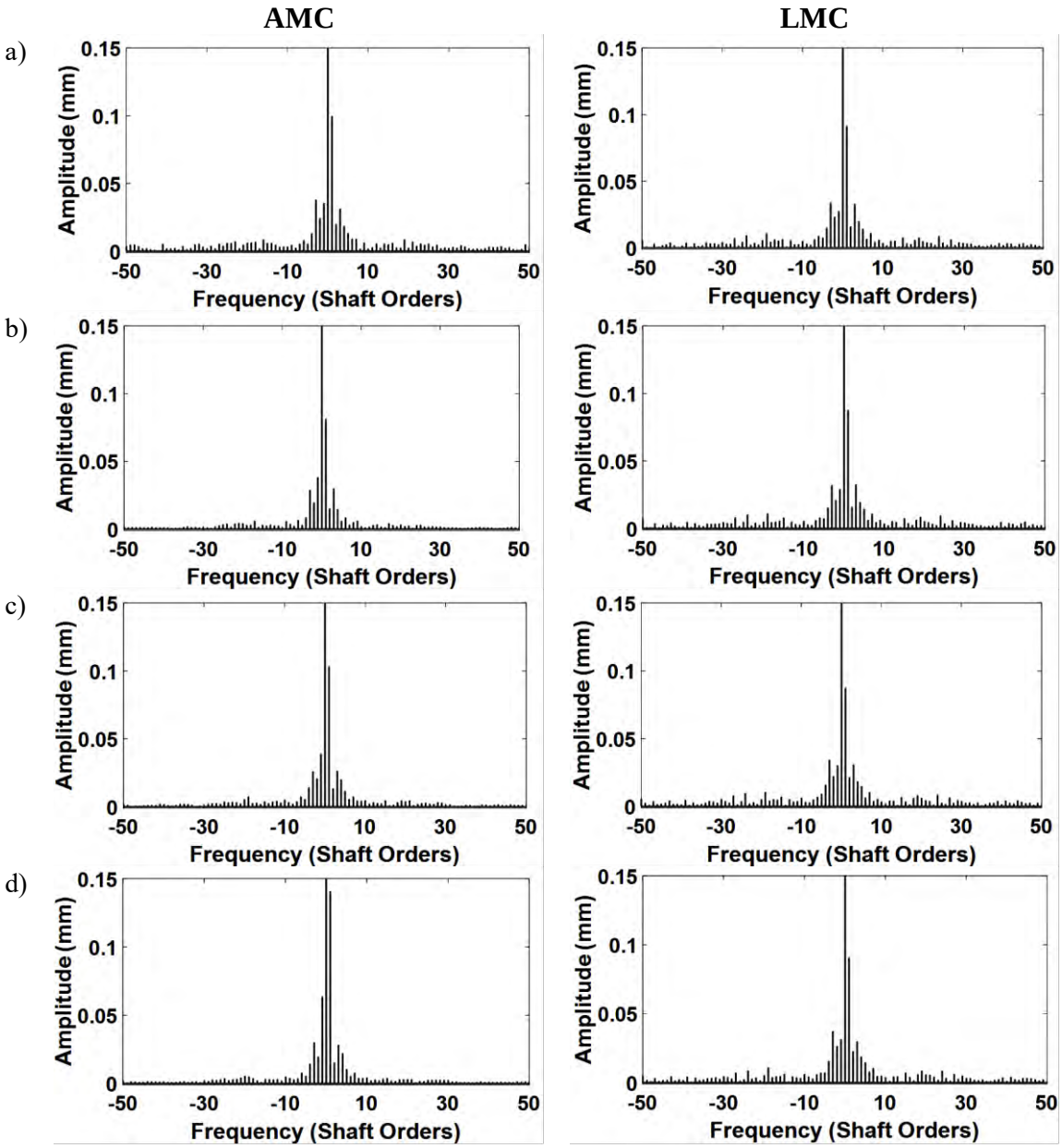

Figure 6. 24 Complex Discrete Fourier Transform of the shaft orders during beam imbalance fault (AMC and LMC) at a) 30 rpm, b)50 rpm, c) 100 rpm, and d) 150 rpm.

The differences between the positive and negative frequencies can obviously be recognized in figure 6.25, which shows the frequency amplitudes on AMC and LMC at the selected speeds.

The increase in 1X shaft order amplitudes on AMC with speed increases is greater than LMC in both positive and negative orders, as in figure 6.25, corresponding to shaft orders in figure 6.24.

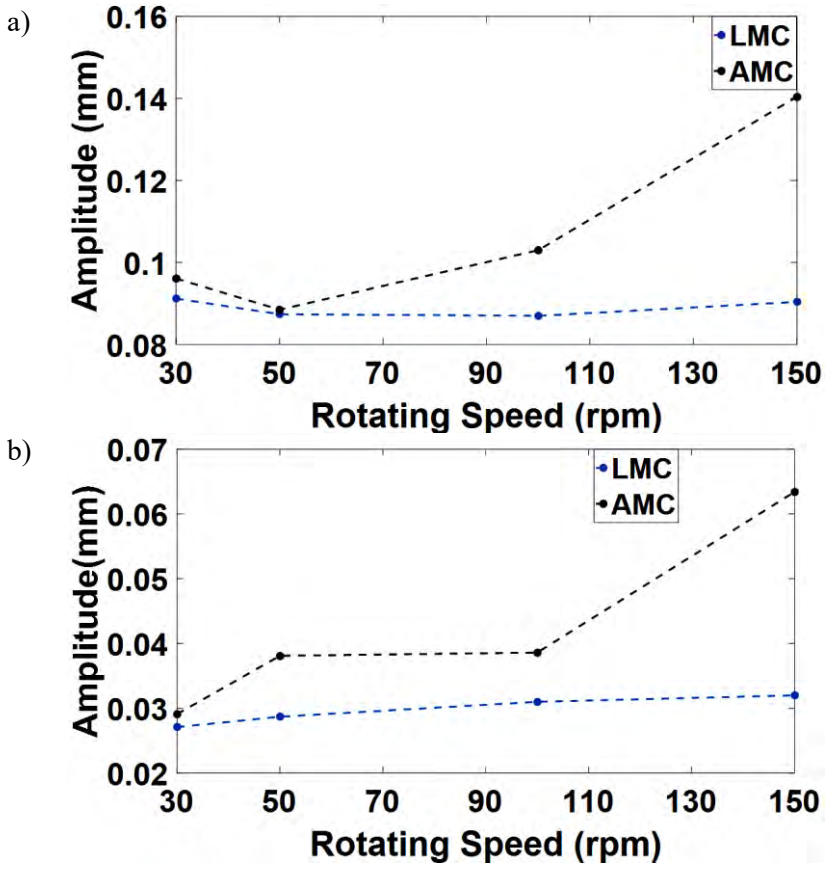

Figure 6. 25 First orders a) positive, and b) negative, during beam faults (AMC and LMC) at 30 rpm, 50 rpm, 100 rpm, and 150 rpm.

6.3 Influence of losing the whole beam on the small-scale wind turbine test rig system dynamic response

A further fault that can be diagnosed during wind turbine operation is the loss of a whole blade from the hub. This was modelled by losing beam 3 from the hub in the current test rig, with one speed of 50 rpm measured to be close to the operational speed of smaller industrial wind turbines and to avoid significant damage to the test rig. Figure 6.26 shows the rotor beam response due to losing one beam from the rotor at 50 rpm. The maximum axial strain vibrations are 35.84 μstrain, while in-plane and out-of-plane strain vibrations were 211.6 μstrain and 67.46 μstrain respectively. Additionally, axial, in-plane and out-of-plane strain per one revolution can further be observed on the right of each raw signal in this figure. Increasing vibration amplitude in all modes can be observed with this experiment comparing with the vibration amplitudes in AMC and LMC.

Adding a mass on the rotor beam, increases centrifugal forces towards the greater mass, and leads to high shaft bending in one direction. It further increases as speed increases due to the increase in imbalance forces. Additionally, losing a beam from the hub leads to non-uniform distribution of the rotary inertia which in turn increases the centrifugal forces and centripetal forces in one direction (towards the greater inertia), hence causing a disorder in the rotation.

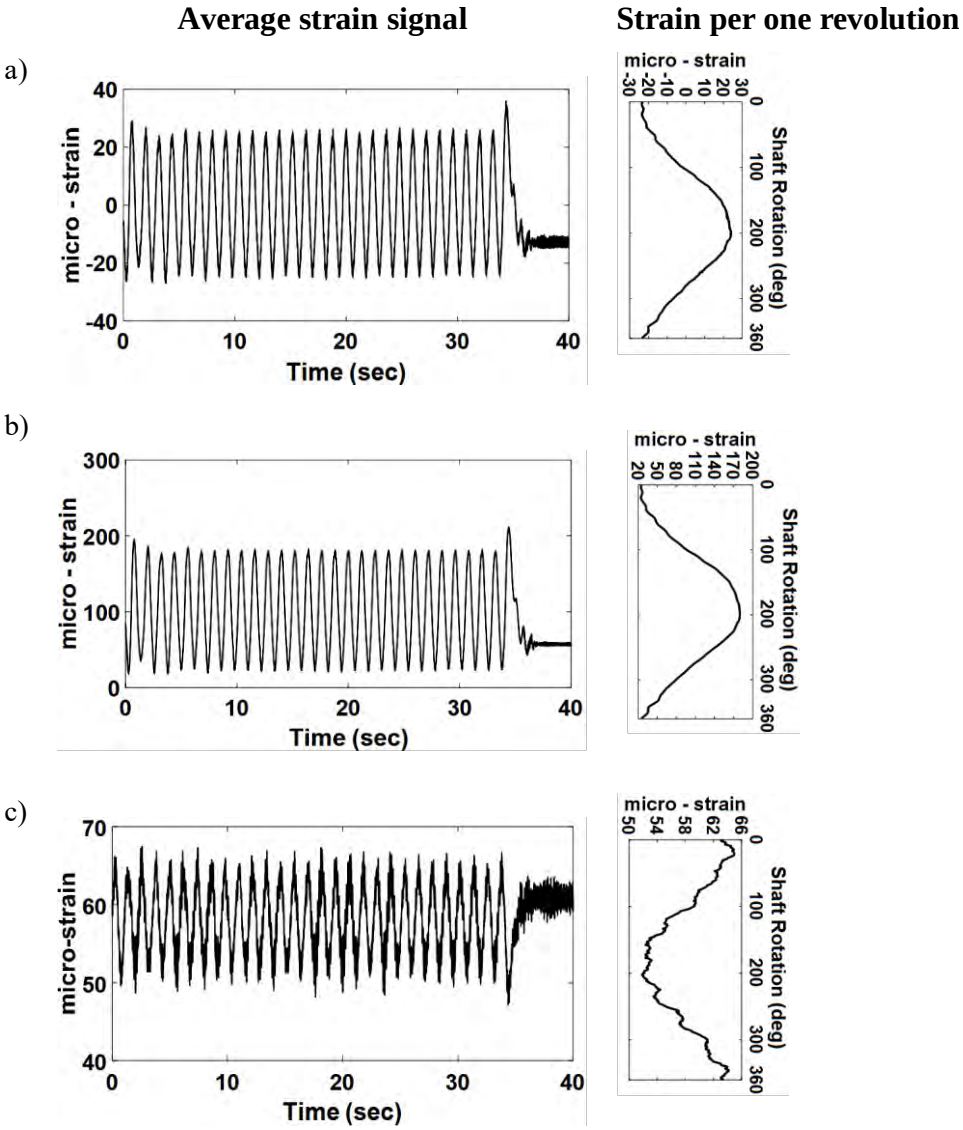

Figure 6. 26 Average beam strain due to losing the whole beam from the rotor at 50 rpm and 40 sec towards; a) axial, b) in-plane, and c) out-of-plane.

The effect of losing a rotating beam can be further identified through monitoring the piezoelectric accelerometer acceleration amplitude, as shown in figure 6.27. This shows a maximum acceleration amplitude of 4.95 m/s^2. The small effect of losing beam3 was due to the small beam inertia 0.067 $Kg.m^2$ in comparison with the whole rotor.

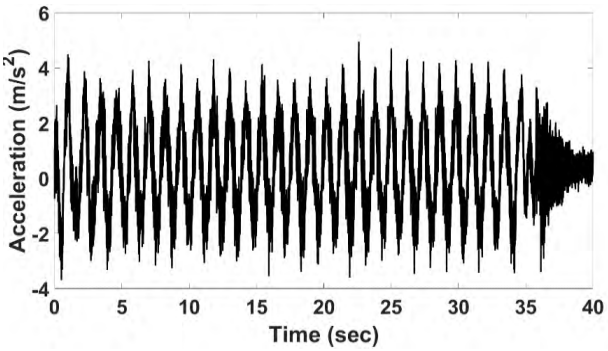

Figure 6. 27 Beam in-plane vibration based on acceleration amplitude measured by the piezoelectric accelerometer.

6.3.1 Influence of losing the whole beam on the drive shaft dynamic bending

The disorder in mass distribution around the hub had an effect on the drive shaft bending during operation as illustrated by figure 6.28. Maximum shaft dynamic bending towards axis1 is 720 microns in figure 6.28a, while it is 250 microns at axis2 in figure 6.28b. Furthermore, bending amplitudes can further be detected in figure 6.29, which illustrates average shaft bending per one revolution at axes 1 and 2. Shaft deflection at axis1 is slightly lower at 218 microns comparable with AMC (maximum shaft bending 250 microns) and LMC (maximum shaft bending 222 microns). The centrifugal and Coriolis forces increase towards beam1 with the increase in rotary inertia, as mentioned before which causes rotation imbalance. Additionally, this affected the servo-motor torque, where damping due to inertia dissimilarity imposed an additional load on the drive motor as well as, high vibration. Additionally, the centripetal force variation increased the required starting torque to reach the desired speed. This difference increases shaft bending towards the bigger inertia, which increases with the increase of speed.

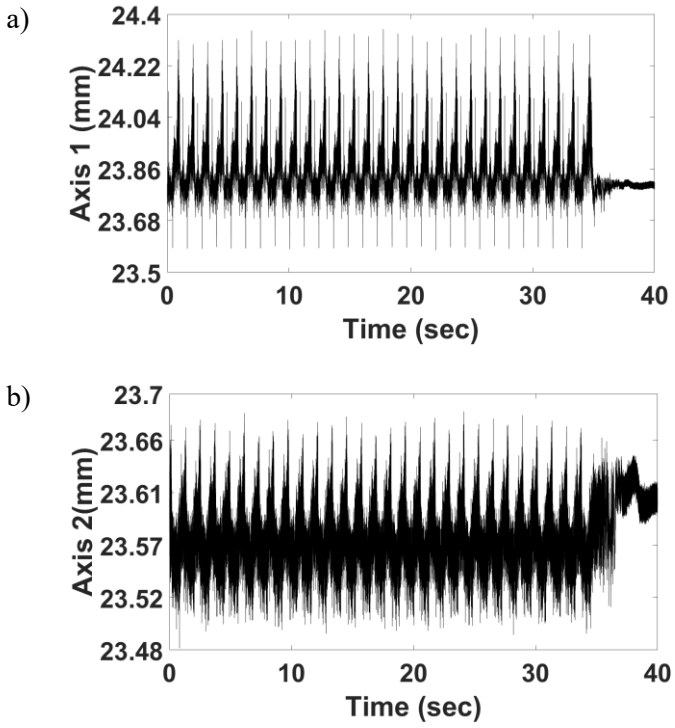

Figure 6. 28 Dynamic shaft displacement measured by laser sensors at 50 rpm during the loss of a whole beam from the rotor.

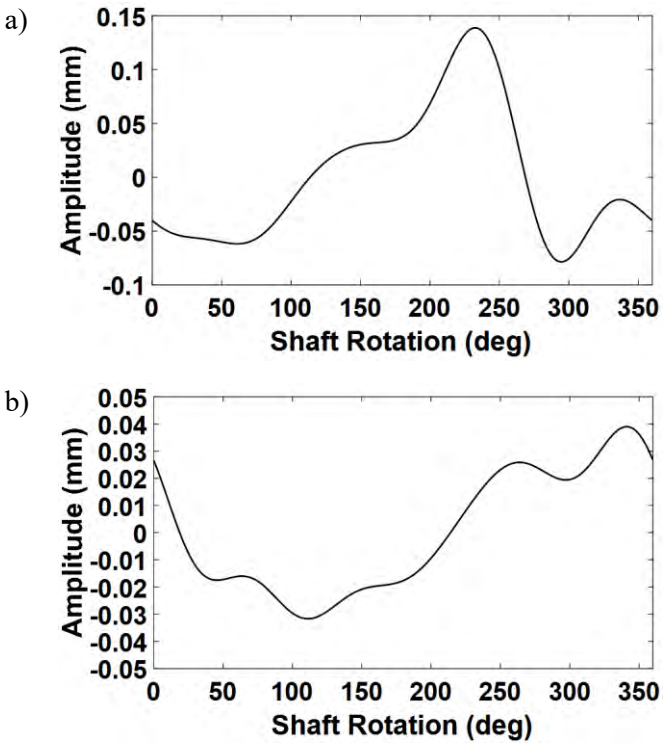

Figure 6. 29 Dynamic average shaft displacement per one revolution at 50 rpm during loss of one rotor beam (beam3) from the hub.

Monitoring the rotor shaft centreline displacement is a further method to understand the nature of faults during the rotation. Figure 6.30 shows shaft centreline displacement at 50 rpm when losing beam3 from the rotor. The predominating feature is the extension on axis1, as well as, shifting the elliptical orbits to the right. This can attributed to increased shaft bending towards the shaft position of greater inertia (maximum displacement of the shaft centreline). After this angle, the shaft tries to revert to its first position, but the centrifugal forces and the greater rotary inertia imposes bending towards the axis2 direction (after 90^{o} from axis1) with a smaller amplitude compared with axis1.

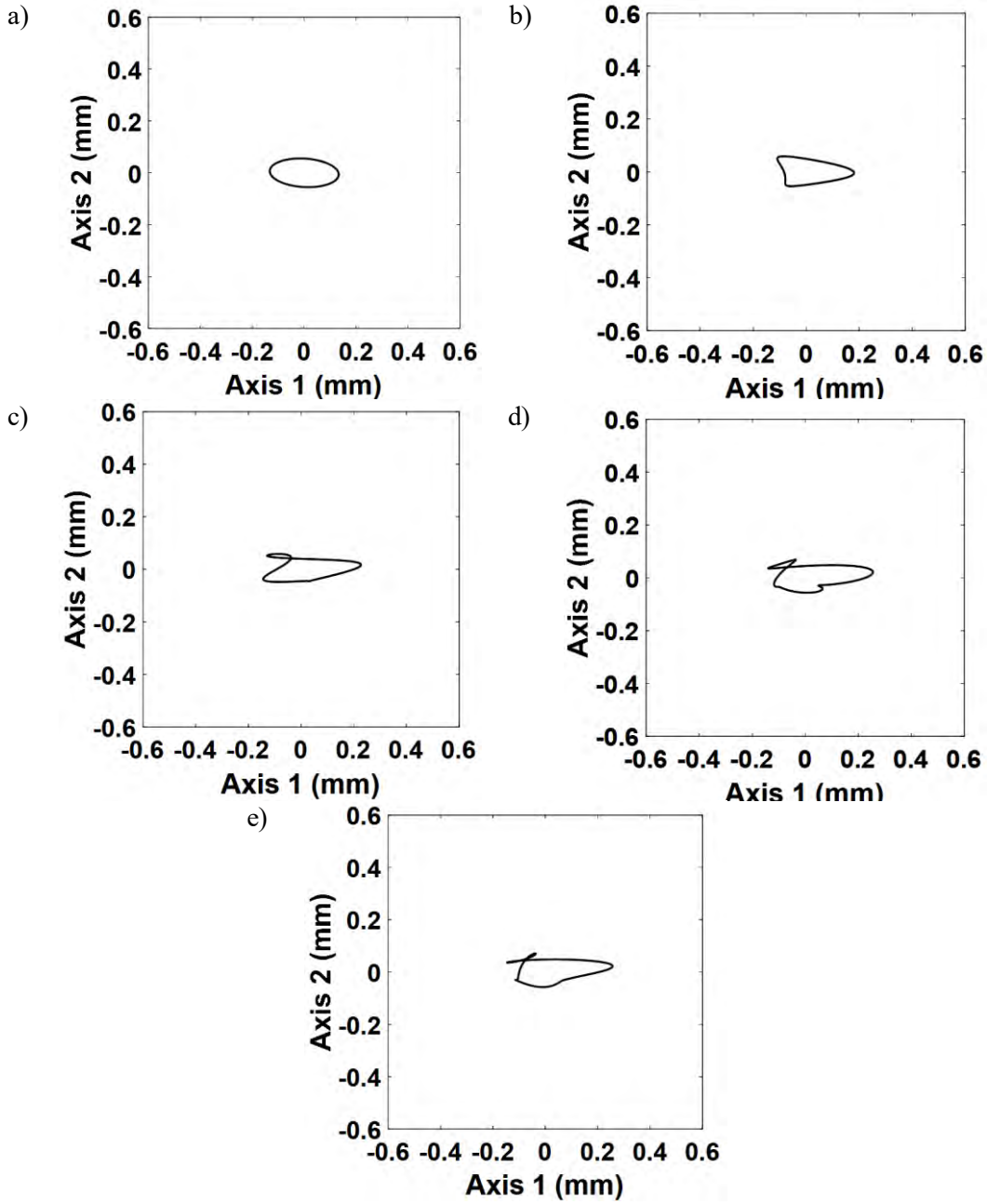

Figure 6. 30 Rotor shaft orbits plots during losing the whole beam from the rotor at 50 a) 1X, b) 2X, c) 3X, d) 4X, e) 5X.

Further, to obtain shaft amplitude at each rotation, figure 6.31 illustrates the shaft amplitude for each shaft order at 50 rpm, when losing one beam. The first shaft order amplitude is 0.0931 mm, while the first negative shaft order amplitude is 0.0389 mm

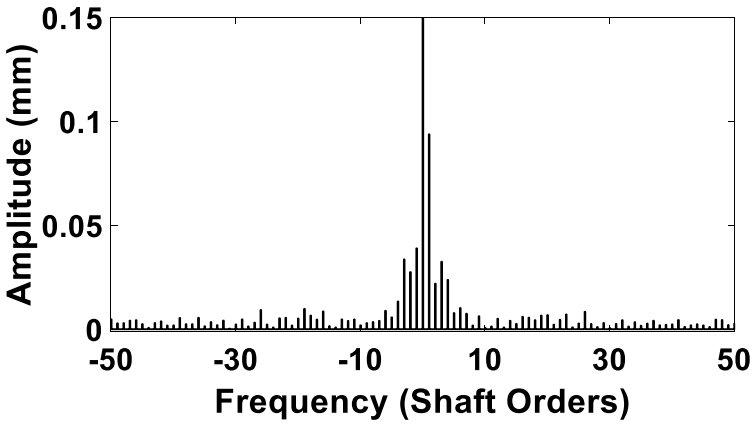

Figure 6. 31 Complex Discrete Fourier Transform of the shaft orders during loss of a whole beam from the rotor at 50 rpm.

6.4 Influence of mass collision on exciting transient vibrations in the rotating beam and the small-scale wind turbine components.

This test has been conducted at 50 rpm as a means of modelling the collision of flying objects with the rotating beam. The significant effect of the collision is the analysis of the consequence after the event, because the colliding bodies can cause defects such as dents after the bending at the collision time, or can lose part of the leading edge of the blade after the strike. For this experiment, a softer impact was investigated by using a 585.92 g mass (rubber and wool) mass to strike the rotating blade at 50 rpm. The flying mass had a velocity towards the rotor beam of 1m/s. At the moment of impact (the rotating beam struck the mass) it impeded the rotation of the beam leading to an increase in blade bending and exciting various blade resonances.

Figure 6.32 illustrates the strain amplitude vibrational response of the rotor beam showing the strike of the 585.92 g mass at 50 rpm. In figure 6.32a, the raw strain signal (on the left side) clearly shows the collision time from the beam axial strain, which increases at 14.8 sec to 537.3 μstrain. The right side from figure 6.32a illustrates the beam axial strain measurement per one revolution (the first peak in the raw strain signal prior to the collision). The bending in the beam span which normally dampens

the rotation leads to an increase in the axial vibration due to increasing Coriolis forces and centrifugal forces which increases closer to the beam tip. The coupling between axial and in-plane vibrations increases the in-plane beam strain to 2950 µstrain at 14.8 sec where the beam continues to vibrate after the collision with high-frequency components, as in figure 6.32b. The impact event has further effect in the out-of-plane direction with maximum strain at the collision time of 1186 µstrain on the compression side. After the collision, the beam continues vibrating for several seconds due to the potential energy acquired from the axial and in-plane vibrations to transform the kinetic energy towards the out-of-plane direction as in figure 6.32c.

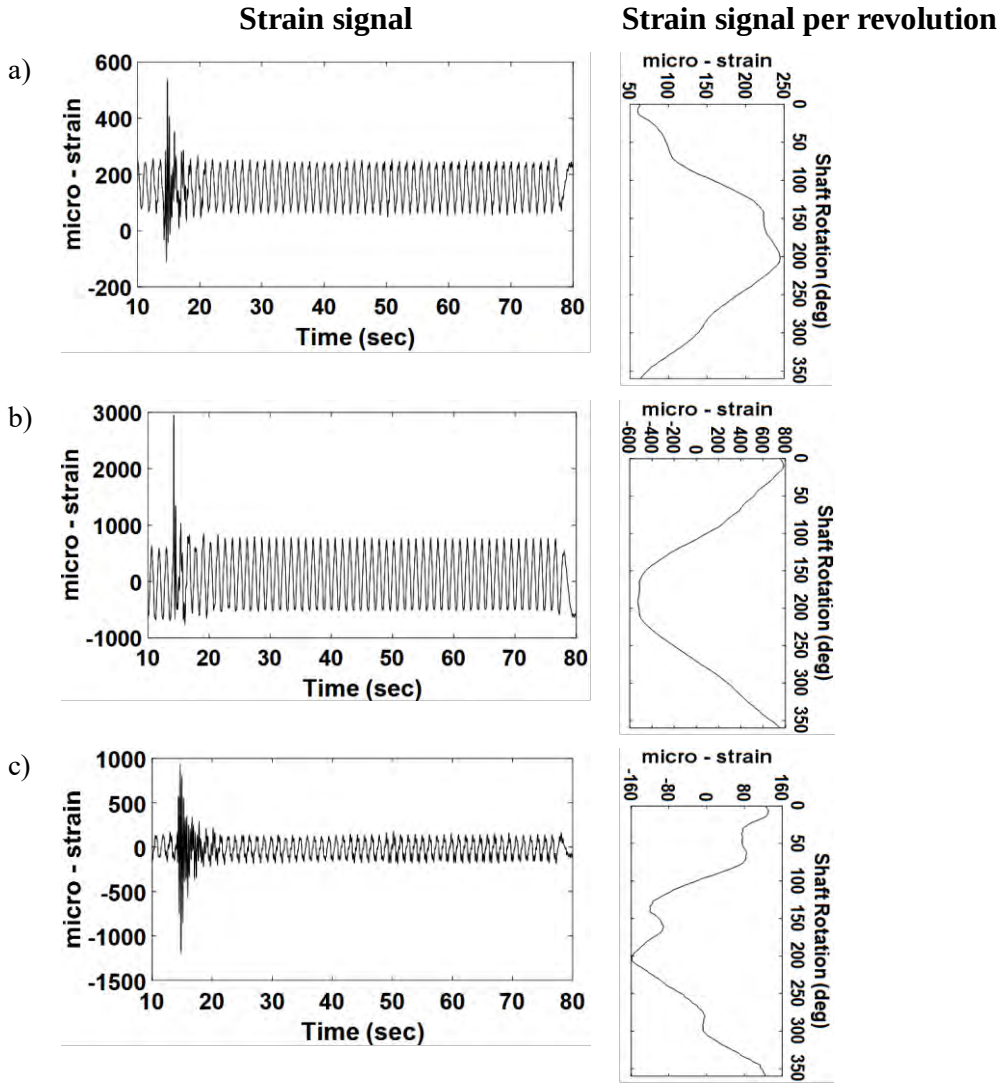

Figure 6. 32 Effect of colliding 585.92gm mass in the rotor beam at 50 rpm a) axial strain, b) in-plane strain, c) out-of-plane strain amplitudes.

6.4.1. Monitoring impact of the transient mass collision with the rotating beam on the piezoelectric accelerometer

A further technique for beam vibration monitoring during the collision event involves detecting the beam acceleration measured by the piezoelectric accelerometer positioned at the beam tip towards the in-plane direction. Figure 6.33 shows that the maximum acceleration amplitude of -307.2 m/s^2 occurred during the impact event at 14.8 sec.

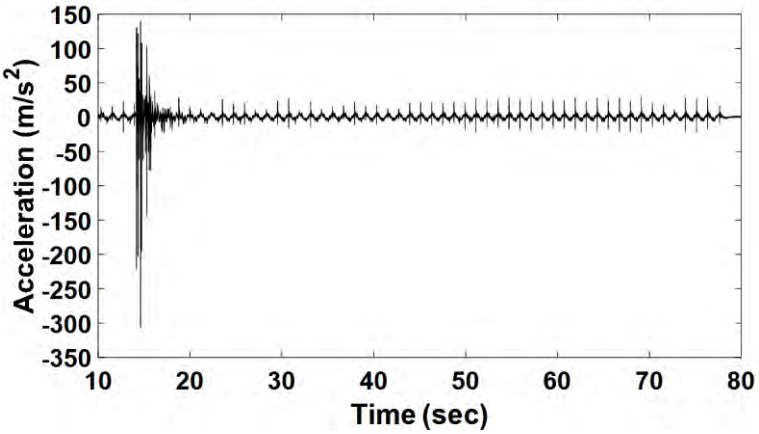

Figure 6. 33 Beam acceleration amplitude measured by the piezoelectric accelerometer during a collision of 585.92gm mass with the rotating beam.

6.4.2. Monitoring impact of the transient mass collision with the rotating beam on the tower vibrations

Tower and beam vibrations have a coupling effect which can be recognized through the analysis of the combined dynamic responses when the collision event occurs. This can be seen most obviously from the axial beam strain and the X-axis tower vibrations, whereas the out-of-plane beam strain vibrations have a direct effect on the Y-axis tower vibrations. Figure 6.34 shows the effect of mass collision with the rotor beam on the tower vibrations. The tower acceleration response reaches the maximum towards Y (1.77 m/s^2) and Z (1.73 m/s^2) direction due to the collision, while it reaches to 0.97 m/s^2 at X-direction. The rotation disruption increases beam bending towards the in-plane direction and hence, increases the beam in-plane vibrations; this results in an

increase in the fluctuation towards the Z-direction. Additionally, the coupling effect was revealed through the synchronised spikes in the tower acceleration amplitude of the X and Z directions and the beam acceleration resulting from the piezoelectric accelerometer, at 18.7 sec, 26.2 sec and 27.3 sec. This can further be identified in the tower Y-direction response due to exciting the beam out-of-plane vibration accordingly.

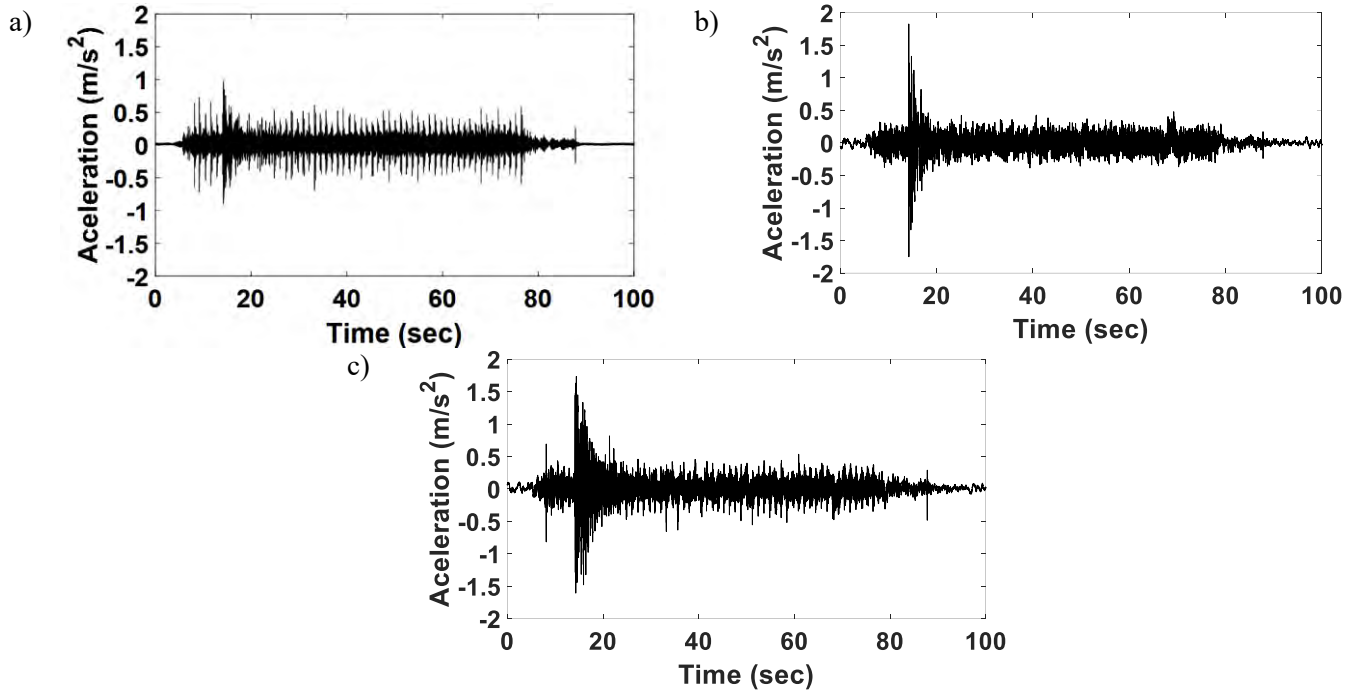

Figure 6. 34 Tower acceleration amplitude (at the whole time) during mass collision towards a) X-axis, b) Y-axis, and c) Z-axis.

6.4.3. Monitoring impact of the transient mass collision on the drive shaft fluctuations.

During the collision with the rotating beam, the drive shaft rotation was affected by fluctuations towards axes 1 and 2 as shown in figure 6.35. The maximum displacement during the collision time (14.8 sec.) is 1020 microns at axis 1 whereas it is 370 microns at axis 2. The left side of figure 6.35 shows the displacement response for the time close to the collision of both axes 1 and 2, with the zoomed response shown in the

right side. While the transient response is larger for the axis 1 signal, it is more obvious for axis 2, due to the smaller amplitude response during the normal rotation.

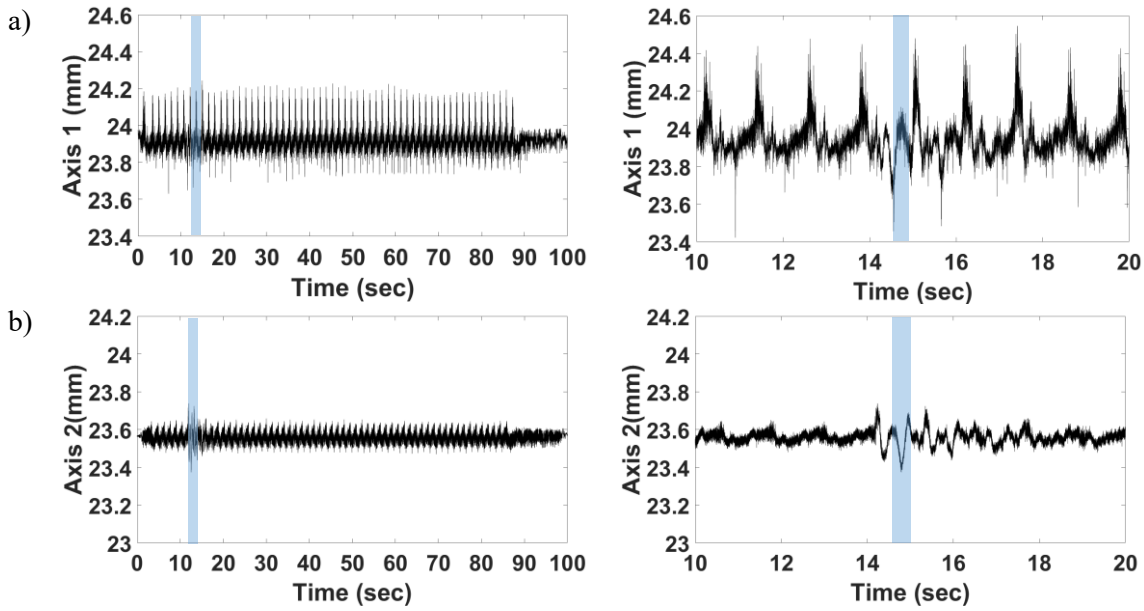

Figure 6. 35 The drive shaft vibrations (at whole time) during a mass collision with the rotor beam at a) axis1, and b) axis2, and zooming the signal on the right.

Additionally, figure 6.36 illustrates the increase of shaft displacement vibration due to the collision effect where the transient effect excited resonances frequencies due to high bending of the rotating beam resulting from the rotation obstruction.

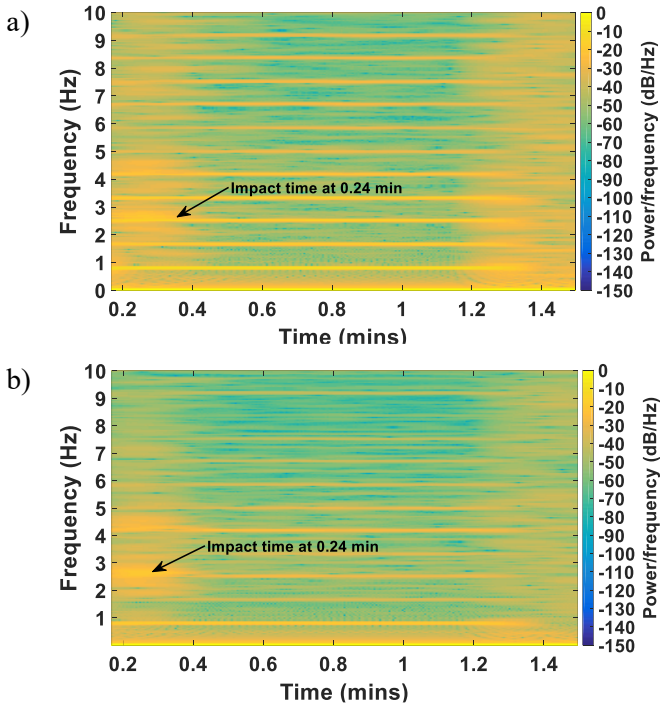

Figure 6. 36 Spectrogram analysis of shaft displacement during a 585.92gm mass collision with the rotating beam using data from a) axis 1, and b) axis 2.

Figure 6.37 shows the shaft rotation orbits during the collision event which happened at shaft rotation 6. This representation enables the monitoring of each shaft rotation to diagnose motion defects of a certain condition.

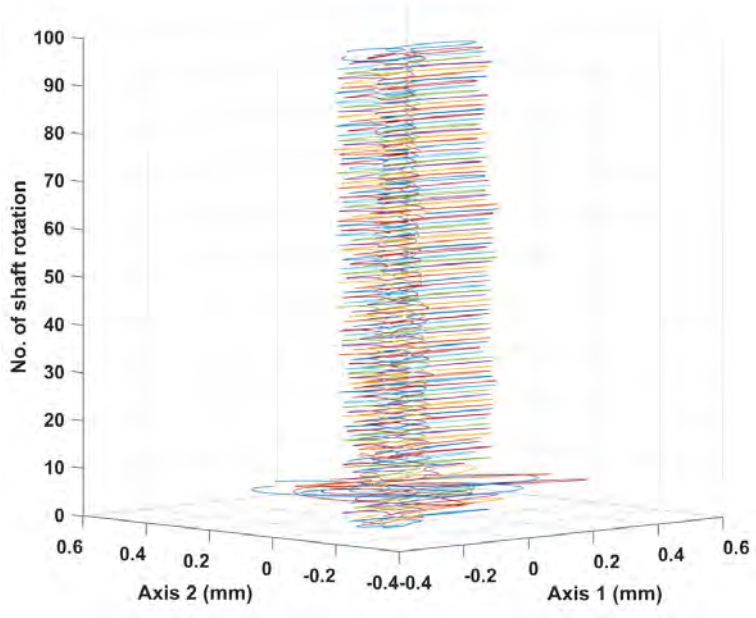

Figure 6. 37 Driveshaft rotation orbits at 50 rpm during the collision of 585.92g mass with the rotating beam.

In order to assess the drive shaft displacements at axis 1 corresponding to axis 2, figure 6.38 illustrates further representation for the shaft motion orbits including two seconds before the collision event (a), within the collision (b), and after the collision event(c). Furthermore, it shows the extension of the drive shaft displacement along axis 2 with changing in the shaft displacement at axis 1. After the collision, the displacement increases at axis 2, as shown in figure 6.38c.

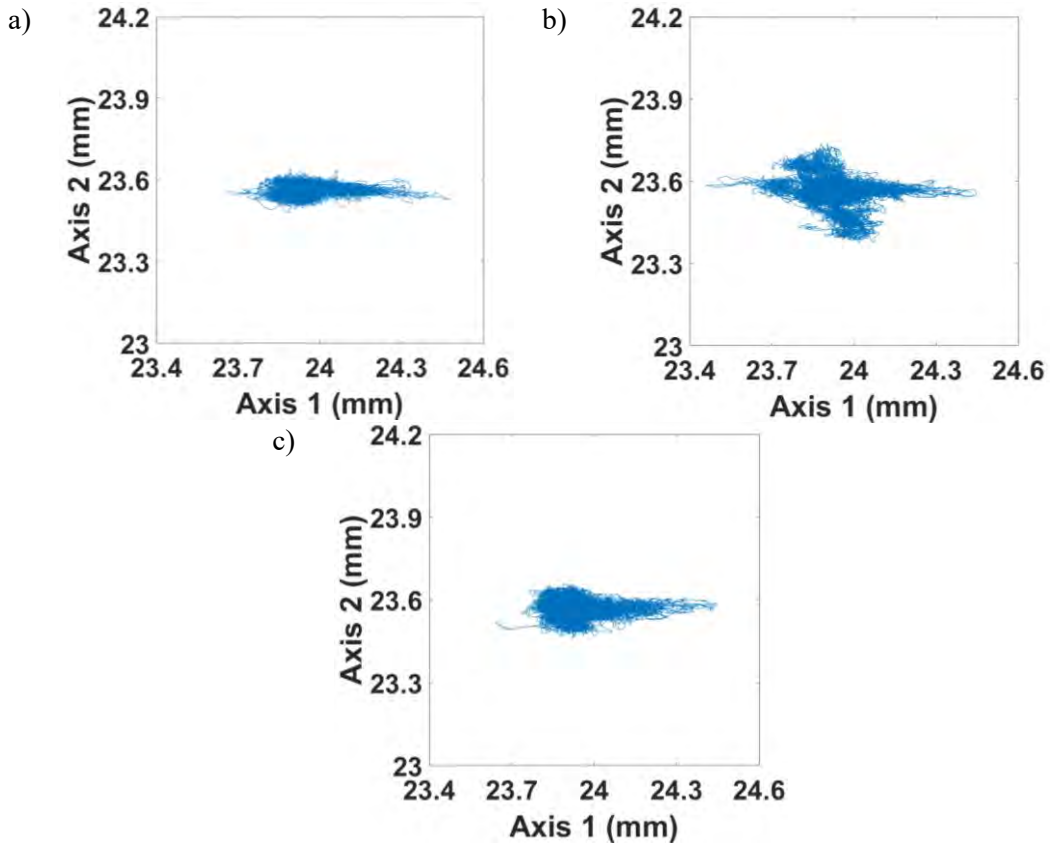

Figure 6. 38 The drive shaft orbit motion at 50 rpm within two seconds, a) before the collision, b) at the collision time, c) after the collision.

6.5 Influence of bearing bolt looseness on the beam vibrations and the test rig components.

In order to model another fault that might happen in the horizontal axis wind turbine, looseness of 2mm(clearance between the bolt and hole) from the left side bolt of the bearing near to the hub in the small-scale wind turbine test rig was investigated. The test was conducted at 50 rpm for monitoring the effect on the rotating and non-rotating

components. Figure 6.39 illustrates the dynamic vibrations of the rotating beam during loosening 2mm from one bolt. Maximum axial amplitude was 38.83 µstrain as in figure 6.39a, while the maximum in-plane amplitude was 234.2 µstrain as in figure 6.39b, as well as, 71.33 µstrain was the maximum amplitude for out-of-plane strain as in figure 6.39c. Additionally, strain amplitude per one revolution can be identified on the right side of each figure. Loosening one of the bearing bolts was found to lead to a small increase of shaft vibration, which in turn affected the rotating beam vibration due to the positive interaction between the drive shaft and rotating beams.

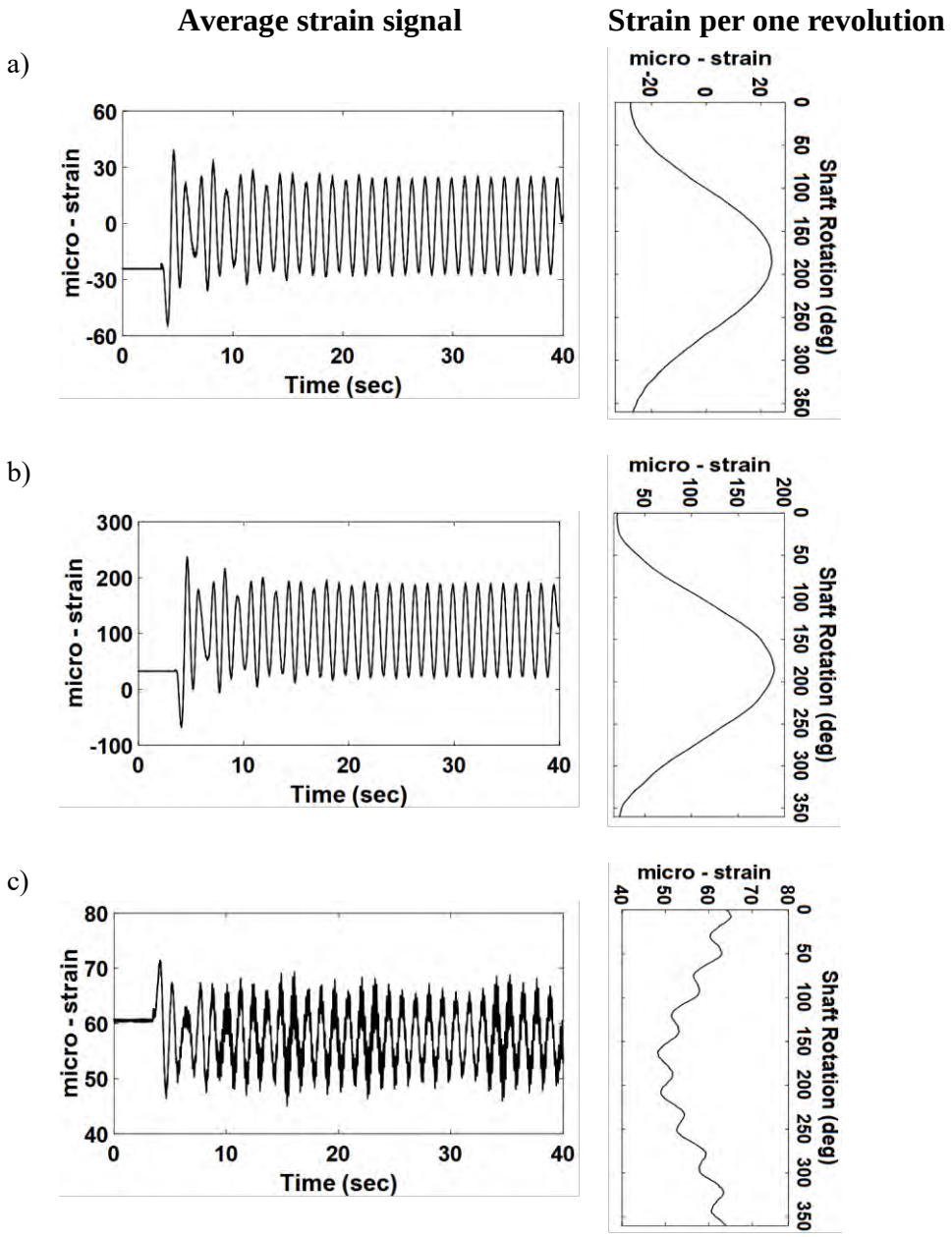

Figure 6. 39 Beam strain dynamic response during 2mm loosening of the bearing bolt (near to the hub)a) axial, b) in-plane, and c) out-of-plane strain.

6.5.1 Influence of looseness of bearing bolt on the tower vibrations

Monitoring tower vibration during the loosening of the bearing housing experiment was also implemented through the triaxial accelerometer located at the top of the tower. Figure 6.40 illustrates the resulting tower vibrations towards the X, Y, and Z directions during the experiment. A small increase in the beam axial response leads to small increases in the tower vibration towards the X-direction, as shown in figure 6.40a. Due to the small movement of the bearing housing perpendicular to the shaft rotation, maximum tower vibration of 1.19 m/s^2 was measured in the X-direction, while 0.9 m/s^2 and 0.6 m/s^2 (backwards) were measured in the Z and Y directions respectively.

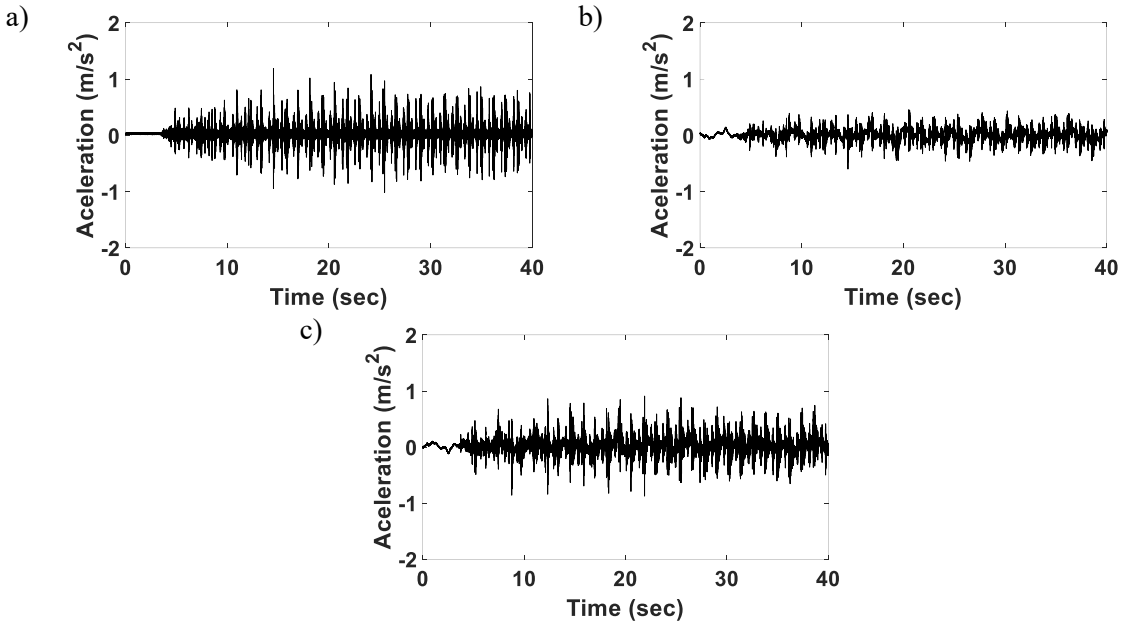

Figure 6. 40 Tower vibration during 2mm loosening of the bearing bolt a) X-axis, b)Y-axis, and Z-axis.

6.5.2 Influence of looseness bearing bolt on the drive shaft vibrations

Figure 6.41 illustrates the drive shaft speed during the test for the artificial looseness of the left bolt from the bearing housing. It can be seen that no effect on the shaft frequency was observed during this case study due to the remaining tightened bolt

(right bolt) of the bearing housing, as well as the small gap resulting from the looseness in the chosen bolt.

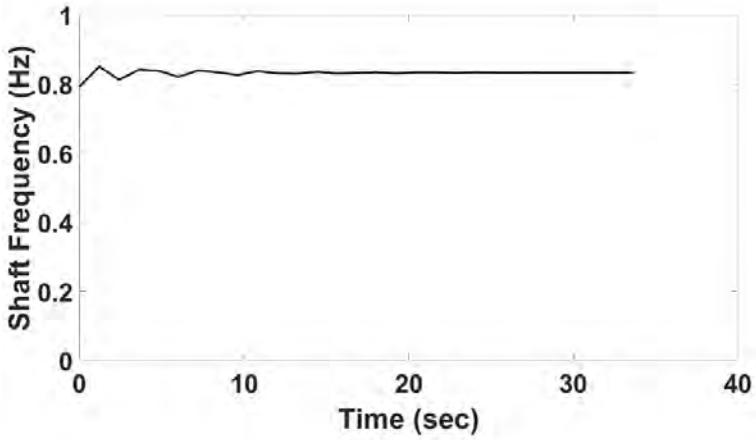

Figure 6. 41 Shaft speed during the 2mm bolt looseness test of bearing housing near the hub.

Additionally, shaft displacement towards axes directions 1 and 2 were not affected by the looseness of the bolt. In fact it seems that the shaft displacement remained within the balanced state. The large inertia of the rotary components connected with the drive shaft, the small looseness of one bolt in comparison to the remaining bolt and the low angular velocity prohibits the shaft from having large vibration. Additionally, the low rotating speed keeps the shaft motion in the average range without any effect from the one loose bolt. Moreover, the drive shaft rotations during looseness experiment can be distinguished through figure 6.42 using laser sensors signal which enables the identification of shaft characteristics during the rotation at 50 rpm. Even slight looseness of the second bolt would be expected to cause significant vibration. This was not experimented with due to the risk of significant damage to the test rig.

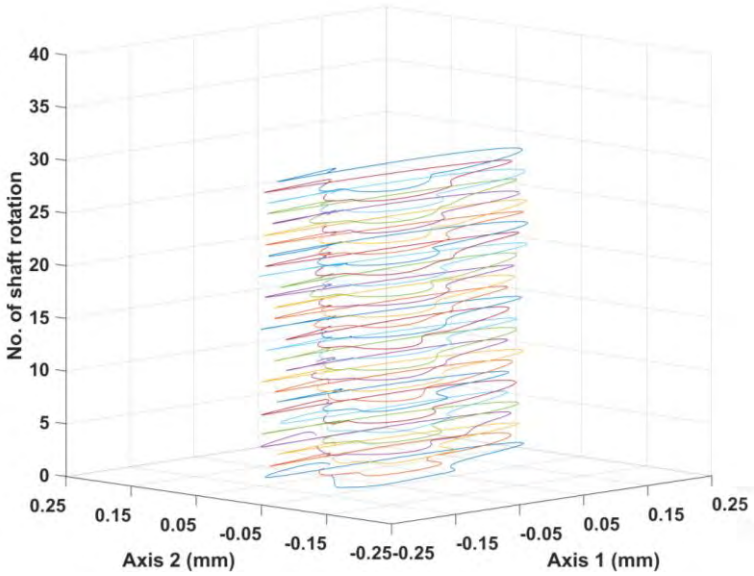

Figure 6. 42 Drive shaft rotations during looseness of 2mm bearing housing bolt at 50 rpm.

6.6 Conclusion

Imbalance conditions represented by additional tip mass (AMC) and losing tip mass (LMC) have been investigated in this chapter for vibration monitoring using the small-scale horizontal axis wind turbine test rig. Coupling between axial and in-plane vibrations has been recognized during the analysis with different rotating speeds and loading conditions. Further, coupling between in-plane and out-of-plane vibrations have been identified through the beam behaviour in different imbalance conditions. Axial beam vibration increases when adding mass to the rotating beam tip, due to the increase of centrifugal and Coriolis forces in one direction which causes extension of the beam length. This small extension has a pronounced effect on increasing beam strain measurements towards axial, in-plane, and out-of-plane directions. Additionally, it has a further effect on the drive shaft behaviour through increasing the dynamic bending towards axes 1 and 2 measured by laser sensors. This increase in the shaft dynamic displacement is different between the arbitrary axes, where it can be noted that axis 1 dynamic amplitude is higher than axis 2.

The LMC test detected different amplitude of the increase in beam strain due to imbalance effect compared to AMC. This was attributed to the small loss mass from

the beam tip, despite there being a pronounced imbalance effect during different rotating speed experiments.

Beam acceleration measurements showed a higher amplitude for the AMC test when compared to the LMC, despite there being a pronounced increase in the acceleration amplitude due to LMC on the balanced state.

The tower vibration response was affected by imbalance conditions represented by AMC and LMC, particularly with the coupling between beam out-of-plane and tower Y-direction vibrations during the various speed tests. Further, the coupling between the tower vibration in the Z-direction and beam in-plane vibrations have been detected, through acceleration and strain measurements during balanced and imbalanced conditions. Simultaneously, beam axial vibrations have a pronounced effect on tower vibrations at X-direction.

Losing the whole beam from the rotor excites higher frequency response, and was found to impose instability of rotation at all speeds. Due to the low beam inertia corresponding to the hub, the imbalance forces were not high compared with AMC and LMC.

The collision of a 585.92g mass with the rotor beam increased beam dynamic strains in the axial, in-plane, and out-of-plane orientations, and excited the beam at higher frequency due to the nature of the impact. This transient event further increased rotor shaft bending towards axes 1 and 2, and resulted in obvious high tower vibration amplitudes in the X, Y, and Z directions.

A 2mm bearing looseness had a small effect on the rotor beam axial vibrations and a small increase in the tower vibration towards the X-direction. Due to the small looseness of only one bearing bolt, there was no change in rotor displacement recorded during this test.

All these case studies with some modifications were implemented and further tested with the blade model in the next chapters, to analysis the dynamic response of the test rig components corresponding to the new blade model.

Chapter 7 Vibration Condition Monitoring Of The Wind Turbine Blade During Different Rotor Speed In The Horizontal Small-Scale Wind Turbine Test Rig.

7.1 Introduction

The complexity of wind turbine blade structures and operation conditions make it susceptible to various sort of vibrations. On-line vibration measurements are applicable to avoid damages and collapse of the turbine system. A simple blade model has been designed and manufactured as a small-scale horizontal axis wind turbine test rig for vibration condition monitoring. The new model has been designed to be light and elastic during the experiments, with dimensions proportional to the tower. This chapter presents the details of the blade vibration at different rotor speeds and the effect on the rotating and non-rotating components in the test rig.

7.2 Influence of static tip load on the blade model response

Three blade models have been manufactured from aluminum sheets, folded carefully to make a hollow shaped blade. A thin diameter 10 mm beam has been welded in the centre along the 1m blade length as shown in figure 7.1. Each blade weighs 1.203 kg with an inertia of 0.129 kg.m^2, bolted to the hub by the 10 mm beam.

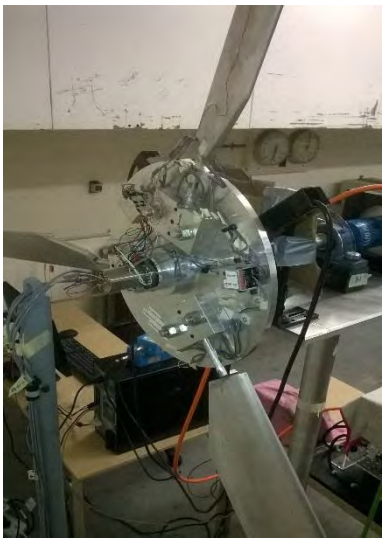

Figure 7. 1 Blade model manufacturing process in the small-scale wind turbine test rig

This blade model has the ability to change the blade pitch angles, is instrumented with rotating sensors, and has additional masses on the blade span. Figure 7.2 shows the first 7 blade natural frequencies which resulted from applying impact load in the blade tip.

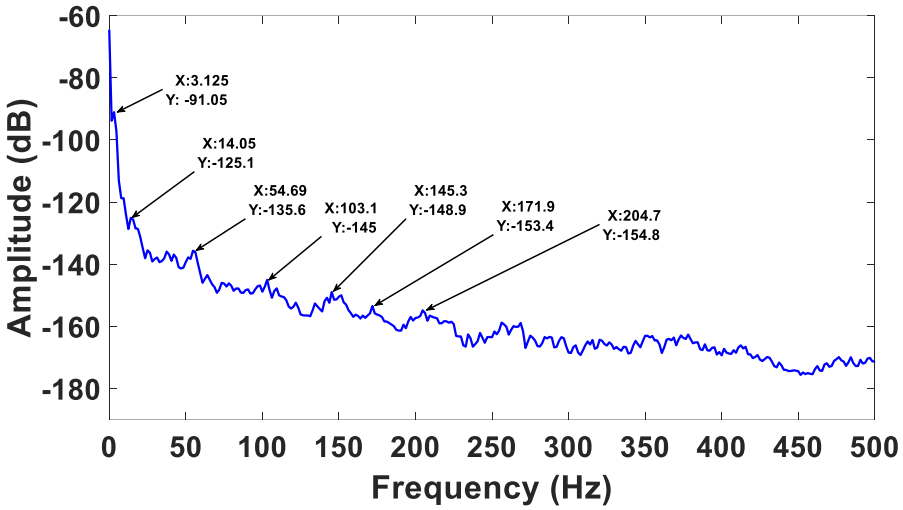

Figure 7. 2 Power spectrum of the blade from impact test showing the first 7 resonances.

Additionally, the tower's 7 natural frequencies can be identified in figure 7.3 during the same impact test.

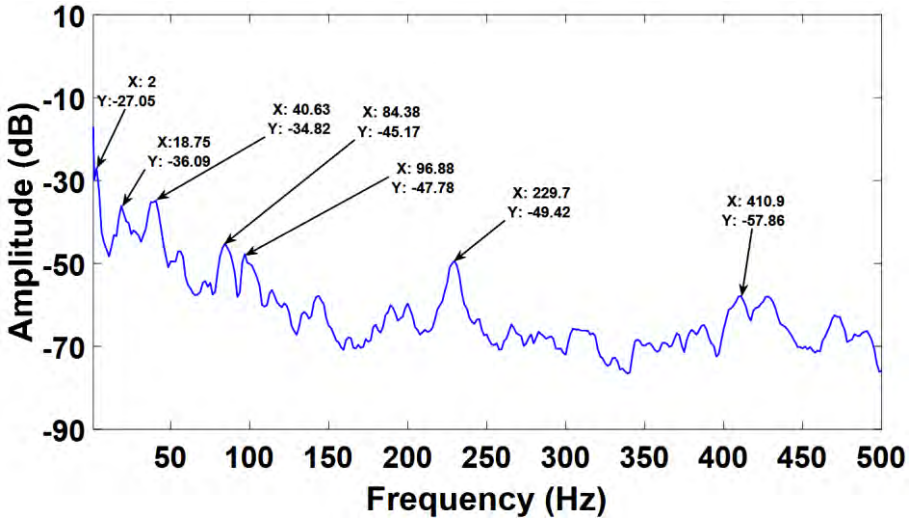

Figure 7. 3 Tower spectral analysis showing the first 7 resonances.

Table 7.1 shows the summary of the first 7 natural frequencies of the rotor blade and tower at a standstill

Table 7. 1 First 7 resonances of the rotating blade and tower at standstill (stationary state).

Mode	Blade Practical natural frequency (Hz)	Tower Practical natural frequency
1	3.125	2
2	14.06	18.75
3	54.69	40.63
4	103.1	84.38
5	145.3	96.88
6	171.9	229.7
7	204.7	410.9

7.3 Influence of changing the rotor speed on the blade vibrational modes

The change in blade angular speeds has a pronounced effect on blade vibration modes, due to the effect of centripetal and centrifugal forces during the rotation. In this part, the change in blade vibrations due to an increase in speed, can be seen shown by strain measurements which is one of the rotating sensors installed on the small-scale wind turbine test rig.

7.3.1 Effect of increasing rotor speed on blade dynamic axial vibrations

Axial strain measurements at the different rotor speeds have been measured through the strain gauges which were placed axially on blade. Figure 7.4 shows the resulting blade strains at rotational speeds ranging from 10 rpm to 120 rpm. At the low speeds from 10 rpm to 30 rpm, there is an increase in blade axial vibrations from 238 µstrain to 273.8 µstrain, and a slight decrease to 251.3 µstrain at 40 rpm as shown in figures 7.4a, 7.4b, 7.4c, and 7.4d. Speeds ranging from 50 rpm to 80 rpm show an increase in axial blade vibrations in figures 7.4e, 7.4f, 7.4g, and 7.4h. This is due to increases in

rotor speeds causing blade length extension in the direction of the centrifugal forces. Further, as the speed increases to 90 rpm, blade axial strain increases to 361.3 µstrain due to the increase in blade vibrations as shown in figure 7.4i. Simlarly, at 100 rpm the axial strain increases to 373.5 µstrain (figure 7.4j) and at 110 rpm the axial strain increased to 380.4 µstrain (figure 7.4k), until a maximum strain of 414.3 µstrain was reached at 120 rpm (figures 7.4l).

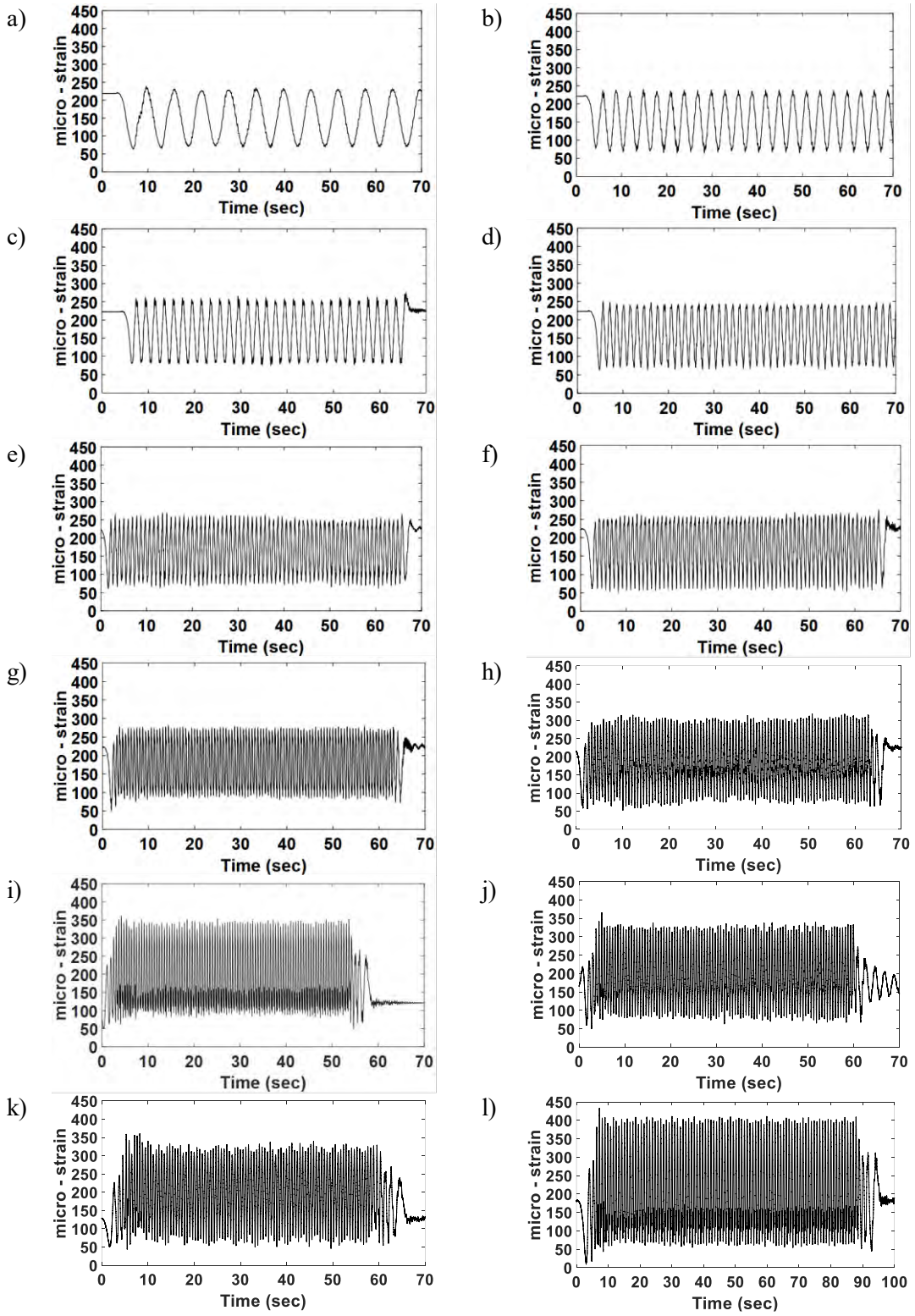

Figure 7. 4 Blade axial strain measurements due to dynamic vibrations at; a) 10 rpm, b) 20 rpm, c) 30 rpm, d) 40 rpm, e) 50 rpm, f) 60 rpm, g) 70 rpm, h) 80 rpm, i) 90 rpm, j) 100 rpm, k) 110 rpm, and l) 120 rpm.

To identify blade behaviour which occurs during the speed range, figure 7.5 illustrates the average axial strain over one revolution for the speed range of 10 rpm to 120 rpm. As the speed increases from 10 rpm to 120 rpm, there is an increase in the average

axial strain from 230.9 µstrain to 341.3 µstrain due to the increase in the centrifugal forces. It is noted that at 100 rpm there is a shifting to the right and a decrease in the average axial strain. This behaviour is attributed to the increase in blade tensile strength at 100 rpm that exceeds the centrifugal force, after which, the centrifugal force increases again with the increase in rotor speed to 100 rpm and 120 rpm.

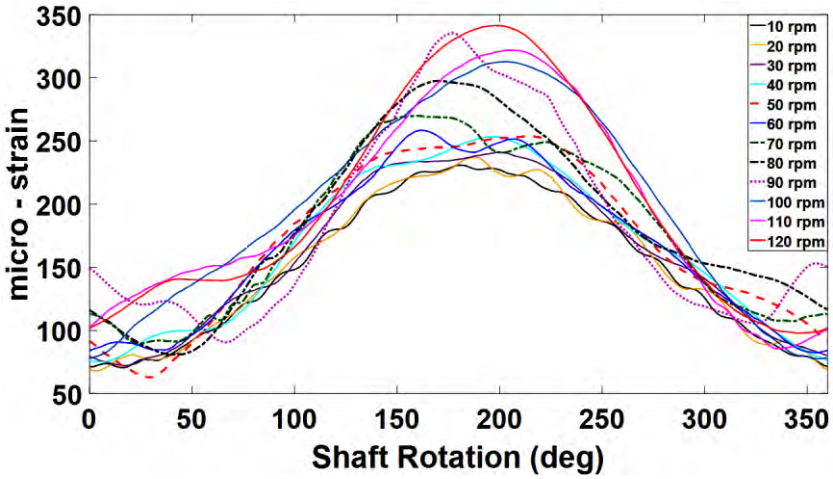

Figure 7. 5 Blade average axial strain measurements over exactly one revolution at the speed range from 10 rpm to 120 rpm.

Figure 7.6 illustrates the significant maximum and minimum of the average axial strain of the rotor blade during the speed range shown in figure 7.5. The rapid increase in axial strain at 90 rpm is attributed to high vibrations in the test rig system during the experiment. The maximum difference between the average axial strain amplitudes is 331.3µstrain which occurs at 120 rpm, while the minimum difference of 158.7µstrain occurs at 10 rpm.

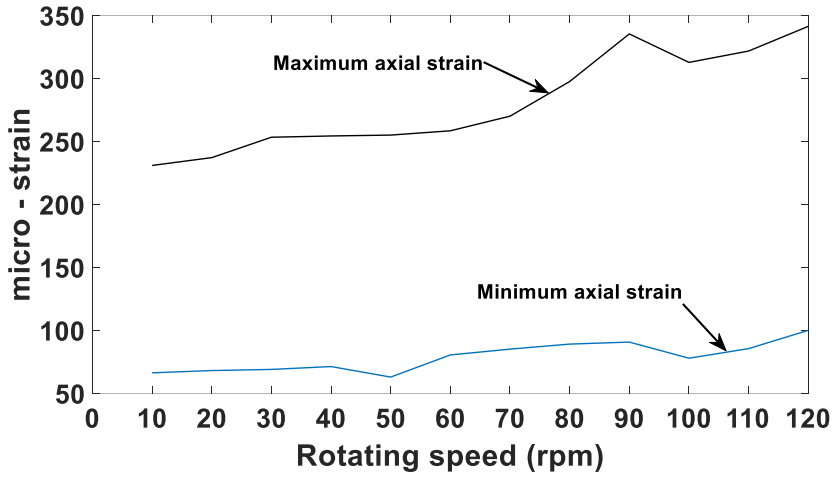

Figure 7. 6 Maximum and minimum of average axial strain for the speed range from 10 rpm to 120 rpm.

7.3.2 Effect of increasing rotor speed on blade dynamic in-plane vibrations

Figure 7.7 shows an increase in blade in-plane strain measurements as the speed increases due to an increase in vibrations. The blades average strain rises from 488.3 µstrain at 10 rpm see figure 7.7a, to 1068 µstrain at 90 rpm (at compression side), as can be seen in figure 7.7g. At 100 rpm, the decrease in vibration amplitude is accompanied with a decrease in the average in-plane strain. Subsequently, an increase in the blade speed to 120 rpm increases the strain due to vibrations to 1222 µstrain. This increase in the blade in-plane strain is attributed to the coupling with tower vibrations.

Additionally, the increase in blade speed has been accompanied with an increase centrifugal forces and Coriolis effect, which have had a positive effect on increasing blade in-plane vibrations.

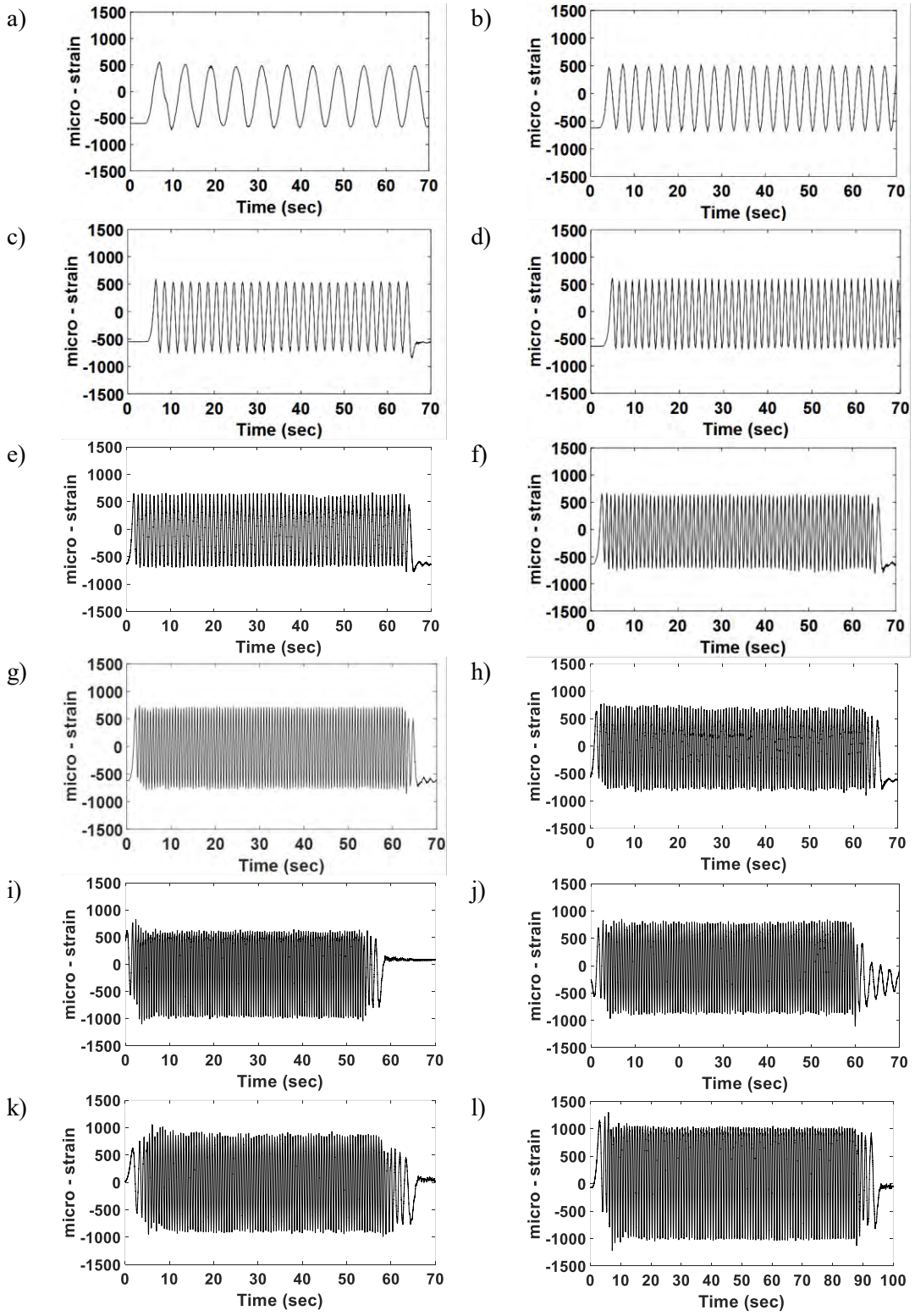

Figure 7. 7 Blade in-plane strain measurements due to dynamic vibrations at; a) 10 rpm, b) 20 rpm, c) 30 rpm, d) 40 rpm, e) 50 rpm, f) 60 rpm, g) 70 rpm, h) 80 rpm, i) 90 rpm, j) 100 rpm, k) 110 rpm, and l) 120 rpm.

To identify the blade behaviour during rotation, figure 7.8 illustrates the average blade in-plane strain over one revolution from 10 rpm to 120 rpm. Different behaviour can be recognized from this plot, such as the shifting in the average in-plane strain after 90 rpm and the rapid increase in the average strain amplitude at 90 rpm (946.8 µstrain on the compression side). This increase has been identified in the average axial strain (figure 7.5) due to the coupling between the axial and in-plane strain or being close to an in-plane resonance frequency.

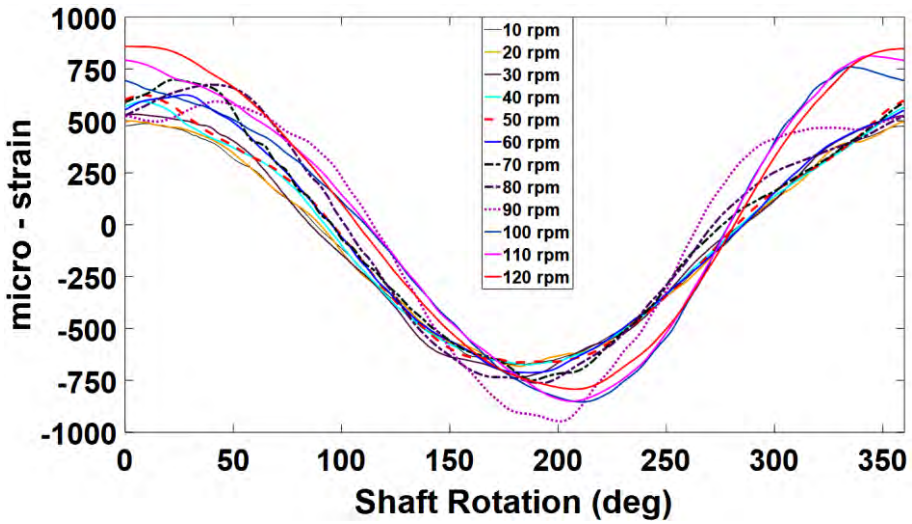

Figure 7. 8 Average blade in-plane strain over exactly one revolution for the speed range of 10 rpm to 120 rpm

Figure 7.9 shows the maximum and minimum of the average blade in-plane strain over one revolution for blade speeds from 10 rpm to 120 rpm. The maximum divergence between the maximum and minimum average strain amplitudes occurs at 120 rpm (1650.3 µstrain) due to high blade in-plane vibrations, whilst the minimum convergence occurs at 40 rpm (1161.7 µstrain).

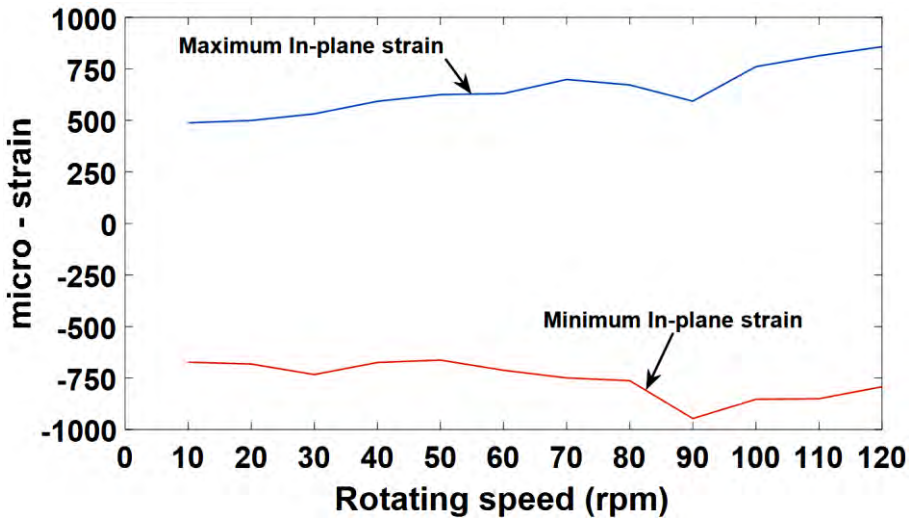

Figure 7. 9 Maximum and minimum average blade in-plane strain over exactly one revolution for the speed range of 10 rpm to 120 rpm

7.3.3 Effect of increasing rotor speed on blade dynamic out-of-plane vibrations

Figure 7.10 show the blade vibrations perpendicular to the rotation plane (out-of-plane) for the particular speed range. The average blade out-of-plane strain is less than the in-plane strain as shown in figure 7.10. However, the average strain shows a pronounced increase from 186.5 µstrain at 10 rpm in figure 7.10a to -800 µstrain at 120 rpm in figure 7.10l. Additionally, the positive effect of the tower vibration towards the y-direction on the blade out-of-plane vibration is a further reason of the strain increases in this direction, as shown at 100 rpm, 110 rpm and 120 rpm in figures 7.10j, 7.10k, and 7.10l respectively.

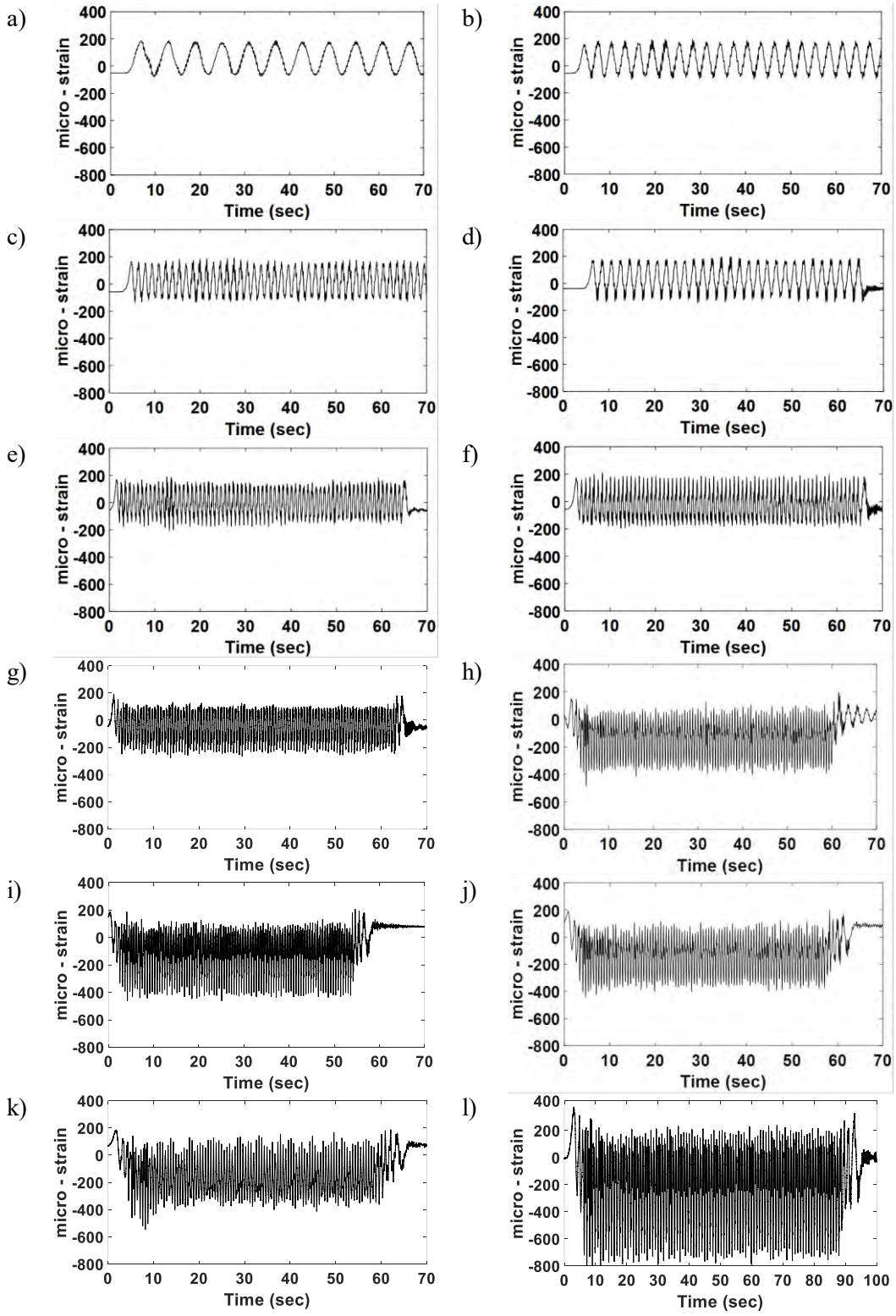

Figure 7. 10 Blade out-of-plane strain measurements due to dynamic vibrations at; a) 10 rpm,b) 20 rpm, c) 30 rpm, d) 40 rpm, e) 50 rpm, f) 60 rpm, g) 70 rpm, h) 80 rpm, i) 90 rpm, j) 100 rpm, k) 110 rpm, and l) 120 rpm.

Figure 7.11 shows the maximum and minimum average blade strain per one revolution amplitudes while figure 7.12 illustrates the maximum and minimum average out-of-plane strain amplitudes per one revolution for the speed range of 10 rpm to 120 rpm. Most average strain amplitudes tend to increase on the blade's compression side as the speed increases.

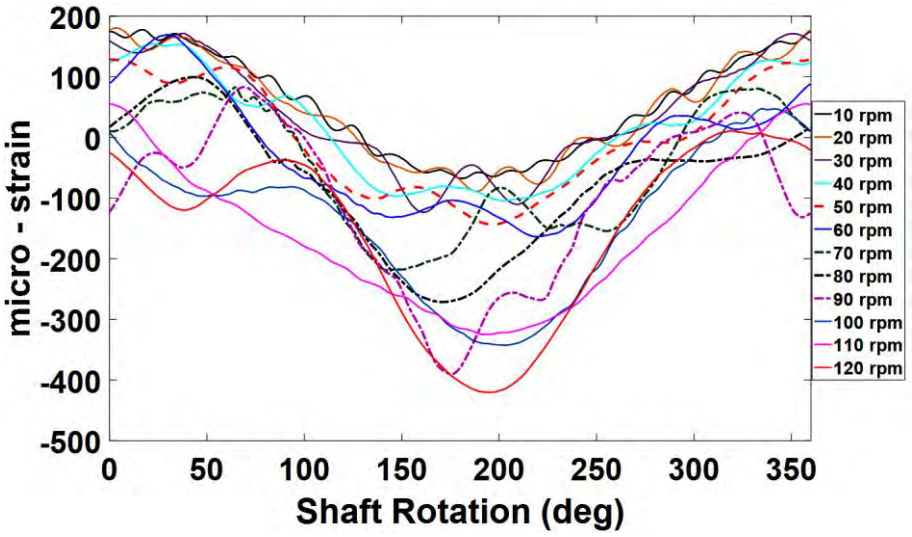

Figure 7. 11 Blade average out-of-plane strain over one revolution for the speed range of 10 rpm to 120 rpm.

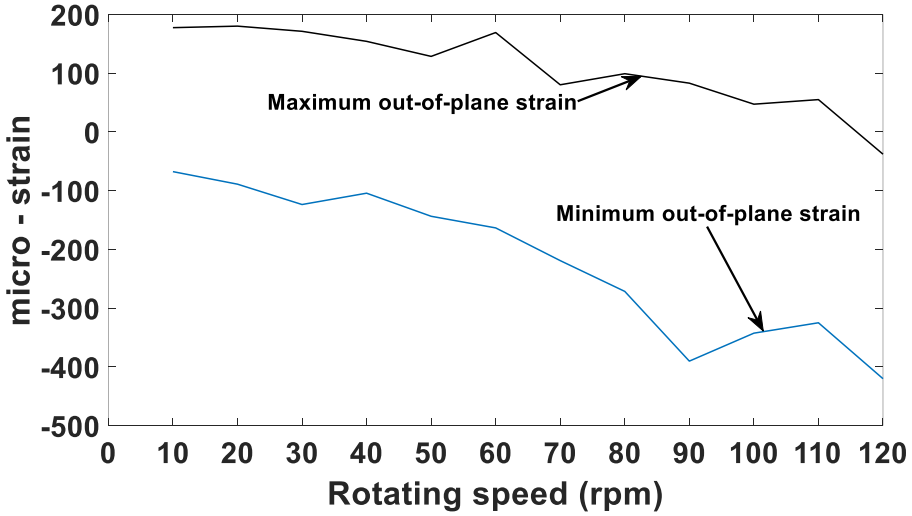

Figure 7. 12 Maximum and minimum blade average out-of-plane strain over one revolution for the speed range of 10 rpm to 120 rpm.

7.4 Influence of increasing rotor speed on the drive shaft vibrations

The drive shaft vibrations were monitored by utilizing the same laser sensors that were positioned perpendicularly on the shaft axis. The time period of 70 seconds in all the experiments represents the effective time during the rotation, whereas the total test time was 100 seconds. The maximum shaft displacement occurs at 120 rpm (776 microns), as shown in figure 7.13l, whereas the minimum shaft displacement is 550 microns at 10 rpm in figure 7.13a. The average drive shaft displacement varied from 560 microns at 20 rpm (figure 7.13b) to 610 microns at 60 rpm (figure 7.13f). After that, it decreased to 580 microns at 70 rpm – see figure 7.13g. The shaft displacement then returned to a pattern of increasing, with 630 microns at 80 rpm as shown in figure 7.13h, and culminated with 762 microns at 110 rpm due to the increase in blade vibrations particularly towards the axial direction.

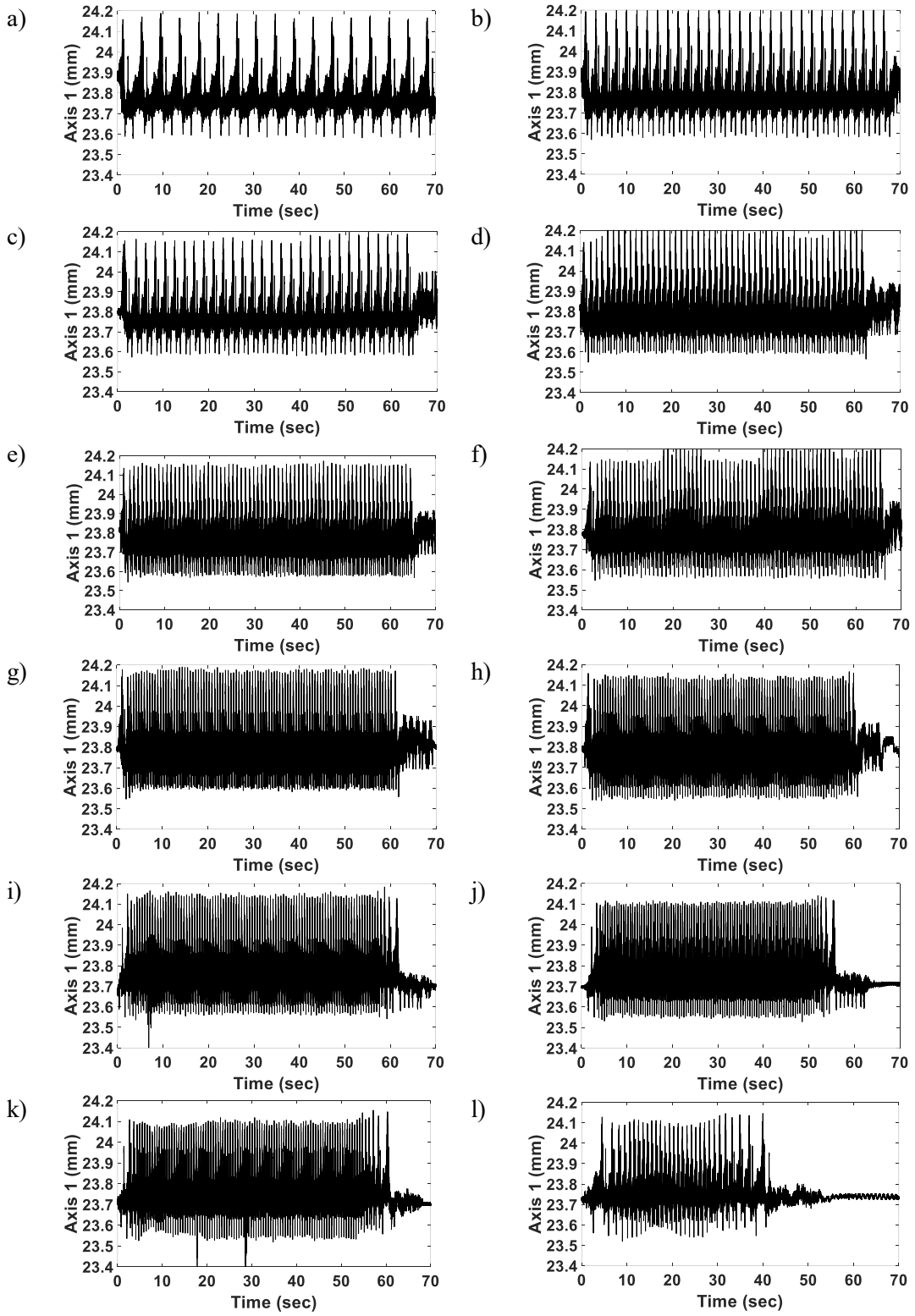

Figure 7. 13 Driveshaft vibration measured by laser a sensor towards axis1 at; a) 10 rpm, b) 20 rpm, c) 30 rpm, d) 40 rpm, e) 50 rpm, f) 60 rpm, g) 70 rpm, h) 80 rpm, i) 90 rpm, j) 100 rpm, k) 110 rpm, and l) 120 rpm.

Average shaft displacement over exactly one revolution perpendicular to axis1 is shown in figure 7.14. A quasi-symmetry between signals amplitude have been identified at all the applied speed range. Increasing the rotor speed generally increases the average shaft displacement amplitudes. This is shown by the increase from 141 microns for the average shaft displacement at 10 rpm to 172 microns at 110 rpm, with the exception of the decrease in the average displacement which occurred at 60 rpm.

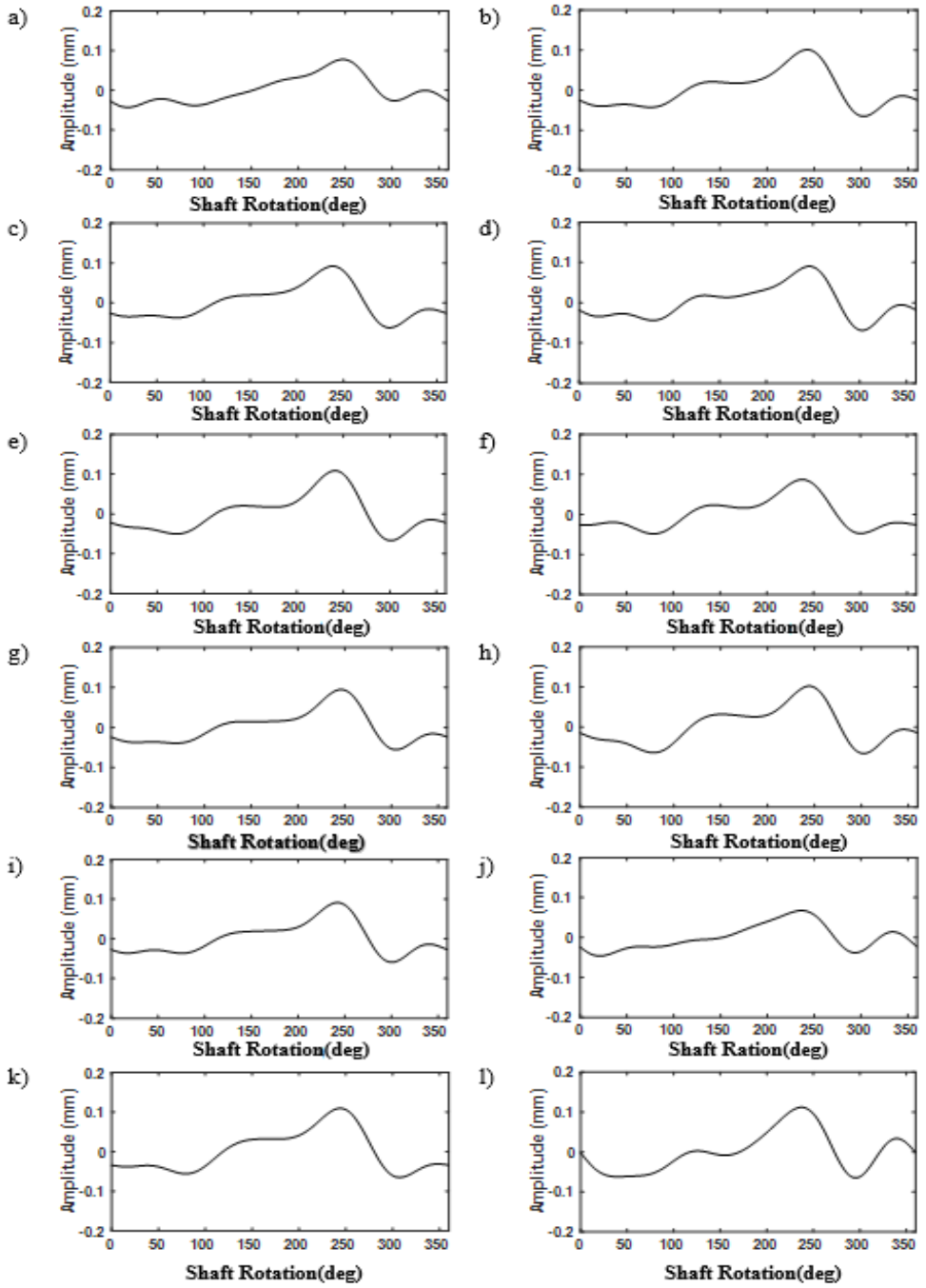

Figure 7. 14 Driveshaft displacement measured by laser sensor towards axis1 over exactly one revolution at; a) 10 rpm, b) 20 rpm, c) 30 rpm, d) 40 rpm, e) 50 rpm, f) 60 rpm, g) 70 rpm, h) 80 rpm, i) 90 rpm, j) 100 rpm, k) 110 rpm, and l) 120 rpm

The drive shaft displacement perpendicular to axis2 is shown in figure 7.15 for the rotor blade speed range from 10 rpm to 120 rpm. The average shaft displacement varied from 170 microns at 10 rpm to 240 microns at 120 rpm due to the increase in blade vibration as the speed increases. Additionally, the increase in shaft dynamic displacement is quasi-regular during the increase in speed from 30 rpm to 70 rpm, as illustrated in figures 7.15c to 7.15g. Subsequently, there is fluctuation in the average shaft displacement, whereby there is an increase to 230 microns at 90 rpm, a decrease to 210 microns at 100 rpm, followed by an increase to 220 microns at 120 rpm.

According to the raw signals, the dynamic displacement towards axis2 is less than shaft displacement towards axis1 at all speeds. This is attributed to when the rotor shaft bends towards axis1 due to the increase in the centrifugal forces, it tries to restore the previous position before arriving axis2.

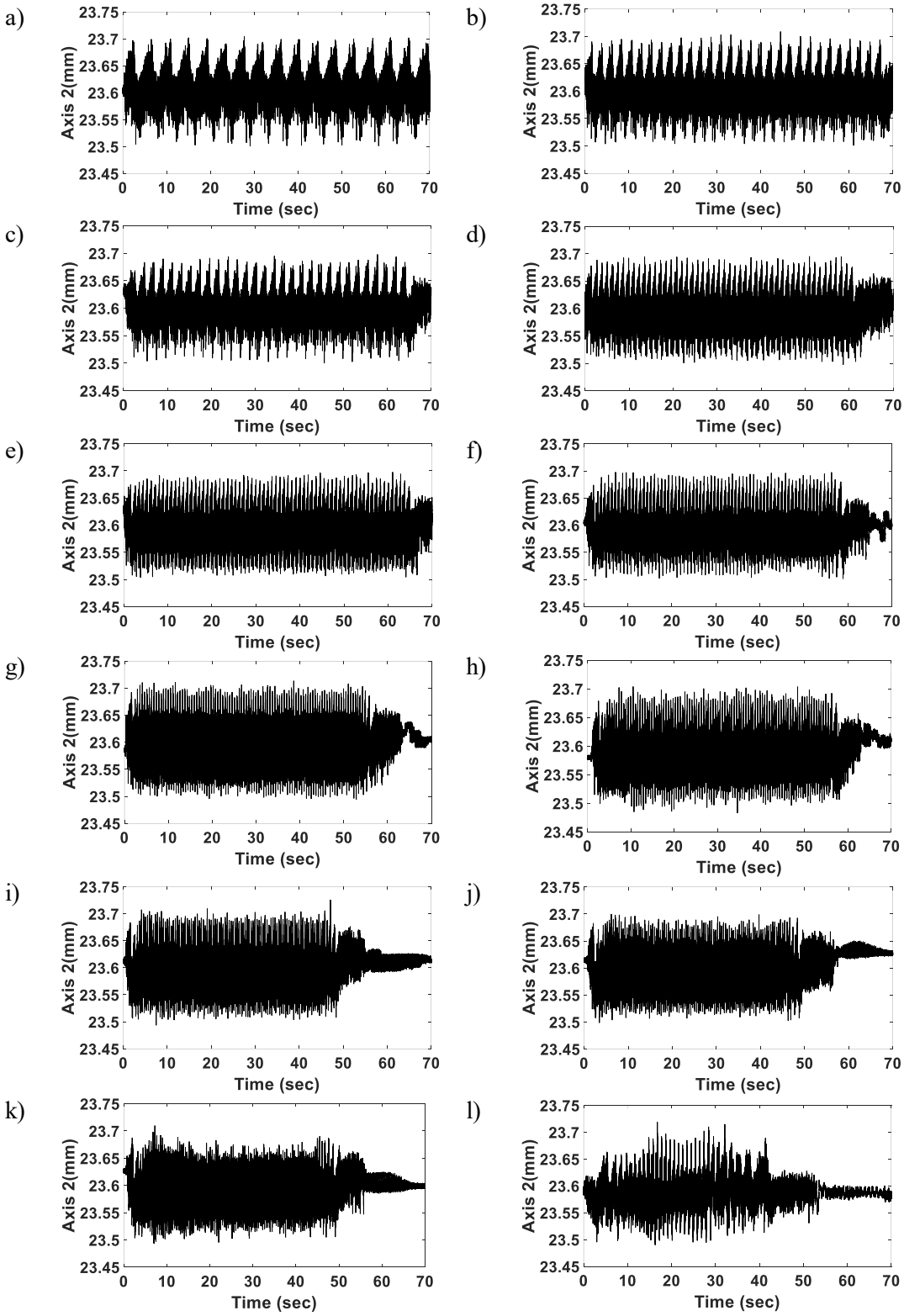

Figure 7. 15 Driveshaft displacement measured by laser a sensor towards axis2 at; a) 10 rpm, b) 20 rpm, c) 30 rpm, d) 40 rpm, e) 50 rpm, f) 60 rpm, g) 70 rpm, h) 80 rpm, i) 90 rpm, j) 100 rpm, k) 110 rpm, and l) 120 rpm.

Additionally, figure 7.16 illustrates the average shaft displacement measured by axis2 over one revolution for the significant rotor speeds. This figure shows the changes in the system dynamics as the rotor speed increases. Additionally, it shows how the rotor shaft fluctuates during one rotation, which corresponds to the raw signal measured by the laser sensor located at axis2. Maximum average shaft displacement is 130 microns at 90 rpm as illustrated in figure 7.16i, whereas, the minimum average is 7.7 microns at 10 rpm as shown in figure 7.16a. The average shaft displacement increases as the speed increases from 10 rpm to 40 rpm to reach 61 microns as shown in figure 7.16d, followed by an increase to 113 microns at 70 rpm as shown in figure 7.16g. Furthermore, shaft amplitude in figure 7.16l revealed that an increase in the average displacement at 120 rpm to 126 microns after it was 97 microns at 110 rpm.

The blade and tower vibrations have further effects on the rotor shaft dynamic displacement, which was shown at the raw signals (axes 1 and 2) when the shaft stopped (rotation stops).

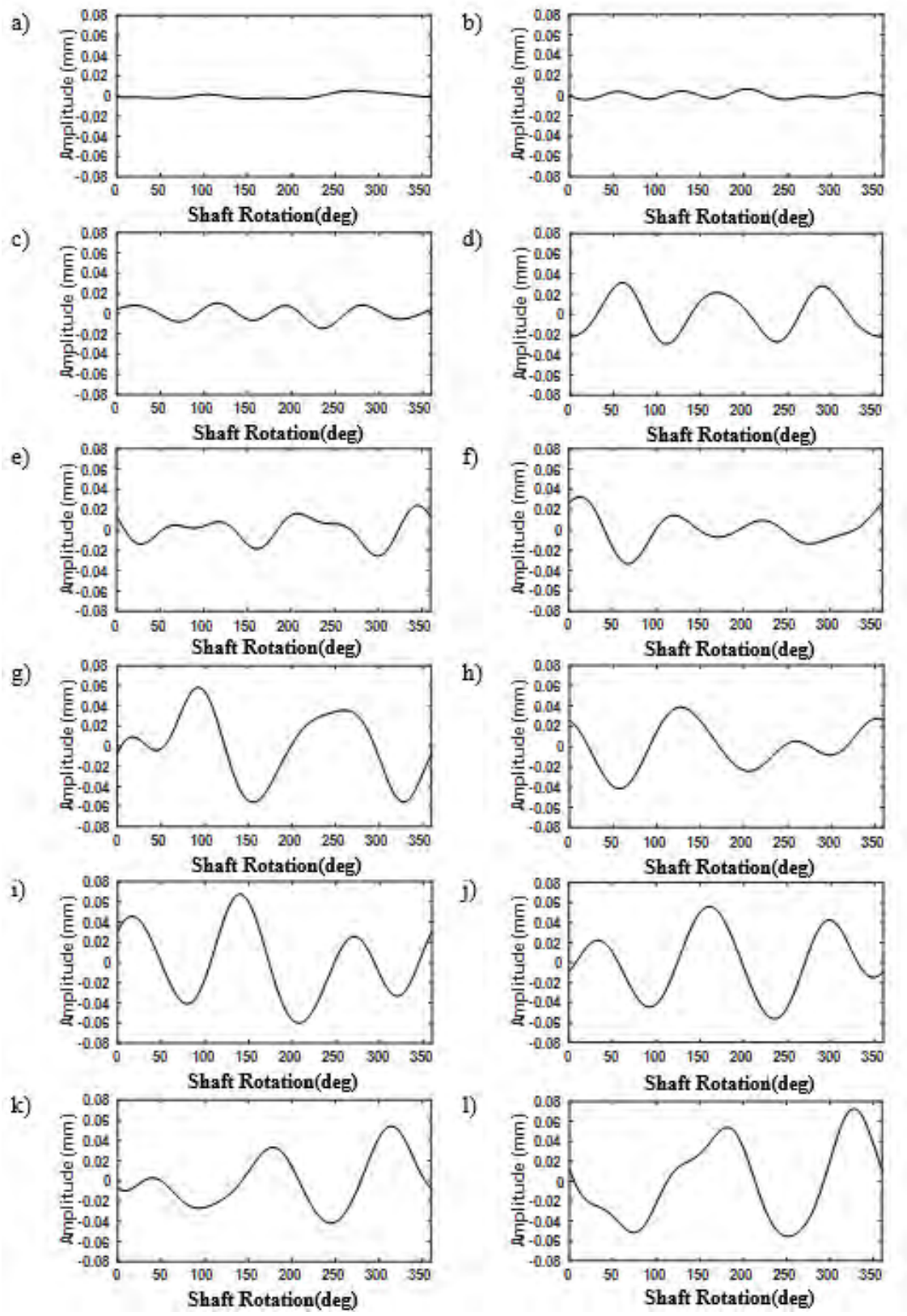

Figure 7. 16 Driveshaft displacement measured by laser sensor towards axis2 over exactly one revolution at; a) 10 rpm, b) 20 rpm, c) 30 rpm, d) 40 rpm, e) 50 rpm, f) 60 rpm, g) 70 rpm, h) 80 rpm, i) 90 rpm, j) 100 rpm, k) 110 rpm, and l) 120 rpm.

Figure 7.17 shows the shaft centreline orbits (1st harmonic) during the speed range from 10 rpm to 40 rpm. Elongation in the shaft orbit can be noticed as the rotor speed increases to 20 rpm. After that, the elongated axis of the shaft orbit shrinks at 30 rpm, and then extends again when the rotor speed reaches 40 rpm.

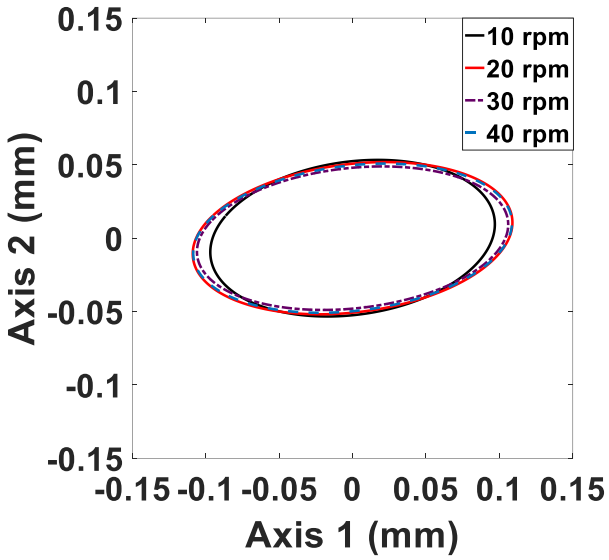

Figure 7. 17 Rotor shaft centreline orbits (1st harmonic) at; a) 10 rpm, b) 20 rpm, c) 30 rpm, and d) 40 rpm.

Figure 7.18 illustrates shaft centreline orbits for the next rotor speed range from 50 rpm to 80 rpm. An increase in rotor speed results in a shift of the orbits to the right and elongates the orbit's axis along axis2, as illustrated by the 80 rpm results in figure 7.18.

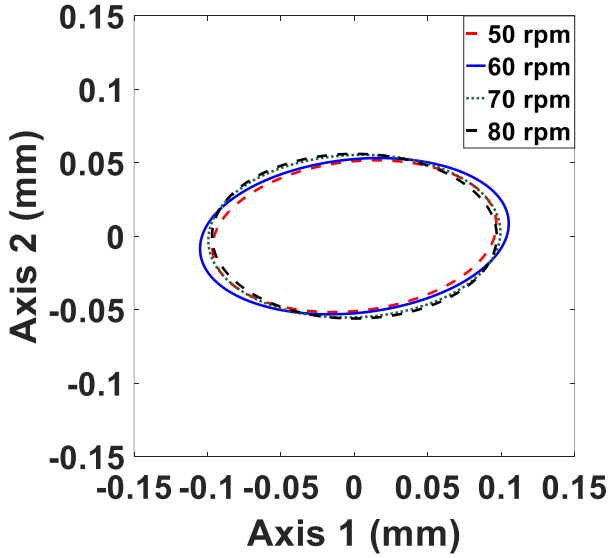

Figure 7. 18 Rotor shaft centreline orbits (1st harmonic) at; a) 50 rpm, b) 60 rpm, c) 70 rpm, and d) 80 rpm.

Increasing the shaft speed to 90 rpm increases the orbit's shift to the right as shown in figure 7.19. At 100 rpm, the orbit shifts to left and the oval elongates along axis2 due to the increase in rotor speed. More shifting to the left in the oval shape can be identified at a speed 110 rpm, due to the change in shaft centreline displacement resulted from increasing rotor blade vibrations. In addition, there is a significant shifting in the centreline orbit at 120 rpm, where the oval shape returns to a shape that closely resembles the orbital path at 90 rpm.

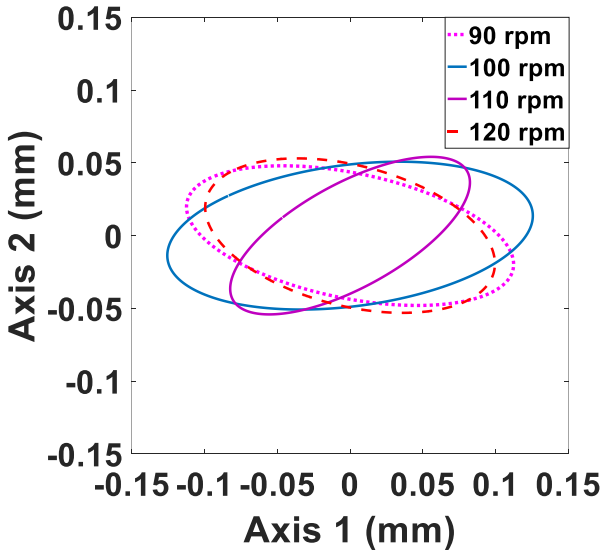

Figure 7. 19 Rotor shaft centreline orbits (1st harmonic) at; a) 90 rpm, b) 100 rpm, c) 110 rpm, and d) 120 rpm.

The rotor shaft centreline orbits for the 2nd harmonic are shown in figure 7.20. The change in orbits as the speed increases from 10 rpm to 40 rpm is illustrated in figure 7.20a, which is shown to be similar to the centreline orbits of the 1st harmonic. The "diamond" shape in this figure is nearly the same at all speed, with the orbit size extending as the speed increases. Changes in the shape and size of the orbits as the rotor speed increases are found in figure 7.20b and figure 7.20c. These figures show that the shaft centreline displacement takes different orbital shapes as the speed increases due to the coupling effect of the blade and tower vibrations.

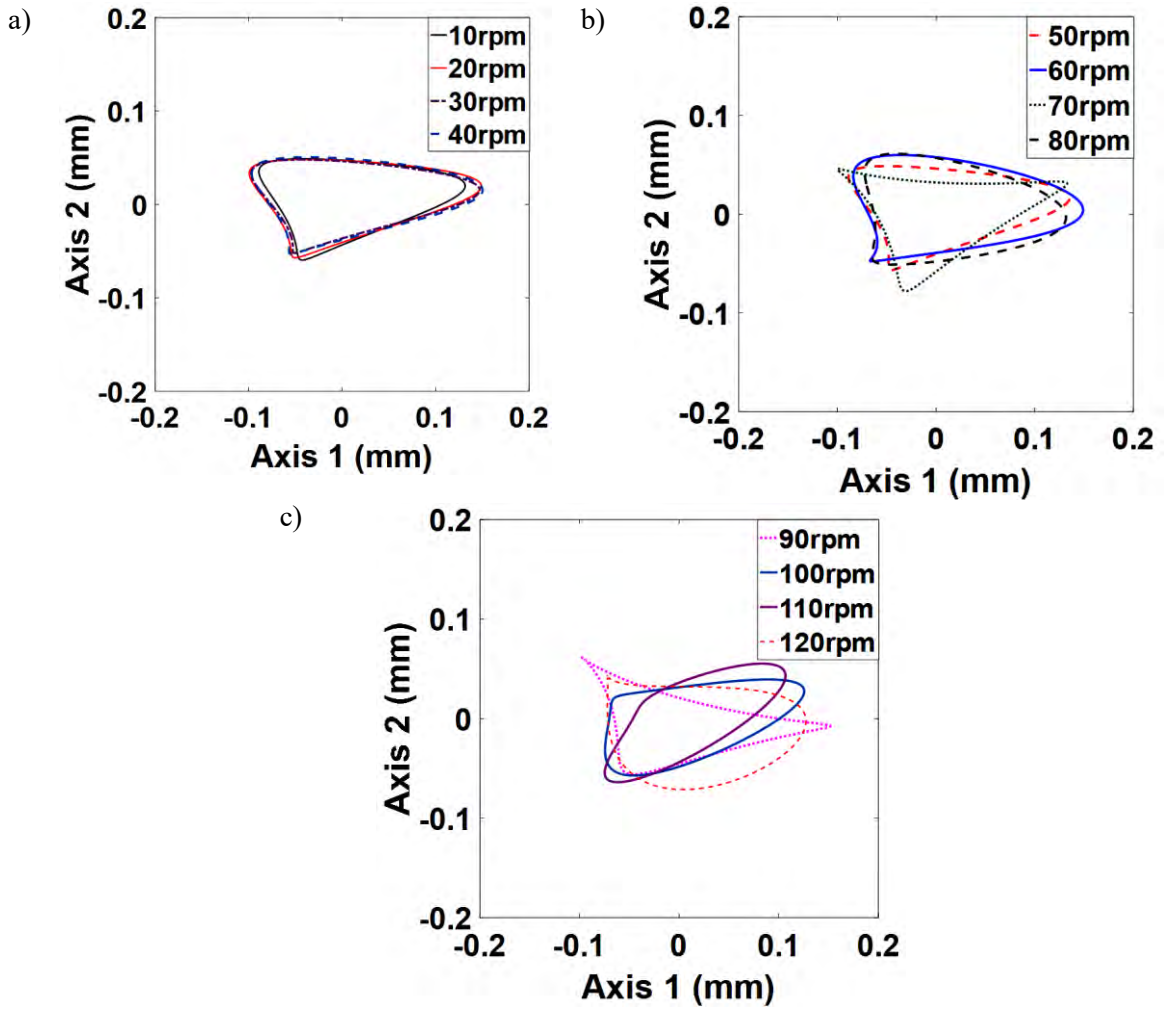

Figure 7. 20 Rotor shaft centreline orbits (2nd harmonic) at speed range; a) from 10 rpm to 40 rpm,b) from 50 rpm to 80 rpm, and c) 90 rpm to 120 rpm.

7.5 Influence of rotor blade speeds on the tower vibrations

The blade vibrations have a pronounced effect on tower vibrations. The coupling between the tower vibrations in the Y-direction and blade out-of-plane vibrations increases vibration amplitude with increasing speed. Additionally, the increase in tower vibrations towards the Z-direction contributed to the coupling effect with the blade in-plane and axial vibrations. Figure 7.21 shows tower vibration in the X, Y, and Z directions at 10 rpm, 20 rpm, and 30 rpm. At 10 rpm, it is noted that the maximum tower acceleration in the X-direction is 0.64 m/s^2 (negative acceleration, downward direction). These influences become equal at 20 rpm, where the maximum tower acceleration is 0.8 m/s^2 (at the X-direction). Additionally, tower fluctuation increases to 0.6 in the Z-direction on the negative side). At 30 rpm, the tower vibration decreases in the X-direction (0.77 m/s^2), while increasing in tower vibration to 0.7

m/s^2 in the Z-direction. Hence, increases in tower vibrations towards Y and Z directions excited the vibrations in the X-direction.

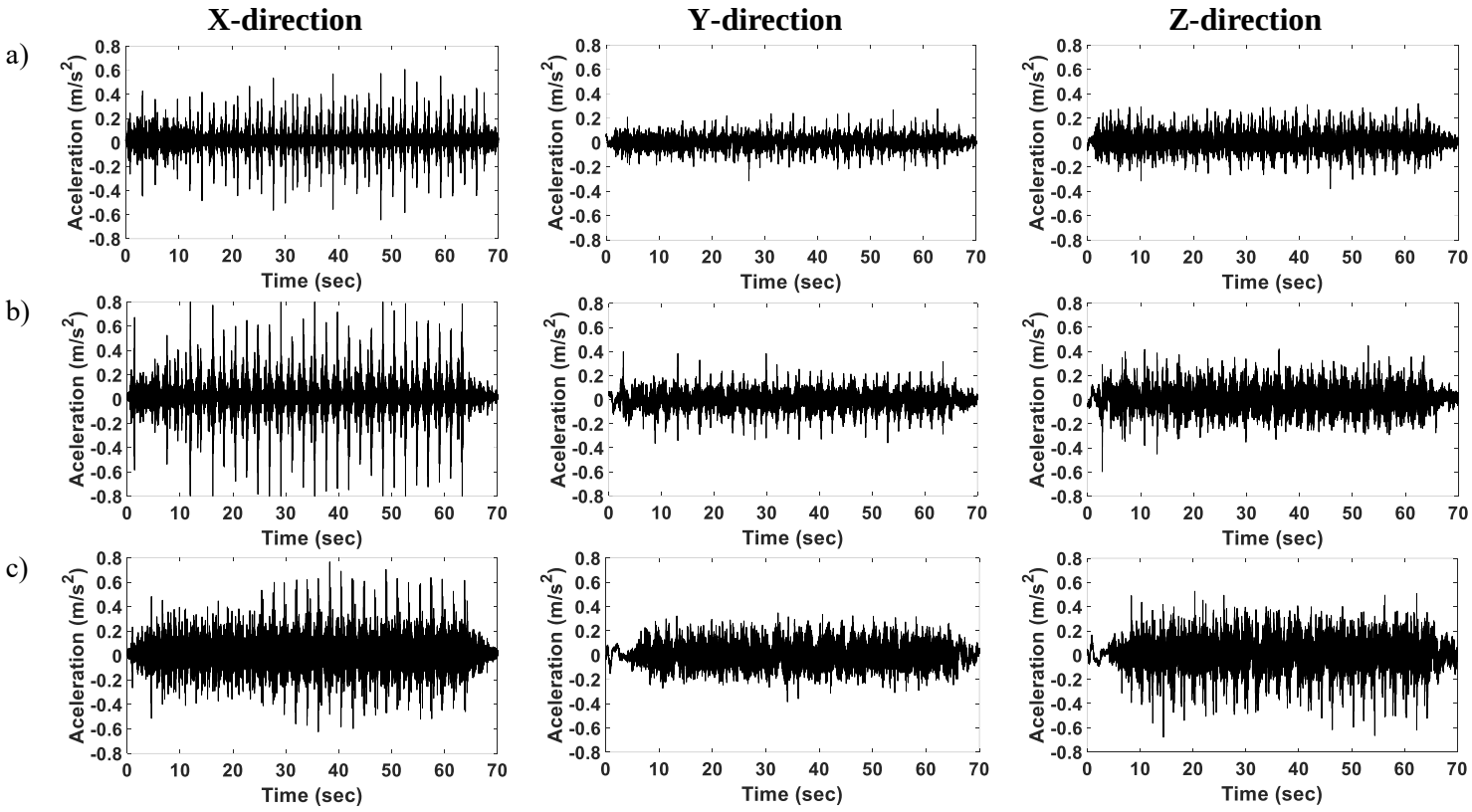

Figure 7. 21 Tower acceleration amplitudes towards X, Y, and Z directions due to speed increases at; a) 10 rpm, b) 20 rpm, c) 30 rpm.

Figure 7.22 illustrates tower vibrations at four significant rotor speed; 40 rpm, 50 rpm, 60 rpm and 70 rpm. The maximum acceleration is -1.1 m/s^2 in the X-direction at 40 rpm. This maximum amplitude decreases to 0.66 m/s^2 at 50 rpm in the same direction, and further decreases to -0.44 m/s^2 at 60 rpm. However, the acceleration towards Z-direction increases from 0.6 m/s^2 at 40 rpm to -0.75 at 50 rpm and to -0.8 m/s^2 at 60 rpm. Additionally, tower acceleration in the Y-direction increases slightly to 0.46 m/s^2 (forward fluctuation) at 60 rpm from 0.42 m/s^2 at 50 rpm. Furthermore, an increase in the tower acceleration in the X-direction to 0.52 m/s^2 was seen when rotor speed increases to 70 rpm, whereas, tower acceleration in the Y-direction reaches -0.65 m/s^2 (backward fluctuation).

The increase in tower vibrations in the Z-direction, which is due to the coupling with blade in-plane and axial vibrations, affected positively on tower vibrations in the X-directions as the speed increases from 40 rpm to 60 rpm. However, the increase in tower vibration in the Y-direction at 70 rpm due to the coupling with the blade out-of-plane vibrations diminished the tower vibrations in the Z-direction.

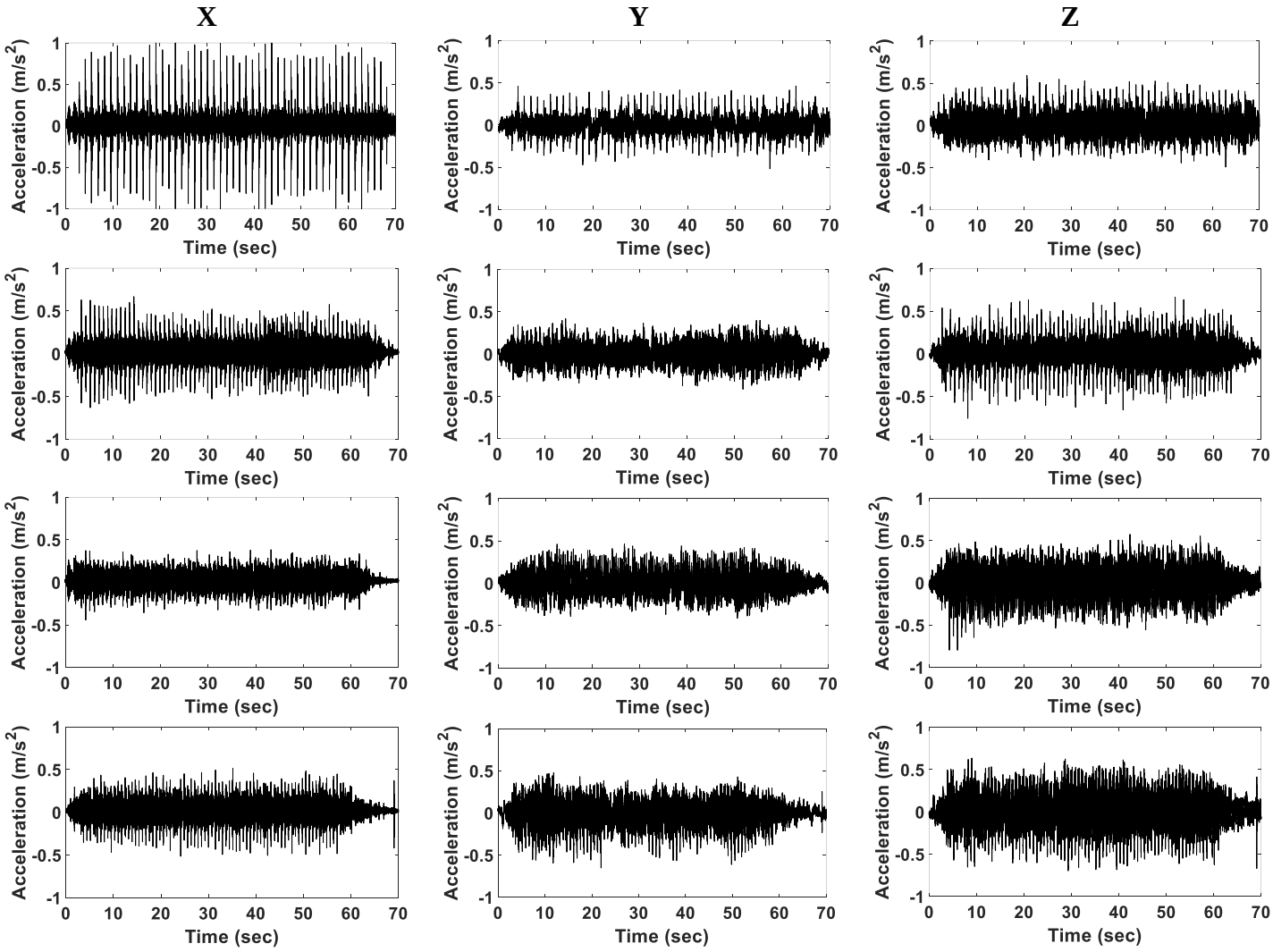

Figure 7. 22 Tower acceleration at X, Y, and Z directions due to speed increases at; a) 40 rpm, b) 50 rpm, c) 60 rpm, and d) 70 rpm.

Figure 7.23 illustrates tower vibrations at speeds of 80 rpm and 90 rpm. Compared to the results in figure 7.22, tower acceleration in the Z-direction increases to 0.87 m/s^2 and -1.1 m/s^2 at 80 rpm and 90 rpm respectively. Additionally, an increase occurred in tower accelerations in all directions at 80 rpm with respect to 70 rpm; maximum tower acceleration at this speed is -0.9 m/s^2 in the X-direction, while maximum acceleration in the Y and Z directions are 0.8 m/s^2 and 0.87 m/s^2 respectively. Tower vibration increases to 1.1 m/s^2 in the Z-direction when rotor speed increases to 90 rpm. This increase in tower fluctuation has a positive effect on the drive shaft vibrations, especially towards axis1. Tower vibrations further continued after the rotation and blade vibrations stopped.

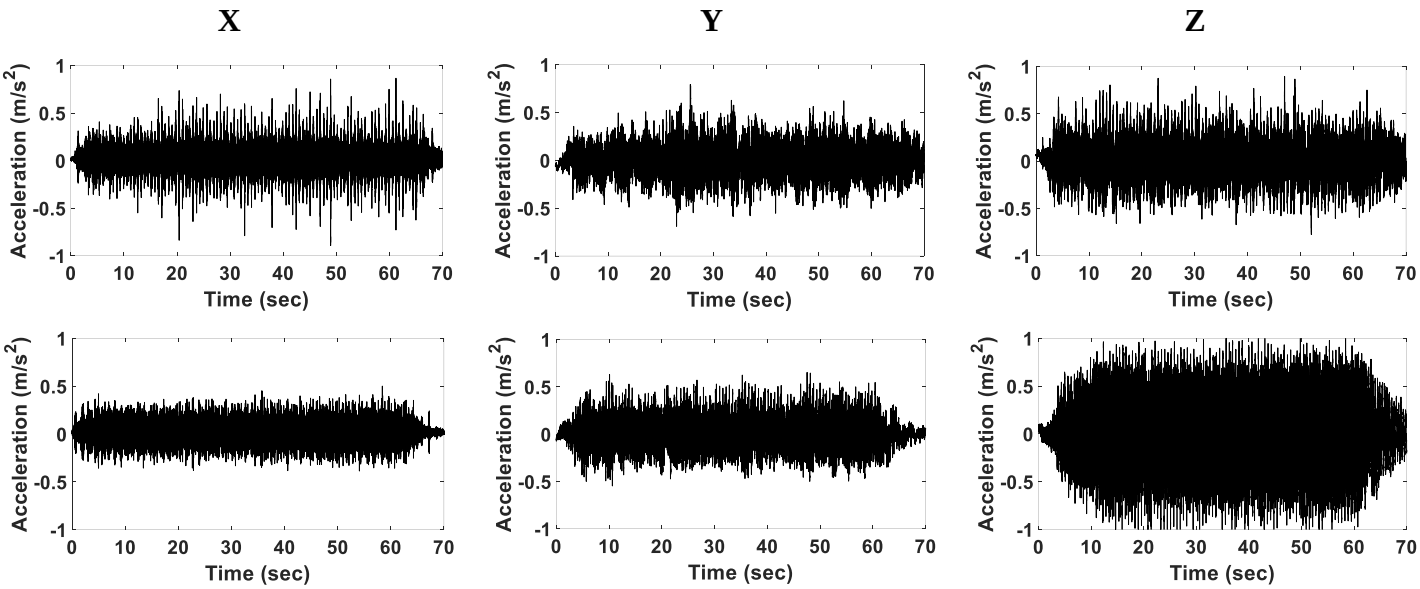

Figure 7. 23 Tower acceleration at X, Y, and Z directions at; a) 80 rpm, and b) 90 rpm.

Figure 7.24 shows tower vibrations at 100 rpm and 110 rpm. Rapid increases in tower vibrations, in the form of spikes, are found at the start of the time period and before the rotation stops. This rapid increase in tower acceleration (especially in the Y-direction) occurs due to the simultaneous increase in the blade out-of-plane vibrations and the centrifugal forces as the servo-motor speeds up. This vibration in the Y-direction is also exacerbated by the movement of the drive train masses in this direction, causing the tower to fluctuate even after the servo-motor stops. This effect occurs periodically during the experiments, which is especially obvious at high speeds, as seen in the speed range in this chapter.

Maximum tower acceleration at 100 rpm is 2.7 m/s^2 due to the spike at 62.6 sec., while it reduces to 2.1 m/s^2 at 110 rpm, at 60.6 sec.

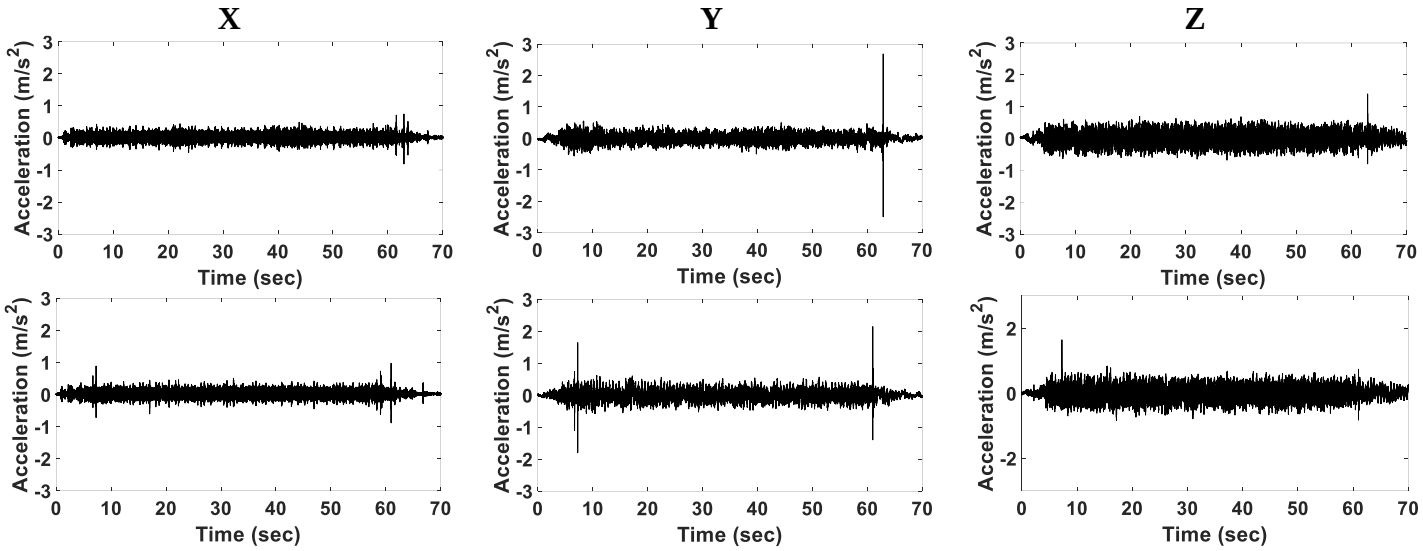

Figure 7. 24 Tower acceleration amplitudes at X,Y, and Z directions at; a) 100 rpm, and 110 rpm.

Figure 7.25 shows high tower acceleration in all directions at 120 rpm compared to the acceleration amplitudes in previous speeds, with maximum tower acceleration of -26.46 m/s^2 in the Y-direction. This is attributed to the increase in the Coriolis force which increases the blade out-of-plane vibrations, coupled with tower Y-direction vibrations.

On the other hand, an instantaneous increase in tower acceleration in the X and Z direction occurs at the same two-time instances: 38.76 sec and 43.23 sec. This indicates that the coupled vibration occurs simultaneously with the blade axial and in-plane vibrations at this speed due to rising in centrifugal force.

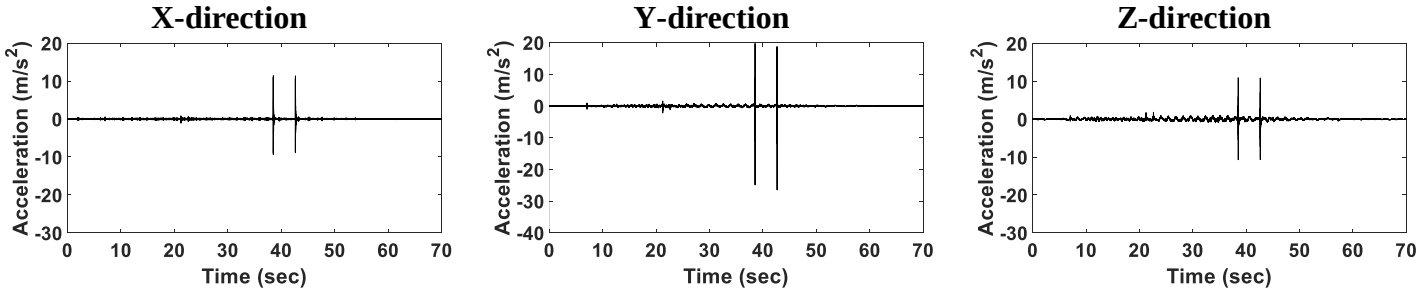

Figure 7. 25 Tower acceleration at X, Y, and Z directions at 120 rpm at; X, Y, and Z directions.

7.6 Influence of variable speeds on the test rig mechanical components

Wind turbines are always prone to variable wind gusts while working in harsh conditions. These conditions have been modelled by operating the servo-motor with variable torque. An investigation was undertaken to determine the effect of blade inertia of the rotating cantilever beam, and other parts of the drive train (e.g. the hub and drive shaft), on the non-rotating parts (e.g. the tower) in the test rig system at variable rotor speeds. Three different speeds have been considered for the experiment. Vibration monitoring during rotor variable speed helps to detect the behaviour of the mechanical components during sudden speed changes.

Figure 7.26 shows the change in shaft frequency during the speed changes from 0 rpm to 140 rpm, which reaches a maximum frequency at 2.33 Hz.

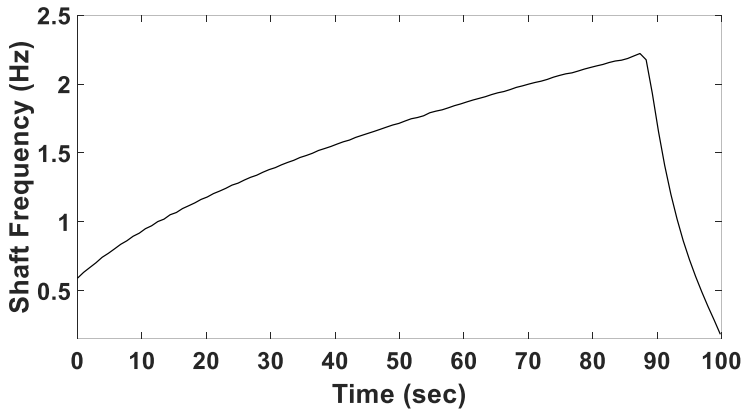

Figure 7. 26 Variation in shaft frequency during the test as speed varies from 0 rpm to 140 rpm.

7.6.1 Effect of variable speed on blade vibrational modes

Variable speeds have been utilized to excite the dynamic vibrations in the test rig components, as shown in figure 7.27. This figure shows the blade axial strain for variable speeds between 0 to 140 rpm. The average blade axial strain at a significant speed are; from 0 to 80 rpm the average axial strain is 290 µstrain; from 80 to 120 rpm the average axial strain is 365 µstrain; and from 120 rpm to 140 rpm the average

axial strain is 410 µstrain. Additionally, the rotor blade vibrated axially after the servo-motor stopped, as can be seen after the test time of 88 sec.

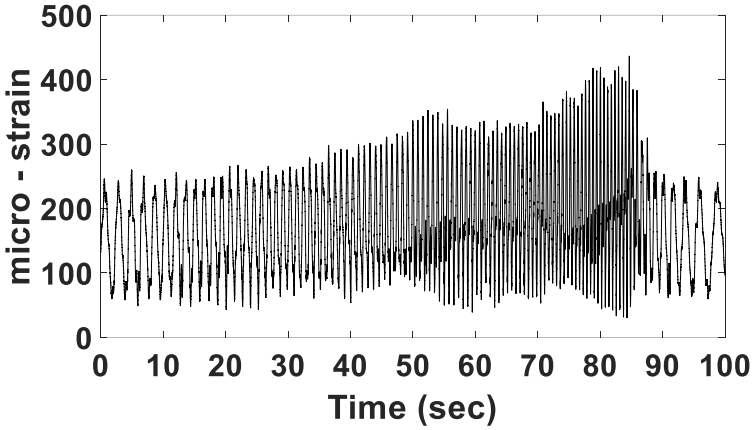

Figure 7. 27 Blade axial strain during variable speeds from 0 to 140 rpm.

Additionally, figure 7.28 shows blade in-plane strain measurements during the change in the rotor speeds for the same stages as mentioned above. Due to the coupling between axial and in-plane blade modes, increases in blade strain towards in-plane direction has been detected in the figure 7.28. The increase in the rotor speed further increased the dynamic bending of the rotating blade. The average in-plane strain is 811 µstrain for the speed interval from 0 to 80 rpm, 1060 µstrain for the speed interval from 80 rpm to 120 rpm, and 1170 µstrain for the speed interval from 120 rpm to 140 rpm.

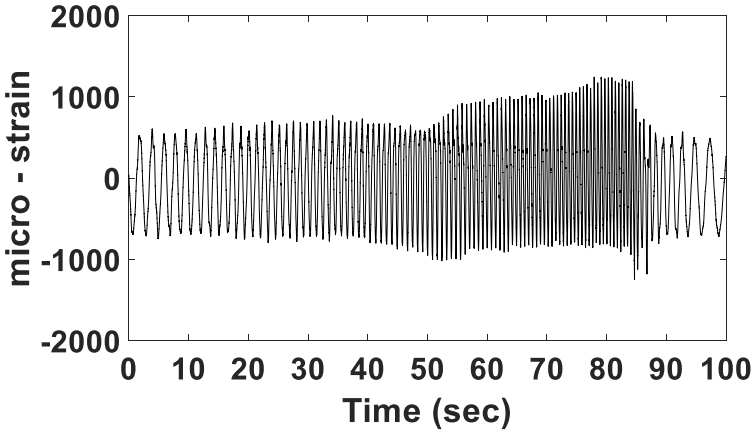

Figure 7. 28 Blade in-plane strain measurements during variable speed from 0 to 140 rpm.

Variable rotor speed has further excited the blade vibrations out-of-plane. Figure 7.29 illustrates blade strain out-of-plane during speeds from 0 to 140 rpm. The tendency of blade out-of-plane mode to increase on the compression side is attributed to the blade vibrating towards one direction more than the other. The average blade strain during the speed varies from 120 rpm to 140 rpm (which is the ultimate) is -610 µstrain.

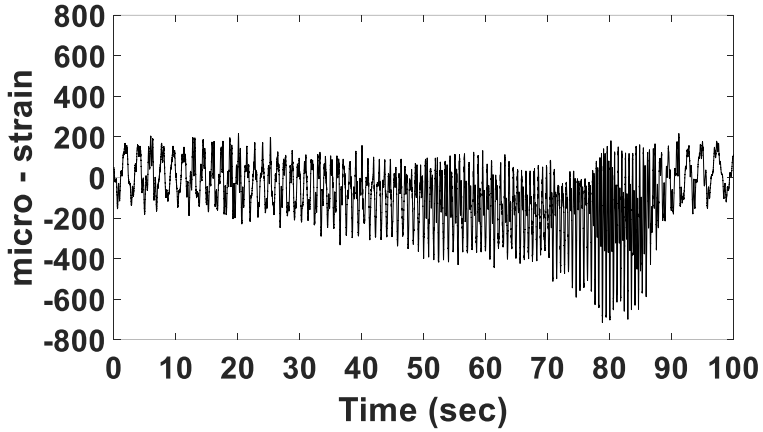

Figure 7. 29 Blade out-of-plane strain measurements during variable speeds from 0 to 140 rpm.

7.6.2 Effect of variable speed on the drive shaft vibration

Figure 7.30 shows the drive shaft dynamic displacements along axes 1 and 2 as the speed changes. Maximum displacement, 554 microns, along axis 1 occurs as the speed changes from 120 rpm to 140 rpm while maximum displacement along axis 2 is 260 microns. Furthermore, this figure shows the number of rotations during the experiment and the change in shaft amplitude as the speed changes. The shaft centre line displacement increases on the intervals of 0 to 60 rpm and 80 rpm to 140 rpm due to the increase in vibration of the rotating and non-rotating mechanical components in the test rig, which excites high shaft frequency.

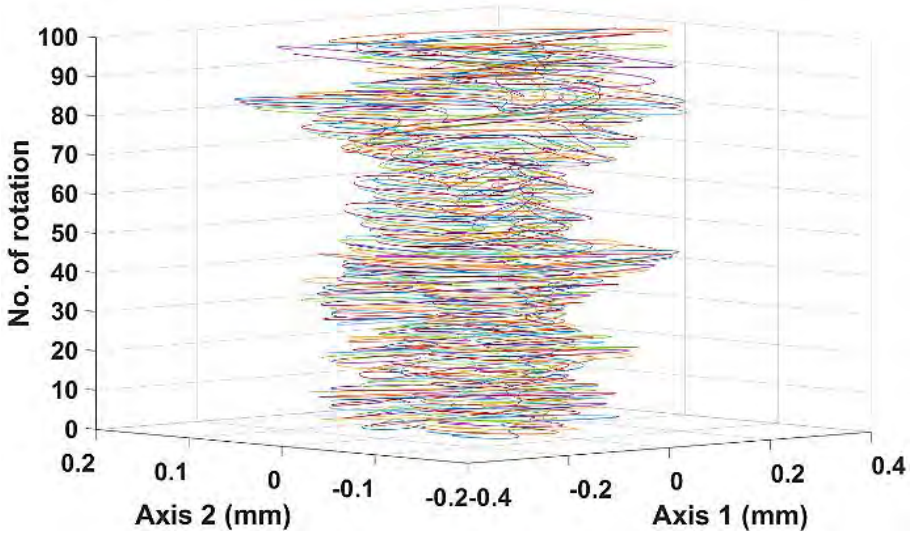

Figure 7. 30 Calculated shaft response during rotor speed variation from 0 - 140 rpm.

7.6.3 Effect of variable speed on the tower vibration

Tower vibrations increase towards the X, Y, and Z direction simultaneously with the increase in the blade and driveshaft vibrations. Figure 7.31 shows the increase in tower vibrations as the rotor speed increases from 0 rpm to 140 rpm, measured by the triaxial accelerometer positioned in the upper part of the tower. The tower achieved maximum vibrations in the Y-direction when the acceleration reached -33.87 m/s^2. However, tower acceleration towards both X and Z directions were 15.3 m/s^2 due to the rapid speed change exciting high back and forth fluctuations. Furthermore, the spikes at 58.8 sec, 67.4 sec, and 70.1 sec indicate that there was vibration synchronization between the rotor blade and tower modes.

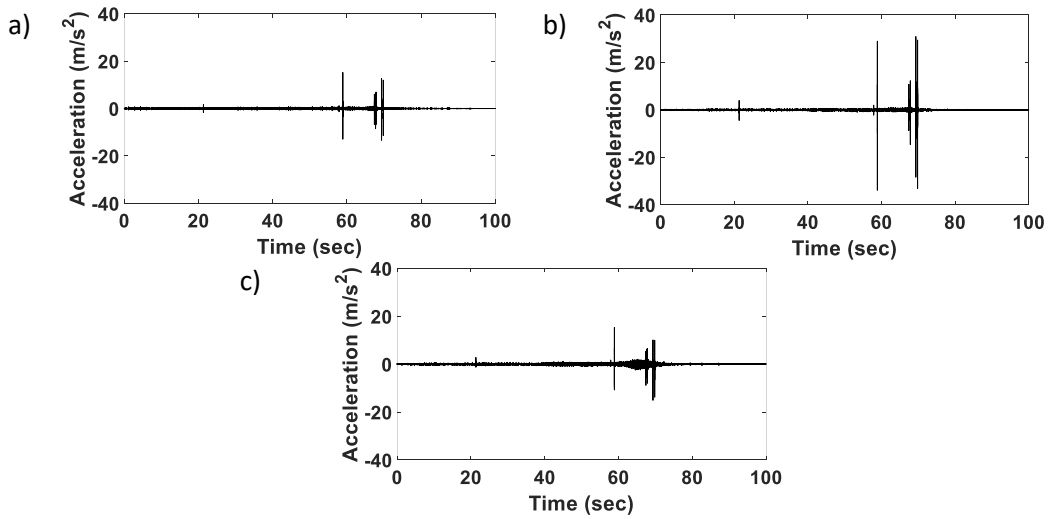

Figure 7. 31 Tower acceleration amplitudes measured by the triaxial accelerometer due to speed variation from 0 - 140 rpm at directions; a) X, b) Y, and c) Z.

Figure 7.32 illustrates the variation in the tower response during the rotor speed change from 0 rpm to 140 rpm. There was an increase in tower acceleration after the 80th rotation due to the speed increasing up to 140 rpm, showing that the vibration response can be monitored during variable speed tests. This figure can further identify the change in the amplitude along the Y and Z axes as the speed increases. The continuous tower vibration imposes fatigue stresses on the foundation welding joints.

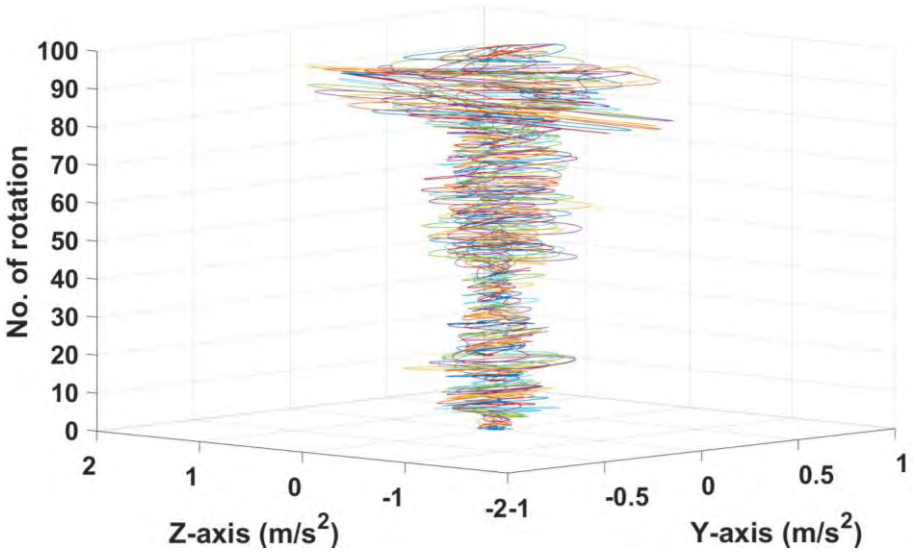

Figure 7. 32 Calculated tower acceleration during variable speed from 0 - 140 rpm

7.7 Conclusion

This chapter presents rotor speed tests on the dynamic behaviour of the rotating blades, drive shaft, and supported tower on the horizontal axis wind turbine test rig. Increases in blade axial vibration as speed increases (particularly after 70 rpm) can be observed due to the increase in the centrifugal forces along the blade model. This increase reaches the maximum amplitude at 120 rpm, which was the maximum speed used. The coupling that exists between blade axial and in-plane modes is exacerbated due to the increase in the vibrations towards in-plane direction with increasing speed. This increase is attributed to the increase in the dynamic bending of the rotating blade with increasing in speed. Increasing the rotor speed excites the blade vibrations towards out-of-plane direction. This can be identified through the increase in the blade out-of-plane strain on the compression side, which reaches the maximum amplitude at 120 rpm. This was attributed to the increase in Coriolis forces as the speed increases.

The drive shaft vibrations have further increased with increases in speed similar to the rotating components in the test rig. The increase in shaft amplitude varies corresponding to axes 1 and 2. Furthermore, it has been seen that as the rotor speed increases, shaft bending increases towards axis 1 greater than axis 2. The blade and tower vibrations have a positive affect on the shaft vibrations. This was pronounced through the shaft centreline orbits (1^{st} harmonic) shifting to the left at 100 rpm and 110 rpm, and shifting to the right close to 90 rpm. In the 2^{nd} harmonic, changes in the shaft centreline orbit occur at 90 rpm and similarly at 120 rpm, which take the same shape with an expansion towards axis 2.

Blade vibration excites tower dynamic bending due to the coupling effect between the blade and tower vibrational modes. Blade axial and in-plane dynamic bending drags the tower to bend sideways (Z-direction), whereas, blade out-of-plane bending (edgewise vibration) causes tower bending towards back and forth (Y-direction). These effects increase with an increase in speed, hence, high acceleration amplitudes are expected at 120 rpm. This technique provides a significant method for monitoring the drive train response, and the potential fault of the test rig components during different speed range.

New loading conditions with speed effect will be considered in the next chapter for monitoring the behaviour of the test rig components.

Chapter 8 Investigation of blade vibration for different loading conditions by case studies in the small-scale horizontal-axis wind turbine test rig.

8.1 Introduction

The vibration characteristics of the blades of a wind turbine vary during its working conditions. The coupling of the vibration which is found between the blade's structure and the turbine components increases the occurrence of failure. To help learn how to diagnose these faults in a real wind turbine, data was accumulated from artificial faults implemented in a horizontal small-scale wind turbine test rig. Hence, this chapter addresses different blade imbalance and transient loading case studies, and the coupling effect on the tower and drive shaft vibrations in different directions.

8.2 Influence of imbalance effect on the blade vibrational modes.

Artificial imbalances were applied to the horizontal-axis wind turbine test rig through attaching additional masses to the blades. A 200g mass has been attached on one blade to simulate an imbalance. In addition, two 200g masses were attached on two out of three blades to simulate a loss mass imbalanced effect. Five speeds have been considered in this chapter for vibration condition monitoring of the rotating blade.

8.2.1 Effect of additional mass condition (AMC) and loss mass condition (LMC) on blade axial vibration.

This type of fault is prevalent in wind turbine blades due to harsh working conditions. Five rotor speeds have been considered for blade vibration monitoring: 40 rpm, 60 rpm, 80 rpm, 100 rpm, and 110 rpm. Rotor speeds over 110 rpm created problems in the data acquisition system due to a high-frequency vibration negatively impacting the test rig components.

Figure 8.1 illustrates blade axial strain measurements during both AMC and LMC at 40 rpm, 60 rpm, 80 rpm, 100 rpm, and 110 rpm. In figure 8.1a, maximum strain due

to AMC is 258.9 µstrain while for the LMC it is 256.8 µstrain, resulting in a difference of 2.1 µstrain. The small difference in the two strains is attributed to the low speed. Figure 8.1b shows blade axial strain at 60 rpm for both AMC and LMC. It can be seen the difference in the blade vibrations between both imbalance cases is 118 µstrain, which resulted from a maximum of 386.5 µstrain for AMC and a maximum of 268.5 µstrain for LMC.

Increasing the rotor speed to 80 rpm leads to an increase in blade vibrations due to the increase in imbalance and centrifugal forces. Maximum axial strain at this speed is 352.9 µstrain for AMC and 321.5 µstrain for LMC to make a difference of 31.4 µstrain between the case studies. At 100 rpm, the maximum blade strain for AMC is 396 µstrain, which has a difference of 46 µstrain with LMC, 350 µstrain, due to the increase in centrifugal forces in one direction (in the direction of the acceleration of the additional mass). A significant increase was found at 110 rpm, where it can be seen that the blade vibration for AMC produced its maximum strain (665 µstrain). However, the maximum strain for LMC was 367 µstrain, which was not as much as for AMC, to make a maximum difference of 298 µstrain.

The increase in blade inertia due to the additional mass increases the centrifugal force in one direction, which leads to an increase in blade axial vibration. This increase doesn't occur for the LMC, since the increase in centrifugal forces at the other two blades compensates for the lack of centrifugal forces that resulted from the mass loss.

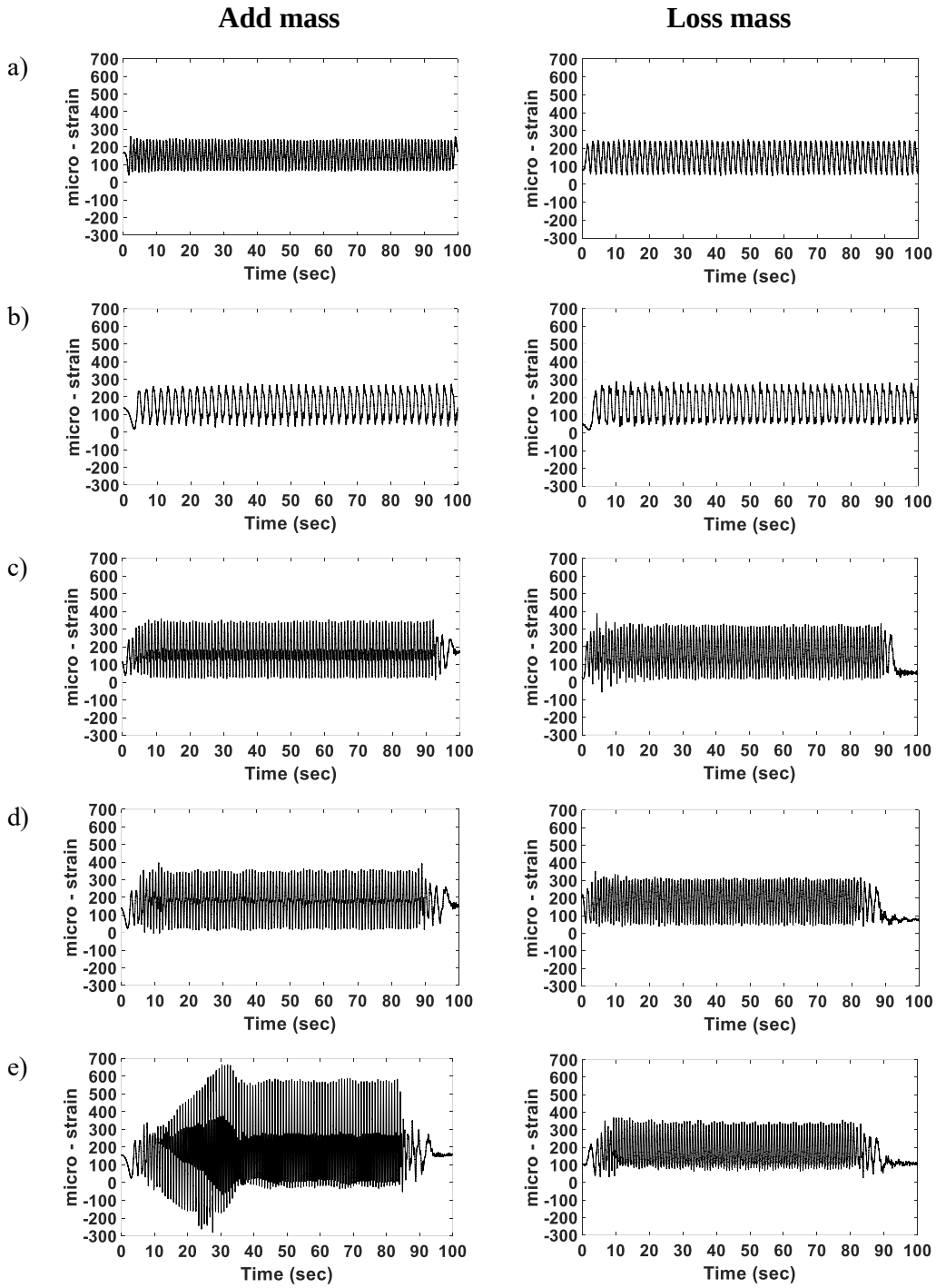

Figure 8. 1 Axial strain measurements during added and loss 200g imbalance mass from the rotating blade at a) 40 rpm, b) 60 rpm, c) 80 rpm, d) 100 rpm, and e) 110 rpm.

Figure 8.2 shows the blade average axial strain over one revolution at significant speeds for both AMC and LMC. As previously stated, adding 200g mass to the rotating blade increases axial vibrations, but with small amplitudes as in figures 8.2a and 8.2b corresponding to 40 rpm and 60 rpm respectively. Maximum average strain during 40 rpm is 240.3 μstrain for the AMC, while for the LMC it is 238.2. Additionally,

increasing rotor speed to 60 rpm (figure 8.2b) increases average axial strain to 259.2 µstrain for AMC and 257.4 µstrain for LMC. Shifting the average axial strain to the right was seen during AMC at 80 rpm when the amplitude reaches to 333.6 µstrain which is the maximum value as in figure 8.2c. Increasing the rotor speed to 100 rpm for AMC shifts the average axial strain slightly to the right to reach the maximum amplitude of 340.6 µstrain. Increasing rotor speed to 110 rpm, increases the blade axial strain for both imbalance effects, namely AMC and LMC, to the maximum amplitudes of 450 µstrain and 330 µstrain respectively, as in figure 8.2e.

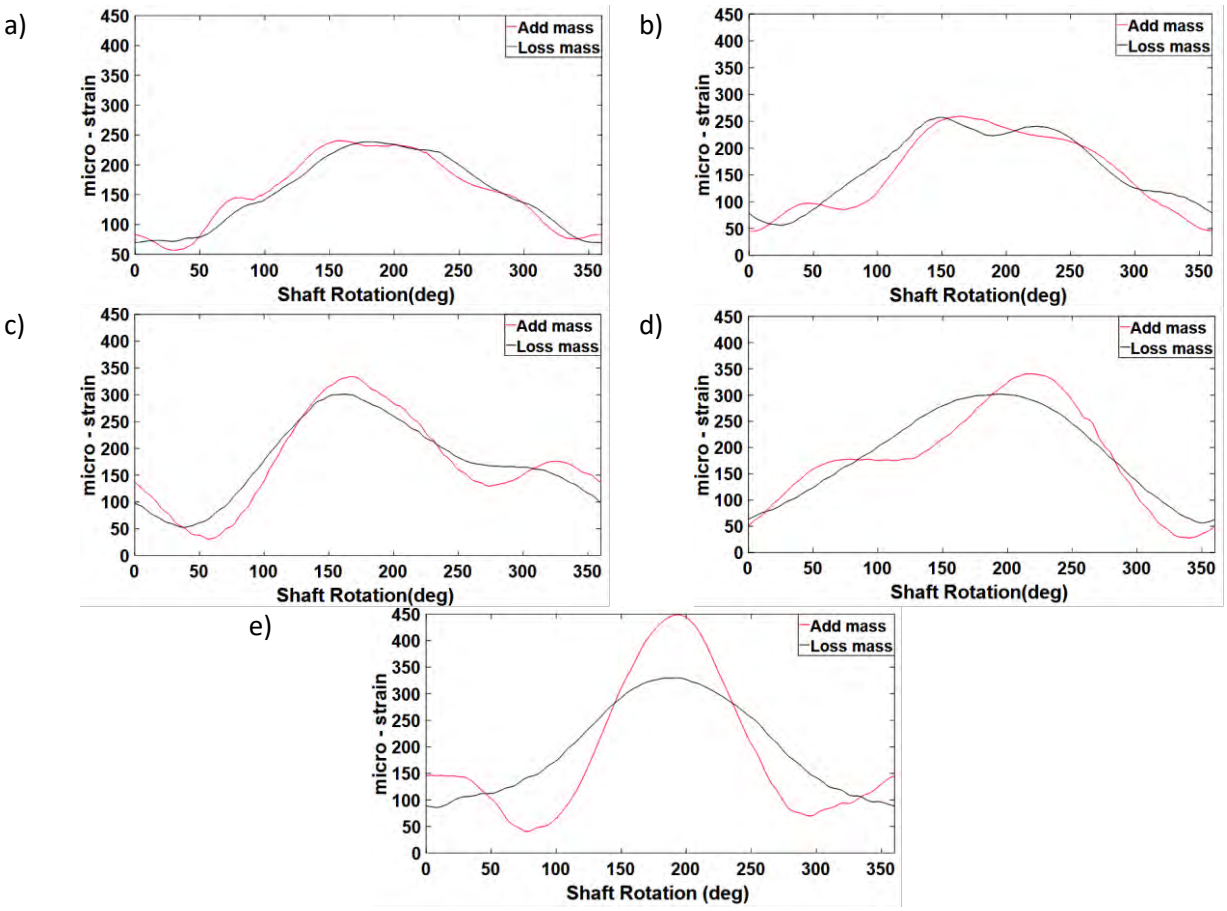

Figure 8. 2 Blade axial strain measurements over exactly one revolution during AMC and LMC at; a) 40 rpm, b) 60 rpm, c) 80 rpm, d) 100 rpm, and e) 110 rpm.

8.2.2 Effect of additional mass condition (AMC) and loss mass condition (LMC) on blade in-plane vibration.

Figure 8.3 illustrates blade in-plane vibrations for five rotor speeds, namely 40 rpm, 60 rpm, 80 rpm, 100 rpm, and 110 rpm. In figure 8.3a, blade in-plane strain (at 40 rpm) increases for both LMC and AMC with a small difference between the two unbalance conditions (average blade in-plane strain is 742.5 µstrain for AMC and 671 µstrain for LMC). At 80 rpm, blade average in-plane strain increases towards the compression side to reach 1012.6 µstrain for AMC and 919.1 µstrain towards tension side for LMC. This is due to the fact that the increases in speed results in increases of the additional mass effect. Subsequently, average in-plane blade strain for AMC increases at the compression side at the same rate with the tension side when the speed goes to 100 rpm (maximum in-plane strain reaches to 1140 µstrain), however, at LMC maximum blade in-plane strain is 1117.4 µstrain towards tension side. The effect of the additional mass increases the blade bending towards the rotation plane, which increases with the speed. In contrast, the loss of mass on the rotor blade, shows that the in-plane strain increases nearly at the same amount towards positive and negative components. Tower vibration effects appear at 80 rpm and 100 rpm in the blade in-plane strain after the rotation stops (after the time 88 seconds in figures 8.3c and 8.3d).

Increasing the blade speed to 110 rpm increases the imbalance forces, which leads to an increase in the vibration in all the directions, as shown in figure 8.3e. The blade in-plane strain reaches the ultimate of 2420 µstrain for AMC and 1215 µstrain for LMC. Additionally, tower vibration towards the Y and X-directions has a pronounced effect on the blade in-plane vibration even after the rotation stops.

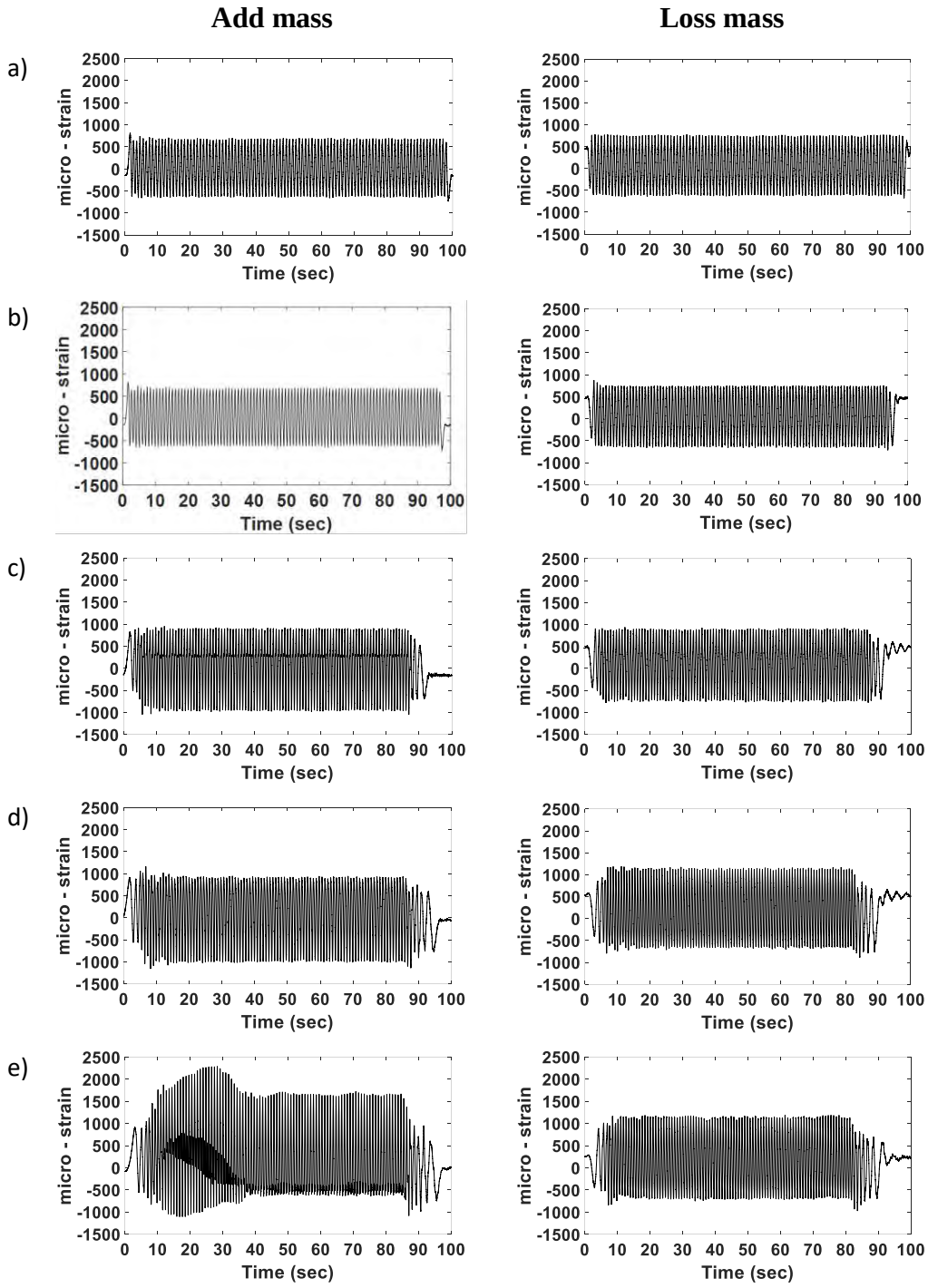

Figure 8. 3 Blade in-plane strain measurements during imbalance conditions of AMC and LMC at; a) 40 rpm, b) 60 rpm, c) 80 rpm, d) 100 rpm, and e) 110 rpm.

Figure 8.4 shows the change of average blade in-plane strain over one revolution during the unbalance effect. The in-plane strain amplitudes increase towards the compression side from 670 µstrain at 40 rpm to 1000 µstrain at 100 rpm for AMC, whereas, the in-plane strain amplitudes tend to increase towards the positive side (1590

μstrain) when the blade speed reaches 110 rpm. On the other hand, an increase in average blade in-plane strain for LMC is from 604.4 μstrain at 40 rpm to 671.6 μstrain at 110 rpm.

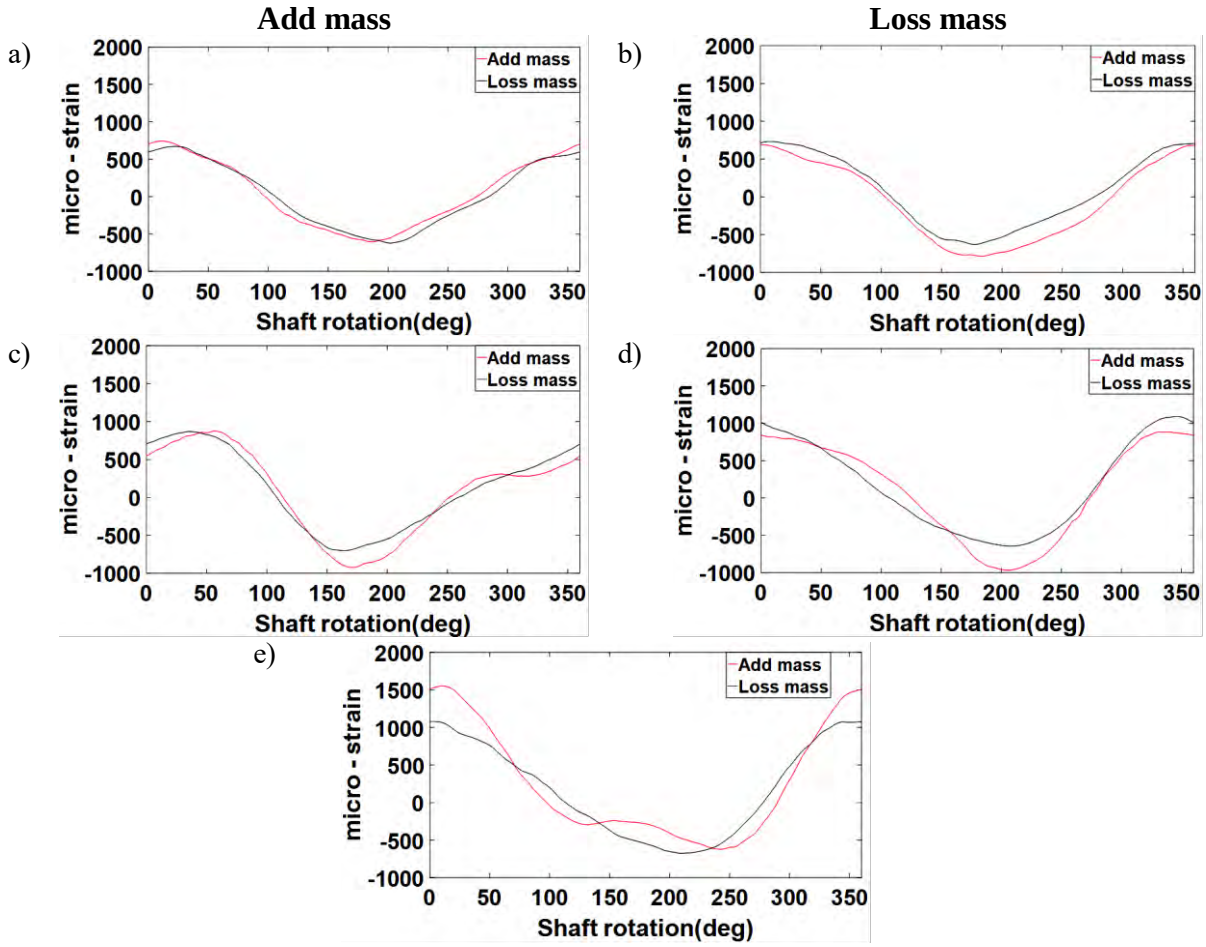

Figure 8. 4 Blade in-plane strain measurements over exactly one revolution during AMC and LMC at; a) 40 rpm, b) 60 rpm, c) 80 rpm, d) 100 rpm, and e) 110 rpm.

8.2.3 Effect of additional mass condition (AMC) and loss mass condition (LMC) on blade out-of-plane vibration.

While implementing the artificial imbalance effects, it was found that blade out-of-plane vibrations increase as blade speed increases. Figure 8.5 shows the blade out-of-plane strain measurements at rotor speeds of 40 rpm, 60 rpm, 80 rpm, 100 rpm, and 110 rpm. The variation of blade out-of-plane strain for AMC while the speed increases from 40 rpm to 60 rpm is 4.6 µstrain, while for LMC it is 7.6 µstrain. Increasing the speed to 80 rpm increases the blade's average out-of-plane strain to 421.3 µstrain, which make the variation reach 207.7 µstrain for AMC (average out-of-plane at 60 rpm is 213.6 µstrain). However, the variation for LMC reaches 162.4 µstrain.

Figure 8.5d, show increases in the blade out-of-plane strain towards the negative side for both AMC and LMC due to increases in blade vibration. The maximum strain reaches 585.6 µstrain for AMC and 485.2 µstrain for LMC. Increasing the rotor speed to 110 rpm increases the dynamic vibrations in all test rig components while the blade out-of-plane strain increases towards the negative side. This can be seen in figure 8.5e for both AMC and LMC. The increase in out-of-plane strain for AMC (Maximum strain=1550 µstrain) is greater than LMC (Maximum strain=570 µstrain). Tower vibrations towards the Y-direction have a direct effect on this blade vibrational mode as the rotor speed increases. This is due to the coupling between the blade out-of-plane and tower Y-direction vibrations.

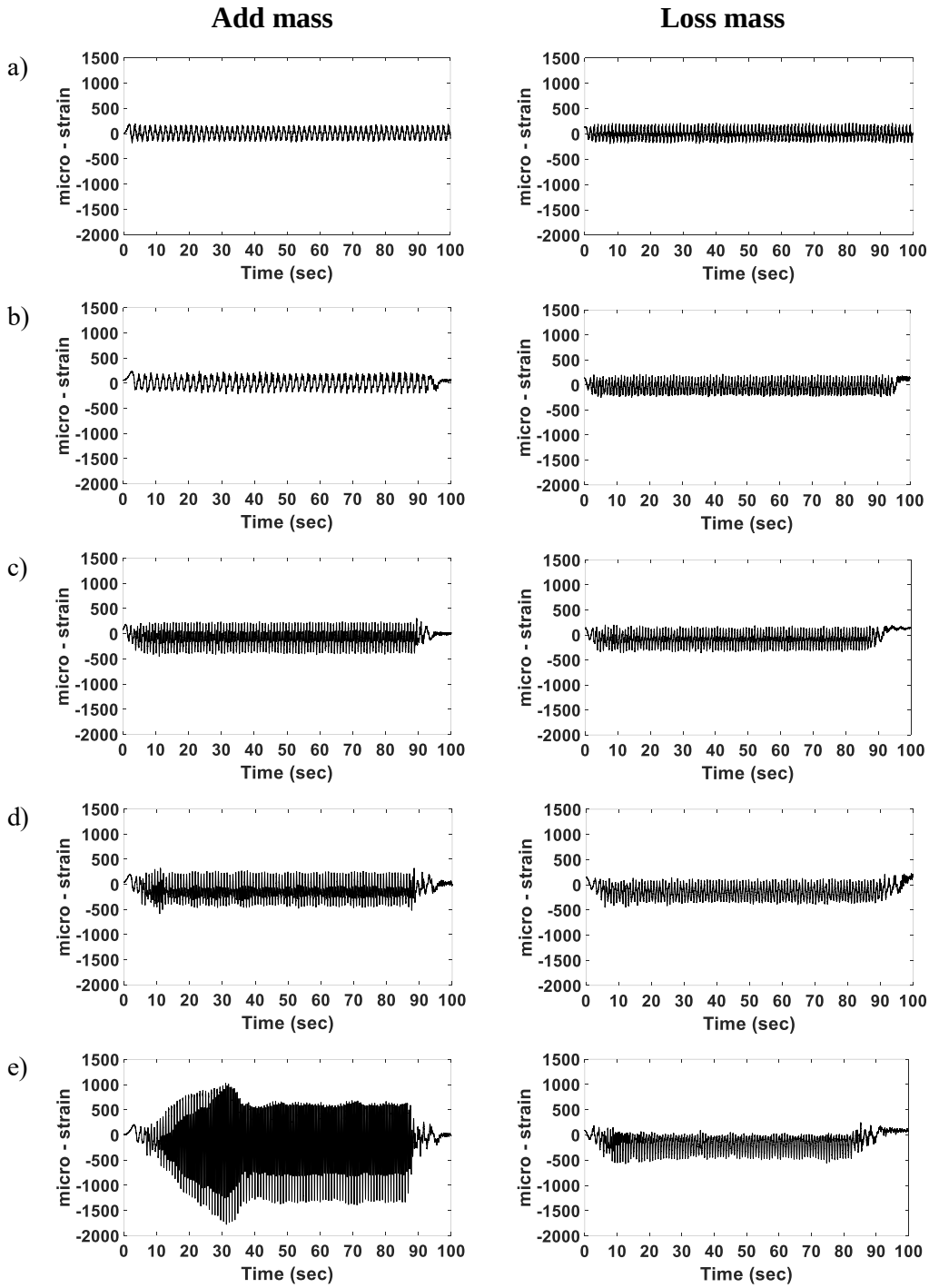

Figure 8. 5 Blade out-of-plane strain measurements during both imbalance conditions of AMC and LMC at; a) 40 rpm, b) 60 rpm, c) 80 rpm, d) 100 rpm, and e) 110 rpm.

Figure 8.6 shows the blade out-of-plane strain over exactly one revolution during the applied artificial imbalances at the significant rotor speeds. In figure 8.6, shows the increase in blade out-of-plane strain towards the negative side when rotor speed increases, as shown in the raw signal above. The average out-of-plane strain at 40 rpm

is 184.2 µstrain during the AMC and 135.4 µstrain during the LMC. At 60 rpm, the average strain for the AMC increases to 200 µstrain, whereas, for the LMC the average strain increases towards the negative side to reach 196.5 µstrain as indicated in figure 8.6b. After that, the average out-of-plane strain of both AMC and LMC increase at the negative side when the rotor blade speed increases to 80 rpm. The average strain at this stage is 360.4 µstrain and 288.4 µstrain for both the AMC and LMC respectively. as shown in figure 8.6c.

Finally, the increase in the blade out-of-plane strain at the negative side is higher than that above when the rotor blade speed increases to 110 rpm. The average strain for the AMC is 918.7 µstrain and 531.2 µstrain for the LMC as illustrated in figure 8.6e.

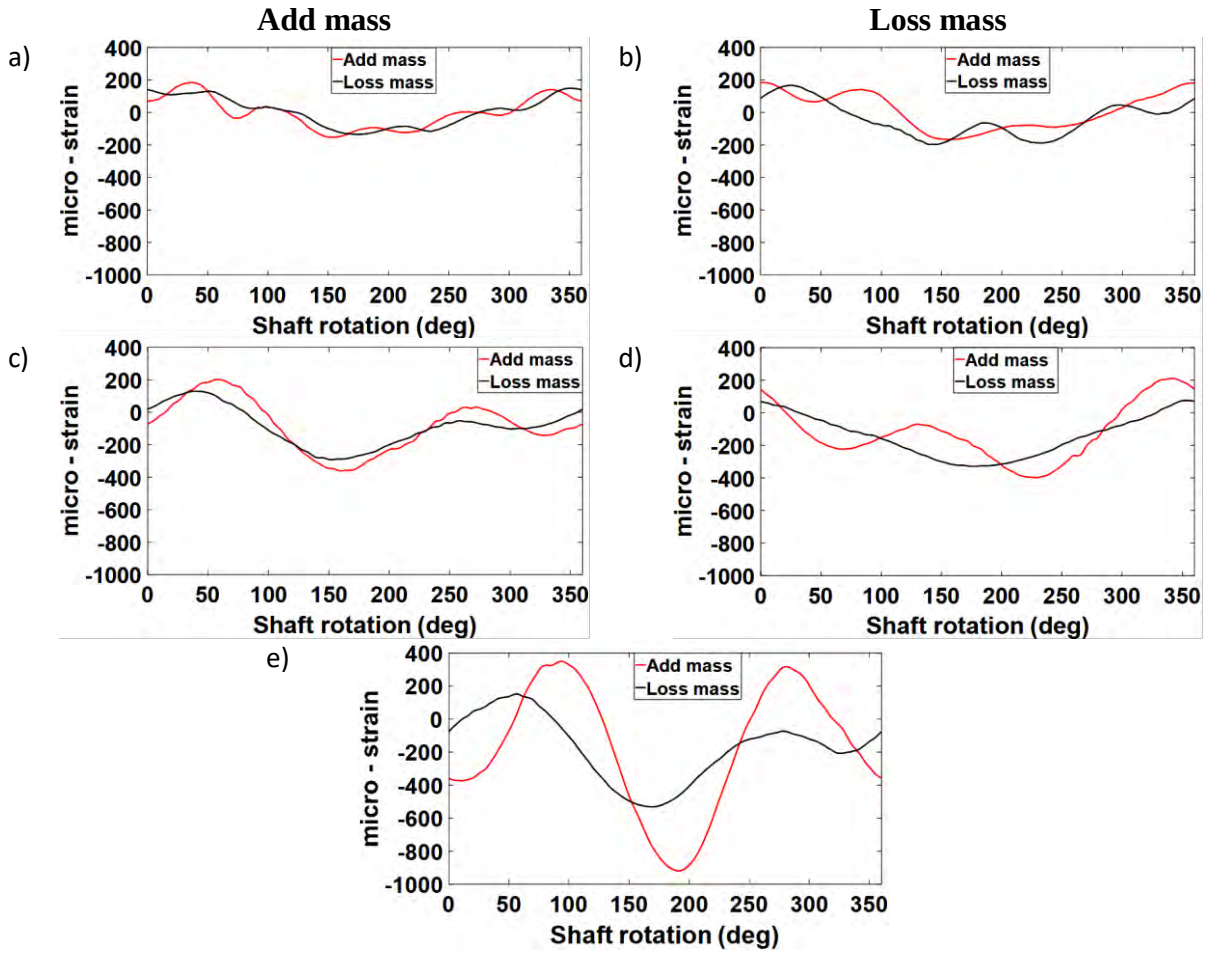

Figure 8. 6 Blade out-of-plane strain per one revolution during imbalance conditions of AMC and LMC at; a) 40 rpm, b) 60 rpm, c) 80 rpm, d) 100 rpm, and e) 110 rpm.

8.2.4 Influence of additional mass condition (AMC) and loss mass condition (LMC) on blade acceleration

Monitoring acceleration amplitude changes during the test is a technique for detecting the variation in blade vibration. Figure 8.7 illustrates the increase in the blade acceleration during speed increases at LMC, for three significant speeds. In figure 8.7a, maximum acceleration amplitude is 33.78 m/s^2 at 40 rpm. This amplitude increases to 41.23 m/s^2 at 60 rpm as shown in figure 8.7b due to an increase in vibration when blade speeds increase. At 80 rpm, the acceleration increases sharply to reaches 550 m/s^2 (maximum acceleration), as illustrated in figure 8.7c due to the imbalance effect with speed increases.

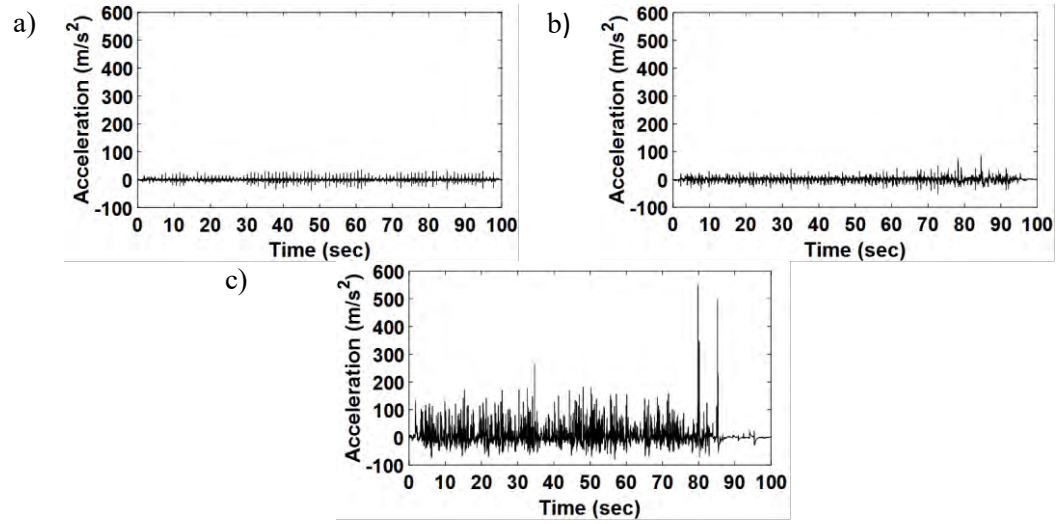

Figure 8. 7 Blade acceleration amplitude measured by the piezoelectric accelerometer during LMC at; a) 40 rpm, b) 60 rpm, and c) 80 rpm.

Figure 8.8 shows high acceleration amplitude while applying 200g additional mass (AMC), compared to the above results. In figure 8.8a, maximum acceleration amplitude is 1608 m/s^2 at 40 rpm, whereas it rises to 2142 m/s^2 at 60 rpm and again increases to 2681 m/s^2 when the speed increases to 80 rpm. The spikes in figures 8.8b and 8.8c showing acceleration values of 5764 m/s^2 and 10000 m/s^2 at 60 rpm and 80 rpm respectively are due to tower vibration at the rotation starts resulting from coupling between blade and tower vibrations. The difference between AMC and LMC

at the first three significant speeds is apparently shown in the acceleration amplitude, measured by the piezoelectric sensor.

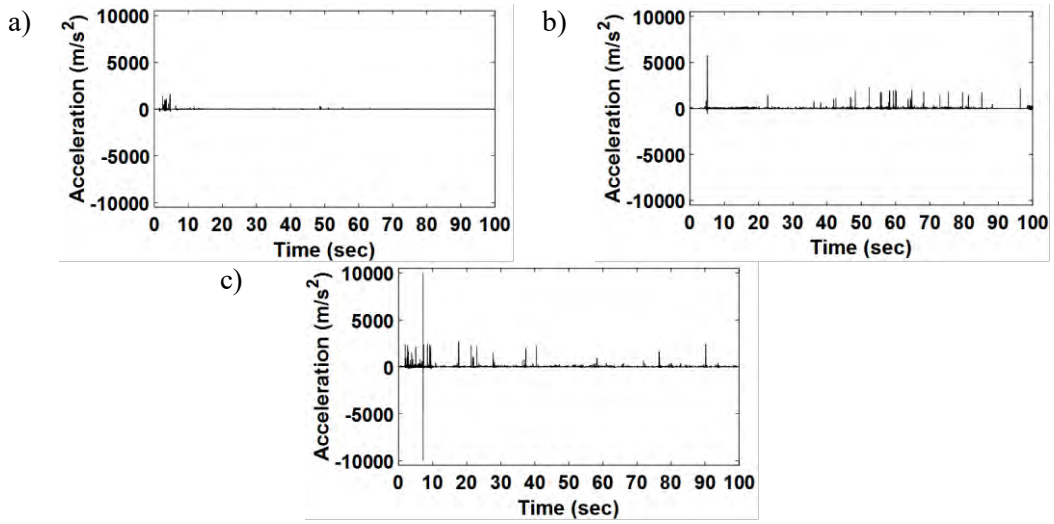

Figure 8. 8 Blade acceleration amplitude measured by the piezoelectric accelerometer during AMC at; a) 40 rpm, b) 60 rpm, and c) 80 rpm.

At 100 rpm, high acceleration amplitude can be noted in figure 8.9 where blade vibrations increase in the rotation plane when the rotor speed reaches the required speed. Maximum acceleration in AMC imbalance is 10000 m/s^2, whereas, in LMC it is 8583 m/s^2 as shown in the figures below.

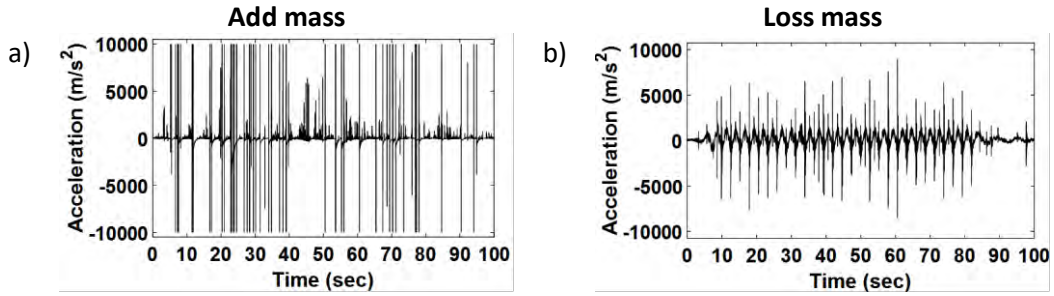

Figure 8. 9 Blade acceleration amplitude measured by the piezoelectric accelerometer during AMC and LMC at 100 rpm.

Figure 8.10 shows the highest acceleration amplitude at 110 rpm, which is measured by the piezoelectric accelerometer during these significant speeds. Different signal

attitude can be seen in AMC and LMC in the figure below with a maximum value of 10000 m/s^2 for both imbalance effects. As mentioned above, tower vibrations are affected by the blade vibrations while applying the artificial blade imbalance, due to the coupling between blade and tower vibrational modes. This coupling increases the horizontal axis wind turbine test rig vibration during speed increases.

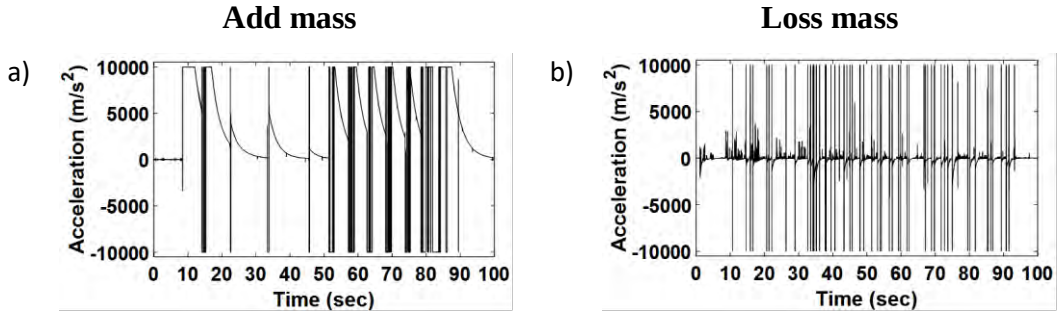

Figure 8. 10 Blade acceleration amplitude measured by the piezoelectric accelerometer during AMC and LMC at 110 rpm.

8.2.5 Effect of additional mass condition (AMC) and loss mass condition (LMC) on the drive shaft vibrations

The imbalance condition affected the drive shaft behaviour during speed changes. Figure 8.11 illustrated shaft bending displacement towards axis 1 during AMC and LMC. Maximum shaft displacement at AMC 750 microns occurs at 110 rpm as shown in figure 8.11e, while figure 8.11a shows the minimum shaft displacement of 540 microns at 40 rpm. While the rotor speed changes from 40 rpm to 110 rpm, shaft bending displacement varies from 630 microns at 60 rpm to 660 microns at 100 rpm. However, in LMC, there is an increase in the shaft displacements as the rotor speed increases from 40 rpm (shaft displacement is 530 microns) to 100 rpm (shaft displacement reaches 550 microns). A decrease in shaft displacement to 500 microns has been noted as the speed increases to 110 rpm. This is attributed to reducing the rotary inertia on the rotor as a result of the decrease in blade mass.

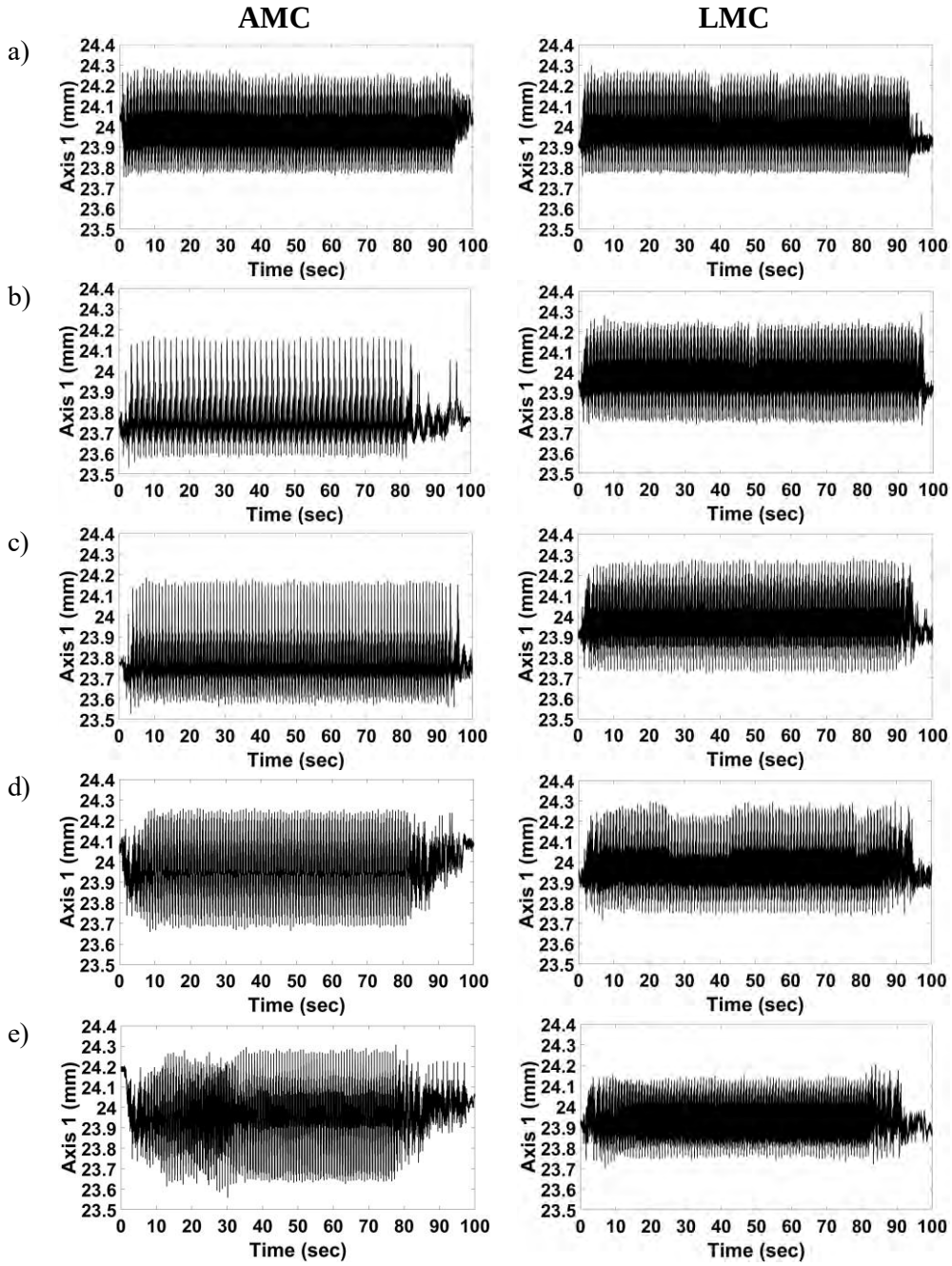

Figure 8. 11 Shaft bending displacement towards axis 1 during applied AMC and LMC imbalances at; a) 40 rpm, b) 60 rpm, c) 80 rpm, d) 100 rpm, and e) 110 rpm.

Additionally, figure 8.12 shows the shaft displacements at axis 1 over one revolution during the AMC and LMC as the speed increases from 40 rpm to 110 rpm. Maximum shaft displacement amplitude (570 microns) during AMC occurs in figure 8.12e at 110 rpm, whereas, minimum shaft amplitude (130 microns) occurs in figure 8.12a at 40 rpm. The additional mass effect becomes significant on the rotor blade during the speed of 100 rpm when the shaft amplitude reaches 244 microns. This effect decreases

at 80 rpm and 60 rpm when the shaft amplitude reaches 190 microns and 140 microns respectively.

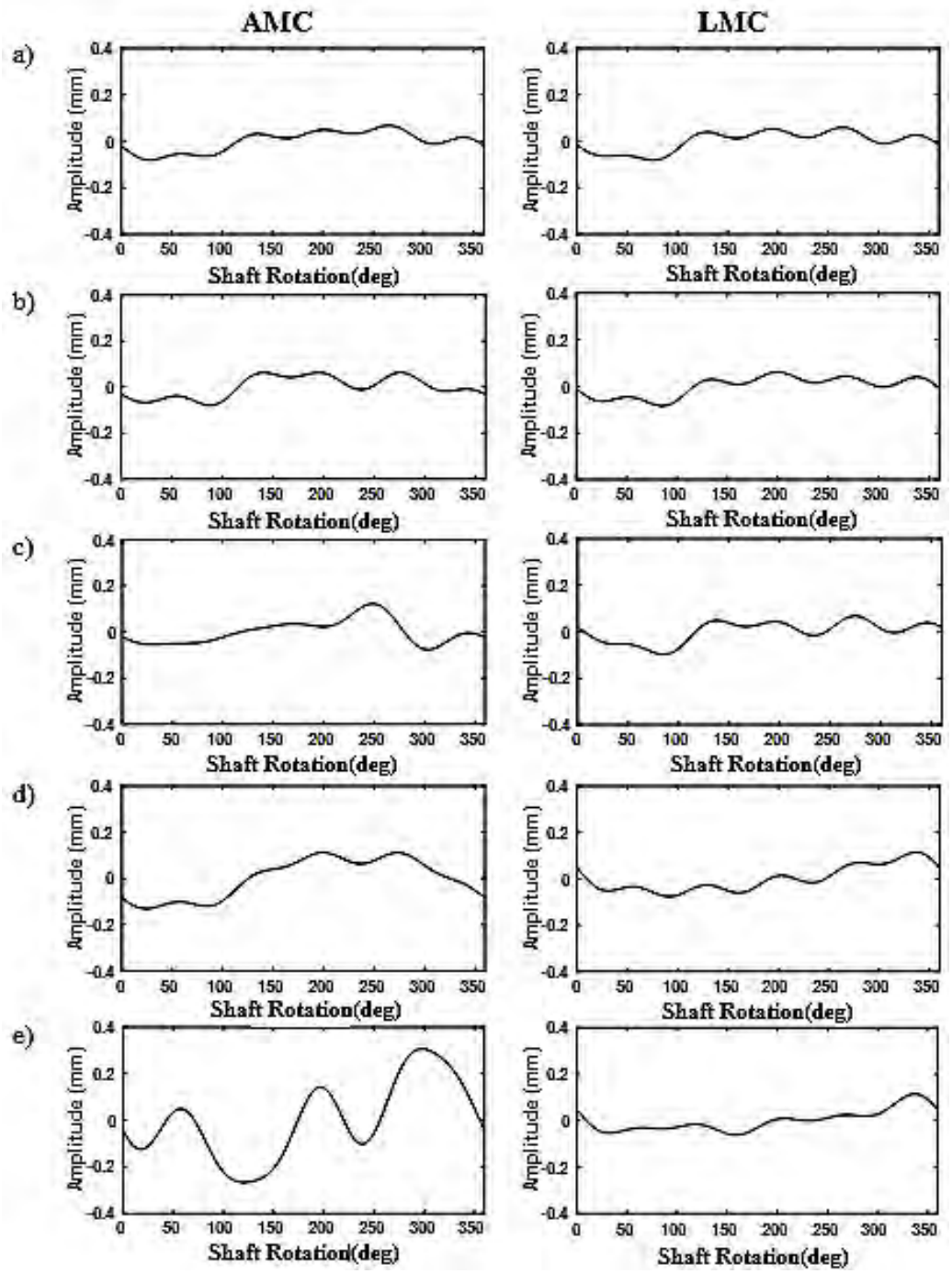

Figure 8. 12 Shaft amplitude over exactly one revolution during applied AMC and LMC on the rotor blade at; a) 40 rpm, b) 60 rpm, c) 80 rpm, d) 100 rpm, and e) 110 rpm.

The decrease in the rotor blade inertia resulting from the loss of 200 g mass has a pronounced effect on the drive shaft amplitude, as shown in figure 8.13 which indicates the shaft bending towards axis 2. Adding a mass to the rotating blade

increases shaft bending displacement as the rotor speed increases. The increase in shaft bending during AMC is obvious at 100 rpm and 110 rpm when the bending displacement reaches 230 microns and 504 microns respectively. However, at LMC, a small change can be noted in the shaft amplitude corresponding to AMC. Maximum shaft displacement in the LMC is 220 microns at 110 rpm, while, the minimum shaft displacement is 174 microns at 40 rpm. Furthermore, the coupling effect between blade vibrations and shaft bending can be noted after rotation stops (after 88 sec.) in most of the speeds, which can be seen when the shaft still vibrates after the test stops due to the excitation from the blade vibrations (80 microns average displacement after the 88 sec.).

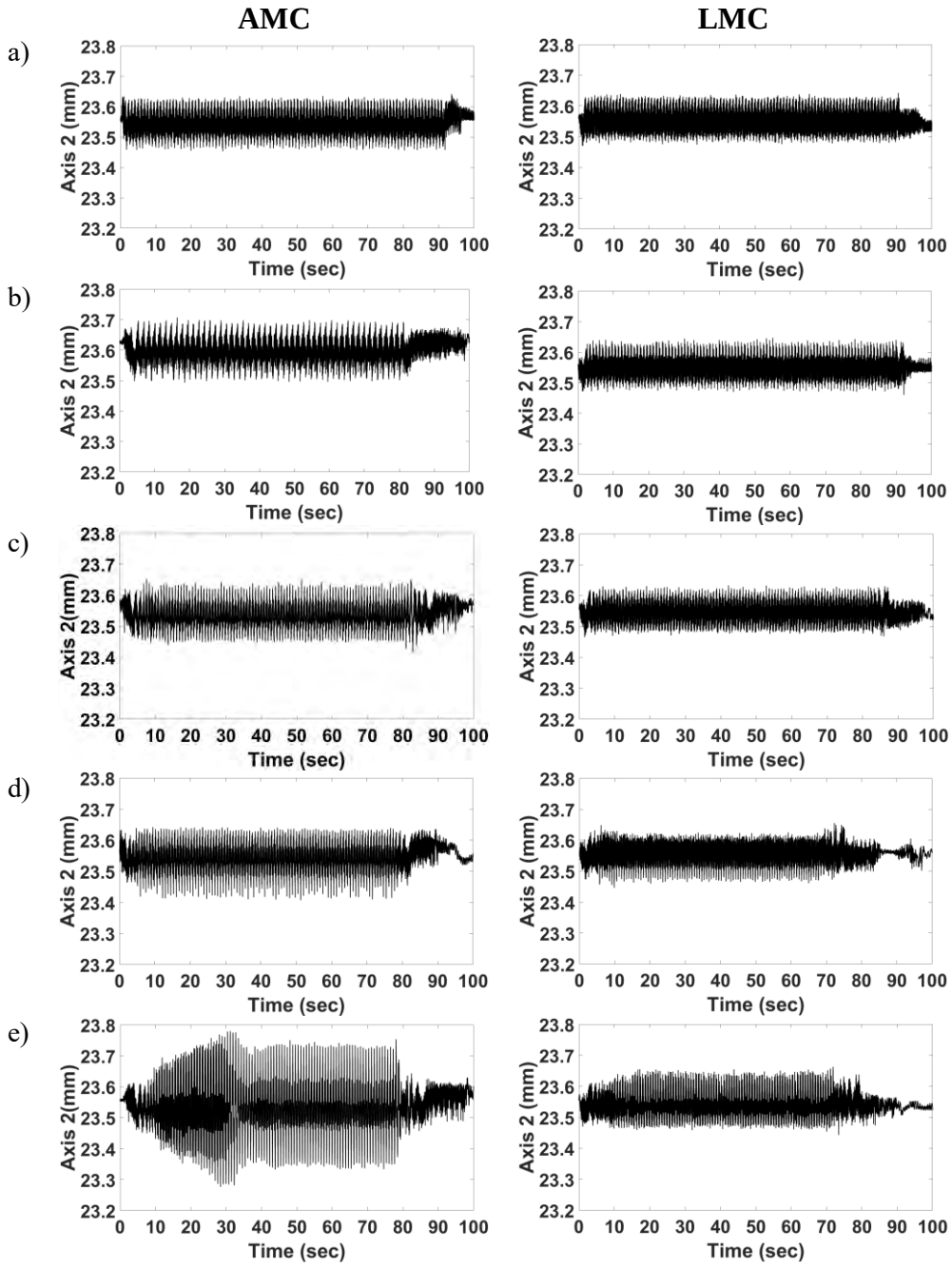

Figure 8. 13 Shaft bending displacement towards axis 2 during applied AMC and LMC imbalances at; a) 40 rpm, b) 60 rpm, c) 80 rpm, d) 100 rpm, and e) 110 rpm.

Additionally, figure 8.14 illustrates the drive shaft bending displacement over one revolution towards axis 2. A similarity in the amplitude attitude can be recognized in figures 8.14a and 8.14b in the AMC and LMC at 40 rpm and 60 rpm. Maximum shaft displacement is 330 microns in AMC at 110 rpm, as shown in figure 8.14e, while minimum shaft bending displacement is 50 microns, as shown in figure 8.14a. At LMC, maximum shaft bending displacement is 130 microns which occurs at 110 rpm

and the minimum is 40 microns as shown in figure 8.14a at 40 rpm. Additionally, shaft bending displacement increases from 180 microns to 192 microns during the speed changes from 80 rpm to 100 rpm in AMC, while, it changes from 100 microns to 120 microns during the increase in the same speed range.

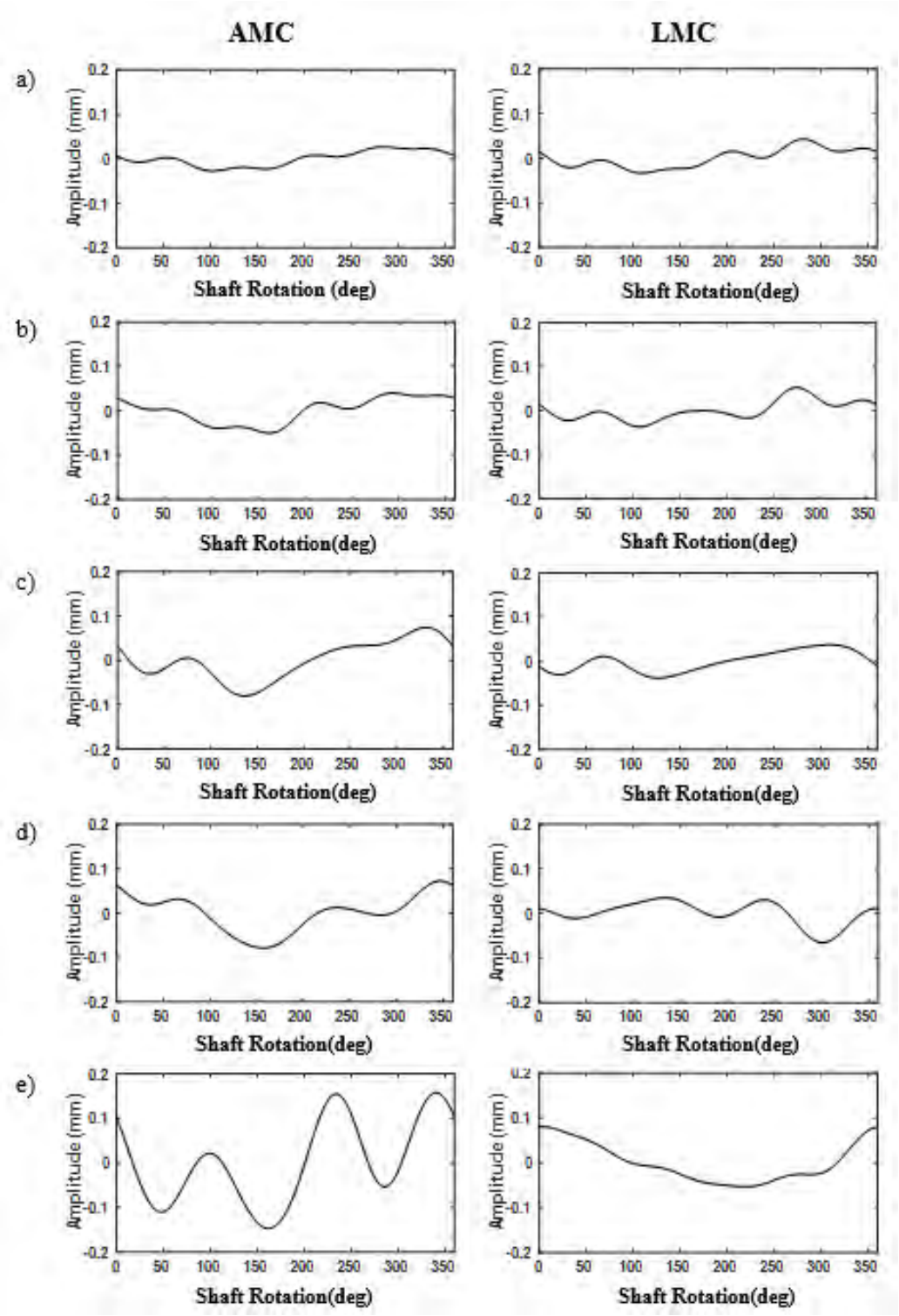

Figure 8. 14 Shaft amplitude over exactly one revolution during applied AMC and LMC on the rotor blade at; a) 40 rpm, b) 60 rpm, c) 80 rpm, d) 100 rpm, and e) 110 rpm.

Shaft centreline displacement orbits were detected during the speed increases with the imbalance effects. Figure 8.15 shows tracking of the shaft centreline displacements for the 1st harmonic. In figure 8.15a the oval shape of the shaft centre line orbit extends due to applying AMC, corresponding to LMC. Additionally, it shifted to the right in the AMC when speed increases to 60 rpm, as shown in figure 8.15b. In addition, the oval shape extended more along axes 1 and 2, as shown in figure 8.15c. The additional mass increases the shaft centreline displacement as the speed increases to 80 rpm, as shown in figure 8.15d. This is in contrast to the LMC, where the shaft centreline shifts to the left while extending along axis 1. However, at 110 rpm, the centreline shifts to the right while extending along axis 2. In addition, there is a shifting to right and an increase in the orbit towards axis 2 at 80 rpm.

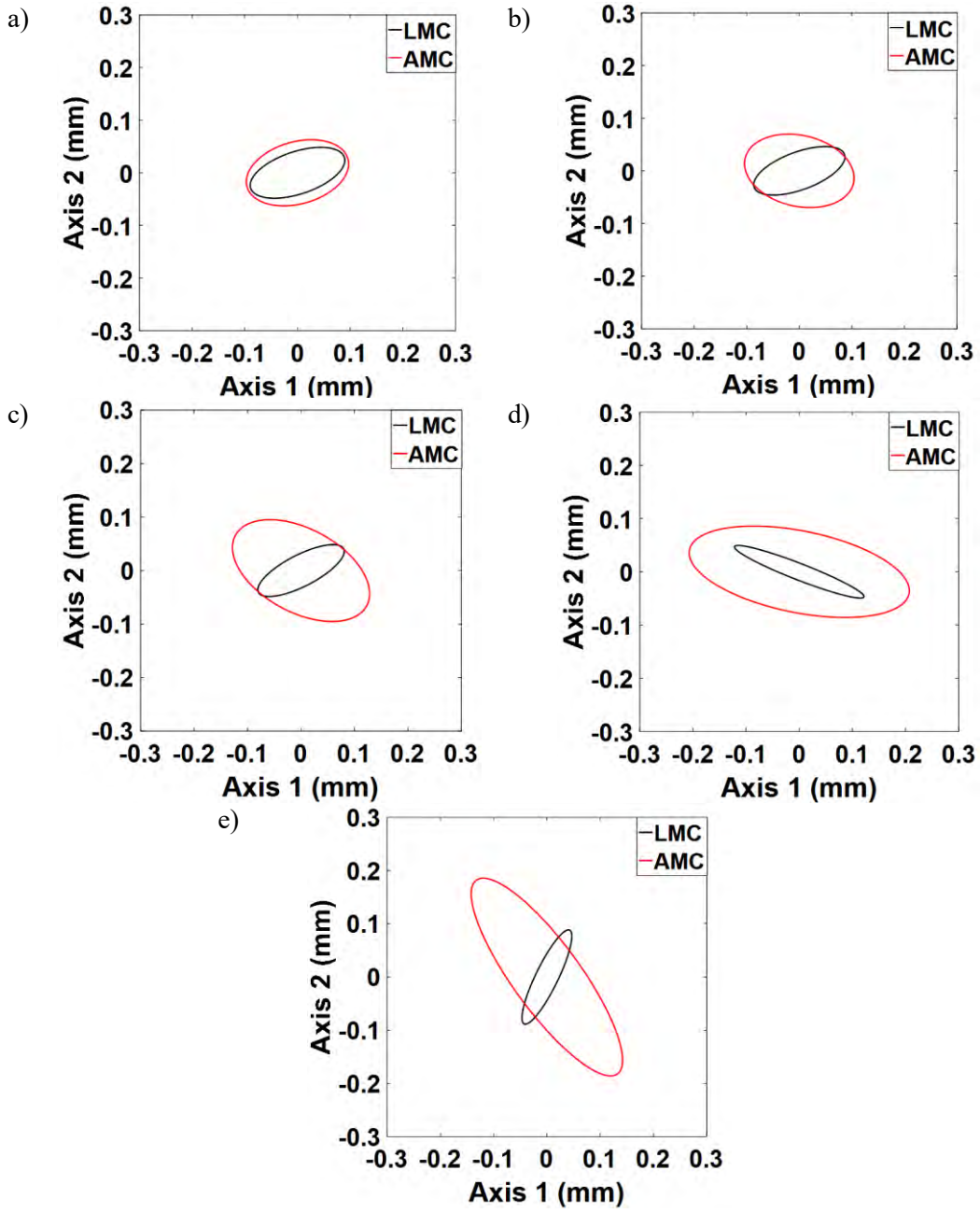

Figure 8. 15 Filtered shaft orbit plots (1st harmonic) in AMC and LMC imbalances at; a) 40 rpm, b) 60 rpm, c) 80 rpm, d) 100 rpm, and e) 110 rpm.

Figure 8.16 shows different orbit shape for the 2nd harmonic during AMC while increasing the speed above 60 rpm. The orbit tends to appear with a different shape from the shaft centreline orbit in LMC. Additionally, after 40 rpm, each speed shows a different oval orbit for the same imbalance condition. At 110 rpm, figure 8.16e shows the same shaft centreline orbit for both 1st and 2nd harmonics.

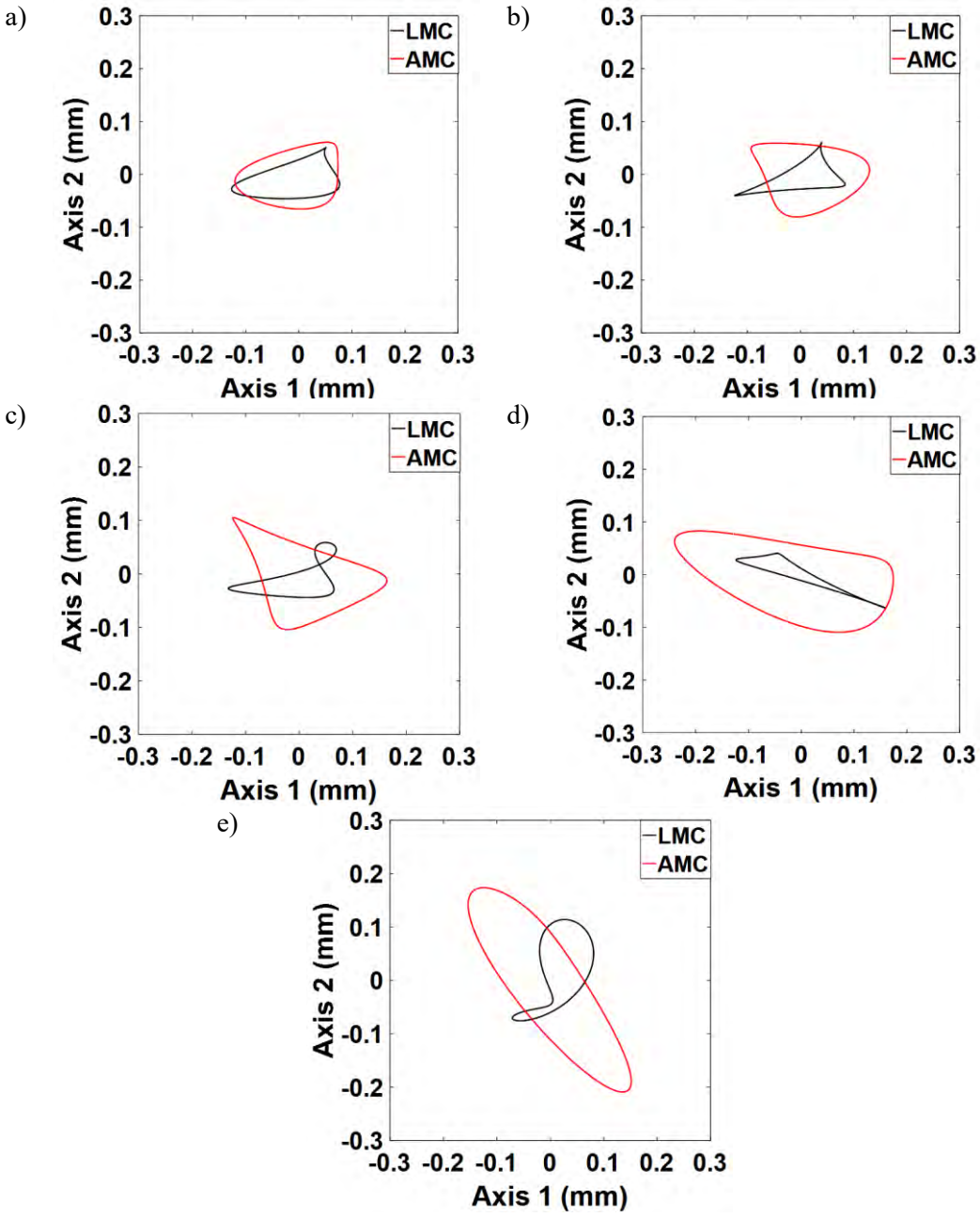

Figure 8. 16 Filtered shaft orbit plots (2nd harmonic) in AMC and LMC imbalances at; a) 40 rpm, b) 60 rpm, c) 80 rpm, d) 100 rpm, and e) 110 rpm.

8.2.6 Effect of additional mass condition (AMC) and loss mass condition (LMC) on the tower vibrations

The rotation containing the imbalance excites the tower vibrations towards the X,Y, and Z directions. Vibration amplitude varies corresponding to the rotor blade speed and two speeds have been considered for tower vibration comparison, the low speed

(40 rpm) and the high speed (110 rpm) corresponding to the applied speed range of the test rig. Figure 8.17 illustrates tower vibration on the X, Y, and Z axes in AMC and LMC at 40 rpm. This is due to the increase in centrifugal forces which resulted from the increase in rotary inertia. The maximum tower acceleration is 1.1 m/s^2 at X-axis for the AMC, whereas, for the LMC it is 1 m/s^2. Tower perpendicular vibration (front vibration) to the rotation plane for AMC is 0.58 m/s^2 and 0.48 m/s^2 for LMC, hence, tower fluctuating (back and forth) increases with AMC due to the increase in the blade mass at one direction. Additionally, tower lateral vibration 0.81 m/s^2 for AMC, while, it is 0.67 m/s^2 for LMC, as shown the figure 8.17.

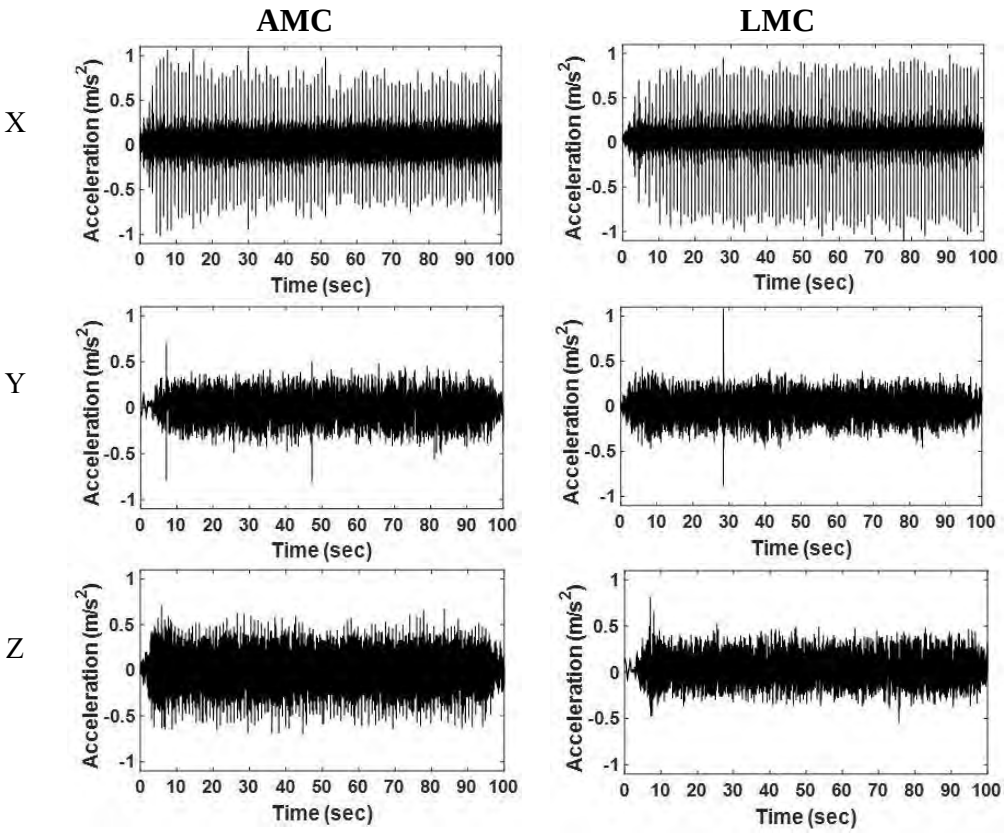

Figure 8. 17 Tower acceleration during imbalance effect of AMC and LMC at 40 rpm towards X,Y, and Z directions

Increasing the speed with the imbalance effect increases dynamic vibrations in the test rig components, as shown in figure 8.18 which exhibits tower acceleration towards the proposed axes at 110 rpm. Maximum tower acceleration in AMC is -76.28 m/s^2 laterally, while, it is -33.71 m/s^2 axially (downward). LMC can be identified by small amplitudes during 110 rpm, where the tower acceleration amplitude decreases to 10.8

m/s^2 in the X-direction, -11.2 m/s^2 in the Y-direction and the maximum amplitude is -17.3 m/s^2 in the Z-direction. The imbalance due to the added mass increases the imbalance forces at one direction (towards the added mass), which increases the tower drag force as the rotor speed increases. In addition, the excitation of the out-of-plane blade vibration with the Coriolis forces increases tower fluctuation back and forth which then increases Y-direction acceleration.

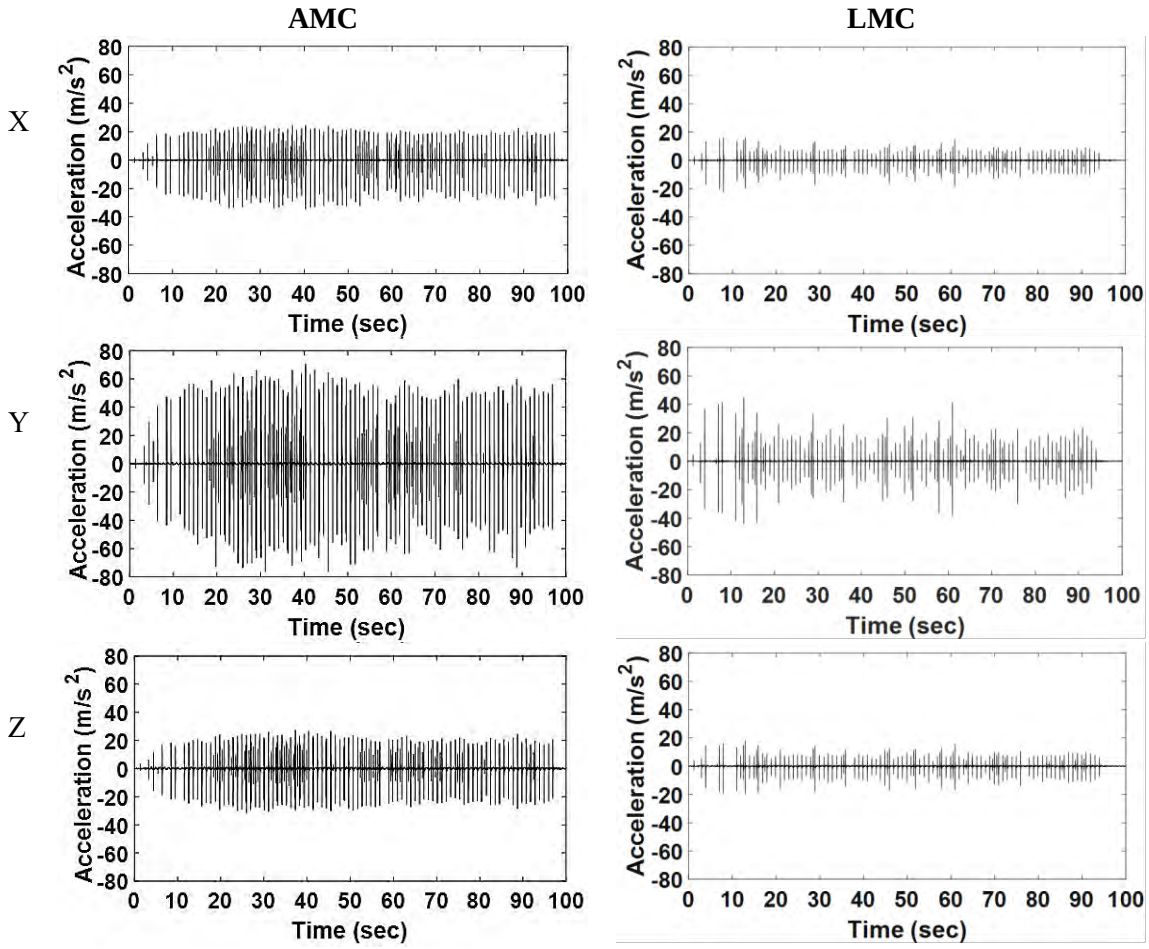

Figure 8. 18 Tower acceleration during imbalance effect of AMC and LMC at 110 rpm towards X,Y, and Z directions.

8.3 Influence of transient mass collision on the rotating and non-rotating components in the test rig

During wind turbine operation, a collision between a bird or any flying mass with the rotor blade can occur, to produce a rotation disruption. This has been modelled by a bunch of wool and cloth (200 g mass) thrown towards the rotor blade rotating at 100 rpm.

8.3.1 Influence of transient mass collision on the blade vibrational modes

Figure 8.19 illustrates the blade strain measurements during the collision event at 24.6 sec. In figure 8.19a, the blade axial strain increases to 104.4 µstrain (to the compression side). The 200 g collision mass impeded the blade rotation, which increases blade bending vibrations towards the in-plane direction to 1462µstrain as shown in figure 8.19b. The transient event excites bending vibrations towards out-of-plane as well. Figure 8.19c presents the increase in the blade out-of-plane strain during the collision event, which reaches 506.2 µstrain at the collision time 24.6 sec.

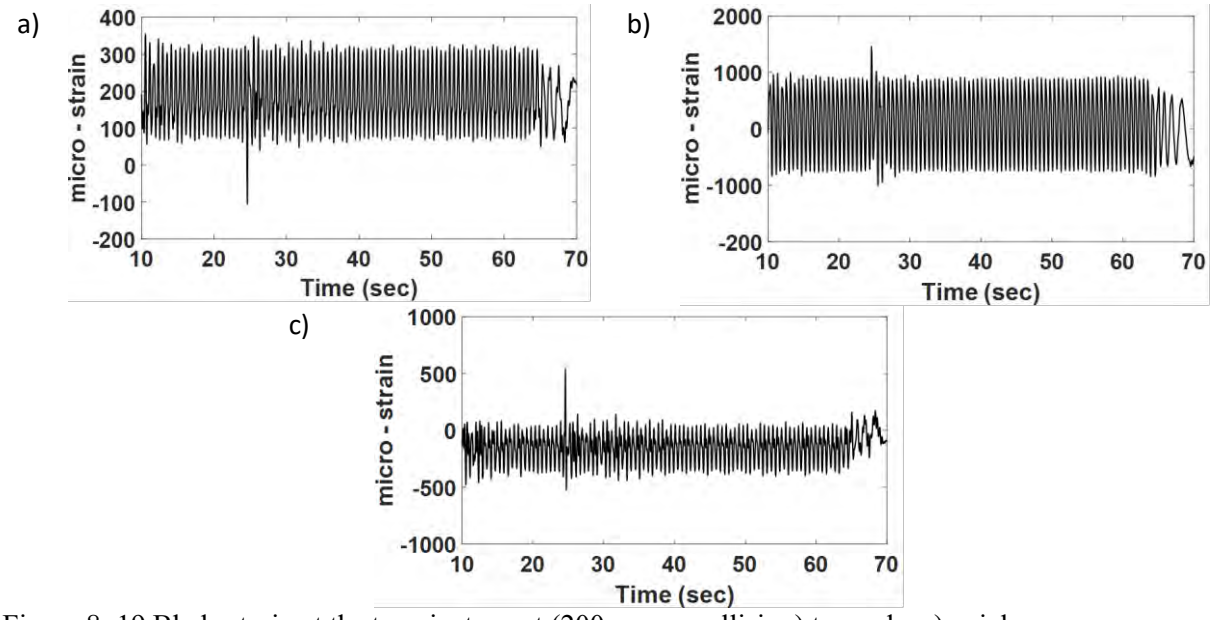

Figure 8. 19 Blade strain at the transient event (200g mass collision) towards; a) axial direction, b) in-plane direction, and c) out-of-plane direction.

Figure 8.20 illustrates the spectrogram analysis for the rotor blade during the collision time at 100 rpm. The transient event excited the rotor blade at a high frequency as presented below. The operating frequency was 1.6 Hz, while, the excited frequency is 3.3 Hz due to the transient event.

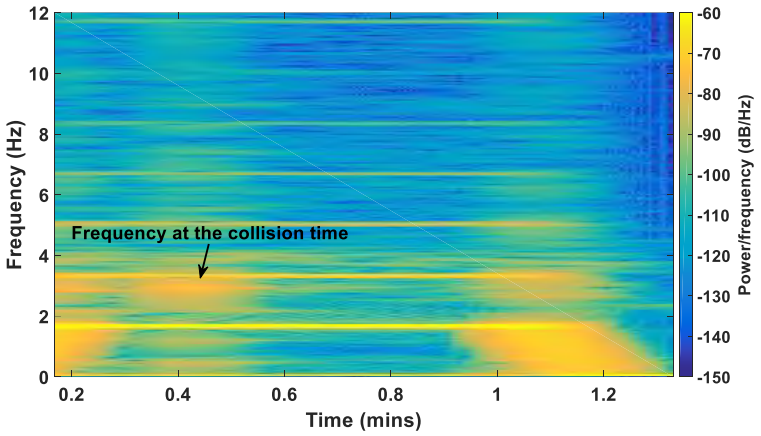

Figure 8. 20 A spectrogram analysis using strain gauge at in-plane direction of the rotor blade during the collision event.

Furthermore, figure 8.21 shows blade acceleration measured by the piezoelectric accelerometer that was positioned in the blade tip during the collision event. Rapid increase of the acceleration amplitude to -183.3 m/s^2 indicates that there is an increase in blade bending with the rotor plane at 100 rpm.

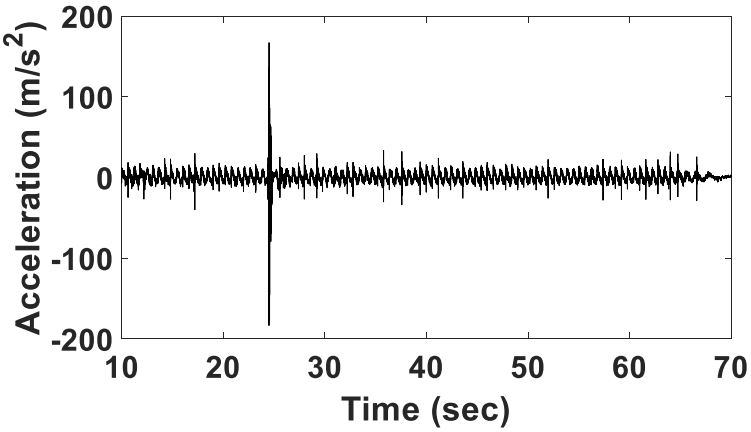

Figure 8. 21 Blade acceleration amplitude during 200g mass collision with the rotor blade at 100 rpm.

8.3.2 Influence of transient mass collision on the tower vibrational modes

The collision event was observed to affect the tower vibrations through the increase in the vibration amplitude towards the applied axes. Figure 8.22 illustrates tower accelerations measured by the tri-axial accelerometer during the collision time. Maximum tower acceleration of -2.43 m/s^2 occurs in the Y-direction at 24.6 sec during rotor speed of 100 rpm.

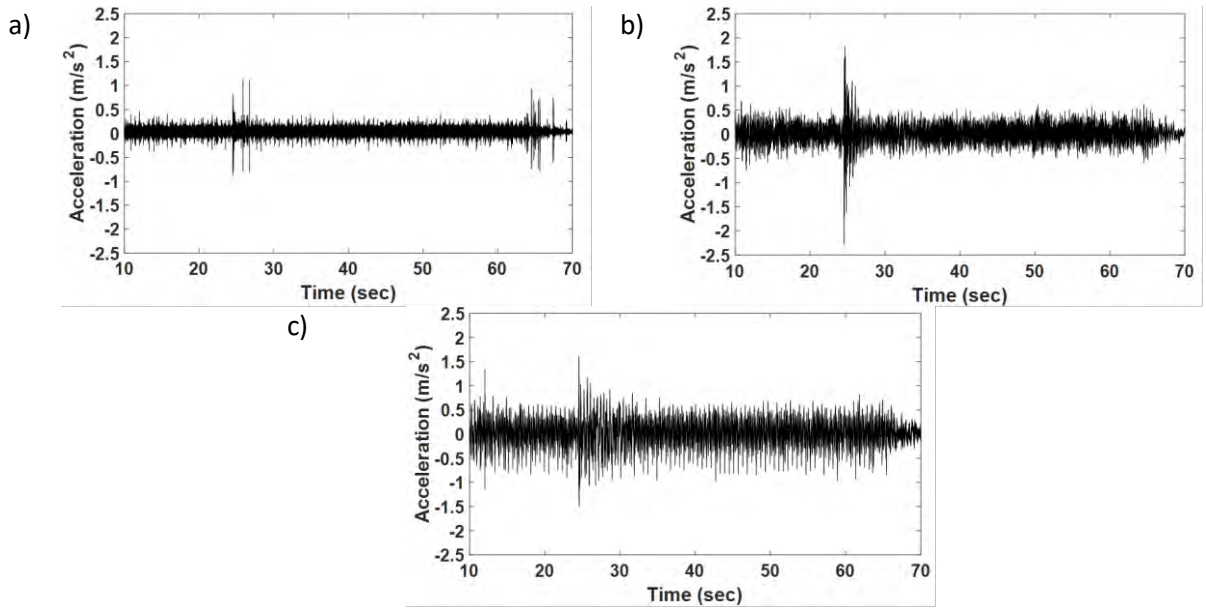

Figure 8. 22 Tower acceleration during a 200g mass collision with the rotor blade towards; a) X, b) Y, and c) Z.

Figure 8.23 illustrates the spectrogram analysis of the tower frequencies during the transient event. It shows that the collision triggered high frequencies at 0.41 min.

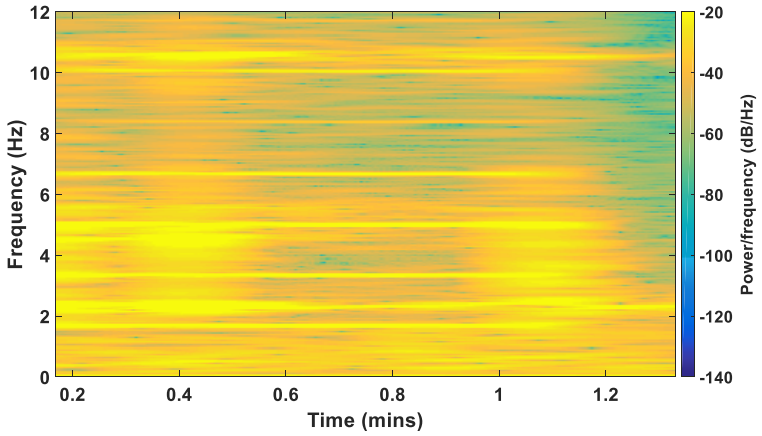

Figure 8. 23 Tower spectrogram analysis during a 200g mass collision with the rotor blade at 100 rpm, using Z-axis data signal.

8.3.3 Influence of transient mass collision on the drive shaft bending displacements

The collision effect was noted to transfer to the drive shaft through monitoring the bending displacement during the collision event. Figure 8.24 illustrates the drive shaft response during the collision event at 24.6 sec, towards the arbitrary axes 1 and 2. The shaft displacement along axis1 was larger than the displacement along axis 2, as shown in figure 8.24a and 8.24b, as well as the effect of the mass collision on the bending displacement along both axes due to the rotation disruption.

a)

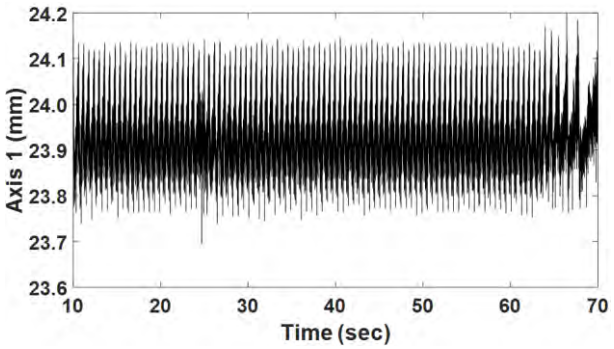

b)

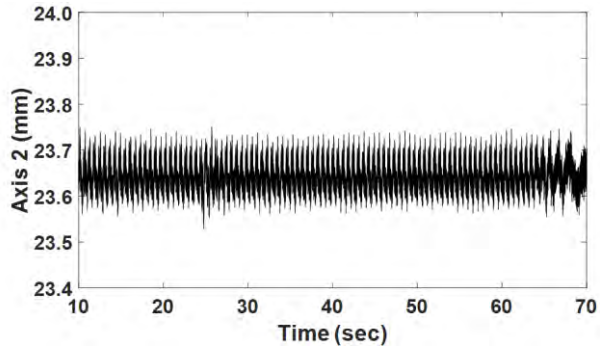

Figure 8. 24 The drive shaft bending displacements measured by laser sensors positioned during the collision at 24.60 sec at ; a) axis1, and b) axis2.

Additionally, the change in the shaft rotation during the test can be recognized in figure 8.25, since the collision increases shaft displacement at revolution 29, which is pronounced in both figures. This representation can help monitor the instantaneous shaft condition by tracking the revolution, which helps identify the existence of faults.

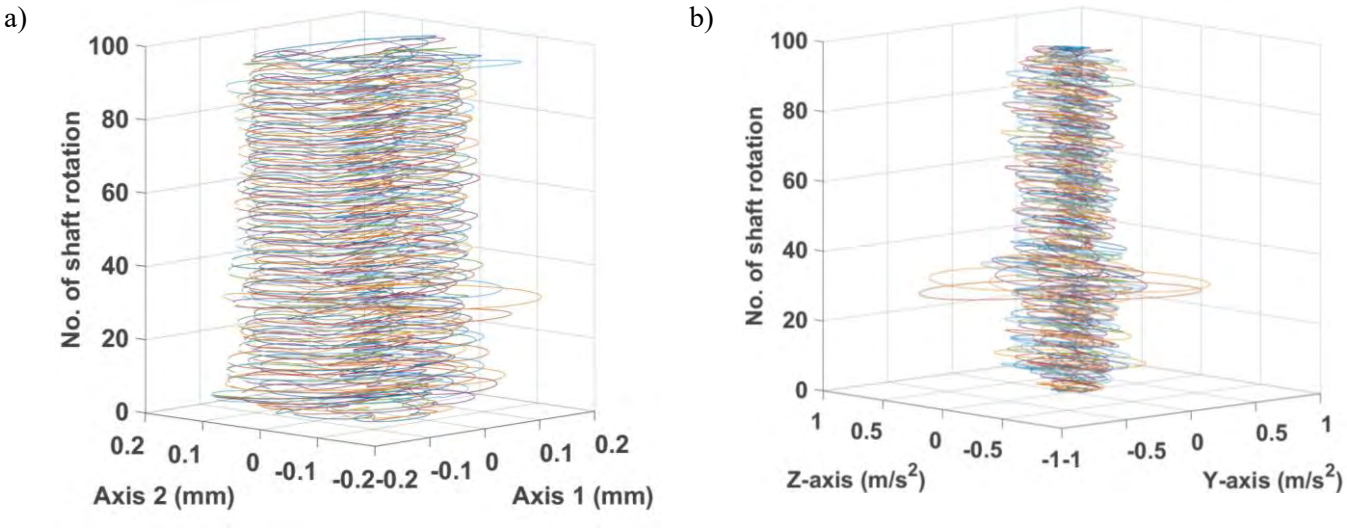

Figure 8. 25 Shaft and tower responses during the collision time 24.6 sec at 100 rpm using a) laser signal data, and b) triaxial accelerometer signal data.

The collision increases shaft centreline displacement as shown in figure 8.26. The first harmonic oval shape expanded towards axes 1 and 2 due to the collision effect, as shown in figure 8.26a. However, shifting of the shaft centreline orbit was monitored in the second harmonic during 200 g mass collision with the rotor blade (M. Al-Hadad, McKee, & Howard, 2019), as illustrated in figure 8.26b. After that, the shaft centreline displacement traces a different orbit during the collision event from the normal rotation (without collision), as shown in figure 8.26c, and it took a similar "cat ears" shape due to the collision in the 4^{th} harmonic, as shown in figure 8.26d. The effect of blade collision with a flying mass is pronounced on the drive shaft dynamic bending, which is transferred to the servo-motor system. The transient event also affects the motor torque, which drops the torque at the collision time and increase the load on the drive shaft, hence needs to compensate for the speed dropping due to the collision event.

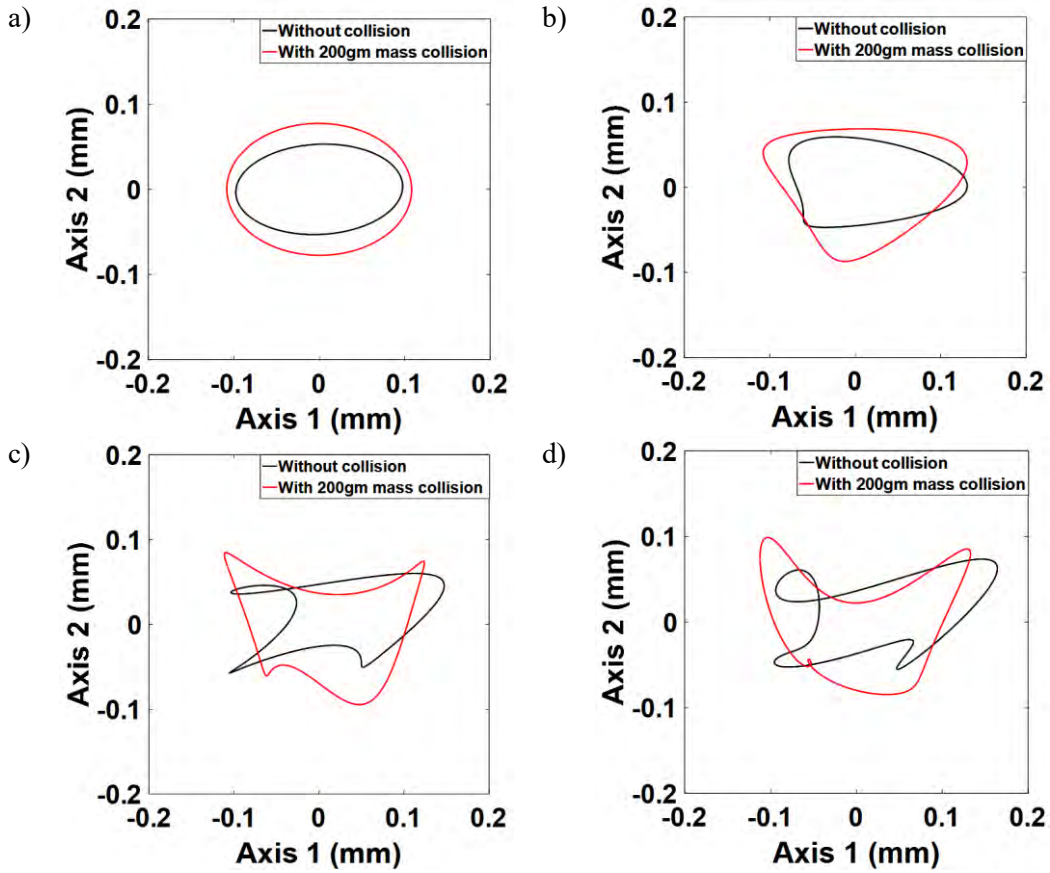

Figure 8. 26 Filtered shaft orbit plots without and with 200 g mass collision at 100 rpm; a) 1X, b) 2X, c) 3X, and d) 4X.

8.4 Influence of transient high-speed gust on the rotor blade and tower modes

A special mechanism for the compressed air has been established for subjecting an air jet burst with 2 bar in front of the rotating blade at 100 rpm, for modelling a gust during wind turbine operation. Figure 8.27 illustrates the applied blade vibrational modes at 100 rpm. A small increase in the blade vibrational modes can be noted due to the transient upwind gust compared with the normal rotation at the same speed, due to the increase in blade out-of-plane vibration which excites the vibrations towards axial and in-plane directions.

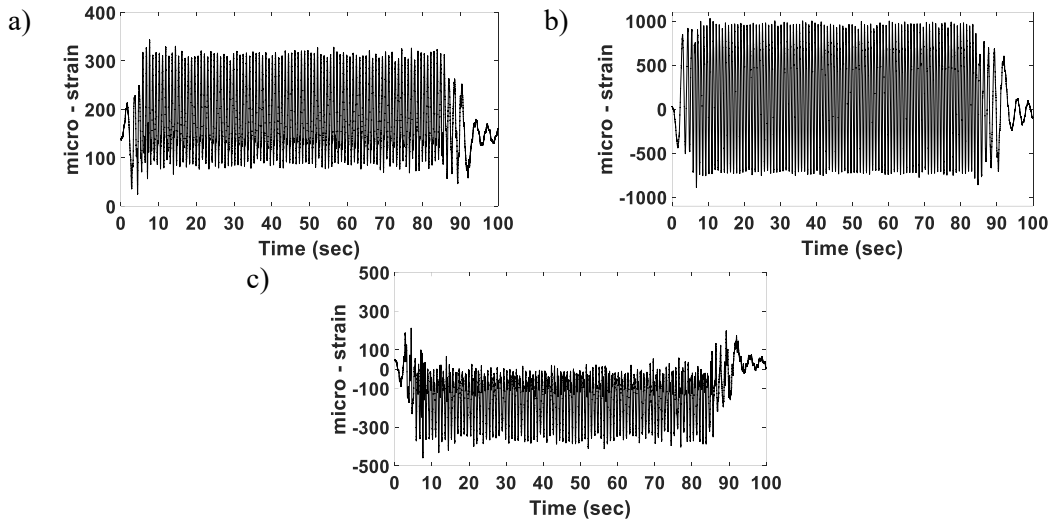

Figure 8. 27 Blade strain measurements during subjected a compressed air upwind at 100 rpm a) axial strain, b) in-plane strain, and c) out-of-plane strain.

Simultaneously, there is a pronounced effect from the downstream compressed air on the tower vibrations. Figure 8.28 shows an increase in tower acceleration to 1.6 m/s^2 axially, 1.5 m/s^2 on the front side, and -2.7 m/s^2 laterally (back side). This effect, as well as speed, increases tower vibrational load (particularly at Y-direction).

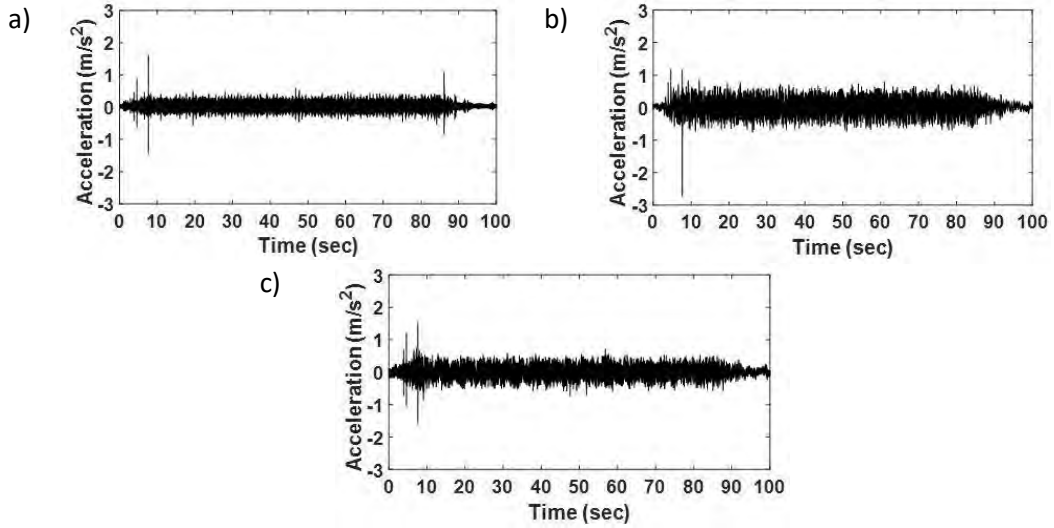

Figure 8. 28 Tower acceleration amplitude at 100 rpm during applied upwind compressed air towards; a) X, b) Y, and c) Z.

Increasing the rotor speed to 120 rpm in front of the compressed air excites high vibrations in the test rig system which increases the blade vibrational modes. Figure 8.29 shows the rotation stops after 23 seconds. This was attributed to the high blade vibrations due to the burst of compressed air towards downstream which added a pressure perpendicularly to the rotation plane. This increasing load affected significantly onto the servo-motor shaft, resulting in an overload warning causing the system to shut off.

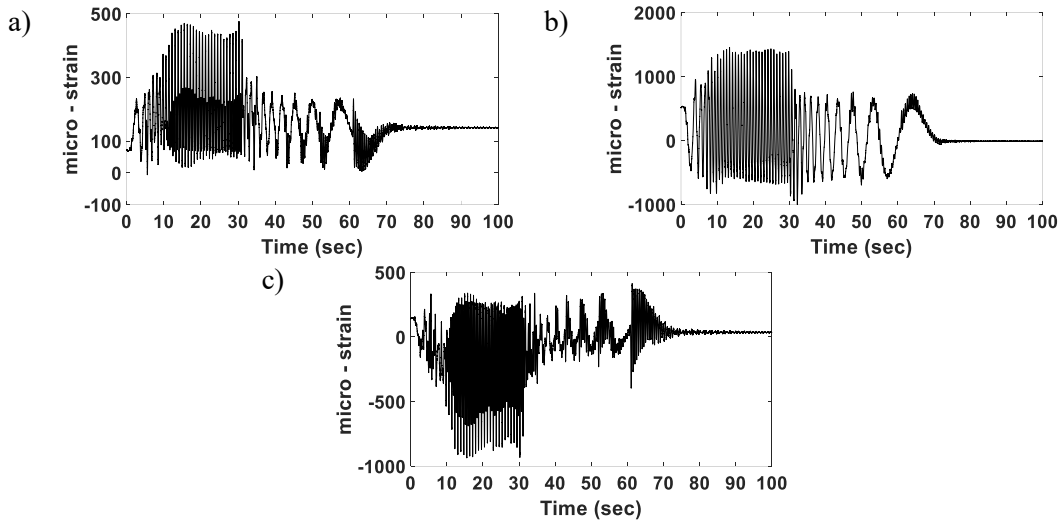

Figure 8. 29 Blade strain measurements during subjected compressed air toward upwind at 120 rpm. a) axial strain, b) in-plane strain, and c) out-of-plane strain.

Additionally, figure 8.30 illustrated the increase in tower vibration amplitude during the increase in speed to 120 rpm, while subjected to the downstream compressed air. Maximum tower acceleration 39.3 m/s^2 occurs in the Y-direction, while, in the X and Z directions are -20.1 m/s^2 and -18 m/s^2 respectively. The increase in tower vibration, towards the Y-direction signalled the pronounced effect of the transient downward gust on increasing the tower vibrations.

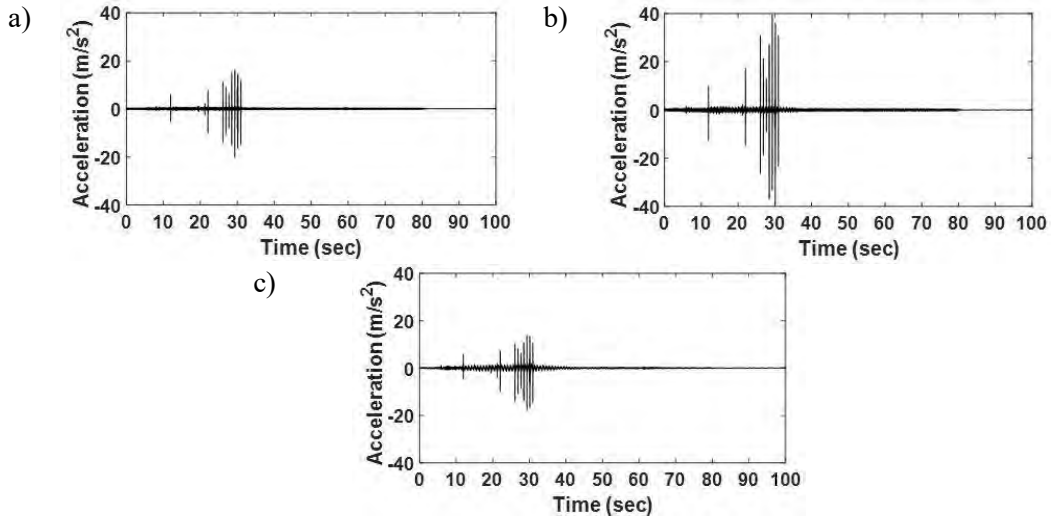

Figure 8. 30 Tower acceleration amplitude at 120 rpm during applied upwind compressed air towards; a) X, b) Y, and c) Z.

Furthermore, the high-speed compressed air doesn't appear to have any effect on the drive shaft during 100 rpm and 120 rpm, therefore, it isn't listed here.

8.5 Influence of bearing bolt looseness on the rotating and non-rotating components in the test rig.

Looseness in the bolts from the drive shaft bearing has a significant effect on the rotating components in the wind turbine system due to failure in the linked parts with shaft system. This test has been performed by creating a looseness of 2 mm from bearing 2 (near to the hub) at 100 rpm.

8.5.1. Influence of bearing bolt looseness on the drive shaft behaviour.

Figure 8.31 shows the shaft response during looseness of 2 mm from the left bolt of the bearing (close to laser sensor at axis1). This test produced different shaft behaviour, resulting in a maximum shaft displacement on axis1 of 900 microns, whilst, maximum shaft amplitude on axis2 is 620 microns. The shaft bending increases due to the clearances that comes from the looseness, while affecting the mechanical components connected with the drive shaft. Additionally, it can be seen that the shaft vibrates after

the rotation stops (after 90 seconds), which makes the average displacement of 165 microns at axis1 and 120 microns at axis2.

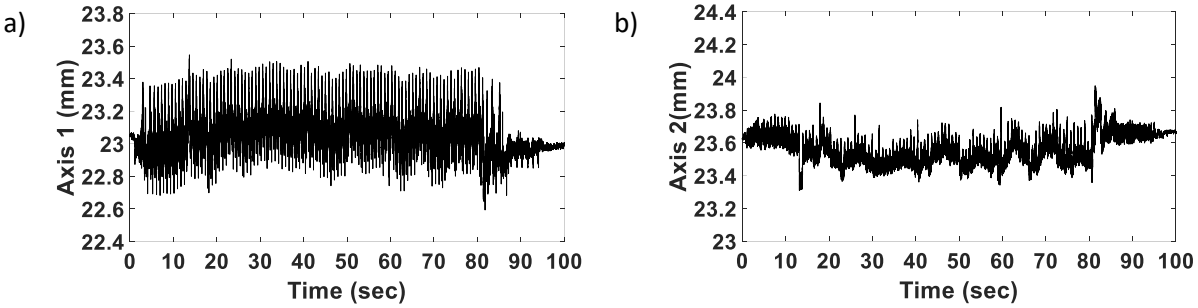

Figure 8. 31 Shaft dynamic displacements during 2mm looseness from the bearing bolt at 100 rpm.

Furthermore, the 2mm gap in the bearing bolt affected the centreline displacement in the bearing housing, as illustrated in figure 8.32. This leads to the oval extending and shifting to the right particularly at the harmonics 1X, 2X and 3X. However, changes in the orbit attitude can be seen at 4X in figure 8.32d. To prevent damages in the rotating components, the rotor speed wasn't increased more than 100 rpm.

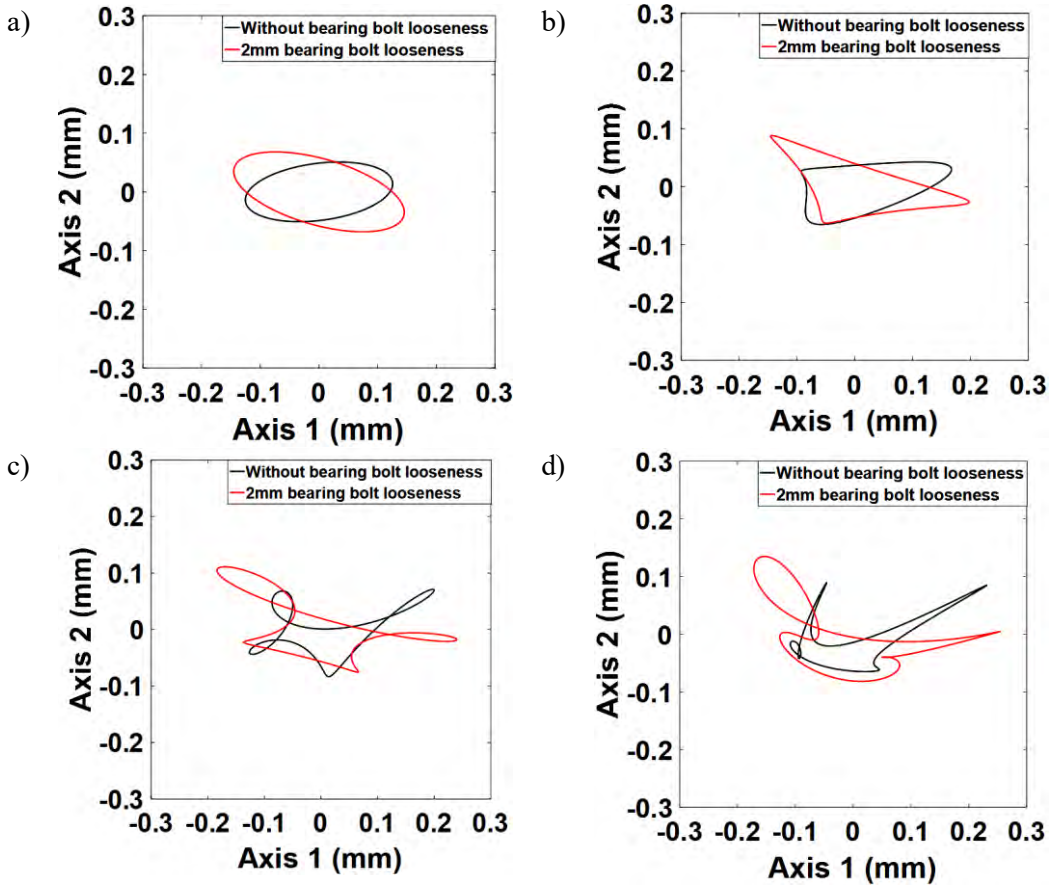

Figure 8. 32 Filtered shaft centreline orbits during 2mm bearing bolt looseness in comparison to the rotation without looseness at 100 rpm; a) 1X, b) 2X, c) 3X, and d) 4X.

Figure 8.33 illustrates the drive shaft rotations during the test with 2mm bearing bolt looseness. The dynamic bending during the rotations indicates the increase in the shaft centreline displacement within the bearing housing due to bolt looseness and the increase in the bearing housing.

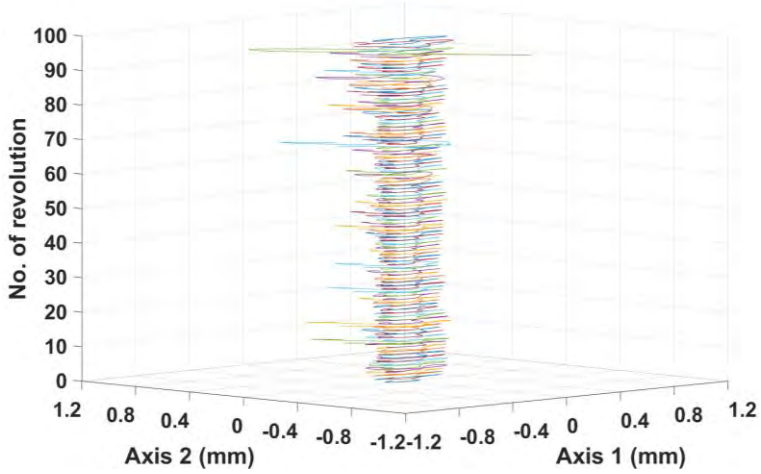

Figure 8. 33 Calculated shaft orbits for every rotation at 100 rpm, during 2mm bearing bolt looseness.

8.5.2. Influence of bearing bolt looseness on the blade modes.

Figure 8.34 shows the increase in blade strain for the rotor blade modes due to bearing bolt looseness at 100 rpm. Average axial blade strain achieved was 312.6 µstrain (figure 8.34a), while a small increase in the average blade in-plane strain can be identified as shown in figure 8.34b when it reaches -800 µstrain. The average out-of-plane strain amounted to 365 µstrain as shown in figures 8.34b and 8.34c. The small effect of bearing bolt looseness on the blade modes is attributed to the high blade inertia corresponding to the rotating cantilever beam. The large effect is on the rotor shaft itself despite the small looseness of one bearing bolt (M. Al-Hadad, Hwais, McKee, & Howard, 2017).

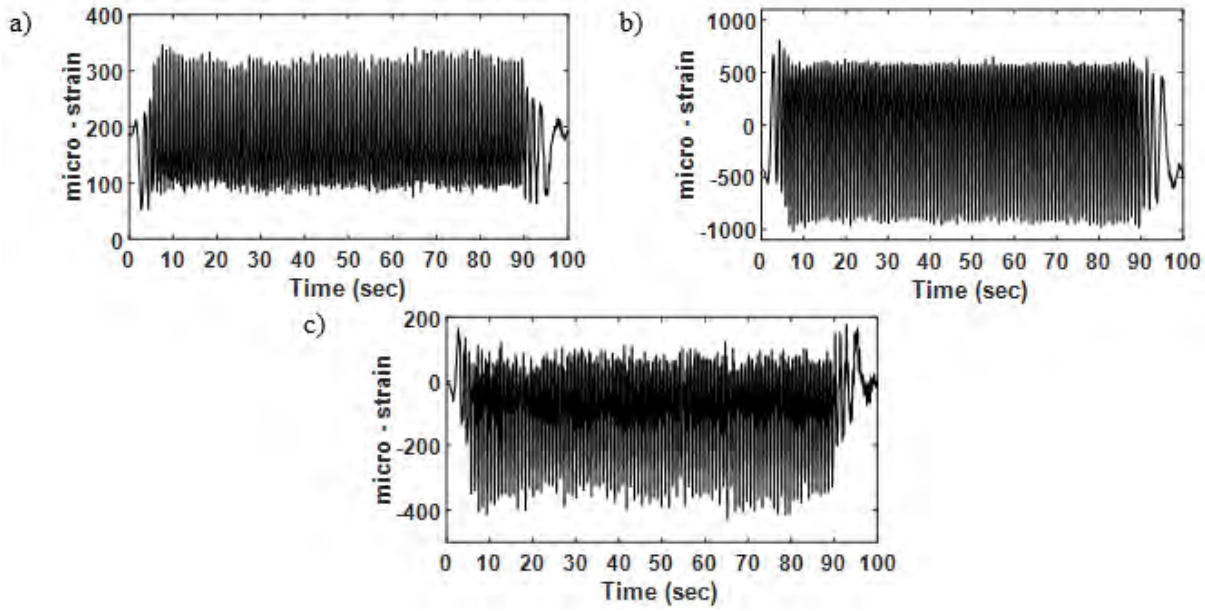

Figure 8. 34 Rotor blade strain measurements at 2mm bearing bolt looseness and 100 rpm; a) axial strain, b) in-plane strain, and c) out-of-plane strain.

8.5.3. Influence of bearing bolt looseness on the tower modes.

Figure 8.35 shows the effect of bearing bolt looseness on the tower vibrational modes. It is obvious that there is a greater effect in the X-direction than in the Y and Z directions. This due to the increases in centrifugal forces when the blade in the vertical position pulls the hub, and hence the drive shaft, towards the blade axial direction. The shaft displacement in the vertical direction increases the tower vibration in the X-direction, which is detected by the triaxial accelerometer. The maximum tower acceleration is 1.33 m/s^2 in the Z-direction, whilst the Y and X directions of the tower acceleration reach -0.7 m/s^2 and -1.15 m/s^2, as shown in figures 8.35b and 8.35c respectively.

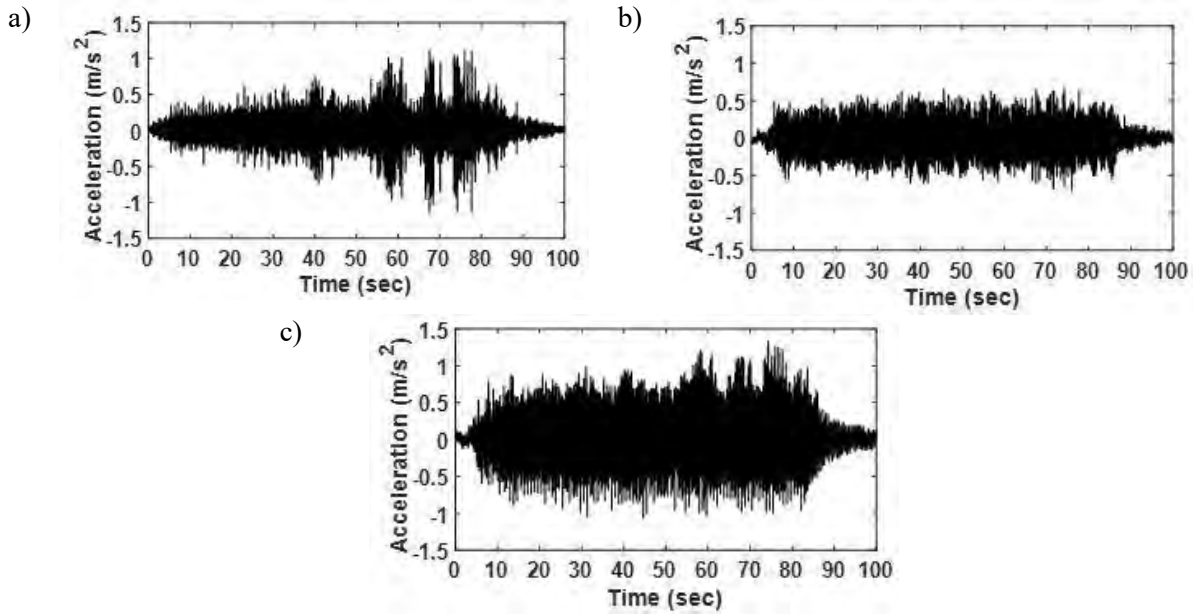

Figure 8. 35 Tower acceleration amplitude during 2mm bearing bolt looseness at 100 rpm at directions; a) X, b) Y, and c) Z.

8.6 Influence of transient mass reduction from the rotor blade on the rotating and non-rotating test rig components

The mass removal from the rotor blade in most cases leads to significant results in the wind turbine system, due to the transient case that the blade experienced during transferring from the balance to unbalance state. This has been modelled by 200g mass removal from the rotor blade at 100 rpm (M. Al-Hadad et al., 2019). The mass was removed at 49.65 seconds during an imbalance test to transfer the rotor blade to the balance state after passing through the transient state (mass reduction event).

8.6.1. Influence of transient mass reduction on the rotor blade dynamic response

Figure 8.36 shows the blade strain during the transient event. Figure 8.36a shows the three stages in blade axial strain measurement during the test. The first stage is the unbalance state during which a 200 g mass was added to the rotor blade. During the second stage, which was a transient case, the mass came off from the blade at 49.65 seconds. In this case the axial strain reduced to 310.5 µstrain. The last stage is the

balanced case when the blade rotates without the additional mass. The three stages can be specified in the other vibrational modes, namely in-plane and out-of-plane as shown in figures 8.36b and 8.36c. Blade in-plane vibration decreases to 724 µstrain at the transient event, while, the blade strain decreases to 37.8 µstrain towards out-of-plane during this event. After that, the blade returns to the balanced state due to the imbalance mass coming off.

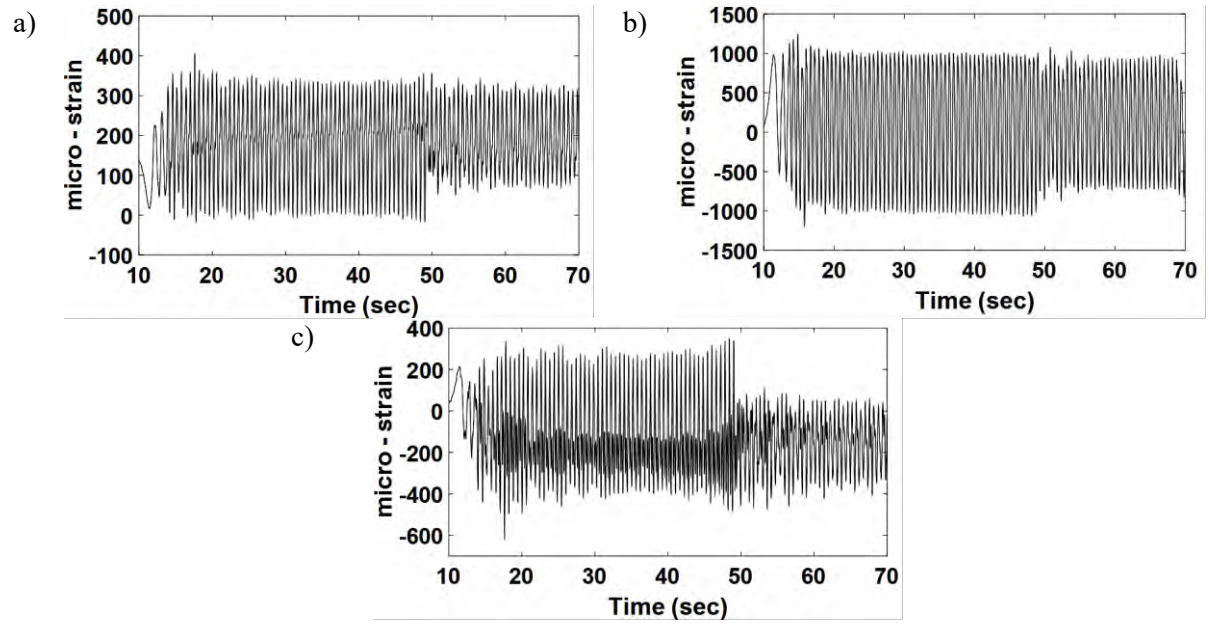

Figure 8. 36 Blade strain measurements during mass removal at 49.65 sec during the rotor blade rotating at 100 rpm; a) axial strain, b) in-plane strain, and c) out-of-plane strain.

Figure 8.37 illustrates the spectrogram analysis of the rotor blade during the 200g mass removal imbalance test at 100 rpm. It is obvious that the transient event triggered high blade vibration, particularly between the frequencies of 2 Hz and 5 Hz in the blade response as shown in the axial, in-plane, and out-of-plane blade modes.

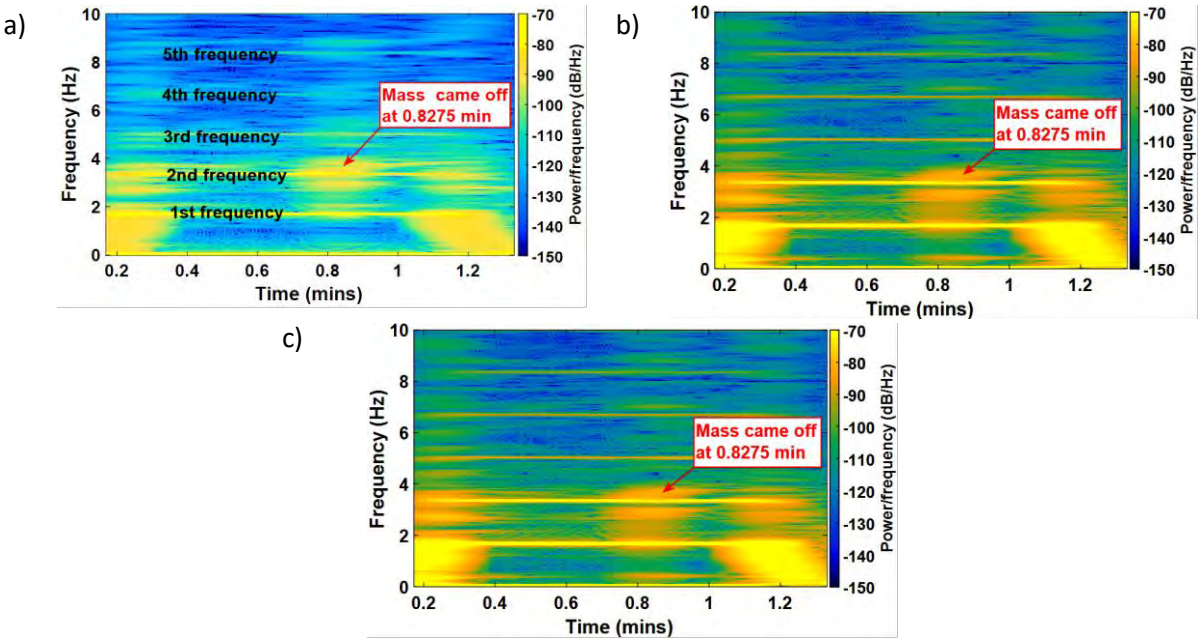

Figure 8. 37 Spectrogram analysis of the rotating blade at 100 rpm during a transient event at 49.65 sec using the strain measurements data at; a) axial, b) in-plane, and c) out-of-plane.

8.6.2. Influence of transient mass reduction on the tower vibrations

The supported tower was affected from the mass reduction during the test. Figure 8.38 presents the tower acceleration measured by the triaxial accelerometer towards the X, Y, and Z directions. The maximum acceleration of 218.3 m/s^2 occurs at Y-direction as shown in figure 8.38b. The excitation after the mass reduction is pronounced in the considered modes. This increase confirms the coupling between the rotor blade and tower vibrational modes during the transient event.

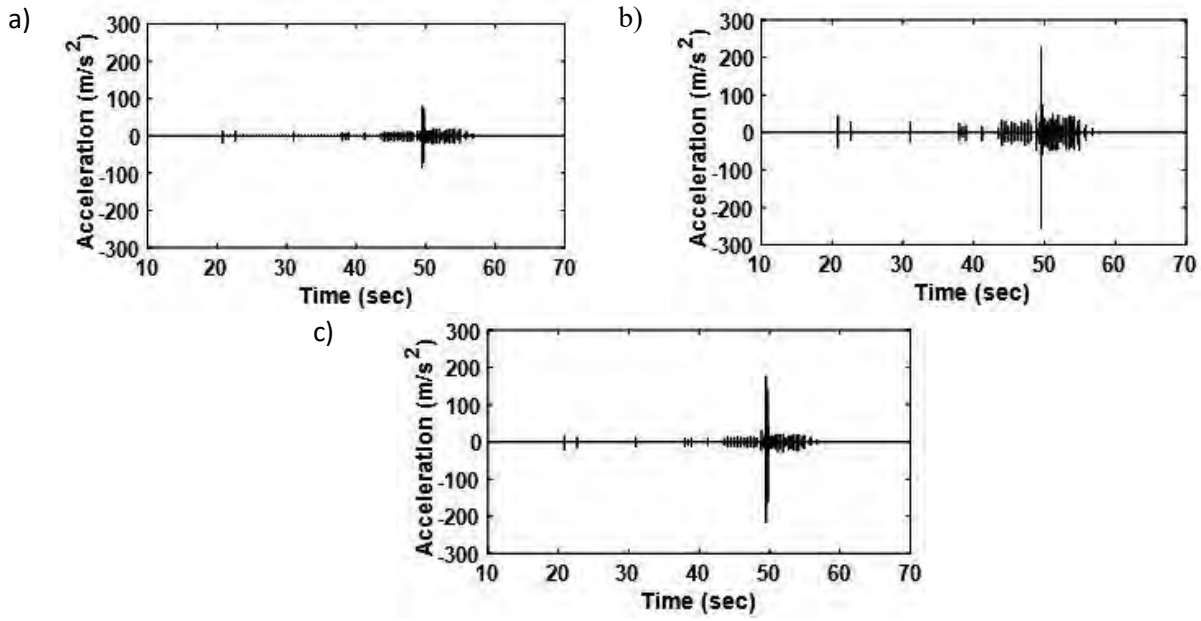

Figure 8. 38 Tower acceleration amplitudes at 100 rpm during 200g mass reduction from the rotor blade at directions of; a) X, b) Y, and c) Z.

Additionally, the transient event excites high tower vibration response which can be seen from the spectrogram analysis. Figure 8.39 shows the increase in tower response at the mass removal time towards X, Y, and Z directions, where the fundamental tower resonance is 2 Hz.

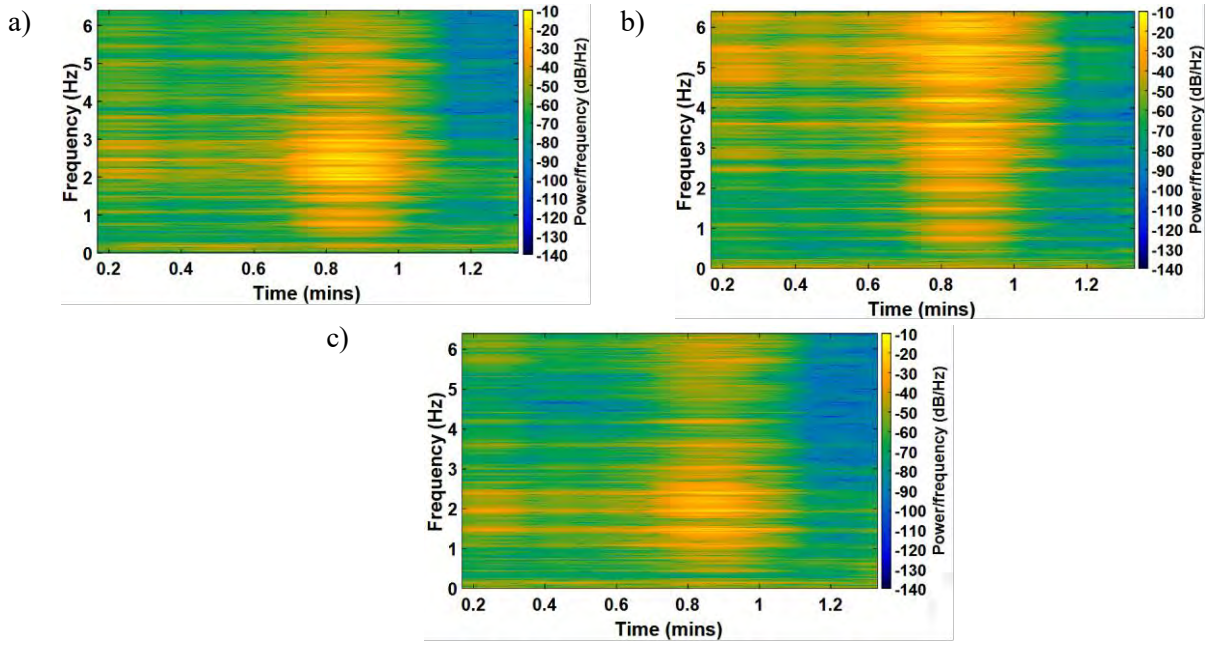

Figure 8. 39 Spectrogram analysis of the tower acceleration at 100 rpm during 200g mass removal at; a) X, b) Y, and c) Z.

8.6.3. Influence of transient mass reduction on the drive shaft bending displacement

The bending of the drive shaft during the mass coming off event from the rotor blade was detected by the laser sensors positioned at axes 1 and 2 orthogonally on the shaft rotation axis. Figure 8.40 shows state transformation from unbalance to balance state passing through the transient case (mass removal). The nominal distance between the laser sensor and the shaft surface is 24 mm. The initial shaft bending displacement is of the order of 500 microns at axis1, while, it is approximately 200 microns along axis2. Additionally, it can be seen that shaft displacement towards axis1 is obviously larger than the displacement towards axis2 due to the differences in the stiffness and the applied load at the two directions. Furthermore, shaft displacement towards axis1 at imbalance case is around 470 microns, which reduced to 180 microns at the transient event and then returned to increase in the balanced case of 230 microns, as illustrated in figure 8.40a.

These shaft displacement amplitudes decrease towards axis2. It shows that 180 microns occurred for the imbalance case, reduced to 100 microns at the transient event, and increases to 110 microns during the balanced case, as presented in figure 8.40b.

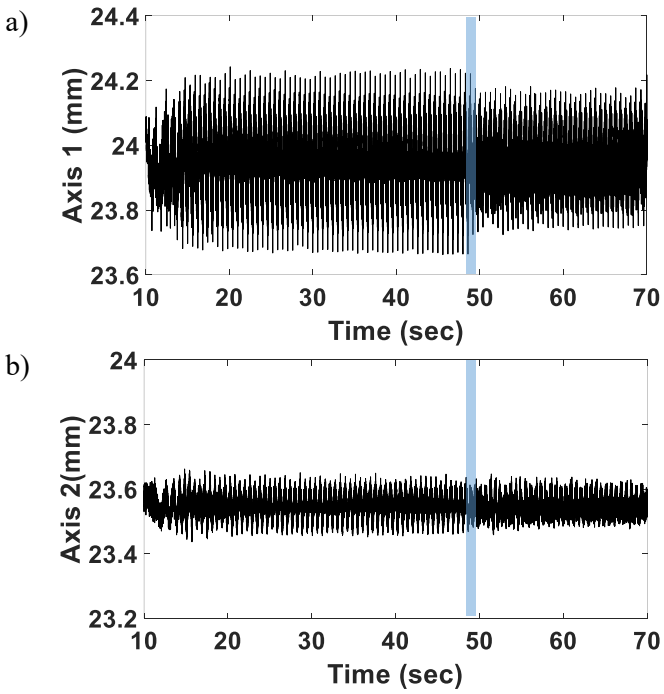

Figure 8. 40 Driveshaft response during a 200g mass removal at 49.65 sec. from the rotor blade during 100 rpm towards; a) axis1, and b) axis2.

The mass reduction during the imbalance test creates three cases in one experiment. The shaft experienced bending displacement changes due to the rapid transformation to the balanced state. Additionally, this change in condition can also be seen through the shaft centreline orbits, as illustrated in figure 8.41. It also shows the change in shaft centreline at the significant shaft harmonics.

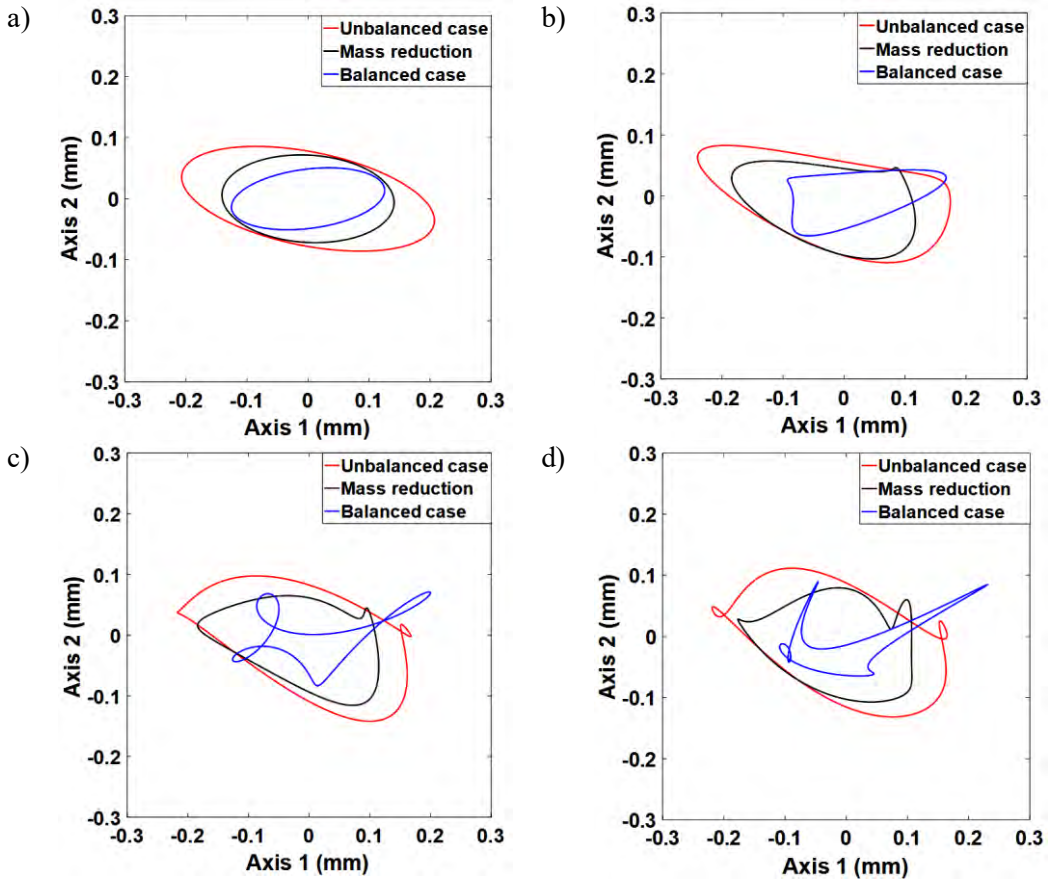

Figure 8. 41Filtered shaft orbits plots at three significant shaft conditions during 200g mass reduction at 100 rpm, a) 1X, b) 2X, c) 3X, and d) 4X.

8.7 Fatigue fracture in the tower foundation due to excessive vibrations in the rotating and non-rotating components.

During different case studies with the rotating cantilever beam and blade model in the test rig, the tower foundation experienced excessive vibrations due to various case studies that were implemented for rotating and non-rotating vibration condition

monitoring. Additionally, the support tower withstands different vibrational loads the rotating components which impose high stresses on the tower foundation during test rig operation. Furthermore, the effect of servo-motor torque changes with the change of rotor speed provides significant loading on the tower vibrational response, which in turn added fatigue loading on the tower foundation. After more than one year, and during tower vibration condition monitoring through accelerations measured by the triaxial accelerometer located at the tower upper part, a 4 cm fatigue crack was detected in the foundation welding joint. Figure 8.42 presents maximum tower acceleration data measured in different loading conditions during the test rig operation covering more than one year. The primary acceleration amplitudes indicate that tower acceleration at Y-direction is Y=0.832 m/s^2, while, at the X and Z directions were 0.494 m/s^2 and 0.536 m/s^2 respectively. Due to the coupling between the blade in-plane and tower Z-direction modes, the increase in the blade in-plane vibration leads to a rise in tower fluctuation towards Z-direction as can be detected in figure 8.42. According to data point 12 (February 2018), the tower vibration increased towards the Z-direction indicating that a fatigue crack had initiated in the tower foundation. Through performing a visual inspection on the foundation, a 4 cm crack was observed during May 2018 (M. A. s. Al-Hadad, Mckee, Howard, & 2018).

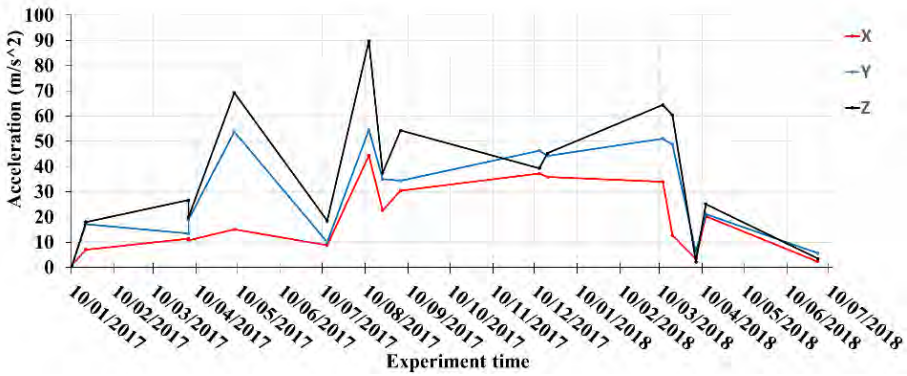

Figure 8. 42 Tower acceleration amplitudes during different tests from 10/01/2017 to 02/07/2018 towards; a) X, b) Y, and c) Z directions.

A repair procedure of the welding joint was implemented, followed with reinforcement and an impact test for checking the fundamental frequencies of the supporting tower. Tower bending frequencies during more than one year of test rig operation in different loading conditions, and after repairing the foundation have been illustrated in figure

8.43, it also shows the new tower resonance (2.25Hz) after reinforcements and welding joint repairs.

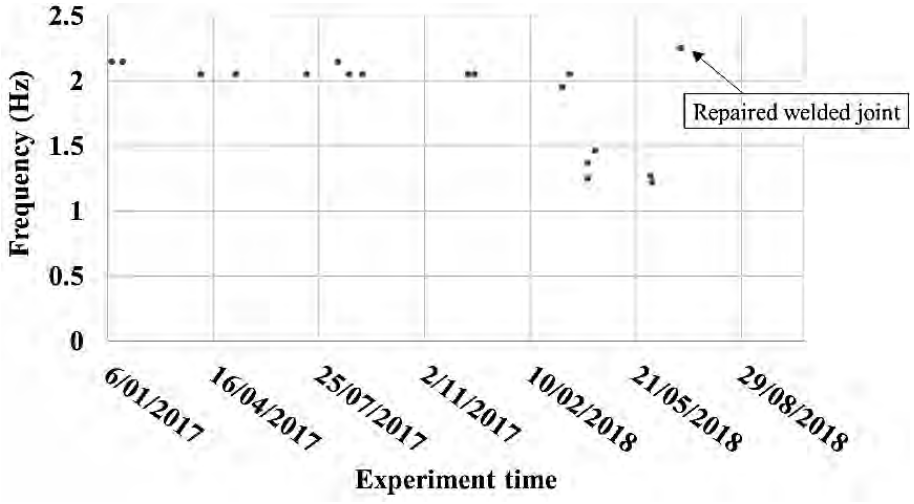

Figure 8. 43 Fundamental tower frequencies during more than one-year operation, during crack initiation in the foundation and after repairing implementation.

8.8 Conclusion

This chapter presents vibration condition monitoring of rotating and non-rotating components during different artificial fault case studies. Tests include implementing imbalance cases with rotor speed increases, to identify the dynamic response of the test rig components during the fault conditions. The change to the blade mass (adding and losing 200 g mass) are the significant faults tests that were fulfilled with speed increases, showing an excitation of high vibrations of the test rig components. The added mass increases blade vibrational modes towards axial, in-plane, and out-of-plane directions due to blade mass increases in one direction, which leads to increase the centrifugal forces with the rotor speed. The increase in blade axial, in-plane and out-of-plane vibration amplitudes during the added mass case has been found to be larger than at losing mass, due to the increase in the rotary inertia. Additionally, the imbalance effect transferred to the tower increases the vibration towards X-direction that is coupling with the blade axial vibrations, Y-direction which is coupling with the blade out-of-plane vibrations and Z-direction that is coupling with blade in-plane vibrations. Furthermore, the change to drive shaft orders due to the bending increases

has been found to be greater at axis1 than axis2 which has been measured by laser sensors located in those directions.

Looseness of one bearing bolt directly affected the drive shaft behaviour. The rise in centrifugal forces with speed increase affected the shaft deflection coupling with the blade axial vibrations. The effect is pronounced on the shaft centreline paths, where it changes the displacements when identifying the calculated shaft centreline orbits at significant shaft harmonics 1X, 2X, 3X, and 4X. The tower vibration at X-direction was found to be more affected than other directions due to the coupling with the blade axial vibrations.

A compressed air burst was subjected directly to the rotor blade upwind for modelling the transient gust effects on the wind turbine. The blade out-of-plane strain and tower acceleration at Y-direction were affected positively more than other directions. However, it didn't show any effect on the relative shaft displacement and phase.

The transient mass collision and reduction were the next tests that were implemented for vibration monitoring. The removed mass was coming off from the rotor blade during an unbalance test (adding 200 g mass), to create three different cases in a single test: unbalanced, transient, and balanced cases. However, the collision mass excited a high vibration response in the blade, drive shaft, and tower due to blade rotation disruption which also affected the applied torque from the servo-motor.

During the more than one year of various imbalance and transient tests, a 4 cm fatigue crack was found to have initiated in the tower foundation. Signal analysis of the tower acceleration measured by the triaxial accelerometer was utilised for identifying the crack initiation. Furthermore, tower fundamental frequencies have been analysed to detect the tower resonance frequency reduction during the crack growth and after the foundation repairs. The reduction in tower frequency from 2.2 Hz to 1.3Hz after February 2018 was detected as the crack in the foundation welding joint grew over time.

Chapter 9 Discussion, conclusion and recommendation

9.1 Discussion

9.1.1 The horizontal-axis wind turbine test rig

The developed wind turbine test rig was successfully utilized for different loading conditions for demonstration of novel vibration condition monitoring methods based on strain and acceleration measurements. This set up provides novel techniques for signal transmission and measurements of simultaneous rotating and non-rotating components for vibration condition monitoring. Additionally, utilizing the Michigan Scientific SR-Series Slip Ring Assembly (SR-SSRA) provided a very efficient mechanism for measuring low-level instrumentation signals and provided low noise strain and acceleration measurements from the rotating components (analog signals) to the CompaqDAQ data acquisition system.

The locations of the strain gauge sensors gave high-precision detection of the blade dynamic vibration, in directions aligned with the rotation plane, out-of-plane and axial components, including both tension and compression effects. The presence of the piezoelectric accelerometer on the beam and blade tip provided reliable results for the different working conditions as well as being robust and readily mounted on the sensitive and rotating components. The built-in source of constant current for the accelerometer operated successfully through a slip ring assembly and provided the means of measuring the acceleration signal from the light weight sensor positioned on the blade tip.

Furthermore, a triaxial accelerometer has also been attached at the top of the tower to detect the fluctuation in three perpendicular planes (XYZ directions) due to transient loads with high-sensitivity to the low-frequency vibrations with low-noise. Laser equipment has been utilized as further novel instrumentation in the current test rig instead of proximity probes for monitoring the bending fluctuation of the rotor shaft due to blade vibrations. It consisted of two LED sensors mounted horizontally at 45^0 with the horizontal axis and the rotor shaft center by two holders designed and manufactured for this test rig. The simultaneous sampling of all 18 channels of sensor

data, including the rotating and non-rotating components, enables significant postprocessing to be achieved, including comprehensive vibration monitoring of the blade and the drive train in the test rig system at various loading conditions.

9.1.2 Theoretical model of the Horizontal-axis wind turbine test rig system

The numerical model of the test rig has been constructed using the SOLIDWORKS software and then assembled into the ANSYS software environment for creating a simulator of the test rig system. The FE beam model has been successfully run with selected analysis after allocating appropriate meshing techniques for each part, to calculate the resulting three-dimensional deformations (in-plane, out-of-plane and axial directions), as well as utilizing explicit analysis to identify the strain analysis at the same directions during impact tests. Utilizing the mechanical contact regions in the test rig model, the relationship between the various contact parts was specified, particularly between the rotating and non-rotating components to model the resulting deformations.

The fundamental resonance frequencies of the test rig have been calculated by using a harmonic response analysis. The dynamic beam strain has been calculated at the 100 rpm shaft rotational speed to simulate the vibration based-strain for the three required directions. The tower acceleration and deformations have been simulated using modal analysis in the three perpendicular directions (Z-lateral, Y-frontal, and X-axial), as well as the rotor shaft deformation during the 100 rpm rotational speed tests. Looseness of one bearing bolt has been dynamically simulated to identify the shaft response during this fault scenario, showing an increase in the rotor shaft displacement due to the increase in the bearing housing gap.

The FE blade model has been simulated at the same loading conditions as tested in the test rig, and showed an increase in the blade deformation corresponding to the experimental beam model deformations. The first 7 fundamental resonance frequencies have been calculated from the harmonic response analysis, and the first few resonances showed good agreement with the measured resonances.

The coupling between the blade in-plane response with tower lateral-Z vibrations and blade out-of-plane response with the tower frontal-Y vibrations have been confirmed

through the analysis with both blade models due to the combined excitation between the rotating and non-rotating components.

9.1.3 Beam vibration condition monitoring in the horizontal small-scale wind turbine test rig

Three solid thin cantilever beams having circular cross section of 1m length and 10 mm diameter were firstly utilized for modelling the wind turbine blades. Two beams were instrumented with strain gauge measurement sensors for vibration condition monitoring during the various tests. Axial vibrations were noted to have a coupling correlation with in-plane vibration due to centrifugal force (and Coriolis force effect) in the rotational plane, whereas increasing the rotational speeds leads to decrease in beam axial vibrations due to the increase in beam stiffness. Increasing the rotor speed to 150 rpm lead to increasing out-of-plane vibrations due to increasing bending forces. However, the in-plane vibration decreased due to decreasing the dynamic bending towards the direction of rotation, providing evidence of the decoupling between in-plane and out-of-plane modes.

The tower vibrations were further affected by the gyroscopic effects caused by the main shaft and tower deflections, further coupling the vibrations in the Y and Z directions. However, decrease in tower axial vibrations can be detected with the increase in rotor speeds. The triaxial direction vibrations increase fatigue on the tower foundation due to the increase in fatigue stresses in the foundation welded joint.
Laser measurements have been utilized for drive shaft vibration condition monitoring, as non-contact sensors for detecting the small shaft displacements due to the beam dynamic vibrations. High rotational speeds can trigger large vibrational amplitudes while the rotor beams pass through critical speeds (resonance speeds), which is due to rising centrifugal forces that excite the beam vibrations. Furthermore, the dynamic vibrations transmitted to the non-rotating parts generates vibrations synchronous with the shaft phase which increase with the rotational speeds. The tower vibration has a pronounced effect on the rotating beam vibrations, and vice-versa, which was obvious on the beam out-of-plane vibrations. Additionally, the coupled effect of the beam axial response and the tower Z-direction vibrations, had a direct effect on increasing the drive shaft axis1 vibrations at around 245^{o} of the shaft rotation.

Rotating and non-rotating sensors showed different sensitivity effects through the various case studies, demonstrating the requirement of using sensitive and low-noise measurements during the tests. It also showed signal consistency with the different loading conditions.

The beam resonant frequencies showed convergence between the theoretical and practical resonant frequencies, with a difference of only 0.04 Hz as shown in table 9.1.

Table 9. 1 The comparison between fundamental beam theoretical and measured resonant frequency

Theoretical Beam resonant frequency	**Practical Beam resonant frequency**
7.85 Hz	7.81 Hz

Additionally, theoretical and practical dynamic strain measurements showed small differences between them when the comparison occured at 100 rpm, as shown in table 9.2. Differences can primarily be attributed to neglecting the aerodynamic effects with the FEA models.

Table 9. 2 Comparison between theoretical and practical rotating beam dynamic strain

Mode	**Theoretical results**	**Practical results**	**Difference %**
Max. axial strain	30.422 e-6	40.124 e-6	9.7
Max. In-plane strain	388.6 e-6	248.56 e-6	140.04
Max. Out-of-plane strain	47.52 e-6	75.844 e-6	28.32

Furthermore, table 9.3 shows the differences between the theoretical and practical tower acceleration amplitudes at 100 rpm.

Table 9. 3 Comparison between theoretical and practical tower acceleration at 100 rpm.

Tower Mode	Theoretical acceleration (m/s^2)	Measured acceleration (m/s^2)	Difference %
Axial (X) direction	0.52	0.58	0.05
Frontal (Y) direction	-0.6	-0.51	0.09
Lateral (Z) direction	0.77	0.73	0.04

Particular artificial faults have been utilized with different rotor speeds for monitoring the rotor beam behaviour and the effect on the drive train during the transient event. The faults comprised imbalance effects; additional tip mass (AMC) and losing tip mass (LMC), to provide imbalance conditions with rotor speed changes. Added mass was noted to increase the axial beam vibrations due to the increase of centrifugal and Coriolis forces in one direction which caused extension of the beam length. This increase resulted in increasing beam strain measurements towards axial, in-plane, and out-of-plane directions, as well as a further effect on the drive shaft behaviour through increasing the dynamic bending towards axes 1 and 2 measured by laser sensors. This increase in the shaft dynamic displacement is different between the arbitrary axes, where it can be noted that axis 1 dynamic amplitude was consistently higher than axis2.

However, LMC illustrated different amplitudes of beam strain measurements compared with AMC. The small loss mass from the beam tip was the apparent reason, despite there being a pronounced imbalance effect during the different rotating speed experiments. Furthermore, beam acceleration measurements showed a higher amplitude for the AMC test when compared to the LMC, despite there being a pronounced increase in the acceleration amplitude due to LMC on the balanced state.

The vibration response of the supported tower was affected by imbalance conditions represented by AMC and LMC, particularly with the coupling between beam out-of-plane and tower Y-direction vibrations during the various speed tests, and between the tower vibration in the Z-direction and beam in-plane vibrations. The tower vibration amplitudes showed increasing amplitudes with imbalance conditions, particularly at 150 rpm. Furthermore, losing the whole beam from the rotor excited higher amplitude response, and was found to impose instability of rotation at all speeds. Due to the low beam inertia corresponding to the hub, the imbalance forces were not high compared

with AMC and LMC. The collision experiment was fulfilled by a 585.92g mass collision with the rotor beam at 50 rpm. This resulted in increasing beam dynamic strains in the axial, in-plane, and out-of-plane orientations, and excited the beam at higher amplitudes due to the nature of the impact. The dynamic bending of the rotor shaft increased towards axes 1 and 2, hence high tower vibration amplitudes were measured in the X, Y, and Z directions.

The bearing fault was applied by inserting a 2 mm looseness from one bearing bolt, though there was minimal change in rotor displacement recorded during this test. The large inertia of the rotary components connected with the drive shaft, the small looseness of one bolt in comparison to the stiffness of the remaining bolt and the low angular velocity prohibited the shaft from having large vibration. Furthermore, the low rotating speed kept the shaft motion in the average range with only minimal effect from the one loose bolt. Utilizing laser sensor signals enabled the identification of shaft characteristics during the looseness experiment at 50 rpm. Despite the slight looseness that was experimented with, vibration was still observed during the test which indicates that bearing faults can be positively identified on the wind turbine test rig system.

9.1.4 Blade vibration condition monitoring in the horizontal small-scale wind turbine test rig

Three blades were manufactured from aluminum sheets, folded carefully to make the hollow blade shape. Thin 10 mm diameter rods were welded in the centre to clamp the blade to the hub by the three Aluminium blocks. Each blade had the ability to adjust the blade pitch angle, and were instrumented with rotating strain gauge sensors, and included the ability to add additional masses on the blade tip. Axial blade vibration was observed to increase as speed increases (particularly after 70 rpm), due to the increase in the centrifugal forces along the blade. This increase reached the maximum amplitude at 120 rpm, which was the maximum speed used for the blade tests. Additionally, the coupling that exists between the blade axial and in-plane modes was exacerbated for the blades due to the increase in the vibrations towards in-plane direction as speed increases. This increase was attributed to the increase in the dynamic

bending of the rotating blade with increases in speed. Increasing the rotor speed also excited the blade vibrations towards the out-of-plane direction. This was identified through the increase in the blade out-of-plane strain at the compression side, which reached the maximum amplitude with speed at 120 rpm. This was also attributed to the increase in Coriolis forces as the speed increases.

Table 9.4 illustrates the differences between theoretical and experimental blade strain results at 100 rpm. Maximum difference of 49.79 µstrain occurred with the in-plane blade strain, while the minimum difference of 28.69 µstrain was observed for the axial strain.

Table 9. 4 Comparison between theoretical and measured rotating blade dynamic strain at 100 rpm.

Mode	Theoretical results	Measured results	Difference %
Max. axial strain	373.5 e-6	344.81 e-6	28.69
Max. In-plane strain	883.6 e-6	833.81 e-6	49.79
Max. Out-of-plane strain	436.5 e-6	482.08 e-6	45.58

Additionally, Table 9.5 shows the differences between the theoretically tower vibrational response and the test rig measurements at the same shaft speed. It can be observed that there was good agreement between the results due to their small differences.

Table 9. 5 Comparison between theoretical and measured tower acceleration at 100 rpm.

Tower Mode	Theoretical acceleration (m/s^2)	Measured acceleration (m/s^2)	Difference %
Axial (X) direction	0.77	0.8	0.03
Frontal (Y) direction	-0.69	-0.71	0.02
Lateral (Z) direction	0.81	0.83	0.02

As the blade vibrations increased with the rotor speed increases, the driveshaft dynamic displacements increase due to the direct effect of the blade response on the

driveshaft bending. Orbit analysis was used for identifying the elliptical path of the drive shaft centreline during the rotor speed changes similar to the rotation with the beam model. It shows that the shaft centreline displacement takes different orbital shapes as the speed increases due to the coupling effect of the blade and tower vibrations.

Increasing the rotor speed generally increases the average shaft orbit amplitudes. This has been observed by bending displacements towards axes 1 and 2, and measured by laser sensors. Depending on the raw signals, the shaft dynamic displacement at axis 1 was consistently greater than shaft displacement towards axis 2 during the considered speed range. The exact reason for this remains unknown, as the laser sensors were carefully and individually calibrated.

The support tower vibration was also affected by increasing rotor speed with the test blades. This effect appeared through tower vibration-based acceleration amplitude towards X, Y, and Z directions, where it was noted that maximum acceleration amplitude response occurred at the highest test speed of 120 rpm. During one test at 120 rpm, it was observed that an instantaneous increase in tower acceleration in the X and Z direction occurred simultaneously at two-time instances: 38.76 sec and 43.23 sec. This demonstrated that coupled vibration occurs simultaneously with the blade axial and in-plane vibrations at this speed due to the rising centrifugal force.

A series of significant fault case studies were investigated with the blade model for confirming appropriate vibration condition monitoring fault detection methods. This comprised of monitoring the rotating and non-rotating component vibrations from the test rig including excitations from both imbalance effects, impact loadings and rotor speed changes. Tests included implementing imbalance cases with rotor speed changes, to identify the dynamic response of the test rig components during the fault conditions. The added mass tests showed increasing blade vibrational responses towards the axial, in-plane, and out-of-plane directions due to blade mass increases in one direction, which lead to an increase in the centrifugal forces with the rotor speed. However, this increase in blade vibrational response during the added mass case has been found to be larger than that measured during the losing mass test, due to the increase in the rotary inertia.

The driveshaft bending displacements were found to increase with the coupling effect (rotor speed increase and imbalance forces) for the AMC and LMC loading conditions. The increase in bending displacement towards axis 2 was less than axis 1, particularly

at 110 rpm. Additionally, a coupling effect between blade vibrations and shaft bending was detected after the rotation stopped by observing that the shaft continued to vibrate due to the excitation from the blade vibrations. Orbit analysis demonstrated the shifting and expanding driveshaft centreline motion due to the imbalance effect. The shaft centreline orbit at AMC tends to appear with a different shape from the shaft centreline orbit in LMC for both 1st and 2nd harmonics. Further, the change to drive shaft orders due to the bending increases was found where axis 1 motion was greater than axis 2 motion, as measured by laser sensors located in those directions.

The tower response was affected by the blade vibration through the increase in vibration towards the X-direction that was coupling with the blade axial vibrations, Y-direction which was coupling with the blade out-of-plane vibrations and Z-direction that was coupling with the blade in-plane vibrations. The imbalance due to the added mass increased the imbalance forces in the direction towards the added mass, which increases the tower twisting response as the rotor speed increases. In addition, the excitation of the out-of-plane blade vibration with the Coriolis forces increases the tower fluctuation back and forth which then increases the Y-direction acceleration.

The looseness of one bearing bolt has a pronounced effect onto the shaft centreline paths due to the increase in centrifugal forces with speed increase, and it affected the shaft deflections coupling with the blade axial mode vibrations. Additionally, it changed the displacements when identifying the calculated shaft centreline orbits at shaft significant harmonics of 1X, 2X, 3X, and 4X rotational speed. However, only a small effect was identified from the bearing bolt looseness on the blade vibrational responses. The tower axial mode showed the greater effect from the bearing bolt looseness than the Y and Z modes due to the increases in centrifugal forces when the blade in the vertical position pulls the hub, and hence the drive shaft, towards the blade axial direction.

The transient mass reduction from the rotor blade was modeled by a sudden 200 g mass removal from the rotor blade at 100 rpm. The mass was removed at 49.65 seconds during an imbalance test to transfer the rotor blade to the balance state after passing through the transient state (mass reduction event). This produced three stages of blade vibrational modes within the same test; unbalance, transient, and balance stages. The transient event excited higher blade frequency response, particularly between the frequencies 2 Hz and 5 Hz, which was shown through the spectrogram analysis.

Additionally, this event affected the tower amplitude through the excitation after the mass reduction, which appeared as spikes in the tower vibrational modes in the X, Y, and Z directions. The driveshaft was also affected by the transient event as it experienced a change in bending displacements due to the change in loading conditions during the three different stages.

The artificial mass collision and reduction tests were performed to demonstrate vibration monitoring of the test rig components. The sudden mass removal test occurred during an unbalance test (adding 200 g mass). However, the collision mass test was used to simulate a bird strike event and was found to excite all components of the blade, drive shaft, and tower due to the blade rotation disruption. The rapid increase in the dynamic vibration dominant signature in the rotor blade, driveshaft, and tower amplitudes occurred at 24.6 seconds which was the collision time. Furthermore, the spectrogram analysis and rotation representation plots (using lasers and triaxial accelerometer signal data), demonstrated the excitation of the higher frequencies.

A special mechanism for compressed air burst excitation was established for subjecting a transient air jet in front of the rotating blade at 100 rpm, for modelling a gust during wind turbine operation. The blade out-of-plane strain was affected positively due to the increase in blade bending. Further, the downstream compressed air affected the tower vibrations, where it was observed to increase the tower lateral (Y-direction) vibration (back side), as well as speed increase effects. However, it didn't produce any noticeable effect on the shaft relative displacement and phase.

9.2 Conclusion

This dissertation presents a study of blade vibration condition monitoring techniques through various case studies implemented on a developed small-scale wind turbine test rig. A solid 10 mm circular cross section cantilever rotating rod was initially chosen for modelling the rotor blades to research the vibration monitoring of the wind turbine test rig, while minimising the aerodynamic effects. The test rig was instrumented with a comprehensive suite of rotating and non-rotating sensors to demonstrate the effectiveness and advantage of the various sensors for fault detection.

Several case studies were considered for experimental testing, chosen to replicate common failure modes experienced in industry, including mass loss, mass reduction, mass collision, imbalance and bearing looseness events. The effect of speed was demonstrated by conducting tests for the case studies at speeds from 10 to 150 rpm.

A Finite element model was created using the finite element method (ANSYS model) of the individual test rig components and the entire assembly considering beam and blade models for comparison with the experiments. The solid rod has also been utilized in the blade root for installation with the rotating hub.

The experiments confirm that the blade behaves like the beam for various case studies (add mass, loss mass, transient mass collision, and transient mass reduction). This was also proved during increasing rotor speed from 40 rpm to 150 rpm where the vibrational response increased significantly through the increased dynamic strain amplitudes at the required directions. The piezoelectric accelerometer affirms the beam behaviour during the increase in rotor speeds through the increase in acceleration amplitude, particularly at the speed range from 110 rpm to 150 rpm. Furthermore, it clarifies the coupling between the tower and blade vibrations. The driveshaft dynamic displacement increases with the increase of blade vibrational modes (axial, in-plane, and out-of-plane), which shows bending towards axes 1 and 2 (arbitrary axes) detected by the laser sensors positioned perpendicular to the shaft rotation plane. The shaft displacement measurements through several tests showed that the rotor shaft fluctuated more towards axis 1 direction than axis 2, possibly due to increasing tip load represented by in-plane and axial beam vibrations.

The effect of imbalance forces with increasing rotor speeds have added new loading conditions on the rotor beam, hence, increasing the amplitude of the tower vibrational response. Furthermore, the tower fluctuation increases more during added mass than losing mass at different rotating speeds. This effect extended to the driveshaft behaviour, where it was noted that the shaft orbits shifted to the right and expanded more in the 1X, 2X, 3X, 4X, and 5X response due to the imbalance effect from added mass more than the losing mass. Losing the whole beam from the rotor system increased the vibrational amplitude in the test rig system due to the imbalance effect of the rotating parts due to the lack of the rotary inertia on the hub, where it excited the vibrations in all the rotating and on-rotating components. Additionally, the

excitation was higher during the transient effect, for instance, mass collision with the rotor beam which increased the vibration rapidly at the collision time.

The applied case studies were performed on a new blade model considering the beam as a supporting part connected with the hub. The increase in axial vibrations with speed was obvious, particularly at speeds higher than 70 rpm due to the increase in the centrifugal forces along with the blade model and the increase in blade dynamic bending leads to increase of in-plane vibrations, and exciting blade out-of-plane vibrations which are increasing with rotating speed as well.

The integrity of the test rig was confirmed by repeatability over many tests, including changing blades, and beams with different loading conditions. Furthermore, the collecting data from different monitoring techniques have also confirmed the integrity of testing procedures using the test rig system. The original test rig condition showed minimal change to shaft motion with speed, confirming blade and hub balance conditions. This was detected by laser sensors during various tests with the beam and blade models with and without artificial faults with different rotating speeds, also demonstrating the calibration integrity.

Rotating and non-rotating sensors showed effective sensitivity to the various case studies. This confirmed the integrity of the transferred signal during different loading conditions and variable rotor speeds. The ease of position and transfer between the blade models was confirmed by the stability of resulting signals and data outcomes as well as the effective detection of low frequency response. Furthermore, the coupling between the vibrational modes was observed by the vibrational measurement of the rotating and non-rotating components during the considered case studies.

The changes in rotating speeds showed consistent trends of the vibration amplitudes in the test rig components during the various tests with the blade and beam. This was confirmed by the identical behaviour of the blade model compared with the cantilever beam at the same speed and loading conditions. Additionally, the strain amplitude of the blade modes increasing with the speed was similar to the beam modes, demonstrating the effective choice of strain gauge positions and connection of the blade to the hub.

A foundation crack was confirmed by various sensors showing a change to the tower fundamental resonance after the fracture occurrence which demonstrated the direct

effect of blade vibration behaviour on the test rig foundation. This incident demonstrated the coupling effect of the vibrations between the wind turbine rotating and non-rotating components. Further, the fatigue failure appeared in the non-rotating parts particularly at the support tower foundation due to the accumulated loading resulting from the rotating parts inertia and excited vibrations.

9.3 Recommendation for future work

The following suggestions are made to consider developing the test rig for future expansion of this research work,

1. Monitoring the torsional vibrations of the tower and main shaft to confirm options for improving condition monitoring.
2. Considering the aerodynamic effect with the case studies by applying a wind gust to generate the rotor motion instead of the servo-motor. A high-velocity fan could be used to provide the required upwind speed and gusts.
3. Considering different blade pitch phase angles in future case studies for blade vibration monitoring.
4. Performing looseness tests of both bearing bolts as a case study.
5. Further investigation of bearing fault detection, including raceway and ball damage tests.
6. Further investigation of implementing particular control system behaviour for blade fault detection and diagnosis.
7. Adopting new aerodynamic blade profiles with similar case studies.
8. Utilizing embedded piezoelectric components for vibration condition monitoring technique to enable monitoring and possible control of blade vibrations.
9. Considering the hub vibration and coupling effect with the non-rotating components with different case studies.
10. Utilizing a graded cantilever beam or hollow beam instead of the solid beam for the comparison between the models.

References

ABB. (2012). MicroFlex e 150 Servo Drive *Mint Basic Programming*.

Abdelrahman, A., & Johnson, D. A. (2014). *Development of a Wind Turbine Test Rig and Rotor for Trailing Edge Flap Investigation: Static Flap Angles Case.* Paper presented at the Journal of Physics: Conference Series.

Adams, D., White, J., Rumsey, M., & Farrar, C. (2011). Structural health monitoring of wind turbines: method and application to a HAWT. *Wind Energy, 14*(4), 603-623.

Al-Hadad, M., Hwais, A. S., McKee, K. K., & Howard, I. (2017). *Rotating and non-rotating sensors for improving condition monitoring of wind turbines.* Paper presented at the 9th Australasian Congress on Applied Mechanics (ACAM9).

Al-Hadad, M., McKee, K. K., & Howard, I. (2019). Vibration characteristic responses due to transient mass loading on wind turbine blades. *Engineering Failure Analysis*.

Al-Hadad, M. A. s., Mckee, K. K., Howard, I., & (2018). Vibration fault detection of fracture in a wind turbine tower foundation. *Conference: SIF2018 At: University of Western Australia*.

Arrigan, J., Pakrashi, V., Basu, B., & Nagarajaiah, S. (2011). Control of flapwise vibrations in wind turbine blades using semi-active tuned mass dampers. *Structural Control and Health Monitoring, 18*(8), 840-851.

Baker, K., Douglas, B., & Howard, I. (1996). *A review of orbit analysis for turbogenerator condition monitoring.* Paper presented at the Proceedings of the First Australasian Congress on Applied Mechanics: ACAM-96.

Banerjee, J., & Kennedy, D. (2014). Dynamic stiffness method for inplane free vibration of rotating beams including Coriolis effects. *Journal of Sound and Vibration, 333*(26), 7299-7312.

Banerjee, J., & Sobey, A. (2002). Energy expressions for rotating tapered Timoshenko beams. *Journal of Sound and Vibration, 254*(4), 818-822.

Basu, B., Zhang, Z., & Nielsen, S. R. (2016). Damping of edgewise vibration in wind turbine blades by means of circular liquid dampers. *Wind Energy, 19*(2), 213-226.

Beards, C. F. (1981). Vibration analysis and control system dynamics. *Chichester, Sussex, England, Ellis Horwood, Ltd.; New York, Halsted Press, 1981. 169 p, 1*.

Bhuta, P. G., & Jones, J. P. (1963). Symmetric planar vibrations of a rotating disk. *The Journal of the Acoustical Society of America, 35*(7), 982-989.

Biswal, S., & Sabareesh, G. (2015). *Design and development of a wind turbine test rig for condition monitoring studies.* Paper presented at the Industrial Instrumentation and Control (ICIC), 2015 International Conference on.

Blanch, M., & Dutton, A. (2003). *Acoustic emission monitoring of field tests of an operating wind turbine.* Paper presented at the Key Engineering Materials.

Buhl, T., Markou, H., Hansen, H., Thomsen, K., & Rasmussen, F. (2006). *Aeroelastic stability analysis and passive instability suppression.* Paper presented at the Proceedings of the 2006 European Wind Energy Conference and Exhibition, Athens, Greece.

Chantharasenawong, C., & Tipkaew, W. (2010). Determination of Wind Turbine Blade Flapwise Bending Dynamics. *Wind Energy, 20*, 22.

Choi, S.-W., Farinholt, K. M., Taylor, S. G., Light-Marquez, A., & Park, G. (2014). Damage identification of wind turbine blades using piezoelectric transducers. *Shock and Vibration, 2014*.

Das, D., Sahoo, P., & Saha, K. (2009). Out-of-plane free vibration analysis of rotating tapered beams in post-elastic regime. *Materials & Design, 30*(8), 2875-2894.

Davide ASTOLFI, F. C., Francesco NATILI. (2019). Wind turbine generator slip ring damage detection through temperature data analysis. *DIAGNOSTYKA, 2019, Vol. 20, No. 3, 20(3)*, 3-9. doi:10.29354/diag/109968

Davidson, J. (2015). simulation and measurement of cycle stresses on a wind turbine test rig. *Curtin University*.

Epaarachchi, J. A., & Clausen, P. D. (2004). *Accelerated full scale fatigue testing of a small composite wind turbine blade using a mechanically operated test rig.* Paper presented at the Structural Integrity and Fracture: Proceedings of the International Conference, SIF 2004.

Esu, O. O. (2016). *Vibration-based condition monitoring of wind turbine blades.* © Ozak-Obazi Oluwaseyi Esu.

Fitzgerald, B., Arrigan,J. and Basu,B. (2010). Damage detection in wind turbine blades using time-frequency analysis of vibration signals. *International Joint Conference on Neural Networks, IJCNN 2010, Barcelona, Spain, 18-23 July, 2010*. doi:DOI: 10.1109/IJCNN.2010.5596790

Gubran, A. A., & Sinha, J. K. (2014). Shaft instantaneous angular speed for blade vibration in rotating machine. *Mechanical Systems and Signal Processing, 44*(1-2), 47-59.

Hall, K. C., Kielb, R. E., & Thomas, J. P. (2006). *Unsteady aerodynamics, aeroacoustics and aeroelasticity of turbomachines*: Springer.

Hansen, M. (2003). Improved Modal Dynamics of Wind Turbines to Avoid Stall-induced Vibrations. *Wind Energy, 6*(2), 179-195.

Hansen, M., Thomsen, K., & Petersen, J. T. (2001). *Rotor whirling modes and their relation to aerodynamic damping (poster).* Paper presented at the 2001 European Wind Energy Conference and Exhibition (EWEC'01).

Hansen, M. H. (2007). Aeroelastic instability problems for wind turbines. *Wind Energy, 10*(6), 551-577.

Hassanzadeh, M. (2012). Cracks in onshore wind power foundations: Causes and consequences. *Elforsk, 11*, 56.

Hoffmann, K. (1974). *Applying the wheatstone bridge circuit*: HBM.

Howard, I. (1995). VIBRATION SIGNAL PROCESSING USING MATLAB®. *Journal of the Australian Acoustical Society, 23*, 9 - 13.

Howard, I., Omerovic, A and Morgan, L. (1997). Frequency Analysis for turbomachinary diagnostics. *Fifth international congress on sound and vibration*, 1001-1009.

Hu, G. Y., Sun, W. L., Wu, A., & Xu, Y. (2012). *Modal Analysis of Three Rotating Blades of Large Wind Turbine.* Paper presented at the Applied Mechanics and Materials.

Huang, C. L., Lin, W. Y., & Hsiao, K. M. (2010). Free vibration analysis of rotating Euler beams at high angular velocity. *Computers & structures, 88*(17), 991-1001.

Inman, D. J. (2017). *Vibration with control*: John Wiley & Sons.
ISO10816. (2015). Mechanical vibration -- Evaluation of machine vibration by measurements on non-rotating parts -- Part 21: Horizontal axis wind turbines with gearbox. *Part 21*(2015).
Jacklin, S. A., & Leyland, J. A. (1987). Small-scale rotor test rig capabilities for testing vibration alleviation algorithms.
Ju, D., & Sun, Q. (2014). Wind turbine blade flapwise vibration control through input shaping. *IFAC Proceedings Volumes, 47*(3), 5617-5622.
Ke, S., Ge, Y., Wang, T., Cao, J., & Tamura, Y. (2015). Wind field simulation and wind-induced responses of large wind turbine tower-blade coupled structure. *The Structural Design of Tall and Special Buildings, 24*(8), 571-590.
Khatri, D. (2009). Structural failures of wind towers and dynamic analysis procedures. *URS Corporation, Los Angeles, USA*.
Kim, H.-C., Giri, P., & Lee, J.-R. (2012). *A real-time deflection monitoring system for wind turbine blades using a built-in laser displacement sensor.* Paper presented at the Proceedings of the 6th European Workshop on Structural Health Monitoring,(EWSHM 2012) 3-6 July 2012, Dresden, Germany.
Krull, F. D. (2014). Wind Turbine Field and Test Rig Testing as Part of the Design Process for Gearboxes: Test and Validation Requirements, Needs and Best Practices for Wind Turbine Gearboxes.
Lai, F.-M., Yang, S.-H., Wu, J.-H., Hsueh, C.-T., Yang, C.-C., Wang, B.-H., & Lan, C.-H. (2011). Development of fatigue test system for small composite wind turbine blades. *Procedia Engineering, 14*, 2003-2013.
Lindenburg, C., & Snel, H. (2003). *Aero-elastic stability analysis tools for large wind turbine rotor blades.* Paper presented at the Proceedings of the 2003 European Wind Energy Conference and Exhibition.
Liu, X., Lu, C., Liang, S., Godbole, A., & Chen, Y. (2015). Influence of the vibration of large-scale wind turbine blade on the aerodynamic load. *Energy Procedia, 75*, 873-879.
Lutschinger, D., & Howard, I. (2013). Experimental tests of wind turbine main shaft motion on a laboratory test rig. *Annual Conference of the Prognostics and Health Management Society 2013*.
Maganti, N. R., & Nalluri, M. R. (2015). Flapwise bending vibration analysis of functionally graded rotating double-tapered beams. *International Journal of Mechanical and Materials Engineering, 10*(1), 1-10.
Malcolm, D. J., & Laird, D. L. (2003). *Modeling of blades as equivalent beams for aeroelastic analysis.* Paper presented at the ASME 2003 Wind Energy Symposium.
Mankowski, O., & Wang, Q. (2016). Real-time Monitoring of Wind Turbine Blade Alignment Using Laser Measurement. *Procedia CIRP, 56*, 128-132.
Mazanoglu, K., & Guler, S. (2017). Flap-wise and chord-wise vibrations of axially functionally graded tapered beams rotating around a hub. *Mechanical Systems and Signal Processing, 89*, 97-107.
Murtagh, P., Basu, B., & Broderick, B. (2005). Along-wind response of a wind turbine tower with blade coupling subjected to rotationally sampled wind loading. *Engineering structures, 27*(8), 1209-1219.
Murtagh, P., Ghosh, A., Basu, B., & Broderick, B. (2008). Passive control of wind turbine vibrations including blade/tower interaction and rotationally sampled turbulence. *Wind Energy, 11*(4), 305-317.

Oette, H. (1974). Calculation of the flapwise bending, edgewise bending, and torsional vibrations of rotor blades with coupled natural modes and frequencies. *Transl. into ENGLISH from the German report DLR-FB-71-108*.

Özdemir, Ö., & Kaya, M. (2006). Flapwise bending vibration analysis of a rotating tapered cantilever Bernoulli–Euler beam by differential transform method. *Journal of Sound and Vibration, 289*(1), 413-420.

Park, G., Farrar, C. R., di Scalea, F. L., & Coccia, S. (2006). Performance assessment and validation of piezoelectric active-sensors in structural health monitoring. *Smart Materials and Structures, 15*(6), 1673.

Park, G., Rutherford, A. C., Wait, J. R., Nadler, B., Farrar, C. R., & Claytor, T. N. (2005). High-frequency response functions for composite plate monitoring with ultrasonic validation. *AIAA Journal, 43*(11), 2431-2437.

Prasad, C. S., Chen, Q.-z., Dimitriadis, G., Bruls, O., & D'Ambrosio, F. (2014). *Advanced Aeroservoelastic Modeling for Horizontal axis Wind Turbines.* Paper presented at the Proceedings of the 9th International Conference on Structural Dynamics, EURODYN 2014.

Qiao, Y.-h., Han, J., Zhang, C.-y., Chen, J.-p., & Yi, K.-c. (2012). Finite element analysis and vibration suppression control of smart wind turbine blade. *Applied Composite Materials, 19*(3-4), 747-754.

Riziotis, V., Voutsinas, S., Politis, E., & Chaviaropoulos, P. (2004). Aeroelastic stability of wind turbines: the problem, the methods and the issues. *Wind Energy: An International Journal for Progress and Applications in Wind Power Conversion Technology, 7*(4), 373-392.

Sever, I. A. (2004). *Experimental validation of turbomachinery blade vibration predictions.* Imperial College London (University of London).

Shum, W. S., & Lin, Z. (2010). Dynamic motion of whirling rods with Coriolis effect. *Applied Mathematical Modelling, 34*(5), 1203-1216.

Spooner, E., Gordon, P., Bumby, J., & French, C. (2005). Lightweight ironless-stator PM generators for direct-drive wind turbines. *IEE Proceedings-Electric Power Applications, 152*(1), 17-26.

Staino, A. (2012). Actuator control of edgewise vibrations in wind turbine blades. *Journal of Sound and Vibration, 331*(6), 1233-1256.

Staino, A., & Basu, B. (2013). *A robust controller with active tendons for vibration mitigation in wind turbine rotor blades.* Paper presented at the Proceedings of the International Symposium on Engineering under Uncertainty: Safety Assessment and Management (ISEUSAM-2012).

Staino, A., & Basu, B. (2015). Emerging trends in vibration control of wind turbines: a focus on a dual control strategy. *Philosophical Transactions of the Royal Society A: Mathematical, Physical and Engineering Sciences, 373*(2035), 20140069.

Wilkinson, M. R., Spinato, F., & Tavner, P. J. (2007). *Condition monitoring of generators & other subassemblies in wind turbine drive trains.* Paper presented at the Diagnostics for Electric Machines, Power Electronics and Drives, 2007. SDEMPED 2007. IEEE International Symposium on.

Xiong, L., Xianmin, Z., Gangqiang, L., Yan, C., & Zhiquan, Y. (2010). Dynamic response analysis of the rotating blade of horizontal axis wind turbine. *Wind Engineering, 34*(5), 543-560.

Yang, W. (2013). Testing and condition monitoring of composite wind turbine blades. *Recent Advances in Composite Materials for Wind Turbine Blade*, 147-169.

Yang, W., Tavner, P., & Wilkinson, M. (2009). Condition monitoring and fault diagnosis of a wind turbine synchronous generator drive train. *IET Renewable Power Generation, 3*(1), 1-11.

Yin, Y.-Q., Zhang, B., Li, Y.-m., & Lu, W.-Z. (2015). Effect of dead load on dynamic characteristics of rotating Timoshenko beams. *Mathematical Problems in Engineering, 2015*.

Zeng, H., & Bert, C. (2001). Vibration analysis of a tapered bar by differential transformation. *Journal of Sound and Vibration, 242*(4), 737-739.

Zhang, Z., & Nielsen, S. R. (2014). *Edgewise vibration control of wind turbine blades using roller and liquid dampers.* Paper presented at the Journal of Physics: Conference Series.

Zhang, Z., Yin, Z., Han, T., & Tan, A. C. (2013). Fracture analysis of wind turbine main shaft. *Engineering Failure Analysis, 34*, 129-139.

Appendix A

This appendix illustrates the MATLAB m-file that used for signal analysis in the small-scale wind turbine test rig.

```
%Script to run data acquisition using National Instrument NI 9234
%Created: November 2015 - Ian Howard
%Developed by Mohammed Al-Hadad: August 2016

    s = daq.createSession('ni');

    s.DurationInSeconds =100;
    Dur = s.DurationInSeconds;

    % sample rate 12800 / sec
    s.Rate = 12800;
    SampleRate = s.Rate
    dt = 1/SampleRate;
    s.addAnalogInputChannel('cDAQ1Mod1', 'ai0', 'Voltage') % strain
gauge blade 1, axial
     StrainFactor1 = 2/(2.13*100*15); % blade 1 strain gauge
    %s.Channels(1).Sensitivity = StrainFactor1;
    s.addAnalogInputChannel('cDAQ1Mod1', 'ai1', 'Voltage') % strain
gauge blade 1, in-plane bending
     StrainFactor2 = 2/(2.13*100*15); % blade 1 strain gauge
    %s.Channels(2).Sensitivity = StrainFactor1;
    s.addAnalogInputChannel('cDAQ1Mod1', 'ai2', 'Voltage') % strain
gauge blade 1, out-of--plane bending
     StrainFactor3 = 2/(2.13*100*15); % blade 1 strain gauge
    %s.Channels(3).Sensitivity = StrainFactor1;
    s.addAnalogInputChannel('cDAQ1Mod1', 'ai3', 'Voltage') % strain
gauge blade 2, in-plane bending
    StrainFactor4 = 2/(2.13*100*15); % blade 2 strain gauge
    %s.Channels(4).Sensitivity = StrainFactor;

    s.addDigitalChannel('cDAQ1Mod2','Port0/Line0:7','InputOnly');

    s.addAnalogInputChannel('cDAQ1Mod3', 'ai0', 'Voltage'); % Laser
displacement L1
    s.addAnalogInputChannel('cDAQ1Mod3', 'ai1', 'Voltage'); % Laser
displacement L2

    [~,idx] = s.addAnalogInputChannel('cDAQ1Mod3', 'ai2',
'Accelerometer'); % Miniature Accelerometer
    s.Channels(idx).Sensitivity = 0.0005123; % V/m/s^2

    [~,idx] = s.addAnalogInputChannel('cDAQ1Mod4', 'ai0',
'Accelerometer'); % Tri-axial Accelerometer
    s.Channels(idx).Sensitivity = 0.01022; % V/m/s^2

    [~,idx] = s.addAnalogInputChannel('cDAQ1Mod4', 'ai1',
'Accelerometer'); % Tri-axial Accelerometer
    s.Channels(idx).Sensitivity = 0.01078; % V/m/s^2

    [~,idx] = s.addAnalogInputChannel('cDAQ1Mod4', 'ai2',
'Accelerometer'); % Tri-axial Accelerometer
```

```
    s.Channels(idx).Sensitivity = 0.01001; % V/m/s^2

  %   s.Channels(13).Sensitivity = 1; % calibration volt/mm
  %   s.Channels(14).SensitivClsity = 1; % calibration volt/mm
  % Start Acquisition

    data2=[];
    data = s.startForeground();
    data(:,1) = data(:,1) * StrainFactor1; % strain gauge blade 1,
axial bending
    data(:,2) = data(:,2) * StrainFactor2; % strain gauge blade 1,
in-plane bending
    data(:,3) = data(:,3) * StrainFactor3; % strain gauge blade 1,
out-of--plane bending
    data(:,4) = data(:,4) * StrainFactor4; % strain gauge blade 2,
(John - in-plane bending)

    % data(:,13) % Laser displacement L1
    % data(:,14) % Laser displacement L2
    % data(:,15) % Minature Accelerometer

    % plotting the time data using the subplot command
        t = 0:dt:Dur-dt;  % Creating time vector

% Strain Gauge Data
        figure(1)
        ax(1)=subplot(4,1,1);
        plot(t,data(:,1),'r-');
        xlabel('Time (sec)');
        ylabel('micro - strain');
        title('Input Voltage data: Channel 1');
     figure(1)
        ax(2)=subplot(4,1,2);
        plot(t,data(:,2),'b-');
        xlabel('Time (sec)');
        ylabel('micro - strain');
        title('Input Voltage data: Channel 2');

        ax(3)=subplot(4,1,3);
        plot(t,data(:,3),'k-');
        xlabel('Time (sec)');
        ylabel('micro - strain');
        title('Input Voltage data: Channel 3');

        ax(4)=subplot(4,1,4);
        plot(t,data(:,4),'g-');
        xlabel('Time (sec)');
        ylabel('Signal (Strain)');
        title('Input Voltage data: Channel 4');


% Digital Encoder Data
        figure(2)
        ex(1)=subplot(3,1,1);
        plot(t,data(:,5),'g-');
        xlabel('Time (sec)');
        ylabel('Signal (Volts)');
```

```
        title('Input Voltage data: Channel 5');

        ex(2)=subplot(3,1,2);
        plot(t,data(:,6),'r-');
        xlabel('Time (sec)');
        ylabel('Signal (Volts)');
        title('Input Voltage data: Channel 6');

        ex(3)=subplot(3,1,3);
        plot(t,data(:,7),'k-');
        xlabel('Time (sec)');
        ylabel('Signal (Volts)');
        title('Input Voltage data: Channel 7');

 % plotting the strain data on the same graph.
       figure(3)
       plot(t,data(:,4),'r');xlabel('Time (sec)'),ylabel('Strain
Amplitude');
       legend('Blade 2 In-plane strain');

% plotting the strain data on the same graph.
      figure(4)
      plot(t,data(:,3),'r');xlabel('Time (sec)'),ylabel('Strain
Amplitude');
      legend('Ou-of-plane bending strain');

% plotting the strain data on the same graph.
     figure(5)
     plot(t,data(:,2),'r');xlabel('Time (sec)'),ylabel('Strain
Amplitude');
     legend('In-plane bending strain');

% plotting the strain data on the same graph.
     figure(6)
     plot(t,data(:,1),'r');xlabel('Time (sec)'),ylabel('Strain
Amplitude');
     legend('Axial bending strain');

% Laser Displacement Sensors
        data2(:,1)=Laser1(data(:,13));
        figure(7)
        lx(1)=subplot(2,1,1);
        plot(t,data2(:,1),'k-');
        xlabel('Time (sec)');
        %ylabel('Laser Signal (Volts)');
        ylabel('Shaft displacement (mm)');
        title('Laser 1: Channel 1');

        data2(:,2)=Laser2(data(:,14));
        lx(2)=subplot(2,1,2);
        plot(t,data2(:,2),'g-');
        xlabel('Time (sec)');
        %ylabel('Laser Signal (Volts)');
        ylabel('Shaft displacement (mm)');
        title('Laser 2: Channel 2');

% Miniature Accelerometer
```

```
        figure(8)
        plot(t,data(:,15),'g-');
        xlabel('Time (sec)');
        ylabel('Acceleration (m/s^2)');
        title('Miniature Acceleration');

% Tri-axial Accelerometer
        figure(26)
        plot(t,data(:,16),'k-');
        xlabel('Time (sec)');
        ylabel('Acceleration (m/s^2)');
        title('Tri-axial Acceleration (X-Direction)');
% Tri-axial Accelerometer
        figure(27)
        plot(t,data(:,17),'k-');
        xlabel('Time (sec)');
        ylabel('Acceleration (m/s^2)');
        title('Tri-axial Acceleration (Y-Direction)');
% Tri-axial Accelerometer
        figure(28)
        plot(t,data(:,18),'k-');
        xlabel('Time (sec)');
        ylabel('Acceleration (m/s^2)');
        title('Tri-axial Acceleration (Z-Direction)');


% Signal average of Strain Gauge 1, 2 and 3
%
       sa_axStrain1= sigavg(data(:,6),data(:,1),dt,1,1024);

%
       sa_InStrain1= sigavg(data(:,6),data(:,2),dt,1,1024);

%
       sa_OutStrain1= sigavg(data(:,6),data(:,3),dt,1,1024);


figure (12)
plot(data2(1:10000,1),data2(1:10000,2));
xlabel('Laser 1 (mm)');
ylabel('Laser 2 (mm)');

figure (13)
plot(data(1:10000,13),data(1:10000,14));
xlabel('Laser 1 (Volts)');
ylabel('Laser 2 (Volts)');


% Laser Displacement Sensors
        figure(14)
        lx(1)=subplot(2,1,1);
        plot(t,data(:,13),'k-');
        xlabel('Time (sec)');
        ylabel('Laser Signal (voltage)');
        title('Laser 1 vs time');

        lx(2)=subplot(2,1,2);
```

```
        plot(t,data(:,14),'g-');
        xlabel('Time (sec)');
        ylabel('Laser Signal (voltage)');
        title('Laser 2 vs time');

% Raw Orbit plot from Lasers
    figure(15)
    plot(data(:,13),data(:,14))
    xlabel('Laser 1 (Volts)');
    ylabel('Laser 2 (Volts)');
% Signal average of Laser displacements
     sa_Laser1=sigavg(data(:,6),data(:,13),dt,1,1024);
     sa_Laser2=sigavg(data(:,6),data(:,14),dt,1,1024);
     f=ospec(sa_Laser1,sa_Laser2);

% Orbit of first shaft order frequency
     [x1,y1] = Orbit_n(sa_Laser1,sa_Laser2,1); odisp(x1,y1)
     set(gca, 'XLim', [-0.3,0.3]);
     set(gca, 'YLim', [-0.3,0.3]);
     set(gca, 'XTick', get(gca, 'YTick'));

% Orbit of first and second shaft order frequency
     [x2,y2] = Orbit_n(sa_Laser1,sa_Laser2,2); odisp(x2,y2)
     set(gca, 'XLim', [-0.5,0.5]);
     set(gca, 'YLim', [-0.5,0.5]);
     set(gca, 'XTick', get(gca, 'YTick'));

% Orbit of first three shaft order frequencies
 [x3,y3] = Orbit_n(sa_Laser1,sa_Laser2,3); odisp(x3,y3);
 set(gca, 'XLim', [-0.5,0.5]);
 set(gca, 'YLim', [-0.5,0.5]);
 set(gca, 'XTick', get(gca, 'YTick'));

% Orbit of first four shaft order frequencies

 [x4,y4] = Orbit_n(sa_Laser1,sa_Laser2,4); odisp(x4,y4);
 set(gca, 'XLim', [-0.5,0.5]);
 set(gca, 'YLim', [-0.5,0.5]);
 set(gca, 'XTick', get(gca, 'YTick'));

 % Orbit of first five shaft order frequencies

 [x5,y5] = Orbit_n(sa_Laser1,sa_Laser2,5); odisp(x5,y5);
 %axis('square',[-.5 .5 -.5 .5])
 set(gca, 'XLim', [-0.5,0.5]);
 set(gca, 'YLim', [-0.5,0.5]);
 set(gca, 'XTick', get(gca, 'YTick'));

 % Orbit of first 10 shaft order frequencies
 [x10,y10] = Orbit_n(sa_Laser1,sa_Laser2,100); odisp(x10,y10);
 %axis('square',[-.5 .5 -.5 .5])
 set(gca, 'XLim', [-0.5,0.5]);
 set(gca, 'YLim', [-0.5,0.5]);
 set(gca, 'XTick', get(gca, 'YTick'));

 % Orbit of first 100 shaft order frequencies
 [x100,y100] = Orbit_n(sa_Laser1,sa_Laser2,100); odisp(x100,y100);
```

```
%axis('square',[-.5 .5 -.5 .5])
set(gca, 'XLim', [-0.5,0.5]);
set(gca, 'YLim', [-0.5,0.5]);
set(gca, 'XTick', get(gca, 'YTick'));

% Orbit of first 500 shaft order frequencies
[x500,y500] = Orbit_n(sa_Laser1,sa_Laser2,500); odisp(x500,y500);
set(gca, 'XLim', [-0.5,0.5]);
set(gca, 'YLim', [-0.5,0.5]);
set(gca, 'XTick', get(gca, 'YTick'));
```

Appendix B

This appendix shows a MATLAB m-files that used for analyse the lase sensors signal to identify average shaft frequency in the small-scale wind turbine test rig

```
function sa = sigavg_no_avg(s,v,dt,vratio,n)
% FUNCTION SIGAVG
% this function computes the time synchronous signal average
% from the two vectors of vibration data and tacho data
% sa = sigavg(s,v,dt,vratio,n)
% where
% s is the signal containing the tachometer data
% v is the signal containing the vibration data
% dt is the sampling time period
% vratio is the fixed velocity ratio between the
% tacho shaft and the shaft of interest
% n is the number of points per revolution required
%  for the signal average
%
% This function uses the M-files
% zcross1 obtain the tacho arrival times
% tacho1 compute the arrival times for the shaft of interest
% and resamp compute the new resampling times for the shaft of
%       interest
%
% written by Dr Ian Howard
% Department of Mechanical Engineering
% Curtin University of Technology
%
% First Compiled 24/03/94
% Latest Modification Date 29/8/08

% compute the arrival times for the shaft of interest

[fs,ts,tsoi] = tacho1(s,dt,vratio);

% display shaft frequency over time record

tdisp1(fs,1/mean(fs));
ylabel('Shaft Frequency (Hz)')
Average_Shaft_Frequency = mean(fs)
Minimum_Shaft_Frequency = min(fs)
% if min(fs)<0.9*mean(fs)
%     disp('Alert with Signal Averaging')
% end

% fs is the rotational frequency vector of the tacho shaft
% ts is the vector of arrival times of the tacho shaft
% tsoi is the vector of arrival times for the shaft of interest

% compute the resample times for the shaft of interest

tr = resamp(tsoi,dt,n);

% resample the vibration data at the resample times
```

```
    % create the vector for the original vibration data
    t = 0:dt:dt*(length(v)-1);

vr = interp1(t,v,tr,'cubic');

% turn vr into a matrix of number of rows mm, number of columns nn
% where mm = n (number of points per rev)
% and nn = length(tsoi)-1, number of complete revolutions

mm = n;
nn = length(tsoi)-1;
number_of_averages = nn
sa = reshape(vr(1:mm*nn),mm,nn);

% average all the rows to obtain the signal average

%sa = sum(sa')/nn;

% display signal average

% tdisp1(sa,360/length(sa)); xlabel('Shaft Rotation (deg)')
```

Appendix C

This appendix illustrates the branches MATLAB m-files that used for spectrum analysis of the measurement signals in the small-scale wind turbine test rig.

```
% this function calculates an estimate of the true power spectrum
% of the time data NOT the PSD as used previously
%
% ps = spectra3(data,lwin,dt,nstep,display)
%
% where
%      data is the time vector
%      lwin is the length of the time window function
%      dt is the sample time period
%      nstep is the number of points to step between each fft
%      display determines whether to use linear or log x axis
scaling
%       display==1 means linear (default)
%       display==0 means log

% check whether axes control was specified
if nargin==4, display=1; end

% number of loops through data
nwin = fix(length(data)/nstep - lwin/nstep)

ps(lwin) = 0;
istart = 1;
iend = lwin;
win = hanning(lwin);
np = lwin/2;
% loop over data vector using window of length lwin
for n = 1:nwin
        % extract data window
        dwin = data(istart:iend);
        % fft the windowed data segment and scale
        freq = fft(win.*dwin)/lwin;
    % compute the magnitude squared and sum
        ps = ps + (freq.*conj(freq))';
    istart = n*nstep + 1;
    iend = istart + lwin - 1;
end

% eliminate negative frequencies,
ps(np+1:lwin) = [];

% double positive frequencies;
ps(2:np) = 2*ps(2:np)/nwin;

% display power spectrum
if (display==0)
    % display spectra using linear x axis and log y axis
    flog(ps,dt,lwin);
elseif (display==1)
```

```
    % display spectra using linear x and y axes
    flin(ps,dt,lwin);
end
```

Appendix D

This appendix shows the signed attribution forms of the co-authors that contributed in the published papers.

Co-author Attribution Approval Statement

Hereby, I, Professor Ian Howard, confirm that the following is my joint publication with Mohammed Al-Hadad. I, as a co-author, endorse that the level of all authors' contribution is accurately and appropriately addressed in the following table. I also consent this paper to be used in the thesis "Vibration Fault Detection for Horizontal Axis Wind Turbines (HAWT)", submitted for the Degree of PhD in Mechanical Engineering of Curtin University.

Paper: Mohammed Al-Hadad, Kristoffer K McKee, Ian Howard, "Vibration characteristic responses due to transient mass loading on wind turbine blades", Engineering Failure Analysis, 102, pp. 187-202.

Author's affiliation (in order of appearance in published version of paper):

1- Mohammed Al-Hadad, Faculty of Science and Engineering, School of Civil and Mechanical Engineering, Curtin University, Perth, Australia.

2- Kristoffer K McKee, Faculty of Science and Engineering, School of Civil and Mechanical Engineering, Curtin University, Perth, Australia.

3- Ian Howard, Faculty of Science and Engineering, School of Civil and Mechanical Engineering, Curtin University, Perth, Australia.

		Conception and Design	Acquisition of method	Data manipulation	Interpretation & discussion	Paper drafting	Paper revising	Final approval
Authors	Mohammed Al-Hadad	X	X	X	X	X	X	X
	Ian Howard			X	X	X	X	X
		I acknowledge that these represent my contribution to the above research output. Signed ..... Date						
	Kristoffer K McKee				X	X	X	X

Co-author Attribution Approval Statement

Hereby, I, Professor Ian Howard, confirm that the following is my joint publication with Mohammed Al-Hadad. I, as a co-author, endorse that the level of all authors' contribution is accurately and appropriately addressed in the following table. I also consent this paper to be used in the thesis "Vibration Fault Detection for Horizontal Axis Wind Turbines (HAWT)", submitted for the Degree of PhD in Mechanical Engineering of Curtin University.

Paper: Mohammed Al-Hadad, Kristoffer K McKee, Ian Howard, "Vibration fault detection of fracture in a wind turbine tower foundation.", Proceedings of the 11th International Conference on Structural Integrity and Failure (SIF-2018) 3-6 December 2018, UWA Perth.

Author's affiliation (in order of appearance in published version of paper):

1- Mohammed Al-Hadad, Faculty of Science and Engineering, School of Civil and Mechanical Engineering, Curtin University, Perth, Australia.

2- Kristoffer K McKee, Faculty of Science and Engineering, School of Civil and Mechanical Engineering, Curtin University, Perth, Australia.

3- Ian Howard, Faculty of Science and Engineering, School of Civil and Mechanical Engineering, Curtin University, Perth, Australia.

		Conception and Design	Acquisition of method	Data manipulation	Interpretation & discussion	Paper drafting	Paper revising	Final approval
Authors	Mohammed Al-Hadad	X	X	X	X	X	X	X
	Ian Howard			X	X	X	X	X
		I acknowledge that these represent my contribution to the above research output. Signed ..... Date						
	Kristoffer K McKee				X	X	X	X

Co-author Attribution Approval Statement

Hereby, I, Professor Ian Howard, confirm that the following is my joint publication with Mohammed Al-Hadad. I, as a co-author, endorse that the level of all authors' contribution is accurately and appropriately addressed in the following table. I also consent this paper to be used in the thesis "Vibration Fault Detection for Horizontal Axis Wind Turbines (HAWT)", submitted for the Degree of PhD in Mechanical Engineering of Curtin University.

Paper: Mohammed Al-Hadad, Abdullah Slebe Hwais, Kristoffer K McKee, Ian Howard, "Rotating and non-rotating sensors for improving condition monitoring of wind turbines. Proceedings of Australasian Congress on Applied Mechanics, ACAM 9, Sydney, November 2017.

Author's affiliation (in order of appearance in published version of paper):

1- Mohammed Al-Hadad, Faculty of Science and Engineering, School of Civil and Mechanical Engineering, Curtin University, Perth, Australia.

2- Abdullah Slebe Hwais, Faculty of Science and Engineering, School of Civil and Mechanical Engineering, Curtin University, Perth, Australia.

3- Kristoffer K McKee, Faculty of Science and Engineering, School of Civil and Mechanical Engineering, Curtin University, Perth, Australia.

4- Ian Howard, Faculty of Science and Engineering, School of Civil and Mechanical Engineering, Curtin University, Perth, Australia.

		Conception and Design	Acquisition of method	Data manipulation	Interpretation & discussion	Paper drafting	Paper revising	Final approval
Authors	Mohammed Al-Hadad	X	X	X	X	X	X	X
	Abdullah Slebe Hwais				X	X		
	Ian Howard			X	X	X	X	X
	Ian Howard	I acknowledge that these represent my contribution to the above research output. Signed ..... Date						
	Kristoffer K McKee				X	X	X	X

Co-author Attribution Approval Statement

Hereby, I, Dr Kristoffer K McKee, confirm that the following is my joint publication with Mohammed Al-Hadad. I, as a co-author, endorse that the level of all authors' contribution is accurately and appropriately addressed in the following table. I also consent this paper to be used in the thesis "Vibration Fault Detection for Horizontal Axis Wind Turbines (HAWT)", submitted for the Degree of PhD in Mechanical Engineering of Curtin University.

Paper: Mohammed Al-Hadad, Kristoffer K McKee, Ian Howard, "Vibration characteristic responses due to transient mass loading on wind turbine blades", Engineering Failure Analysis, 102, pp. 187-202.

Author's affiliation (in order of appearance in published version of paper):

1- Mohammed Al-Hadad, Faculty of Science and Engineering, School of Civil and Mechanical Engineering, Curtin University, Perth, Australia.

2- Kristoffer K McKee, Faculty of Science and Engineering, School of Civil and Mechanical Engineering, Curtin University, Perth, Australia.

3- Ian Howard, Faculty of Science and Engineering, School of Civil and Mechanical Engineering, Curtin University, Perth, Australia.

		Conception and Design	Acquisition of method	Data manipulation	Interpretation & discussion	Paper drafting	Paper revising	Final approval
Authors	Mohammed Al-Hadad	X	X	X	X	X	X	X
	Kristoffer K McKee				X	X	X	X
		I acknowledge that these represent my contribution to the above research output. Signed ..... Date .....10 July 2019…….						
	Ian Howard			X	X	X	X	X

Co-author Attribution Approval Statement

Hereby, I, Dr Kristoffer K McKee, confirm that the following is my joint publication with Mohammed Al-Hadad. I, as a co-author, endorse that the level of all authors' contribution is accurately and appropriately addressed in the following table. I also consent this paper to be used in the thesis "Vibration Fault Detection for Horizontal Axis Wind Turbines (HAWT)", submitted for the Degree of PhD in Mechanical Engineering of Curtin University.

Paper: Mohammed Al-Hadad, Kristoffer K McKee, Ian Howard, "Vibration fault detection of fracture in a wind turbine tower foundation.", Proceedings of the 11th International Conference on Structural Integrity and Failure (SIF-2018) 3-6 December 2018, UWA Perth.

Author's affiliation (in order of appearance in published version of paper):

1- Mohammed Al-Hadad, Faculty of Science and Engineering, School of Civil and Mechanical Engineering, Curtin University, Perth, Australia.

2- Kristoffer K McKee, Faculty of Science and Engineering, School of Civil and Mechanical Engineering, Curtin University, Perth, Australia.

3- Ian Howard, Faculty of Science and Engineering, School of Civil and Mechanical Engineering, Curtin University, Perth, Australia.

		Conception and Design	Acquisition of method	Data manipulation	Interpretation & discussion	Paper drafting	Paper revising	Final approval
Authors	Mohammed Al-Hadad	X	X	X	X	X	X	X
	Kristoffer K McKee				X	X	X	X
		I acknowledge that these represent my contribution to the above research output. Signed …… Date ……10 July 2019……						
	Ian Howard			X	X	X	X	X

Co-author Attribution Approval Statement

Hereby, I, Dr Kristoffer K McKee, confirm that the following is my joint publication with Mohammed Al-Hadad. I, as a co-author, endorse that the level of all authors' contribution is accurately and appropriately addressed in the following table. I also consent this paper to be used in the thesis "Vibration Fault Detection for Horizontal Axis Wind Turbines (HAWT)", submitted for the Degree of PhD in Mechanical Engineering of Curtin University.

Paper: Mohammed Al-Hadad, Abdullah Slebe Hwais, Kristoffer K McKee, Ian Howard, "Rotating and non-rotating sensors for improving condition monitoring of wind turbines". Proceedings of Australasian Congress on Applied Mechanics, ACAM 9, Sydney, November 2017.

Author's affiliation (in order of appearance in published version of paper):

1- Mohammed Al-Hadad, Faculty of Science and Engineering, School of Civil and Mechanical Engineering, Curtin University, Perth, Australia.

2- Abdullah Slebe Hwais, Faculty of Science and Engineering, School of Civil and Mechanical Engineering, Curtin University, Perth, Australia.

3- Kristoffer K McKee, Faculty of Science and Engineering, School of Civil and Mechanical Engineering, Curtin University, Perth, Australia.

4- Ian Howard, Faculty of Science and Engineering, School of Civil and Mechanical Engineering, Curtin University, Perth, Australia.

		Conception and Design	Acquisition of method	Data manipulation	Interpretation & discussion	Paper drafting	Paper revising	Final approval
Authors	Mohammed Al-Hadad	X	X	X	X	X	X	X
	Abdullah Slebe Hwais				X	X		
	Kristoffer K McKee				X	X	X	X
		I acknowledge that these represent my contribution to the above research output. Signed ..... Date .....10 July 2019						
	Ian Howard			X	X	X	X	X

Co-author Attribution Approval Statement

Hereby, I, Abdullah Slebe Hwais, confirm that the following is my joint publication with Mohammed Al-Hadad. I, as a co-author, endorse that the level of all authors' contribution is accurately and appropriately addressed in the following table. I also consent this paper to be used in the thesis "Vibration Fault Detection for Horizontal Axis Wind Turbines (HAWT)", submitted for the Degree of PhD in Mechanical Engineering of Curtin University.

Paper: Mohammed Al-Hadad, Abdullah Slebe Hwais, Kristoffer K McKee, Ian Howard, "Rotating and non-rotating sensors for improving condition monitoring of wind turbines. Proceedings of Australasian Congress on Applied Mechanics, ACAM 9, Sydney, November 2017.

Author's affiliation (in order of appearance in published version of paper):

1- Mohammed Al-Hadad, Faculty of Science and Engineering, School of Civil and Mechanical Engineering, Curtin University, Perth, Australia.

2- Abdullah Slebe Hwais, Faculty of Science and Engineering, School of Civil and Mechanical Engineering, Curtin University, Perth, Australia.

3- Kristoffer K McKee, Faculty of Science and Engineering, School of Civil and Mechanical Engineering, Curtin University, Perth, Australia.

4- Ian Howard, Faculty of Science and Engineering, School of Civil and Mechanical Engineering, Curtin University, Perth, Australia.

		Conception and Design	Acquisition of method	Data manipulation	Interpretation & discussion	Paper drafting	Paper revising	Final approval
Authors	Mohammed Al-Hadad	X	X	X	X	X	X	X
	Abdullah Slebe Hwais				X	X		
		I acknowledge that these represent my contribution to the above research output. Signed [redacted]..... Date ...10/7/2019.....						
	Kristoffer K McKee				X	X	X	X
	Ian Howard			X	X	X	X	X